Structure and composition of bismuth and silver bismuth films electrodeposited from deep eutectic solvents

A thesis submitted for the degree of

Doctor of Philosophy

University of Leicester

by

Shiroma Iranga Marian Perera

Department of Chemistry

October 2018

Structure and composition of bismuth and silver bismuth films electrodeposited from deep eutectic solvents

∾✾∽

Shiroma Iranga Marian Perera

Electrodeposited coatings of silver and bismuth (as individual metals, alloyed or multi-layered) are used extensively in a range of engineering applications. Fabrication of these coatings is commonly achieved via electrochemical deposition using aqueous electrolytes containing strong alkali or cyanide that present environmental issues. We investigate the possibility of bismuth metal deposition and silver-bismuth co-deposition from an environmentally benign, deep eutectic solvent (DES), ethaline 200 (choline chloride: ethylene glycol in 1:2 stoichiometric ratio). We report the first application of a range of electroanalytical techniques (potential step voltammetry, linear sweep voltammetry, cyclic voltammetry, electrogravimetry using a quartz crystal microbalance) to quantitatively characterise the properties of electrochemical reactions for these metal systems in a DES. These techniques were based on both static and hydrodynamic electrodes (i.e. rotating disk electrode (RDE)). A fundamental study into nucleation mechanisms and growth kinetics of silver, bismuth and silver/ bismuth deposition was carried out. We found nucleation for silver and bismuth to be instantaneous at high overpotentials and progressive at low overpotentials; both were followed by diffusion controlled 3D growth. The average stripping efficiencies for silver and bismuth had a range between 74 -89% while stripping efficiency for silver/ bismuth co-deposit was ca. 36%. RDE methods were used to calculate diffusion coefficients, heterogeneous rate constants, transfer coefficients and standard rate constants for these metal systems. The metal films deposited were analysed using simultaneous thickness and electrochemical potential (STEP) measurements for multi-layer metals, X-ray diffraction (XRD), energy dispersive X-ray spectroscopy (EDAX) and atomic force microscopy (AFM). From these methods we were able to identify intermetallics of silver/ bismuth, crystalline phases formed, composition (Ag: Bi ratio), surface morphology (including surface roughness) and film thickness respectively. We report observations of deposition and dissolution of these metals using the novel, non-invasive techniques: combined electrochemical quartz crystal microbalance (EQCM)/ probe beam deflection (PBD). Electrochemistry (E) provides control of the interfacial reactions and gives an overall measure of rate, the acoustic wave (QCM) response yields the deposited mass at the interface and the optical signal (PBD) provides information on solution chemistry of the reactants and products.The experimental protocol was shown to be successful in analysis of metal systems in DES. The combined data were used to deduce mechanistic details e.g. changes in speciation of metals involved during each potential region, underpotential deposition regions of bismuth, mole fractions of Ag:Bi during co-deposition.

Statement

ၜၟ

The accompanying thesis submitted for the degree of Ph.D. entitled "Structure and composition of bismuth and silver-bismuth films electrodeposited from deep eutectic solvents" is based upon work conducted by the author in the Department of Chemistry at the University of Leicester during the period between October 2014 and October 2018. All the work recorded in this thesis is original unless otherwise acknowledged in the text or by references. None of the work has been submitted for another degree in this or any other university.

20-06-2019

Signed

Date

S. I. M. Perera

Acknowledgements

❧

It would not have been possible to write this doctoral thesis without the help and support I received from family, friends, colleagues and collaborators. I am truly grateful to every one of you.

I would like to thank my supervisors Professors A. Robert Hillman and Karl S. Ryder for their immense guidance and support throughout my PhD.

I would like to thank Nina-Juliane Steinke of ISIS (Harwell, UK) and Robert Barker of ILL (Grenoble, France).

My parents Shreene and Nihal and my grandfather Francis for inspiring me to study electrochemistry. Above all, my appreciation and gratitude goes to Harshana for his support throughout the course of my PhD.

List of Abbreviations

AFM atomic force microscopy

CE   counter electrode

CVD chemical vapor deposition

DES   deep eutectic solvent

EDAX energy-dispersive X-ray spectroscopy

EDL   electrical double layer

EDTA ethylenediaminetetraacetic acid

EQCM electrochemical quartz crystal microbalance

ITO   indium tin oxide

MEMS micro-electromechanical system

PBD   probe beam deflection

PVD   physical vapor deposition

QAS   quarternary ammonium salt

QCM quartz crystal microbalance

RDE   rotating disk electrode

RE   reference electrode

SEM   scanning electron microscope

STEP simultaneous thickness and electrochemical potential

ULSI ultra-largescale integration

WE working electrode

XRD X-ray diffraction

Nomenclature

α transfer coefficient

$\bar{\nu}$ kinematic viscosity

ChCl Choline chloride

Δf frequency change

δm mass change (g)

λ wave length

μ dynamic viscosity of the fluid

μ_q shear modulus of Quartz for an AT cut crystal

ω speed of rotation

ϕ electrostatic potential

ρ density of the fluid

Θ beam divergence angle

θ angle of deflection

θ^+ optical deflection of designated positive direction

θ^- optical deflection of designated negative direction

θ_{max} maximum angle of deflection

A piezo electric active area of crystal

BD beam diameter

d beam electrode distance

d_0 initial laser beam diameter

d_z distance between laser and the focusing lense

dm change in mass (small)

dQ change in charge (small)

F Faraday constant

f focal length

f_0 resonant frequency (Hz)

f_{PBD} RMM Relative molar mass

J_0 diffusional flux

J_k the flux due to species k

l a characteristic linear dimension

M molar mass

M_{av} average mass exchange

M_{ion} mass of ions

$M_{neutral}$ mass of neutral species

n' number of molecules exchanged

p_q density of quartz

Q total charge

r radius of the electrode

Re Reynolds number

S laser beam interaction length

u velocity of the fluid

V applied voltage

V_x velocity of solution in x direction

x distance

X_{Ag} molar fraction of Ag

X_{Bi} mole fraction of bismuth

BD_{fp} beam diameter at focal point

Contents

Chapter 1

Introduction

Contents

1.1 Background

1.1.1 Historical background

Electrodeposition can be defined as the process of producing a coating of a metal, alloy, semi-conductor or polymer film on a substrate using an electric current.[1] In most instances the aim of electrodeposition is to achieve a uniform, adherent and thick coating. The coating is deposited by making the substrate the negative electrode for metals and alloys in an electro-chemical cell where the electrolyte contains the ions of the metal to be deposited (or making the substrate positive electrode for metal oxides e.g. MnO_2, PbO_2). The current passed through the electrodes deposit the metal which changes the properties of the underlying substrate.

Scientists started generating an interest in depositing metals in the early 1800s. The first successful electrodeposition was achieved by Italian chemist Luigi Brugnatelli in 1805.[2] He electrodeposited gold using the voltaic pile, discovered by his colleague Alessandro Volta in 1800.[3] He made his circuit by connecting a wire between a voltaic pile (a battery) and a metal object in a solution of dissolved gold and as the current flowed the gold deposited on to the surface of the metal object to give a shiny coating. During the next few decades, there was limited progress on extending this to an industrial scale due to the absence of a reliable power source that generated steady current flow at a low voltage for a long duration. In 1936, J. F. Daniell developed the Daniell cell, a self-polarising cell, enabled a thin but uniform metal coating to to be deposited.[4] Subsequently, gold and silver plating using respective metals dissolved in potassium cyanide were discovered by John Wright of Birmingham in 1840. This approach later achieved considerable commercial success in plating hollowware and flatware.[5]

Modern electrodeposition (or electroplating) has lead to scientific development that allows depositing materials atom by atom with sophisticated, controllable structures and properties from solutions containing ionic species (salts).[6] External properties of the surface such as grain dimension, preffered orientation, atomic density gradients and composition can be changed during the fabrication of thin films.[7] Depending on the material, substrate and the condition of deposition, electrodeposition yields a range of nano- and microstructures.[8–14] The majority of electrodeposits exist in one of three crystallographic forms (habits): face-centered cubic (fcc), body-centered cubic (bcc) or hexagonal close packing (hcp).[15] Crystals are formed by atoms arranged in a uniform three-dimensional array and they combine into grains. Grain shape and size are determined by the plating conditions and the composition of the solution.[16] The substrates' interatomic distance in a particular crystal plane may determine the type of the deposit if they closely match each other. There may be many factors affecting epitaxial growth. In a granular electrodeposit, there is a higher percentage of atoms associated with grain boundaries, interfacial zones and hence are high-energy regions facilitating the grain growth.[17] The crystalline arrangement can change at grain boundaries to accommodate different orientations. This creates defects which can be dislocations (slipping), twins (special type of grain that possesses two boundaries), and co-deposited foreign atoms or molecular groups (due

to additives or impurities).[5]

Due to modern analysis and processing methods, electrodeposition has become a nanotechnology enabler[18] facilitating many innovations: nano sized copper grain deposition,[19] ultra-large-scale integration (ULSI) and micro-electromechanical system (MEMS) packaging,[20] thermoelectric,[21,22] magnetics,[23] solar energy conversion,[24,25] stress-controlled structures,[26] catalysts, and phase change materials.[27] Furthermore electrodeposition has its classical uses in terms of corrosion protection, abrasion resistance and decorative quality to the surface (Fig. 4.1).

Optical properties

- Colour: aesthetic appearance (brass-plated furniture and lighting fittings)
- Brightness: decorative appearance/reflectivity (chromium-plated taps, silver mirrors)

Physical properties

- Electrical conductivity: current conduction on surface (copper tracks on printed circuit boards)
- Thermal conductivity: improved heat transfer on surface (copper-plated saucepan bottoms for electric-cookers)
- Magnetic conductivity: high coercivity (cobalt-nickel alloys on magnetic storage)

Chemical properties

- Chemical protection: resistance to chemical attack (lead-tin coatings as etched resistance for printed circuit boards)
- Corrosion protection: resistance to corrosion attack (zinc and its alloys on steel components)

Mechanical properties

- Ductility: improved plastic performing (copper coatings on drilling punches in multi-layer printed circuit boards)
- Hardness: improved adhesive wear-resistance (nickel or phosphorus coatings for mining equipment)

Technological properties

- Friction reduction: improved dry-running (lead-tin-copper coatings)
- Adhesion: improved adhesion (brass coatings on steel wires)
- Solderability: soldering without aggressive fluxes (zinc-lead coatings on printed circuit board tracks)
- Lubricity: improved mobility (copper plating for wire drawings)
- Wear resistance: improved lifetime (hard chromium-plated tools)
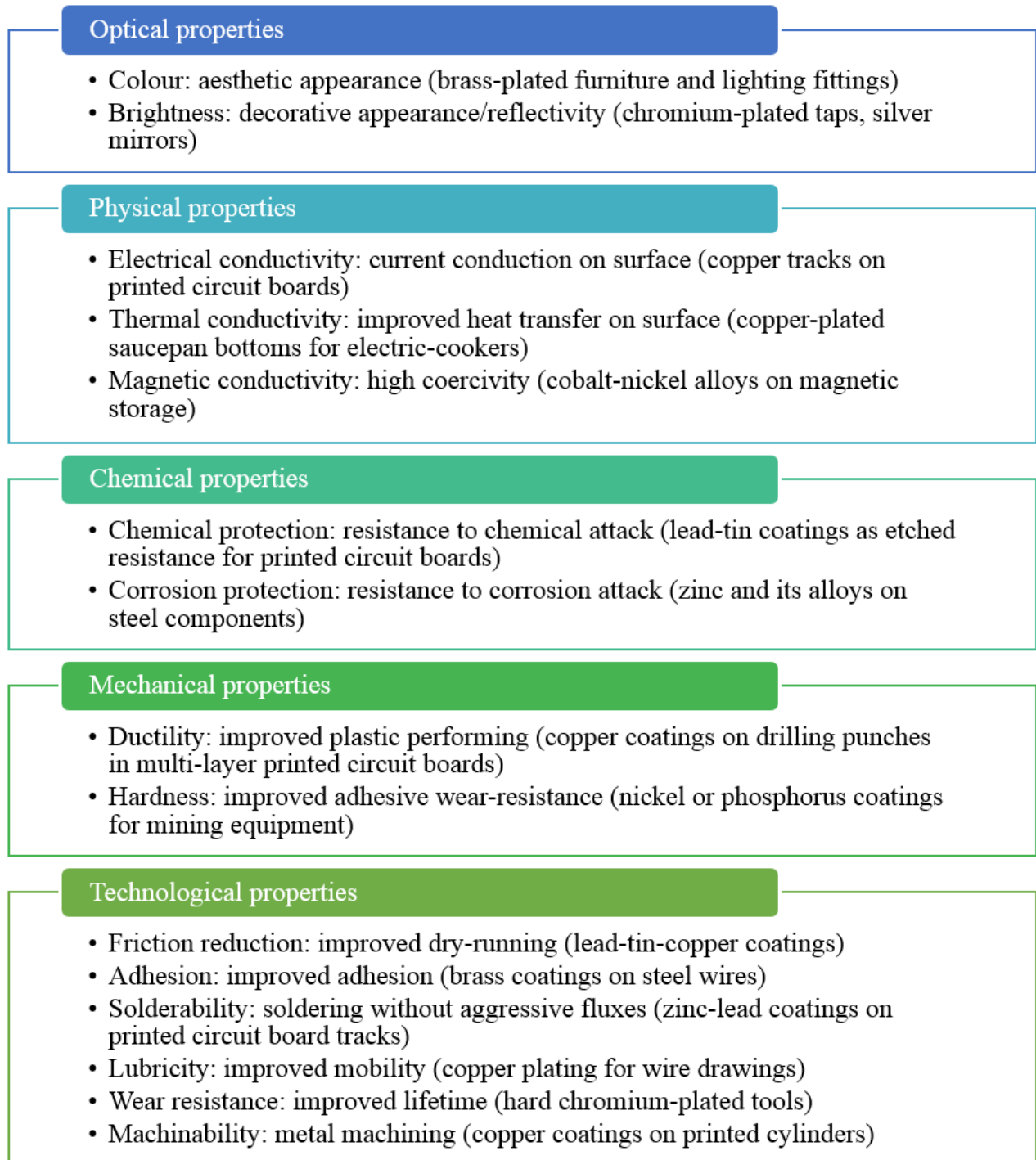- Machinability: metal machining (copper coatings on printed cylinders)

Fig. 1.1 Properties and application examples of electrodeposited coatings[28]

1.1.2 Electrodeposition of silver

Electrodeposition of silver has numerous applications[29,30] despite coatings having drawbacks such as low hardness, low wear resistance, tarnishing and relatively high friction coefficient. Silver is commonly applied in the semiconductor industry due to its properties such as excellent thermal and electrical conductivity.[31–33] Numerous methods have been used to overcome the drawbacks e.g. reducing the grain size to the hundred nanometre scale,[34–39] introducing hard nanoparticles forming composites of Ag[40–42] and making Ag-based alloys.[31,34,43–47]

Many techniques have been reported for silver deposition: physical vapor deposition (PVD), chemical vapor deposition (CVD), and magnetron sputtering and electrodeposition.[48] From all these methods, electrodeposition has attracted a great deal of research interest due its economical feasibility, tunable nature to produce metallic alloys with unique compositions and novel micro/nanostructures.[35,41,49]

Despite awareness of the environmental threat posed by cyanide, industrial electrodeposition processes are still predominantly cyanide based, similar to those devised by John Wright and the Elkington brothers in the 1840s.[50] This method typically uses silver as $KAg(CN)_2$, potassium cyanide and pottasium carbonate. Complexes of antimony, selenium and sulphur containing organic compounds are used to increase the hardness (and consequentially the brightness) of the deposits. Addition of selenium usually results in improved electrical properties. Frequent issues in this process include anode purity (due to impurities such as copper, iron, lead, bismuth, selenium, sulphur) which results in inhibited dissolution of silver and insufficient concentration of free cyanide which results in improper dissolving of the anode.

High-speed selective electrodeposition is used by the electronic industry when lead frames in electronic components are selectively deposited with silver. The silicon chips and aluminum wires are bonded to silver using ultrasonic or thermosonic bonding methods. Orthophosphates or nitrates (with borates) are used as conducting salts to facilitate buffering to prevent cyanide depletion due to lowering pH during electrodeposition. Noncyanide systems have been explored in order to establish a more environmentally friendly alternative for depositing silver. Five main groups of compounds have been studied for this purpose.[50]

1. **Iodide solutions:** solution typically consists of silver iodide, potassium iodide and hydrogen iodide/hydrogen chloride. The main drawback of this solution is the high cost of iodide salts.

2. **Trimetaphosphate solution:** solution typically consists of silver trimetaphosphate, sodium trimetaphosphate, tetrasodium pyrophospate, tetrasodium EDTA and sodium fluoride. This electrolyte was developed for electrodepositing silver on magnesium and alloys.

3. **Thiosulfate solutions:** electrolytes usually contains silver thiosulfate, sodium thiosulfate and sodium metabisulfite. Sodium metabisulfite is used to reduce precipitation of insoluble silver compounds that may form due to the rapid oxidation of the silver complex.

A key advantage of using this solution is that the thickness distribution of the coating is better on complex-shaped objects. However, the electrodeposits are reported to tarnish quicker in air than those prepared using cyanide solutions.

4. **Succinimide solutions:** solutions consist of potassium silver disuccinimide, succinimide and potassium sulfate (or potassium citrate). Addition of amines (e.g. ethyldiamine) increases brightness of the deposit.

5. **Organic solvent solutions:** A mixture of silver chloride, thiourea and aluminum chloride in a dimethylformamide solvent can be used for silver deposition. In subsequent parts of this chapter, we will focus on nonaqueous solvents with a particular focus on ionic liquids.

1.1.3 Electrodeposition of bismuth

Early applications of bismuth included the use as semi-conductor alloys[51] and and in liquid metal fuel reactors.[52] In recent years, bismuth has been used as a environmentally safer alternative replacing mercury and lead in various applications (e.g. ballistics, soldering for water pipes etc.). Bismuth is predominantly used as metallurgical and pharmaceutical additives and most of these applications make it difficult to recycle the bismuth used.[53] There are growing concerns about the high usage of bismuth in cosmetic products. A study conducted in Stockholm found that approximately 24% of the total Bi amount per year reaching waste water treatment was due to cosmetic products. This form of bismuth ends up in sewage sludge, limiting reuse of this valuable metal resource.[54] Morphologies of bismuth electrodeposits are influenced by the conditions during the process (Fig. 1.2). Research by Gerwirth and co-workers reported an adlayer structure of bismuth on Au(111) using in situ methods in $HClO_4$ solution.[55] Subsequently, Morin and co-workers explored epitaxial single crystal films of bismuth on Au(111).[56,57] In their study, in aqueous $HClO_4$ solution, they reported a nearly rectangular unit cell with 3.9 ± 0.1 and 4.3 ± 0.1 nm dimensions. This can be understood as having the short side for unit cell along long edge of Bi needles and this effectively stops the addition of atoms along the edges. Therefore, they explained diffusion and incorporation of atoms at the needle tip resulting in observed anisotropy in Bi growth.

The importance of bismuth in modern industry has increased due to its unique chemical, physical and electrical properties. When exposed to a magnetic field, bismuth shows a greater change of resistance than any other substance. This tendency of changing electrical resistance in the presence of an external magnetic field is known as magnetoresistance.[58–60] In bismuth, it has been found that this property changes with the orientation of its crystal structure. Materials with complex crystal structures contain quite intricate Fermi surfaces. This is largely owing to the highly anisotropic Fermi surface created through the existence of multiple bands crossing the Fermi energy along the specific direction. The increase of resistance has been found to be largest when the cleavage plane of the crystal is parallel to the magnetic field, and when the current is flowing perpendicular to it. The anisotropic nature of the Fermi surface has resulted
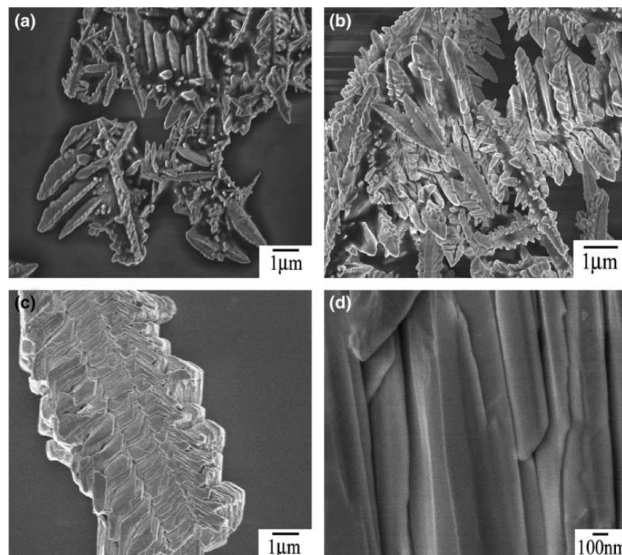
Fig. 1.2 SEM images of different morphologies of Bi deposits produced under different conditions (a) Prickly rod-like shape, 0.01 mol l^{-1} Bi(NO$_3$)$_3$, ITO sheet,i_c=30 mA. (b) Branch-like shape, 0.01 mol l^{-1} Bi(NO$_3$)$_3$, Pt substrate, i_c=30 mA.(c) Skeleton-like shape, 0.01 mol l^{-1} Bi(NO$_3$)$_3$ with 0.01 mol l^{-1} EDTA, ITO sheet, V_c= -0.4 V. (d) Strip-like shape, 0.03 mol l^{-1} Bi(NO$_3$)$_3$ with 0.01 mol l^{-1} EDTA, Al substrate, V_c= -0.2 V.[58]

in what is known as anisotropic magnetoresistance (AMR). AMR is an important method towards developing magnetic sensors for applications such as geomagnetic field sensing, electrical current measurement and traffic detection.

When a current is passed through bismuth in a magnetic field, a large initial resistance is seen which gradually goes down to its final value causing a time lag to current flow. Therefore bismuth has a larger resistance for alternating currents than for direct currents.[61] Also, bismuth displays only a small energy gap between the conductance band and the valence band, hence the electronic properties of bismuth are considered to be tunable. Tunability makes bismuth a useful candidate for electronic and thermoelectric devices.[62–64] Additionally, it serves a catalytic action in electro-reduction of H$_2$O$_2$ and O$_2$[65] in aqueous fuel cells,[66,67] as well as the oxidation of formic acid on Pt[65,68–71] and for contact formation on semiconductors.[72] Deposition dynamics of bismuth has been previously explored in various contexts.

1.1.4   Electrodeposition of bismuth alloys

The earliest recorded electrodeposition in which a combination of metals were used is around 1840. There are reports of the growth of bismuth-bearing zincblende (ZnS occurs in two common polytypes, zincblende and wurtzite) alloy in the literature.[73–77] Different growth methods were used to produce InSbl$_{1-x}$Bi$_x$ alloys and with ca. 2.6 mole percent bismuth, due to the solid-solubility limit of InBi in InSb. Zilko and Green[78,79] grew metastable solid solutions of InSbl$_{1-x}$Bi$_x$ with ca. 12 mole percent InBi / InSb, at 20 K. Metastable InSbl$_{1-x}$Bi$_x$ exhibited good temporal and thermal stability to phase separation.

Electroplated alloys can be used to achieve properties or combinations of properties which are

not met by electroplated pure metals or by melting. Bismuth is frequently co-deposited with metals such as antimony, cadmium, copper, indium, lead or tin for research as well as industrial applications. Bismuth alloys are used for bearings where cold welding of the bearing to the shaft needs to be avoided.[80] Electrolytic (derived by electrolysis) bismuth alloys with low-melting metals (lead, indium, cadmium) are applied as soldering coatings for printed-circuit cards, electric contacts in semi-conductors, and electroplating of bearings.[81] Copper-bismuth alloys have been extensively studied to understand the dynamics of bismuth-induced embrittlement of copper grain boundaries.[82–85]

The Ag-Bi phase diagram (Fig. 1.3) under atmospheric pressure conditions consist of a liquid, L, and two solids, (Ag) and (αBi). According to Karakaya et al.,[86]) the system was an eutectic type with very low solubility on silver rich solid and almost no solubility in the Bi side. Karakaya et al., reported that the solid solubility of bismuth in silver to be ca. 3% X-ray work.
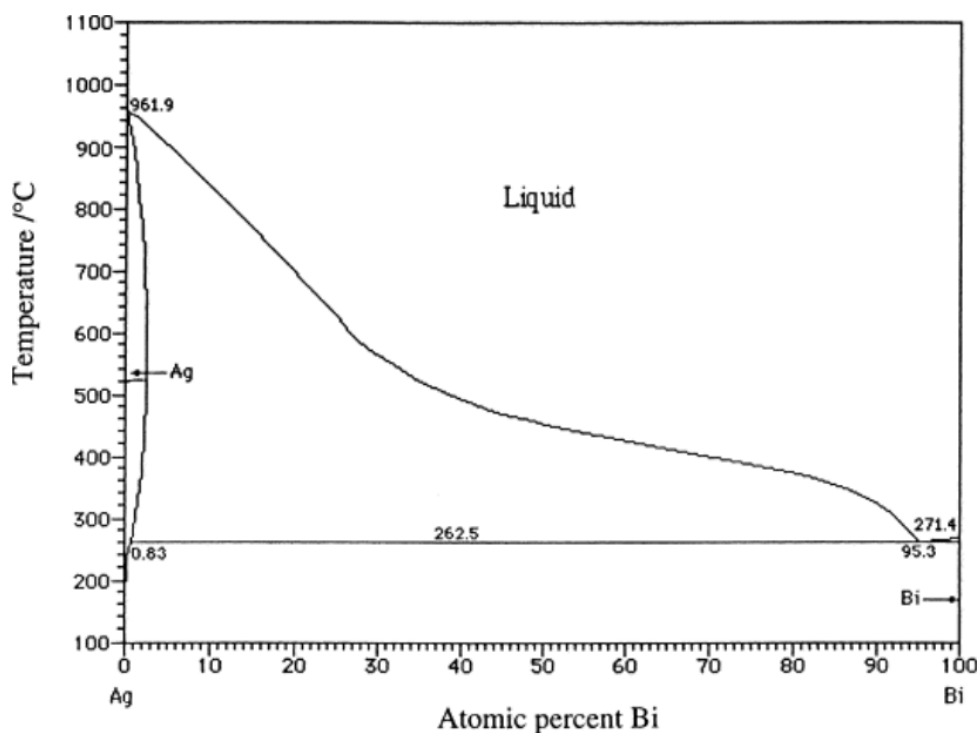
Fig. 1.3 AgBi phase diagram - atomic percentage[86]

Silver/ bismuth deposition is at present carried out from alkaline electrolytes. The alloying rectifies the physico-mechanical parameters of the simple metal coating.[87,88] Alloying bismuth with silver is useful in electronics, radiotechnics and coatings for severe conditions such as friction under high pressure.[88,89] Co-deposition of silver with less noble metals (e.g. bismuth) resulted in pure silver coatings or solid solution (in silver) at low current densities. On the other hand, at higher current densities, a richer phase of the alloying metal/ silver lattice with the alloying metal is formed.[90] The alloying process occurs straightforwardly due to the deposition potentials of both metals being relative similar to each other. The composition of the electrodeposit can be controlled by changing the concentration of cyanide in the electrolyte. Low cyanide concentration results in a higher positive potential for the silver redox couple increasing the yield of silver, whereas with high cyanide concentrations, deposition potential

of silver moved negatively giving deposits with higher yield of bismuth.[91] Also it has been demonstrated that when the current density is low, there is a greater deposition of bismuth.[43] X-ray diffraction studies on Ag-Bi thin films prepared by galvanostatic electrodepositon in organic dimethylsulfoxide baths produced a mixture of silver-rich solid solution phase and pure bismuth phase. Furthermore, it was found that the resistivity decreased as the thickness of the film increased.[92] Microstructural investigations carried out using Transmission Electron Microscopy have indicated that the addition of bismuth to silver increases the hardness of the material and reduces the electrical resistivity.[93] There has also been attempts to enhance the emergent properties of combining silver and bismuth by introducing further additives. In one such study, silver and bismuth were alloyed with a rare earth metal (e.g. Holmium) to develop an alternative to lead soldering.[94]

1.2 Electrodeposition in non-aqueous systems

For over 100 years almost all electrodeposition processes have been mainly based on aqueous solutions of metal salts with additives used to control morphology and properties. The plating industry has been dominated by deposition of Cr, Ni, Cu, Au, Ag, Zn, Cd and Co and their alloys from aqueous solutions. Few other metals/alloys are deposited in niche applications and mostly using plasma[95–97] and chemical vapour deposition techniques.[98–101] Aqueous medium has been the favourite due to being non-flammable, high solubility of electrolytes, low ohmic losses and good throwing power due to high conductivity, low cost and high rate of mass transfer.[102] For these reasons water remains the main solvent in the electroplating industry. However, there are many issues of using aqueous solutions due to limited potential windows (ca. 1.4 V) and gas evolution leading to hydrogen embrittlement. Also, passivation of metals causes problems with anodic and cathodic materials requiring complexing agents such as cyanides, the attendant environmental issues arising due to high level of purification needed for large volumes of used water, with high waste metal concentrations before returning to the water course.[103] Due to these reasons there has been research into the use of other solvents, both ionic/molecular and polar/ nonpolar.

Polar organic solvents give better solubility, high fluidity and high conductivity but have the drawback of coordinating strongly due to their electronegative components with metal ions that make them difficult to reduce and hence to deposit. Non-polar organic solvents (aromatic hydrocarbons) provide the advantage of having larger potential windows but poor conductivity makes them less popular (including current methods used for Sn, Cu, Pd, Pb, Cd, Ti, and Cr). Izutu et al. conducted a review explaining non-aqueous solutions.[104] Due to the various drawbacks of molecular solvents described above, full ionic media has attracted substantial interest due to their tuneable physicochemical properties. For metals such as Li, Na, Ti and Al high temperature molten salts have been used for a long time which had the main drawback of high operating temperatures.[105]

Ionic liquids have progressed to have wide range (based on various types of chemistry) with

rapid progression in research areas such as organic synthesis, electrochemistry, bio-processing, pharmaceuticals, catalysis, separations, and a range of other industrial applications.[106–111] Due to the vast range of possible cation and anion variations there can be as may as 10^{12} different ionic liquids that can be made depending on the application. Seddon et al. conducted a comprehensive review on successful application of ionic liquids.[112] Some of these applications were due to their properties including amphiphilic solvation power, wide liquid temperature range, insignificant volatility, non-flammability, wide electrochemical window, usability in high vacuum systems and as a replacement of environmentally hazardous processes (e.g. in silver and chromium electrodeposition).

The introduction of solvents that give a pure ionic environment at room temperatures, room temperature ionic liquids (RTIL), overcame the drawback of high operating temperature of molten metal salts.[113] These compounds were made of the large non-symmetric ions with low lattice energy causing the melting point to be below 100 °C. The earliest ionic liquids derived in this category were sensitive to oxygen, moisture and were based on aluminium chloride.[114,115]

A new generation of ionic liquids reported by Abbott and co-workers described ionic solvents formed by complexation of quaternary ammonium salts with hydrogen bond donors (HBD).[116] The charge delocalization due to hydrogen bonding between the halide anion and the hydrogen donating moiety causes deep decrease of the freezing point relative to the melting points of the individual components hence the name deep eutectic solvents (DES) (Fig. 1.4).
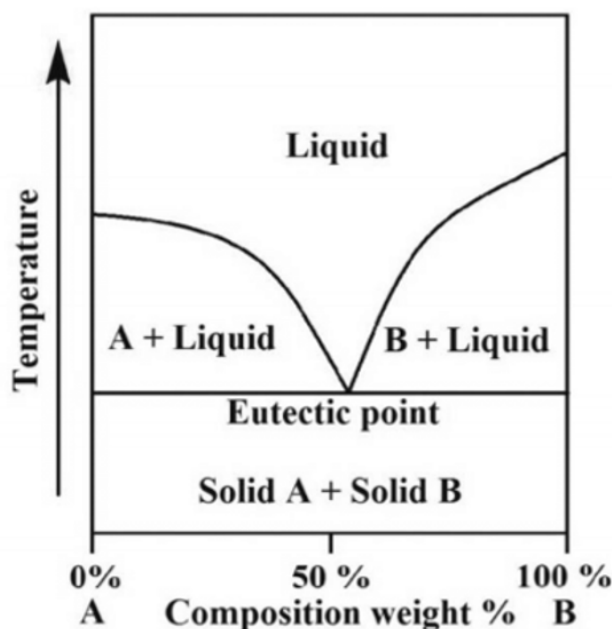
Fig. 1.4   Schematic diagram of an eutectic mixture formation

Deep eutectic solvents can be described by the general formula Cat^+X^-zY, where Cat^+, in principle, can be ammonium, phosphonium, or sulfonium cation, and X is a Lewis base, which is usually a halide anion. The X^- anion interacts with z number of Y molecules to form a complex anionic species between X^- and either a Lewis or Bronsted acid Y (z refers to the number of Y molecules that interact with the anion). Compared to the traditional ILs, DES can be made

using non ionic species and the deep depression of the freezing point compared to the individual components is prominent at the eutectic composition of QAS and HBD mixture. In terms of practical applications, many of DES's display physico-chemical properties of imidazolium based IL's with advantages of low cost,[117] 100% atom economy, inertness towards air/ water, low toxicity and biodegradability. As a result, the emphasis has been placed on more practical systems using choline chloride [$ChCl, HOC_2H_4N \equiv (CH_3)_3Cl$] in the majority of studies.[118,119] DES has significant potential with applications ranging from design of novel catalytic processes,[120] as soldering fluxes, as non-volatile solvents, in energy storage and in the fields of ion metallurgy, electroplating and electrowinning. Abbott and co-workers have so far identified four types of DES (Fig. 1.5). Examples of anionic and cationic DES are given in Fig. 1.6. Types I → III formulations share a similar complexation pathway. This can be described by the following generic equation:

$$\text{cation} + \text{anion} + \text{complexing agent} \rightarrow \text{cation} + \text{complex anion}$$

or

$$\text{cation} + \text{anion} + \text{complexing agent} \rightarrow \text{anion} + \text{complex cation}$$

Pan and Freyland studied electrodeposition of bismuth using the Lewis acidic ionic liquid, 1-methyl-3-butylimidazolium chloride-aluminium chloride.[121] Bi was electrodeposited on Au(III) and investigated by cyclic voltammetry and in-situ STM. They observed two different UPD processes at 0.9 V and 1.2 V versus Al/ Al(III). A unaxially formed monolayer and multiple domain structures were seen at these voltages respectively. The coadsoprtion of $AlCl_4^-$, the main anion in the ionic liquid has been considered as the reason for the formation of many Bi adlayer structures. In the OPD region (i.e. above 0.8 V verses Al/Al(III) nucleation was seen prefer terraces than step-edges of Au(III). After critical nuclei was formed the cluster formation was seen at longer polarization times (of the order of minutes).

Two radically different morphologies of Bi deposits were achieved in the underpotential region by Mao and co-workers by using $BiCl_3$ dissolved in chloro and non-chloroaluminate IL in 2010.[122] Agapescu reported bismuth deposition from urea and oxalic acid based DES in two studies.[123,124] ChCl based DES appear to be an attractive alternative for currently used acid and alkaline based plating solutions.

A number of metals have been deposited from DES including Zn,[125–127] Sn, Cu,[128,129] Ni,[130] Ag,[131] Cr,[116] Al,[132] Co[133] and Sm.[133,134] They have been studied under different electrochemical techniques (e.g. constant current or constant voltage regimes) and the morphology, speciation and kinetics of the processes have been characterised by various methods. Electrodeposition of Cr onto a metal or plastic object is known as chrome plating, a process which can be important due to its decorative, corrosion resistance or surface hardness characteristics. Though hexavalent chromium is used in industry for chrome plating, its high toxicity level and carcinogenicity have forced to look at less toxic alternatives. The DES made from choline chloride and the trivalent chrome salt, $CrCl_3 \cdot 6\,H_2O$ with additives offers a safer alternative for this problem and chromium deposits have been produced in several morphologies.[135] It has been shown that

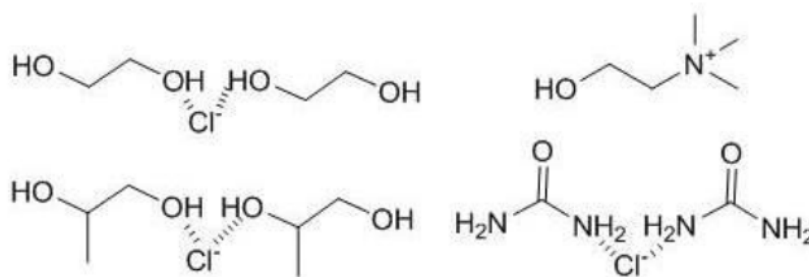| Type	Complexing agent	DES : Y
Type I	$R_1R_2R_3R_4N^+X^-$ (e.g. ChCl)	Metal salts; MCl_x, M = Zn, Sn, Fe, Al, Ga
Type II	$R_1R_2R_3R_4N^+X^-$ (e.g. ChCl)	Hydrated; $MCl_x.yH2O$, M = Cr, Co, Cu, Ni, Fe
Type III	$R_1R_2R_3R_4N^+X^-$ (e.g. ChCl)	HBD; e.g. urea, ethylene glycol, acetamide or hexanediol
Type IV	Metal salt (e.g. $ZnCl_2$)	HBD; e.g. urea, ethylene glycol, acetamide or hexanediol

Fig. 1.5 Types of DES (Cat^+X^-Zy

Fig. 1.6 Examples of anionic and cationic species postulated in the DES. From top left clockwise: ethylene glycol – chloride complex anion, choline cation, propylene glycol – chloride complex anion and urea –chloride complex anion.

good chromium deposits can be formed without additional complexing agents.[136] Electrolysis of Al_2O_3 eutectic with Na_3AlF_6 at temperature of ca. 1100 °C is used for the production of aluminium metal. Due to the aluminium oxide layer aluminium has good resistance to corrosion. Electrodeposition, spray coating, roll binding and hot dipping methods are used to deposit aluminium.[105] Electrodeposition of aluminium is conducted by using organic aprotic solvents or molten salts under an inert atmosphere which is free of moisture. Room temperature ionic liquids (e.g. benzyltrimethyl- ammonium chloride (BTMAC)/$AlCl_3$) have been found to be successful in overcoming these issues and in producing adherent, smooth aluminium coating for nickel and steel surfaces.

Co-deposition of metals is an important industrial process. Electrodeposition of bi-metallic and tri-metallic coatings Ni/Co/Sn,[137] Cu/In,[138] Sm/Co,[133] Zn/Cu,[139] Zn/Mn,[139] Ni/ Zn,[140] Fe/Ni/Cr,[141] Cu/Ga,[142] and Co/Sm[143] have been reported.

1.3 Electrodeposition at the atomistic level

The electrodeposition of a metal occurs at the electrode/electrolyte interface when subjected to an electrical field. The process involves several phase formation phenomena. Electrocrystallization is a typical metal deposition process which has been generating interest across many areas of physical science.[144] Fischer introduced electrocrystallization as a process in which mass transfer is accompanied by a charge transfer.[145] The formation of the new phase goes through a metastable state. The applied potential has a significant dependency on the deposition process where it can determine the type of nucleation and growth kinetics of the electrodeposition process. It can also indirectly influence electrodeposition by affecting solvent decomposition.

An idealised electrocrystalization process can be given as:

- Transport of the hydrated metal ion or complex from bulk solution to the cathode

- Partial stripping the hydration sheath from the metal ion at the metal/solution interface (in aqueous solution)

- Charge transfer with formation of adsorbed atom (ad-atom) at the cathode surface

- Formation of crystal nuclei by diffusion of the ad-atoms at the cathode surface

- Clustering of ad-atoms to form critical nuclei

- Formation of thermodynamically stable crystal nuclei to form a metallic nuclei to form a metallic layer

Nucleation and crystal growth or electrocrystallization depends on the near electrode area interfacial layers. The structure of this region influences the kinetics of the metal deposition process. The interface region consist of following three zones: Electrical Double Layer, Concentration Profile Layer and Fluid Velocity Layer.

1.3.1 Electrical double layer

The electrochemical reaction between an electrode/electrolyte interface is a heterogeneous reaction where we have a charged surface and a balancing counter charge in the solution. The applied potential causes the charge separation resulting in an Electrical Double Layer (EDL).

The earliest model was proposed by Helmholtz which represented the EDL as a rigid array of charged species at the metal solution interface implying the electrons on the cathode side and the metal ions on the electrode side co-exist in equal measure and separated by order of ionic radius. This model represents EDL mathematically as a simple parallel plate capacitor with a constant capacitance value. This was derived from making approximations such as ions are effectively point charges, the only significant interactions are coulombic, electrical permittivity is constant throughout the double layer and the solvent composition is uniform at the atomic scale.
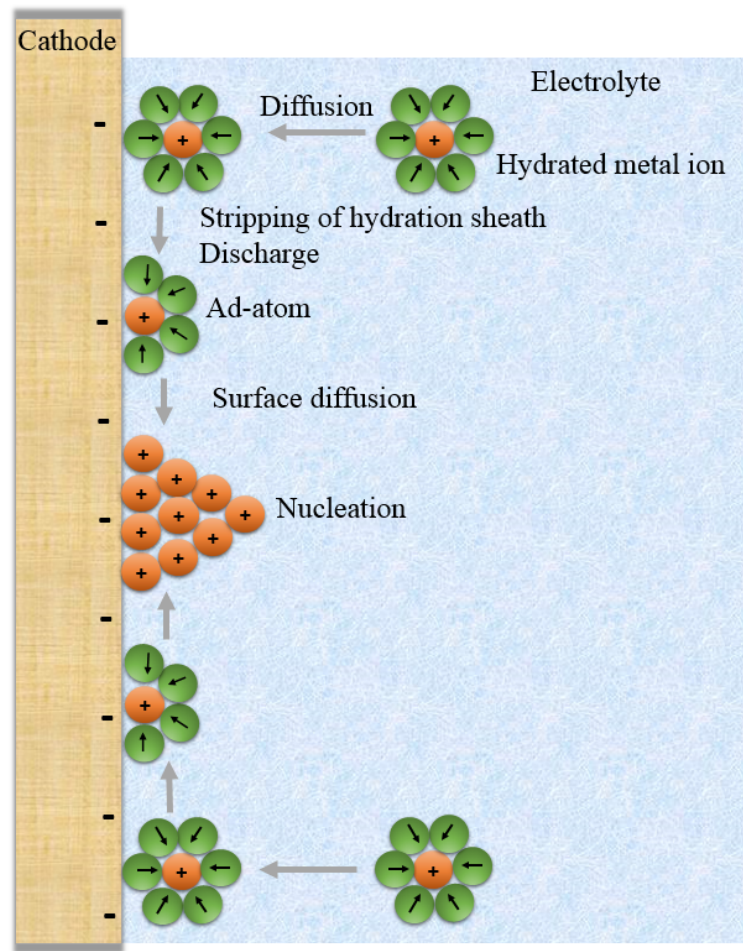
Fig. 1.7   Migration of hydrated metal ions to a cathode to form a crystal nuclei at the cathode surface

The potential gradient within the Helmholtz layer (δ_H) is linear:

$$\left(\frac{d\varphi}{dx}\right)d_{linear} = const \tag{1.1}$$

This model does not account for the statistical spatial distribution of metal ions due to thermal motion and electrostatic attraction but can be used for highly concentrated electrolytes. Gouy and Chapman proposed a new model from the premise that the ions further from the electrode are dispersed as depicted in Fig. 1.9. and the concentration of metal ions falls in exponential manner with the increasing distance from the electrode.

The potential gradient at the interface according to the Gouy-Chapman model is shown below.

$$\Delta\varphi = \varphi_{DL} + \varphi_{diffuse} \tag{1.2}$$

This model embodies a rigid inner portion of electrical double layer with adsorbed metal ions and a layer of electrolyte with spatially distributed ionic charge. Therefore the potential in the inner layer (Helmholtz) has a near linear gradient compared to outer Gouy-Chapman layer where it becomes an exponential function.
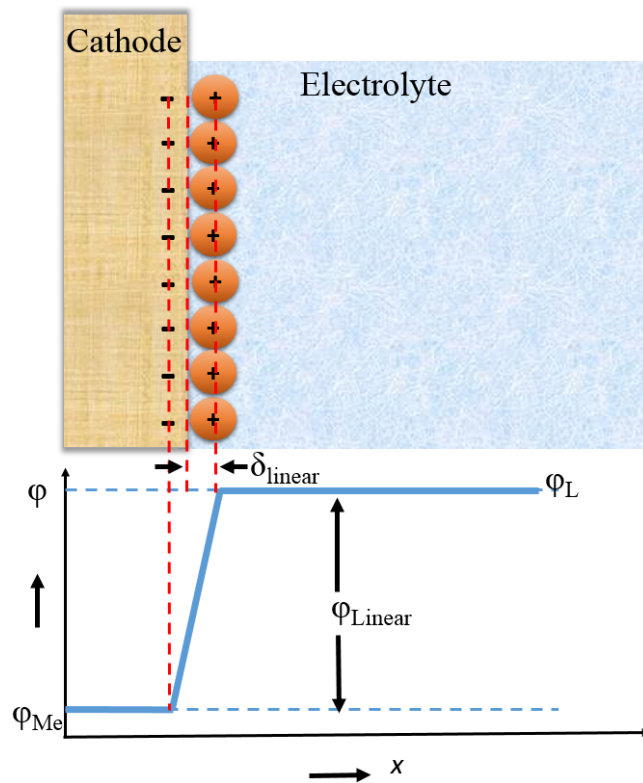
Fig. 1.8   Helmholtz-Perrin model of the electrical double-layer
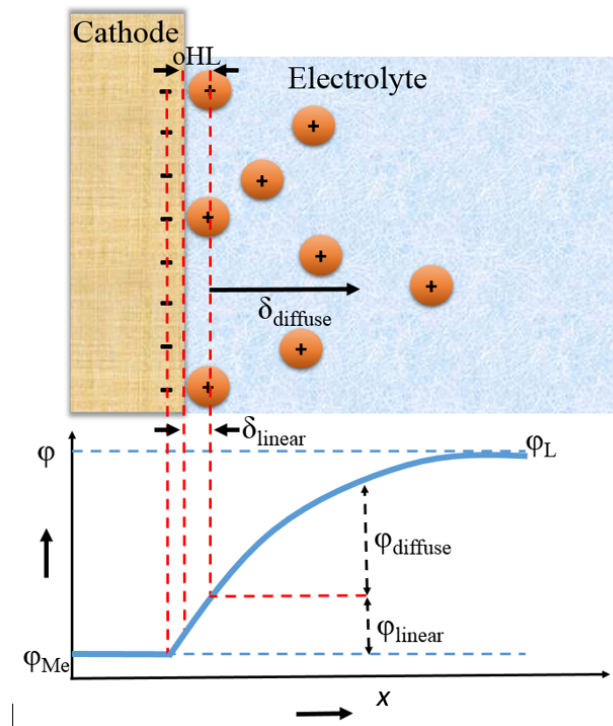
Fig. 1.9   Gouy-Chapman model of the electrical double-layer

It has been experimentally proven that at the cathode surface, an adsorbed layer of water dipoles can exist comparable to the hydration sheath around metal ions. Organic molecules or surface-active anions can displace the primary adsorbed water layer and get adsorbed to the cathode. The anions with their larger ionic radius are less strongly hydrated than cations and can get strongly adsorbed to the cathode while losing the hydration sheath partially and this
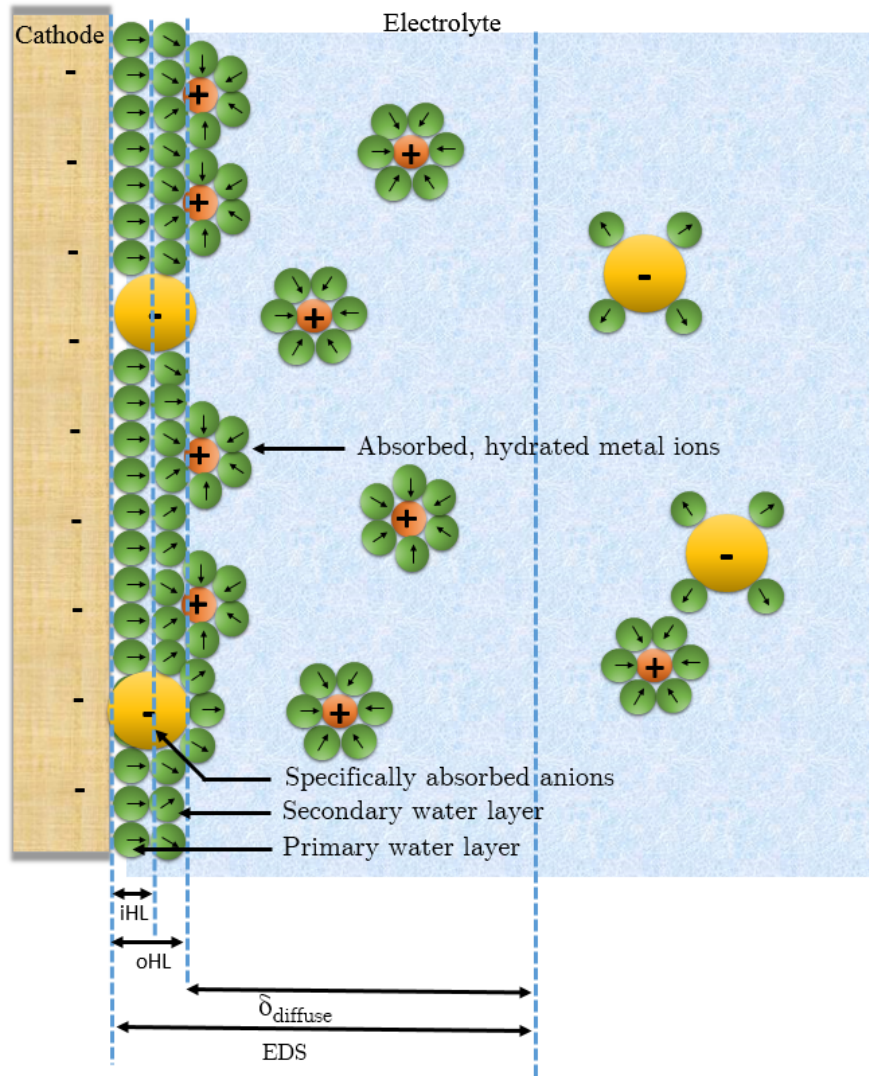
Fig. 1.10 Stern-Graham model of the electrolyte double-layer

was proposed in the Stern-Grahame model. These "specifically adsorbed ions" give rise to three regions as shown in Fig. 1.10. The inner Helmholtz plane (IHP) passes through the centres of the specifically adsorbed ions. The outer Helmholtz plane (OHP) passes through the centres of solvated ions at the distance of their closest approach to the electrode. Finally the diffuse layer is the region beyond the OHP.

1.3.2 Concentration profile

This layer arises due to the depletion or build up of the electrolyte species near the electrode surface due to convective diffusion. At the limiting current, the reaction is under complete mass transport control and the surface concentration has reached zero. The Nernstian diffusion layer thickness (δ_N) may be defined by assuming a (fictitious) linear diffusion profile by

$$K_L = \frac{D}{\delta_N} \tag{1.3}$$

where K_L is mass transport coefficient, D is a the diffusion coefficient (see Fig. 1.11).

Fig. 1.11 Electrolyte layers near the electrode surface (a) the concentration boundary layer (b) the fluid boundary

1.3.3 Fluid velocity layer
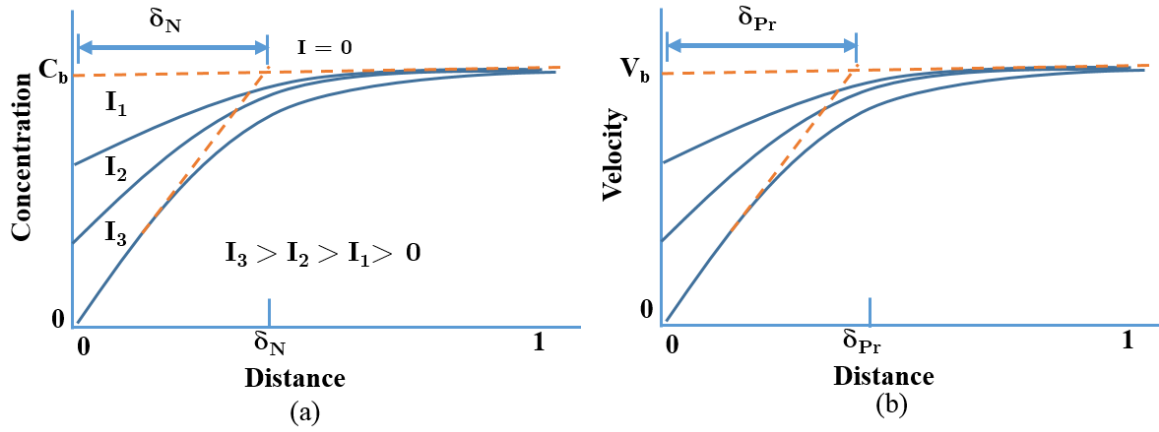
The layer arises due to the localized differences in electrolyte convection due to fluid shear and flow development. The bulk velocity is increasingly retarded as the electrode surface is approached. At the surface itself, the fluid is stationary relative to the electrode. Assumption of a linear profile allows Prandtl (hydrodynamic) boundary layer (δ_N), thickness to be obtained (see Fig. 1.11).

1.4 Nucleation and growth

There are two types of nucleation that will be covered in subsequent sections: instantaneous nucleation and progressive nucleation.

1.4.1 Instantaneous and progressive nucleation

Nucleation centers (N) can form due to defects on the surface of real crystals upon reaching a potential in the deposition region. There will already be a fixed density of defects (N_0) and local growth will start at these nucleation centers. Therefore,

$$N = N_0 \tag{1.4}$$

This process is defined as instantaneous nucleation. We consider diffusion-controlled hemispherical growth as an exemplar in the following explanation. The current of N_0 individual nuclei that grow independently of each other was calculated by Hills, Schiffrin, and Thomson.[146]

$$i = nF\pi(2DC)^{3/2}\left(\frac{M}{\rho}\right)^{1/2} N_0 \, t^{1/2} \tag{1.5}$$

They also proposed an equation for a progressive increase of the number of nucleation centers that occur once the potential reaches the deposition region and named it as progressive nucleation. For progressive nucleation, the density of nuclei as a linear function of time (t) can be expressed by the equation

$$N(t) = N_0 A_n t \tag{1.6}$$

where A_n is the nucleation rate and N_0 corresponds to the initial number of nucleation sites. The current density can be given by the equation

$$i = \frac{2}{3} n F \pi (2Dc)^{3/2} \left(\frac{M}{\rho}\right)^{1/2} N_0 \, t^{3/2} A_n \tag{1.7}$$

During the growths of the nuclei first develop in the form of semi-spherical shapes and subsequently overlap with time. We can express the area of the diffusion zone projected on the surface plane (S) by the equation

$$S = \pi k'' D t \tag{1.8}$$

The overlapping of the growing diffusion areas is illustrated in Fig. 1.12(a). Avrami proposed a relationship between the real surface coverage with diffusion zones (Θ) and surface coverage.

According to Avrami,[147] if there is unlimited growth of the diffusion zones,

$$\Theta_{ex} = N \pi k'' D t \tag{1.9}$$

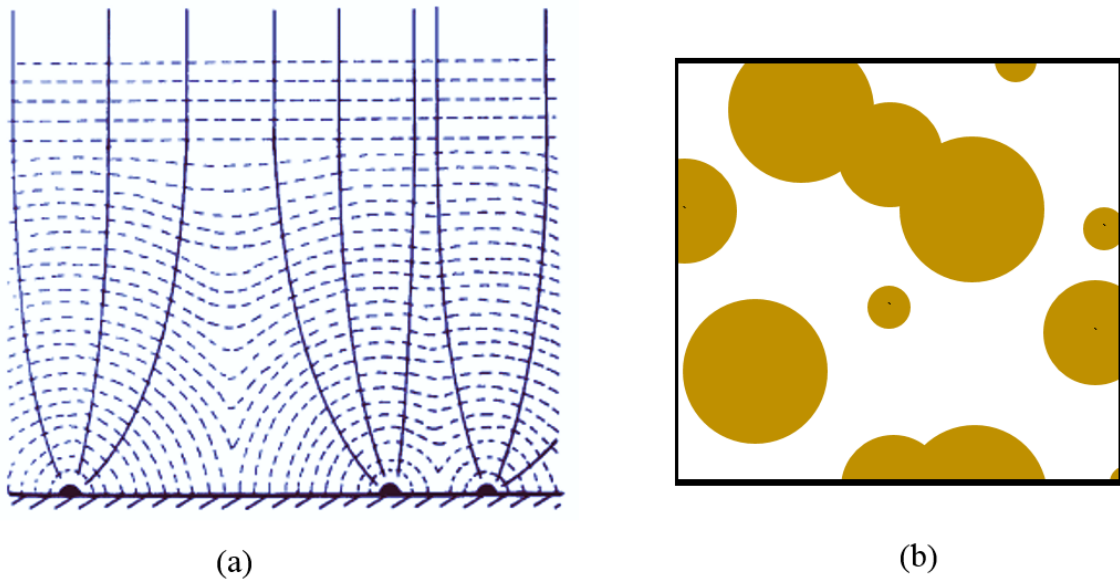$$\Theta = 1 - exp(-N\pi k'' D t) \tag{1.10}$$

(a) (b)

Fig. 1.12 (a) Process of developing diffusion zones around hemispherical nuclei on an electrode surface (b) Two-dimensional projection of overlapping diffusion zones around hemispherical nuclei on an electrode surface

Equations representing current transients were derived by Scharifker and Hills based on the

above mentioned considerations.[148] Current density as a function of time for instantaneous nucleation can be represented by the equation

$$i = nFc\left(\frac{D}{\pi t}\right)^{1/2}\left[1 - exp(N\pi k''Dt)\right] \tag{1.11}$$

Comparison of Eq.1.11 for $t \to 0$ with Eq.1.5 gives k''

$$k'' = \left(\frac{8\pi cM}{\rho}\right)^{1/2} \tag{1.12}$$

We can express the current density as a function of time for progressive nucleation as

$$i = nFc\left(\frac{D}{\pi t}\right)^{1/2}\left[1 - exp\left(-\frac{A_n}{2}\pi k'''Dt^2\right)\right] \tag{1.13}$$

Comparison of Eq.1.13 for $t \to 0$ with Eq.1.7 gives k'''

$$k''' = \frac{4}{3}\left(\frac{8\pi cM}{\rho}\right)^{1/2} \tag{1.14}$$

Current transients for instantaneous and progressive nucleation are shown in Fig. 1.13 (plot of i/i_{max} vs t/t_{max}). Further work on nucleation and current transients has been carried out by Scharifker et al.[149] and Heermann et al..[150]
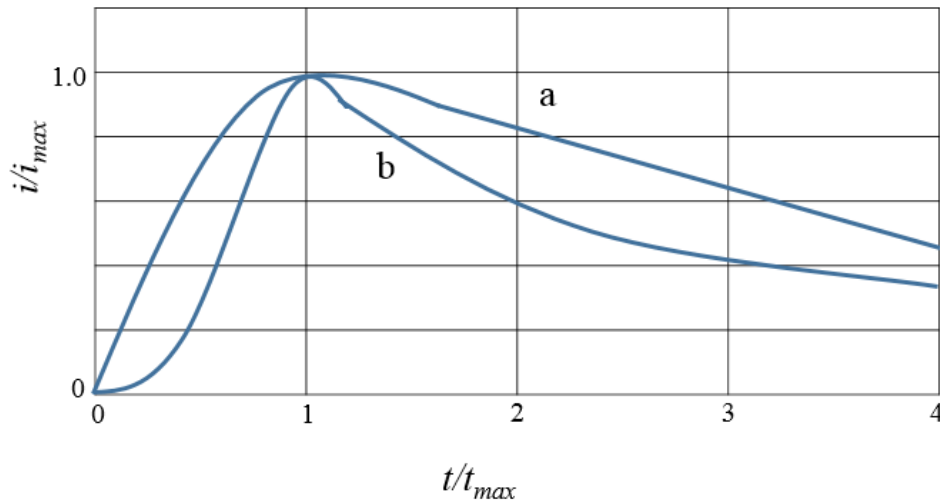
Fig. 1.13 Instantaneous and progressive nucleation (a) instantaneous nucleation, (b) progressive nucleation

The applied potential determines the type of nucleation and the growth kinetics for electrodeposition, side reactions involving the potential window of the electrolyte and the overall deposit achieved (alloy, metal/ metal oxide composite, combined crystallographic phases). Inadequate control of the applied potential would create problems in the electrodeposition. For example,

under-potential deposition (UPD) of a metallic monolayer creating a two dimensional array of absorbed metal adatoms, the side reactions involving increasing pH which leads to oxide or hydroxide formation, electrode corrosion with the formation of intermetallic compounds or anodic precipitation due to exceeding solubility limits.

Also competitive electrochemical reactions may lead to electrocatalysis, and localised potential/ current changes affecting morphology, chemical composition or phase composition of the products. Plating conditions such as high over-voltages, high current densities some additives favours formation of three-dimensional nuclei or new grains removing substrate deposit connection. Most of the time, high temperatures and low current densities promote migration of atoms to new sites, adding to an existing structure hence the epitaxial growth. Also, substrate may dissolve and deposit on the metal as an alloy despite being in the cathodic regime.

With the emergence of nanotechnology the study of structure and properties of electroplated surfaces entered a new stage. Most of these surfaces are nanocrystalline or amorphous as they are formed and their hardness, wear resistance, and electrical resistivity are strongly governed by nuclei size. However their thermal expansion, Youngs modulus, and saturation magnetization display no nuclei size dependence. Therefore investigating nucleation has potential applications in corrosion, wear-resistant coatings and magnetic materials for magnetic-recording.
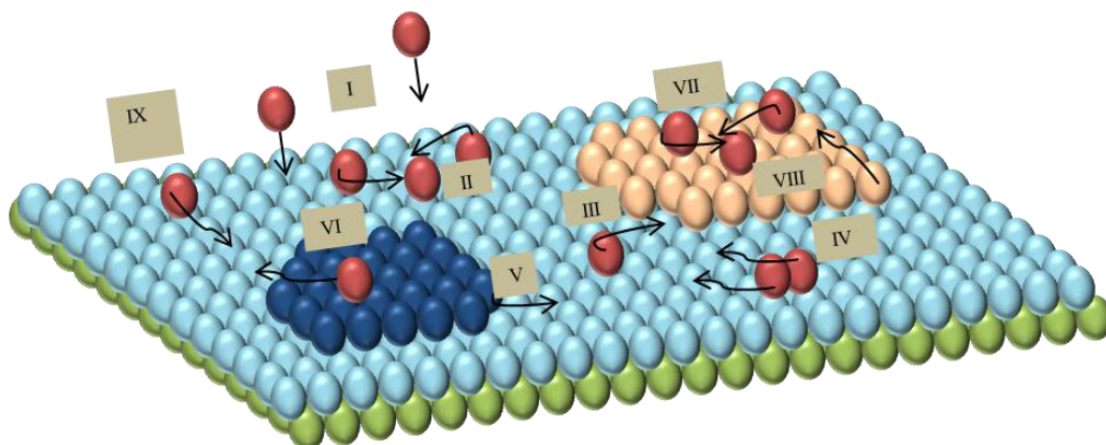
Fig. 1.14 Schematic diagram of nucleation and growth, (I) arrival (II) nucleation on island (III) attachment to island (IV)diffusion of dimer (V) detachment from an island (VI) diffusion to lower terrace (VII) binding and nucleation on second layer (VIII) diffusion along step edge (IX) diffusion on terrace[151]

1.4.2 Formation of the new phase

In the path that begins with a metal ion in bulk solution and ends with the formation of metal lattice any step can be the rate determining step and hence the bottleneck for the process. The ions moving from the bulk to the vicinity of the electrode can be mainly due to natural or enhanced convection. The ions then reach the outer part of the Nernstian diffusion layer and diffuse through due to the concentration gradient. Convection ceases to operate to a larger extent although it can reduce the thickness (δ_n), and hence increase the concentration

gradient. Subsequently, the ions transit the double layer, become adsorbed ad-atoms, laterally diffuse across the surface and form metal atoms incorporated in a lattice. To enhance the electrodeposition, identifying and controlling the rate determining step is important. Each step in the path is associated with its own overpotential and the total overpotential is the sum of individual overpotential components: concentration overvoltage, activation (or charge transfer) overvoltage, crystallisation overvoltage and resistance overvoltage. The critical step (r.d.s.) could either be the transition of metal ion through electrical double layer (hence the charge transfer overvoltage) or diffusion of metal ions prior to their discharge (hence concentration overvoltage) are more common in most electrodeposition processes.

The growth of a new phase begins with the formation of a nucleus. Erdey-Gruz and Volmer produced the first detailed description of the nucleation process.[152] Nucleation is kinetically limited by the Gibbs formation energy, which is linked to an increase of the Gibb's energy of the system. This can be considered as an assemblage of ad-atoms at the cathode surface having reached the critical size and growing further by attaching more ad-atoms. The critical size of the nucleus depends on the critical Gibbs energy of nucleation between unstable and stable growths. There are mainly two pathways for formation of nuclei of at least critical size: the metal ions can directly pass to an energetically favourable nucleation site (Fig. 1.15(b)) or pass through energetically less favourable sites through lateral movement (Fig. 1.15(b)). Depending on the placement and the resulting nucleus, four different sites can be seen. These are point sites, and one-, two- and three-dimensional sites (edge, plane or corner sites respectively). It has been found that the dimensionality of the active sites play a significant role in the transfer of ions from the electrolyte to the substrate surface. The probability of the deposition of metal ions is high on rough, high-indexed surfaces or on stepped vicinal or planes with a high density of kink sites. Active sites can also be formed through oxidation/ reduction of a surface, ad/desorption of anions, reconstruction processes, or solvent molecules.

In three-dimensional nucleation the nucleus formed on a substrate as a cluster that grows in all three dimensions. The spatial aggregation of ad-atoms have no relationship to the lattice structure of the substrate. The special significance is the existence of lattice defects such as edges, corners and steps which act as active sites, triggering nucleation and growth. A two-dimensional nucleus may form on a substrate (a monomolecular layer growth) due to the strong interaction between the substrate and deposited metal as in under potential deposition. The orientation of ad-atoms will often be related to the structure of underlying cathode material. One dimensional nucleation a series of ad-atoms congregate along the edge of an atom on the substrate. The growth can occur in one dimensional (dendrites), two dimensional (formation of discs that eventually become a thin layer) or three dimensional (commonly modelled as pyramidal, cone or hemispheres). In each case the growth can be driven by kinetic or diffusional control. So number of possibilities/ combination are vast and setting out all of them mathematically is beyond the scope of this study. However, for the purpose of the systems under study only three dimensional deposits are of relevance and will be discussed in the subsequent sections with two types of nucleation models. Comprehensive reviews on nucleation and growth

Cathode

Electrolyte

Electrolytic
double-layer

(a)

(b)

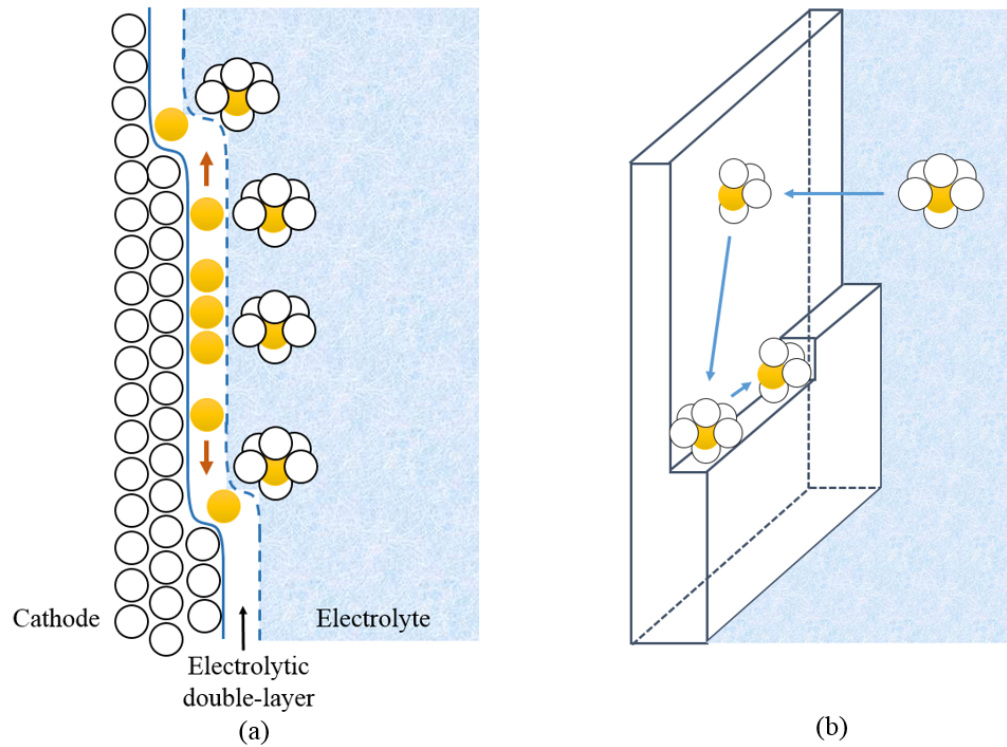**Fig. 1.15** (a) Passage of metal ions through the electrolyte double-layer to active sites; for example, step dislocations (b) Lateral diffusion of ad-atoms at the cathode surface towards energetically favoured growth locations, for example, at steps or corners
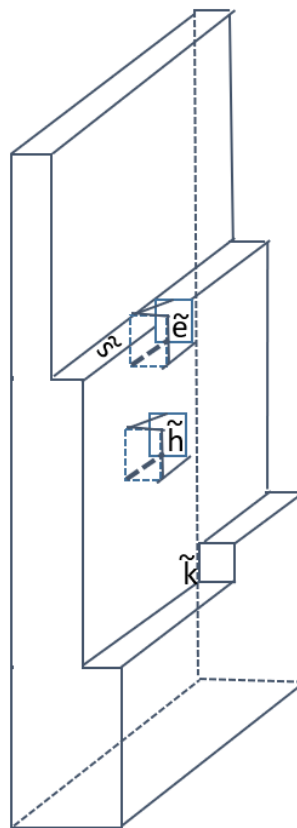

Fig. 1.16 Growth sites at a cathode surface. $\tilde{e}$ = corner; $\tilde{h}$ = recess; $\tilde{k}$ = edge; $\tilde{s}$ = step.

have been published elsewhere.[153–155]

1.5 Thesis aim objectives

1.5.1 Thesis aim

The overall aim of the project was to investigate electrodeposition of bismuth and silver/bismuth metal coatings using deep eutectic solvents.

1.5.2 Thesis objectives

Fundamental objectives

There are three fundamental objectives:

- Understand the fundamentals of redox chemistry and mass transport of deposition and dissolution of metals in ionic liquids using the novel technique of Probe Beam Deflection/Electrochemical Quartz Crystal Microbalance. To achieve this objective, deposition of silver and bismuth separately and simultaneously in deep eutectic solvent (DES) based on ethylene glycol and choline chloride will be carried out. Also the optical, gravimetric and electrochemical responses will be analysed.

- Understand the fundamentals of nucleation and growth of metals in ionic liquids due to significant impact on potential applications. To achieve this objective we would carry out electrodeposition of silver and bismuth metal system in DES and use the current transients to analyse and apply standard nucleation models (specific objective).

- Investigate electrode/ electrolyte kinetics during metal deposition and understanding fundamental methods of evaluating parameters such as rate constants and diffusion coefficients using silver and bismuth systems in DES and study their morphology and composition.

Application oriented objectives

- Produce formulations for smoother, more adherent thin coatings of bismuth and silver-bismuth (with a higher bismuth percentage in the alloy) using DES.

1.5.3 Strategy

The first objective of this study is to understand fundamentals of redox chemistry and mass transport of the silver/ bismuth system in DES using novel insitu technique of probe beam deflection. In order to achieve this objective, the following systematic plan would be implemented.

Firstly, in order to validate the experimental methodology and to calibrate the initial setup according to Henderson's original study,[156] the experiments would be conducted using $AgNO_3$ in aqueous media.[157] Probe beam method of optical analysis is a novel technique and the application of this technique to metal deposition in DES has not been explored. The challenges that would arise due to the high viscosity of DES will need to be addressed. Secondly, we intend to use the silver deposition/ dissolution (as a well behaved system) in DES and to determine parameters/ controls needed for the use of Electrochemical Quartz Crystal Microbalance-Probe Beam Deflection.in DES. Thirdly, we intend to apply the parameters identified for bismuth and silver/ bismuth systems to study speciation and mass transfer during deposition/ dissolution of these metals/ alloys.

The second objective involves analysis of nucleation and initial growth of silver, bismuth and silver/ bismuth during deposition using DES. The theoretical models derived by Scharifker and Hills, Scharifker and Mostany for multiple nucleation with diffusion would be applied for the above systems, using potentiostatic methods. Graphical analysis of the results would be compared between systems.

The third objective involves evaluating fundamental parameters involved in electrode/ electrolyte kinetics during silver, bismuth and silver/ bismuth metal deposition in DES. To achieve this objective, Cottrell, Randles-Sevcik studies would be carried out. EQCM-PBD method and deflectogramms would be used to derive diffusion coefficients for these systems. Hydrodynamic electrodes can be used to find transfer coefficients, rate constants and diffusion coefficients under controlled convection conditions. The diffusion coefficients derived would be compared with diffusion coefficients obtained using other methods.

The application oriented and fourth objective was to produce formulations for smoother, more adhesive coatings of bismuth and silver/ bismuth in DES. For this purpose, different formulations would be formed and the morphology of films can be analysed by atomic force microscopy (AFM). The composition of the film can be analysed by simultaneous thickness and electrochemical potential (STEP) measurements for multilayer metals (STEP) method, X-Ray diffractometry (XRD) and energy dispersive X-Ray analysis (EDAX).

References

[1] J.-P. Celis, M. De Bonte and J. Roos, Transactions of the IMF, 1994, **72**, 89–93.

[2] C. Raub, in Metal Plating and Patination, Elsevier, 1993, pp. 284–290.

[3] A. Volta et al., Philosophical Transactions of the Royal Society of London, 1800, **90**, 403–431.

[4] P. D. Buchanan, Platinum Metals Review, 1981, **25**, 32–41.

[5] G. Di Bari, Modern Electroplating, Edited by Mordechay Schlesinger and Milan Paunovic, 2000.

[6] J. Dini, Electrodeposition: the materials of coating and substrates (chapter 9), 1993.

[7] K. Robbie, L. Friedrich, S. Dew, T. Smy and M. Brett, Journal of Vacuum Science & Technology A: Vacuum, Surfaces, and Films, 1995, **13**, 1032–1035.

[8] I. Gurrappa and L. Binder, Science and Technology of Advanced Materials, 2008, **9**, 043001.

[9] J. D. Madden and I. W. Hunter, Journal of Microelectromechanical Systems, 1996, **5**, 24–32.

[10] J. Whitaker, J. Nelson and D. Schwartz, Journal of Micromechanics and Microengineering, 2005, **15**, 1498.

[11] A. M. van der Putten and J. W. G. de Bakker, Journal of The Electrochemical Society, 1993, **140**, 2221–2228.

[12] J. Hu and M.-F. Yu, Science, 2010, **329**, 313–316.

[13] H. Sato, T. Homma, K. Mori, T. Osaka and S. Shoji, Electrochemistry, 2005, **73**, 275–278.

[14] H. Sato, T. Homma, H. Kudo, T. Izumi, T. Osaka and S. Shoji, Journal of Electroanalytical Chemistry, 2005, **584**, 28–33.

[15] I. S. F. Policy, Policy, ICSU Scientific Freedom, 2013, 1.

[16] L. J. Durney, Graham's Electroplating Engineering Handbook, Springer Science & Business Media, 1984.

[17] G. Gottstein and L. S. Shvindlerman, Grain boundary migration in metals: thermodynamics, kinetics, applications, CRC press, 2009.

[18] S. Tjong and H. Chen, Materials Science and Engineering: R: Reports, 2004, **45**, 1–88.

[19] L. P. Bicelli, B. Bozzini, C. Mele and L. D'Urzo, Int. J. Electrochem. Sci, 2008, **3**, 356–408.

[20] M. Datta and D. Landolt, Electrochimica Acta, 2000, **45**, 2535–2558.

[21] E. Koukharenko, X. Li, I. Nandhakumar, N. Fréty, S. Beeby, D. Cox, M. Tudor, B. Schiedt, C. Trautmann, A. Bertsch et al., Journal of Micromechanics and Microengineering, 2008, **18**, 104015.

[22] F. Xiao, C. Hangarter, B. Yoo, Y. Rheem, K.-H. Lee and N. V. Myung, Electrochimica Acta, 2008, **53**, 8103–8117.

[23] P. Allongue, F. Maroun, H. F. Jurca, N. Tournerie, G. Savidand and R. Cortès, Surface Science, 2009, **603**, 1831–1840.

[24] K. Rajeshwar, N. De Tacconi and C. Chenthamarakshan, Current Opinion in Solid State and Materials Science, 2004, **8**, 173–182.

[25] I. Dharmadasa and J. Haigh, Journal of the Electrochemical Society, 2006, **153**, G47–G52.

[26] C. Koch, Journal of Physics: Conference Series, 2009, p. 012081.

[27] Q. Huang, A. Kellock and S. Raoux, Journal of The Electrochemical Society, 2008, **155**, D104–D109.

[28] N. Kanani, Electroplating: basic principles, processes and practice, Elsevier, 2004, p. 14.

[29] M. Miranda-Hernández, M. Palomar-Pardavé, N. Batina and I. González, Journal of Electroanalytical Chemistry, 1998, **443**, 81–93.

[30] D. Hernández-Santos, M. B. González-García and A. Costa-García, Electrochimica Acta, 2005, **50**, 1895–1902.

[31] M. Antler, Wear, 1985, **106**, 5–33.

[32] F. Findik and H. Uzun, Materials & design, 2003, **24**, 489–492.

[33] I. Krastev, T. Valkova and A. Zielonka, Journal of Applied Electrochemistry, 2004, **34**, 79–85.

[34] F. Mao, M. Taher, O. Kryshtal, A. Kruk, A. Czyrska-Filemonowicz, M. Ottosson, A. M. Andersson, U. Wiklund and U. Jansson, ACS Applied Materials & Interfaces, 2016, **8**, 30635–30643.

[35] S. L. Tay, Ph.D. thesis, University of Auckland, 2016.

[36] M. Kumar and S. Deka, ACS applied materials & interfaces, 2014, **6**, 16071–16081.

[37] M. Adamik, P. Barna and I. Tomov, Thin Solid Films, 2000, **359**, 33–38.

[38] S. Zhong, T. Koch, M. Wang, T. Scherer, S. Walheim, H. Hahn and T. Schimmel, Small, 2009, **5**, 2265–2270.

[39] K. Kumar, S. Suresh, M. Chisholm, J. Horton and P. Wang, Acta Materialia, 2003, **51**, 387–405.

[40] B. Yu, K. M. Leung, Q. Guo, W. M. Lau and J. Yang, Nanotechnology, 2011, **22**, 115603.

[41] P.-A. Gay, P. Bercot and J. Pagetti, Surface and Coatings Technology, 2001, **140**, 147–154.

[42] R. Pasricha, S. Gupta and A. K. Srivastava, Small, 2009, **5**, 2253–2259.

[43] I. Krastev, T. Valkova and A. Zielonka, Journal of Applied Electrochemistry, 2003, **33**, 1199–1204.

[44] W. Butler and G. Stocks, Physical Review B, 1984, **29**, 4217.

[45] S. Chithra, S. Lele and K. Chattopadhyay, Acta Materialia, 2011, **59**, 2009–2019.

[46] T. Alford, D. Adams, T. Laursen and B. Manfred Ullrich, Applied Physics Letters, 1996, **68**, 3251–3253.

[47] R. Crisp and J. Rungis, Philosophical Magazine, 1970, **22**, 217–236.

[48] B. Navinšek, P. Panjan and I. Milošev, Surface and Coatings Technology, 1999, **116**, 476–487.

[49] Y. Wang, Y. Ju, S. Wei, W. Lu, B. Yan and W. Gao, Materials Characterization, 2015, **102**, 189–194.

[50] A. Blair, Metal Finishing, 2002, **100**, 284–290.

[51] M. A. Berding, A. Sher, A.-B. Chen and W. Miller, Journal of Applied Physics, 1988, **63**, 107–115.

[52] J. Weeks, Lead, Bismuth, Tin and Their Alloys as Nuclear Coolants, Brookhaven national lab., upton, ny technical report, 1971.

[53] G. G. Briand and N. Burford, Chemical reviews, 1999, **99**, 2601–2658.

[54] J. Amneklev, A. Augustsson, L. Sörme and B. Bergbäck, Journal of Industrial Ecology, 2016, **20**, 99–106.

[55] C. H. Chen and A. A. Gewirth, Journal of the American Chemical Society, 1992, **114**, 5439–5440.

[56] C. A. Jeffrey, D. A. Harrington and S. Morin, Surface Science, 2002, **512**, L367–L372.

57 C. A. Jeffrey, S. H. Zheng, E. Bohannan, D. A. Harrington and S. Morin, Surface science, 2006, **600**, 95–105.

58 S. Jiang, Y.-H. Huang, F. Luo, N. Du and C.-H. Yan, Inorganic Chemistry Communications, 2003, **6**, 781–785.

59 F. Yang, K. Liu, K. Hong, D. Reich, P. Searson and C. Chien, Science, 1999, **284**, 1335–1337.

60 S. Cho, Y. Kim, A. Freeman, G. Wong, J. Ketterson, L. Olafsen, I. Vurgaftman, J. Meyer and C. Hoffman, Applied Physics Letters, 2001, **79**, 3651–3653.

61 P. Kapitza, Proc. R. Soc. Lond. A, 1928, **119**, 358–443.

62 Y.-M. Lin, S. B. Cronin, J. Y. Ying, M. Dresselhaus and J. P. Heremans, Applied Physics Letters, 2000, **76**, 3944–3946.

63 L. Hicks and M. Dresselhaus, MRS Online Proceedings Library Archive, 1993, **326**, year.

64 L. L. Y. J. X. Yongqi, Journal of Beijing University of Aeronautics and Astronautics, 2003, **3**, 014.

65 D. DeLongchamp and P. T. Hammond, Advanced Materials, 2001, **13**, 1455–1459.

66 G. A. Snook, P. Kao and A. S. Best, Journal of Power Sources, 2011, **196**, 1–12.

67 R. Bhattacharya, M. M. de KOK and J. Zhou, Applied Physics Letters, 2009, **95**, 314.

68 Y. Xu, Y. Wang, J. Liang, Y. Huang, Y. Ma, X. Wan and Y. Chen, Nano Research, 2009, **2**, 343–348.

69 M. A. Namboothiry, T. Zimmerman, F. M. Coldren, J. Liu, K. Kim and D. L. Carroll, Synthetic Metals, 2007, **157**, 580–584.

70 T. Christen and M. W. Carlen, Journal of Power Sources, 2000, **91**, 210–216.

71 E. Frackowiak, V. Khomenko, K. Jurewicz, K. Lota and F. Béguin, Journal of Power Sources, 2006, **153**, 413–418.

72 E. W. Paul, A. J. Ricco and M. S. Wrighton, The Journal of Physical Chemistry, 1985, **89**, 1441–1447.

73 A. Jean-Louis and C. Hamon, Physica Status Solidi (b), 1969, **34**, 329–340.

74 B. Joukoff and A. Jean-Louis, Journal of Crystal Growth, 1972, **12**, 169–172.

75 K. Oe, S. Ando and K. Sugiyama, Japanese Journal of Applied Physics, 1981, **20**, L303.

76 A. Noreika, W. Takei, M. Francombe and C. Wood, Journal of Applied Physics, 1982, **53**, 4932–4937.

[77] A. Noreika, J. Greggi Jr, W. Takei and M. Francombe, Journal of Vacuum Science & Technology A: Vacuum, Surfaces, and Films, 1983, **1**, 558–561.

[78] J. Zilko and J. Greene, Applied Physics Letters, 1978, **33**, 254–256.

[79] J. Zilko and J. Greene, Journal of Applied Physics, 1980, **51**, 1560–1564.

[80] GB Patent 590 412 (1947).

[81] V. Povetkin and T. Shibleva, Protection of metals, 2006, **42**, 516–519.

[82] B. Powell and D. Woodruff, Philosophical magazine, 1976, **34**, 169–176.

[83] B. Powell and H. Mykura, Acta metallurgica, 1973, **21**, 1151–1156.

[84] M. Yan, M. Šob, D. E. Luzzi, V. Vitek, G. J. Ackland, M. Methfessel and C. Rodriguez, Physical Review B, 1993, **47**, 5571.

[85] G. Duscher, M. F. Chisholm, U. Alber and M. Rühle, Nature materials, 2004, **3**, 621.

[86] I. Karakaya and W. Thompson, Journal of Phase Equilibria, 1993, **14**, 525–530.

[87] D. F. B.M. Luce, in Modern Electroplating, ed. F. Lowenheim, J. Wiley and Sons, New York, 1974, ch. 14, p. 358.

[88] P. Vjacheslavov, Lenizdat, Leningrad, 1974, 213.

[89] P. Vjacheslavov, S. J. Grilihes, G. Burkat and E. Kruglova, Mashinostroenie, Leningrad, 1970, **1**, year.

[90] I. Krastev, Journal of Engineering & Processing Management, 2009, **1**, 104–112.

[91] E. Raub and A. Engel, Z. Metallkunde, 1950, **41**, 485.

[92] G. Li, L. Kay, G. Liu, P. Liu and Y. Tong, Electrochemical and solid-state letters, 2006, **9**, C32–C35.

[93] Y. Wang, G. Cheng, S. L. Tay, Y. Guo, X. Sun and W. Gao, Materials, 2017, **10**, 932.

[94] R. M. Shalaby, M. Allzeleh and M. Kamal, Journal of Advances in Physics, 2018, **14**, 5504–5519.

[95] V. M. Donnelly, I. P. Herman and M. Hirose, 1987.

[96] A. Sherman, Chemical vapor deposition for microelectronics: principles, technology, and applications, 1987.

[97] R. F. Bunshah and C. Weissmantel, Handbook of hard coatings, Noyes publications Park Ridge, NJ, 2001.

[98] K. Choy, Progress in Materials Science, 2003, **48**, 57–170.

99 C. Ryu, K. Kwon, A. Loke, H. Lee and T. Nogami, IEEE Trans. Electron Devices, 1999, **46**, 1113.

100 B. Chin, P. Ding, B. Sun, T. Chiang, D. Angelo, I. Hashim, Z. Xu, S. Edelstein and F. Chen, Solid State Technology, 1998, **41**, 141–145.

101 J. Reid, S. Mayer, E. Broadhent, E. Klawuhn and K. Ashtiani, Solid State Technology, 2000, **43**, 86–86.

102 C. G. Fink, Science, 1950, **112**, 12.

103 A. P. Abbott, I. Dalrymple, F. Endres and D. R. MacFarlane, Electrodeposition from Ionic Liquids, 2008, 1.

104 K. Izutsu, Electrochemistry in nonaqueous solutions, John Wiley & Sons, 2009.

105 M. Galiński, A. Lewandowski and I. Stępniak, Electrochimica Acta, 2006, **51**, 5567–5580.

106 V. Kumar and S. V. Malhotra, Ionic liquid applications: Pharmaceuticals, therapeutics, and biotechnology, 2010, 1–12.

107 P. D. de María, Ionic liquids in biotransformations and organocatalysis: solvents and beyond, John Wiley & Sons, 2012.

108 Z. Fang, R. L. Smith and X. Qi, Production of biofuels and chemicals with ionic liquids, Springer, 2014.

109 J. Dupont, T. Itoh, P. Lozano and S. Malhotra, Environmentally friendly syntheses using ionic liquids, CRC Press, 2014.

110 A. Kokorin, InTech, New York, NY.

111 R. Rogers, N. Plechkova and K. Seddon, ACS Symposium Series, 2009.

112 K. R. Seddon, Nature materials, 2003, **2**, 363.

113 T. Welton, Chemical Reviews, 1999, **99**, 2071–2084.

114 H. L. Chum, V. Koch, L. Miller and R. Osteryoung, Journal of the American Chemical Society, 1975, **97**, 3264–3265.

115 J. S. Wilkes, J. A. Levisky, R. A. Wilson and C. L. Hussey, Inorganic Chemistry, 1982, **21**, 1263–1264.

116 A. P. Abbott, G. Capper, D. L. Davies, R. K. Rasheed and V. Tambyrajah, Chemical Communications, 2003, 70–71.

117 R. A. Sheldon, Green Chemistry, 2007, **9**, 1273–1283.

118 I. J. Lin and C. S. Vasam, Journal of Organometallic Chemistry, 2005, **690**, 3498–3512.

[119] F. Endres, ChemPhysChem, 2002, **3**, 144–154.

[120] Q. Zhang, K. D. O. Vigier, S. Royer and F. Jérôme, Chemical Society Reviews, 2012, **41**, 7108–7146.

[121] G.-B. Pan and W. Freyland, Electrochimica Acta, 2007, **52**, 7254–7261.

[122] Y.-C. Fu, Y.-Z. Su, H.-M. Zhang, J.-W. Yan, Z.-X. Xie and B.-W. Mao, Electrochimica Acta, 2010, **55**, 8105–8110.

[123] C. Agapescu, A. Cojocaru, A. Cotarta and T. Visan, Journal of Applied Electrochemistry, 2013, **43**, 309–321.

[124] C. Agapescu, A. Cojocaru, F. Golgovici, A. Cristian Manea and A. Cotarta, Rev. Chim.(Bucharest), 2012, **63**, 911.

[125] A. Abbott, J. Barron and K. Ryder, Transactions of the IMF, 2009, **87**, 201–207.

[126] A. P. Abbott, J. C. Barron, G. Frisch, K. S. Ryder and A. F. Silva, Electrochimica Acta, 2011, **56**, 5272–5279.

[127] F. Endres, A. P. Abbott and D. R. MacFarlane, Phys. Chem. Chem. Phys, 2006, **8**, 4265–4279.

[128] A. P. Abbott, K. El Ttaib, G. Frisch, K. J. McKenzie and K. S. Ryder, Physical Chemistry Chemical Physics, 2009, **11**, 4269–4277.

[129] A.-M. Popescu, A. Cojocaru, C. Donath and V. Constantin, Chemical Research in Chinese Universities, 2013, **29**, 991–997.

[130] A. Abbott, K. El Ttaib, K. Ryder and E. Smith, Transactions of the IMF, 2008, **86**, 234–240.

[131] A. P. Abbott, K. El Ttaib, G. Frisch, K. S. Ryder and D. Weston, Physical Chemistry Chemical Physics, 2012, **14**, 2443–2449.

[132] H. M. Abood, A. P. Abbott, A. D. Ballantyne and K. S. Ryder, Chemical Communications, 2011, **47**, 3523–3525.

[133] E. Gómez, P. Cojocaru, L. Magagnin and E. Valles, Journal of Electroanalytical Chemistry, 2011, **658**, 18–24.

[134] E. L. Smith, A. P. Abbott and K. S. Ryder, Chemical Reviews, 2014, **114**, 11060–11082.

[135] A. P. Abbott, G. Capper, D. L. Davies and R. K. Rasheed, Chemistry–A European Journal, 2004, **10**, 3769–3774.

[136] E. S. Ferreira, C. Pereira and A. Silva, Journal of Electroanalytical Chemistry, 2013, **707**, 52–58.

137 J. Vijayakumar, S. Mohan, S. A. Kumar, S. Suseendiran and S. Pavithra, International journal of hydrogen energy, 2013, **38**, 10208–10214.

138 J. C. Malaquias, M. Steichen, M. Thomassey and P. J. Dale, Electrochimica Acta, 2013, **103**, 15–22.

139 P. De Vreese, A. Skoczylas, E. Matthijs, J. Fransaer and K. Binnemans, Electrochimica Acta, 2013, **108**, 788–794.

140 P. Chung, P. Cantwell, G. Wilcox and G. W. Critchlow, Transactions of the IMF, 2008, **86**, 211–219.

141 H. Yang, X. Guo, X. Chen, S. Wang, G. Wu, W. Ding and N. Birbilis, Electrochimica Acta, 2012, **63**, 131–138.

142 S. M. Gengan Saravanan, Int. J. Electrochem. Sci, 2011, **6**, 1468–1478.

143 M. Steichen, M. Thomassey, S. Siebentritt and P. J. Dale, Physical Chemistry Chemical Physics, 2011, **13**, 4292–4302.

144 E. Budevski, G. Staikov and W. Lorenz, Electrochimica Acta, 2000, **45**, 2559–2574.

145 H. Fischer, Elektrolytische Abscheidung und Elektrokristallisation von Metallen, Springer, 1954.

146 G. Hills, D. Schiffrin and J. Thompson, Electrochimica Acta, 1974, **19**, 657–670.

147 M. Avrami, The Journal of Chemical Physics, 1941, **9**, 177–184.

148 B. Scharifker and G. Hills, Electrochimica Acta, 1983, **28**, 879–889.

149 B. Scharifker and J. Mostany, Journal of Electroanalytical Chemistry and Interfacial Electrochemistry, 1984, **177**, 13–23.

150 L. Heerman and A. Tarallo, Journal of Electroanalytical Chemistry, 1999, **470**, 70–76.

151 M. Azam, Ph.D. thesis, University of Leicester, 2012.

152 T. Erdey-Grúz and M. Volmer, Zeitschrift für physikalische Chemie, 1930, **150**, 203–213.

153 M. E. Hyde and R. G. Compton, Journal of Electroanalytical Chemistry, 2003, **549**, 1–12.

154 N. Kaiser, Applied optics, 2002, **41**, 3053–3060.

155 J. Venables, G. Spiller and M. Hanbucken, Reports on Progress in Physics, 1984, **47**, 399.

156 M. J. Henderson, A. R. Hillman and E. Vieil, Journal of Electroanalytical Chemistry, 1998, **454**, 1–8.

157 M. J. Henderson, A. R. Hillman, E. Vieil and C. Lopez, Journal of Electroanalytical Chemistry, 1998, **458**, 241–248.

Chapter 2

Methodology

Contents

2.1   Analytical techniques

This section gives a summary of the fundamental principles that underpin the techniques used in the study, instrumental details and general analytical data analysis procedures.

2.1.1   Electrochemical techniques

The two main principles of electrochemical techniques are discussed in this section. This includes understanding concepts associated in the study of the interplay between electricity and chemistry i.e. analysing relationships between measurable electrical quantities (potential, charge, current) and chemical parameters. Electrochemical processes take place at the electrode-solution interface unlike most chemical studies that involve homogeneous bulk solutions. Two main types of electroanalytical measurements are potentiostatic (controlled potential) and potentiodynamic. Eqn. 2.1 shows a redox reaction where O and R are reduced and oxidised.

$$O_{(sol)} + e^-{}_{(metal)} \underset{k_{ox}}{\overset{k_{red}}{\rightleftharpoons}} R_{(sol)} \tag{2.1}$$

The potential measured at such an instance can be given by Nernst equation (Eqn. 2.2).

$$E = E^\circ + \frac{2.3RT}{nF} \, log \, \frac{C_O}{C_R} \tag{2.2}$$

where E° - standard potential for the redox reaction
R - universal gas constant (8.314J K^{-1} mol^{-1})
T - temperature (K)
n - number of electrons transferred in the reaction
F - Faraday constant (96490 C mol^{-1})
C_O - concentration of the oxidised species
C_R - concentration of the reduced species

At potentials more negative than E° oxidised form tends to be reduced. Current generated (Faradaic current) is an indication of rate of reaction and the plot of current vs potential derives a voltammogram. For simple reactions the rate of electrode reaction involves mass transport of reactant to the electrode interface, electron transfer between the interface and reactant followed by the removal of product from the near electrode area. The effectiveness of this process is governed by:

- reactivity and nature of the reactant and the electrode

- the applied potential

- the characteristics of the interfacial region and other surface interactions and

- chemical pathways that would further complicate the reactions.

Application of a voltage to an electrode alters the energy of the Fermi-level by supplying electrical energy and makes it thermodynamically favourable for electron transfer (Fig. 2.1).

Electron energy levels are filled bottom upwards creating a continuum of levels in metals. The highest occupied energy by the electron (i.e.the Fermi-level) is moved by applying a voltage to an electrode.
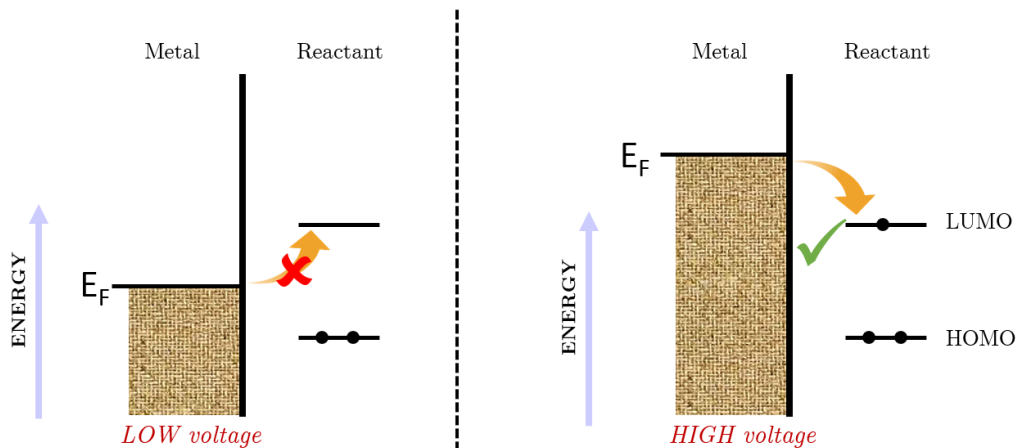

Fig. 2.1 The figure represents Fermi-level within a metal along with the orbital energies (HOMO and LUMO) of a molecule (O) in solution and thermodynamically unfavourable (left) and thermodynamically favourable (right) electron transfers. HOMO -highest occupied molecular orbital; LUMO -lowest unoccupied molecular orbital

This process (electrolysis) generates a flow of current that depends on the rate of electron transfer (kinetics) and the rate of mass transport of material to and from the electrode interface.

$$O_{(sol)} + e^-_{(metal)} \underset{k_{ox}}{\overset{k_{red}}{\rightleftarrows}} R_{(sol)} \tag{2.3}$$

The current flowing in either the reductive or oxidative steps can be predicted using the following expressions:

$$i_c = -FAk_{red}[C]_0 \tag{2.4}$$

$$i_a = -FAk_{ox}[C]_0 \tag{2.5}$$

where i - corresponding current
A - electrode area
$[C]_0$ - surface concentration of the reactant
k - rate constant for the electron transfer (red: reduction, ox: oxidation)
F - Faraday's constant (96490 C mol^{-1})

By applying transition state theory from chemical kinetics the expression for rate constants k_{ox} and k_{red} can be derived. The rate of reaction (k) for a chemical process:

$$k = Z \, exp\frac{-\Delta G^{\ddagger}}{RT} \tag{2.6}$$

where $\Delta G^{\ddagger}$ - free energy change
R - gas constant (8.314 J K^{-1} mol^{-1})
T - temperature (293 K)
Z - pre-exponential factor

More specifically, $\Delta G^{\ddagger}$ indicates the the free energy change in taking the reactant/product from its initial value to the transition state (activation energy barrier). At a single fixed voltage the formation of the species R or O will be thermodynamically favoured. When the voltage is scanned from a lower to a high, the Fermi level is raised (or lowered), changing the energy state of the electrons and hence changes the thermodynamically favoured product. The applied voltage also changes the activation energy barrier and hence the rate constants.

Assuming free energy change will follow a linear relationship, activation free energies for reduction and oxidation can be given as a function of the applied voltage as follows:

$$\Delta G^{\ddagger}_{red} = \Delta G^{\ddagger}_{red\,no\,voltage} + \alpha FV \tag{2.7}$$

$$\Delta G^{\ddagger}_{ox} = \Delta G^{\ddagger}_{red\,no\,voltage} - (1-\alpha)FV \tag{2.8}$$

where $\Delta G^{\ddagger}_{red} / \Delta G^{\ddagger}_{ox}$ - free energy of activation
  $\Delta G^{\ddagger}_{red\,no\,voltage}$ - free energy of activation when no voltage is applied
  V - applied voltage
  F - Faraday constant (96490 C mol^{-1})

The parameter α represents the transfer coefficient and typically is found to have a value of 0.5. Substitution of the activation free energy terms above in Eqn. 2.6 gives:

$$k_{red} = Z exp\left\{\left(\frac{-\Delta G^{\ddagger}_{red\,no\,voltage}}{RT}\right)\left(\frac{-\alpha FV}{RT}\right)\right\} \tag{2.9}$$

$$k_{ox} = Z exp\left\{\left(\frac{-\Delta G^{\ddagger}_{ox\,no\,voltage}}{RT}\right)\left(\frac{(1-\alpha)FV}{RT}\right)\right\} \tag{2.10}$$

This is the basis of voltammetry. This shows that the rate of electron transfer can be influenced by the applied voltage with an exponential relationship. However the current does not increase exponentially since the available reactant concentration is also controlled by mass transport to the electrode (Eqn.(2.4) and Eqn. (2.5)).

2.1.1.1 Modes of mass transport

Modes of mass transport include: Diffusion, Convection and Migration.[1] The current flow in an electrolysis experiment will be defined by each of these processes.

• **Diffusion** Diffusion is the movement of species due to the concentration gradient to minimise the concentration difference.

The rate of movement of material by diffusion can be predicted mathematically and Fick proposed two laws to quantify the processes. The first law:

$$J_0 = -D\left(\frac{\partial C}{\partial x}\right) \tag{2.11}$$

Here diffusional flux J_0 is related to the concentration gradient through diffusion coefficient D_0.
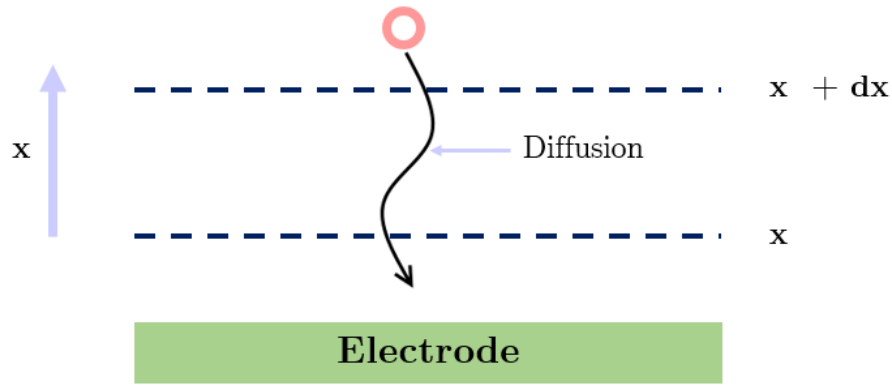
Fig. 2.2 Movement of material by diffusion (x denotes distance)

Also, C_0 and x represents concentration and position, respectively. The direction of movement from high to low concentration is given by the negative sign. The temporal aspect of this is described in Fick's second law where time is denoted by t:

$$\frac{\partial C}{\partial t} = -D\left(\frac{\partial^2 C}{\partial x^2}\right) \tag{2.12}$$

- **Convection** Convection results from gross physical movement due to a force on the solution. It can either be natural convection by small thermal or density differences creating a random, unpredictable convection or forced convection with several orders of magnitude greater than any natural convection. Forced convection effectively removes the random aspect from the experimental measurements and can be used to introduce a laminar flow profile.[2]
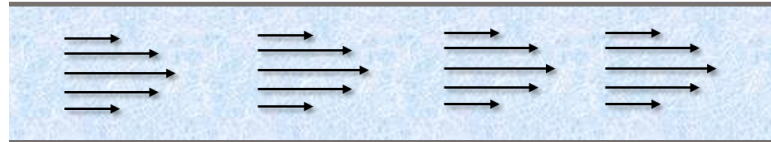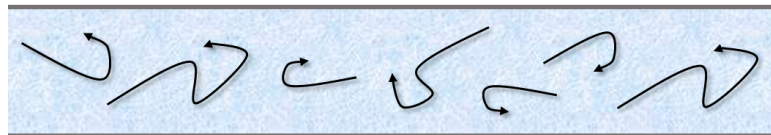

Fig. 2.3 Laminar flow: solution is introduced from the left hand side, flow is controlled with no mixing in the lateral direction

Convection can be described by the following:

$$\frac{\partial C_0}{\partial t} = -v_x\left(\frac{\partial C_0}{\partial x}\right) \tag{2.13}$$

where ν_x is the velocity of the solution.

Reynolds number is a dimensionless quantity that can be used to determine whether the fluid flow in a laminar or turbulent in different situations.This is the ratio of inertial forces to viscous forces within a fluid which is subjected to relative internal movement due to different velocities

of fluids. Inertial forces resist a change in velocity of an object and are the cause of fluid movement. i.e. the relative motion that gives rise to fluid friction.This is the reason that gives rise to turbulent flow. Viscous forces are forces resistant to flow. i.e. viscosity of the fluid opposes this effect.

When viscous forces are dominant (i.e. at slow flow rates and low Re), the forces can keep all the fluid particles in a laminar flow. When the inertial forces are much larger than viscous forces (i.e. at high flow rates and high Re), the flow becomes turbulent.[3]

$$Re = \frac{Inertial\,forces}{Viscous\,forces} = \frac{\rho u l}{\mu} = \frac{u l}{\bar{\nu}} \tag{2.14}$$

where ρ - fluid density (kg m^{-3})
u - velocity of the fluid (ms^{-1})
l - a characteristic linear dimension (travelling length of the fluid; hydraulic diameter) (m)
μ - dynamic viscosity of the fluid (Pa s)
$\bar{\nu}$ - kinematic viscosity of the fluid (m^{2}s^{-1}) where $\bar{\nu} = \mu/\rho$

Osborn Reynolds studied the conditions in which fluid movements transitioned from luminar flow to turbulant flow.[4]

The Reynolds number can be derived as follows:

$$Re = \frac{Inertial\,forces}{Viscous\,forces} = \frac{ma}{\tau A_r} \tag{2.15}$$

$$Re = \frac{(\rho.Vol)\frac{dv}{dt}}{\mu \frac{du}{dy} A_r} \tag{2.16}$$

$$Re = \frac{\rho\, l^3 \frac{du}{dt}}{\mu \frac{du}{dy} l^2} \tag{2.17}$$

$$Re = \frac{\rho\, l \frac{dy}{dt}}{\mu} \propto \frac{\rho\, u_0\, l}{\mu} \tag{2.18}$$

$$Re = \frac{u_0\, l}{\bar{\nu}} \tag{2.19}$$

where m - mass
a - acceleration
t - time
y - position of the cross section
$u = dx/dt$ - speed of flow
τ- sheer stress
A_r- cross sectional area of the fluid
u_0- maximum velocity of object related to fluid
ρ- fluid density
u - velocity of the fluid
l - a characteristic linear dimension (hydraulic diameter)
μ - dynamic viscosity
$\bar{\nu}$ - kinematic viscosity $\bar{\nu} = \frac{\mu}{\rho}$

- **Migration** This occurs due to the transfer of charged species in an electrical field which is an electrostatic effect from the application of a potential to the electrodes. The migratory flux induced is given mathematically (in 1 dimension) using

$$\frac{\partial C_0}{\partial t} = -\mu \, C_0 \left(\frac{\partial \phi}{\partial x} \right) \tag{2.20}$$

$$\mu = \frac{z \, F \, D}{R \, T} \tag{2.21}$$

where ϕ - electrostatic potential
z - number of electrons transferred in the reaction
F - Faraday constant (96490 C mol^{-1})
D - diffusion coefficient (cm^2 s^{-1})
R - universal gas constant (8.314J K^{-1} mol^{-1})
T - temperature (K)

We can simplify by removing migratory effects by adding a large quantity of the background electrolyte (relative to the reactants) to the medium. This also helps conduction for passage of current through the solution.

Therefore, we can effectively remove much of the mass transport complexity by changing the design of the experiment. The electrochemical methods encompass all methods that make use of electric potential or current to drive or analyse chemical reactions. Essentially an outline of some of the fundamental concepts of electrochemistry, experimental equipment and techniques adapted that are used in the study are given in Fig. 2.4.

All voltammetric methods measure electrode currents as a function of potential in order to determine composition, reactivity of an analyte or the rate of the reaction studied.[5,6] There are numerous forms of voltammetry used in these experiments: potential step,[7,8] linear sweep[9] and cyclic voltammetry.[10–14] Here a predetermined voltage or series of voltages are applied to the electrode at which the reaction occurs and the corresponding current generated is monitored. The reaction takes place in an electrochemical cell which depends on the type of experiment conducted. Essentially a three electrode system is used: working electrode (WE) which is the interface at which the reaction occurs; counter electrode (CE) which is used to complete the circuit and to measure the current generated but otherwise inert; reference electrode (RE) which has a stable known potential relative to the working electrode and used for the measurement of WE/RE potential difference.
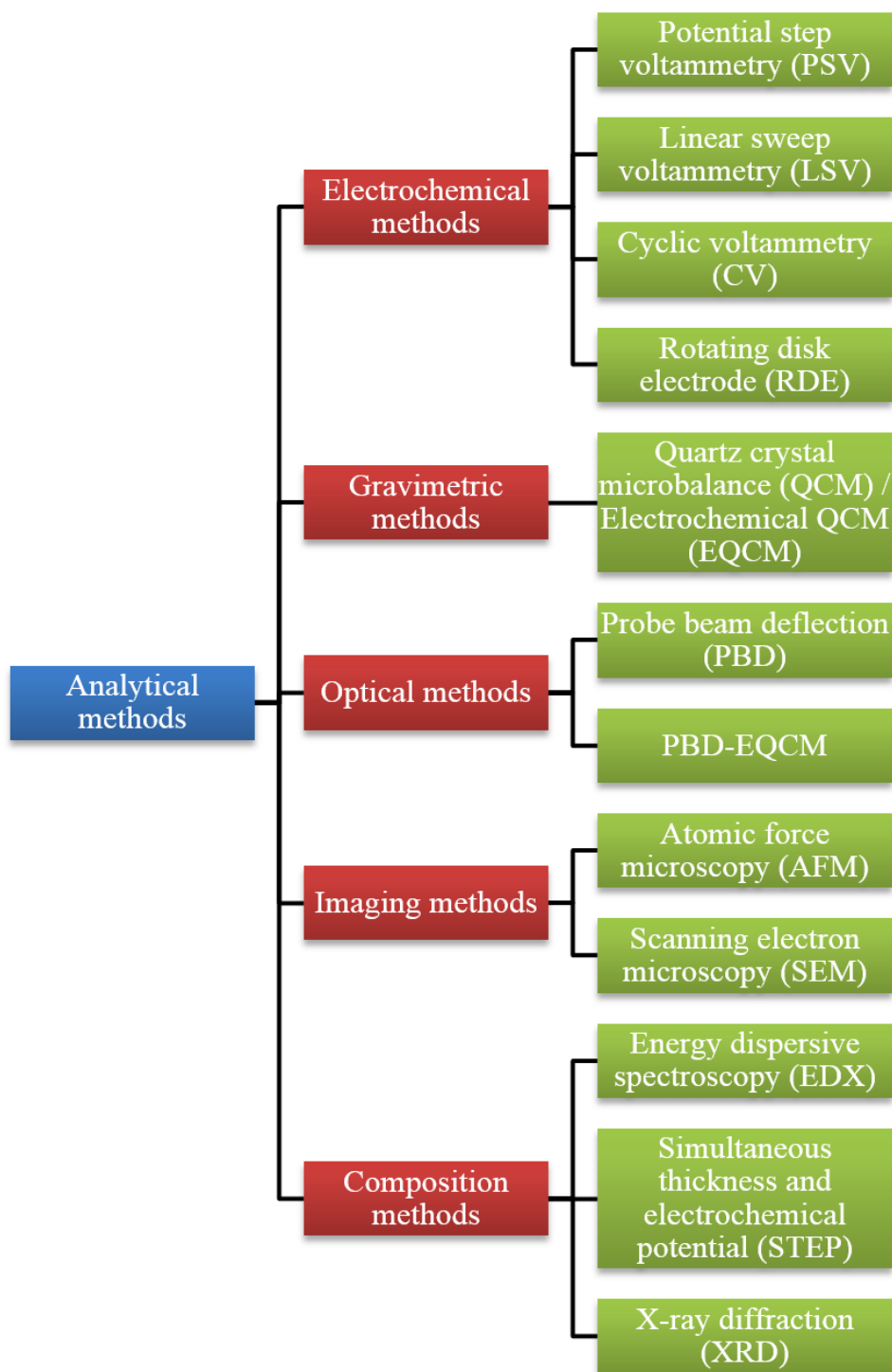
Fig. 2.4   Analytical methods

2.1.1.2 Potential Step Voltammetry

In the potential step measurements the applied voltage is instantaneously jumped from an initial equlibrium value V1 to predetermined value V2. The resulting current is measured as a function of time (Fig. 2.5). The current jumps instantaneously at the change in voltage and then begins to depreciate as a function of time. Before the application of voltage the composition of the analyte in the near electrode area is constant but as the reaction progresses it needs a supply of fresh reactants to diffuse to the electrode surface.

When a sufficient overpotential is applied all the reactants at the electrode-analyte interface get consumed generating a large current. The rate of diffusion and the amount of current generated is controlled by the concentration gradient i.e. diffusional flux. With the progress of time the reactants diffuse further from the electrode and cause the concentration gradient to decrease which drops the current response (Fig. 2.5). The decaying current follows the Cottrell eqn. which shows i vs $\frac{1}{\sqrt{t}}$ trend.[15,16]

$$i = nFAC_\infty \left(\frac{D}{\pi t}\right)^{1/2} \tag{2.22}$$

where i - current (A)
   n - number of electrons
   F - Faraday constant (96490 C mol^{-1})
   A - area of the electrode (cm^2)
   D - diffusion coefficient of the reactant (cm^{2}s^{-1})
   C_∞ - bulk concentration (mol dm^{-3})
   t - time (s)

The rate limiting process is the diffusion of species to the surface of the film. A plot of i vs $t^{-1/2}$ yields the diffusion coefficient (D) via the slope.
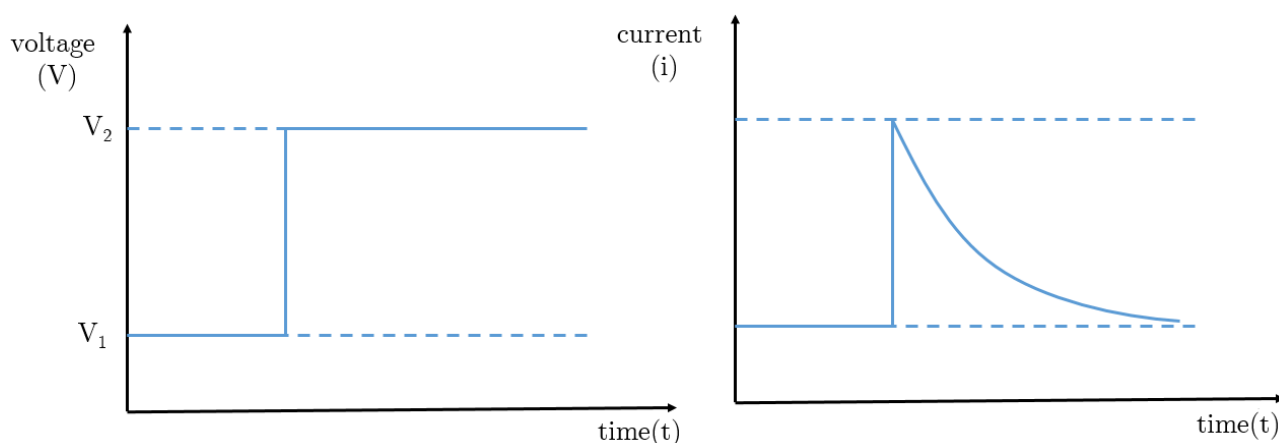

Fig. 2.5 Instantaneous jump of applied voltage from V_1 to V_2 in potential step measurement and the resulting current response

2.1.1.3 Linear Sweep Voltammetry

In linear sweep voltammetry (LSV) voltage is scanned from a lower limit to an upper limit as the current response is plotted as a function of voltage (Fig. 2.6).
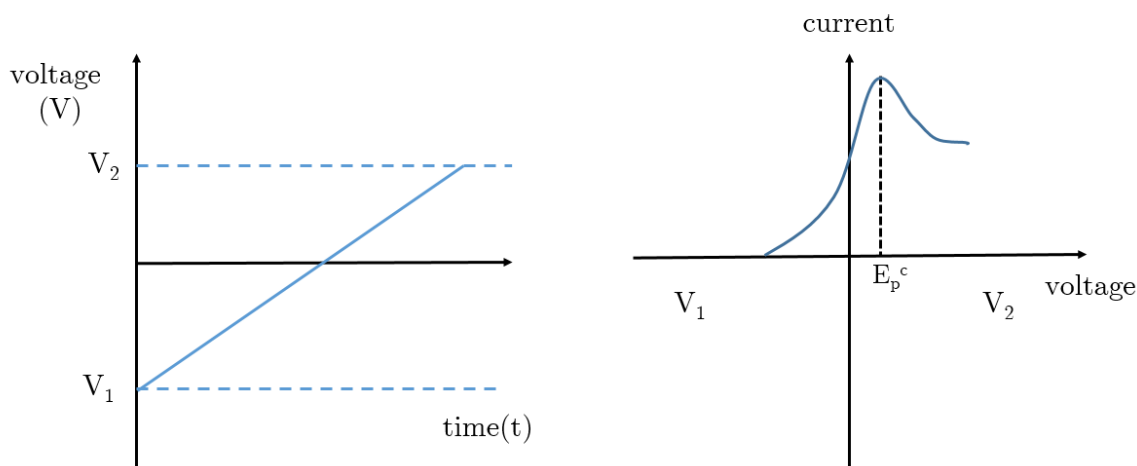

Fig. 2.6 Linear sweep voltammetry application of voltage ramp and current response

The current increase with the voltage since more reactants are converted. With time as the diffusion layer grows on the surface, time taken to get the flux to the electrode surface through the diffusion layer increases and the current begins to drop, as predicted by the Cottrell equation. The Faradaic current increases with increasing scan rate (Fig. 2.7).

At a slow scan rate the diffusion layer will grow much thicker and further from the electrode surface compared to a fast scan rate. Therefore, lowering the flux to the electrode surface decreasing the resulting current.

The peak current occurs at the same voltage if the electron transfer kinetics are rapid i.e. reversible electron transfer. For quasi-reversible or irreversible electron transfer reactions (slow electron transfer) peak current position will depend on the rate constant and also the voltage scan rate (Fig. 2.8). When the electron transfer rate and the mass transport rate is comparable in value, the peak potentials increase with the applied scan rate and hence categorised as quasi-reversible.[17] When the electron transfer rates are sluggish compared to the mass transport rates they are deemed to be irreversible reactions.[18]

2.1.1.4 Cyclic Voltammetry

In Cyclic voltammetry (CV) the electrode potential of the WE is linearly scanned (is swept from V_1 voltage to V_2) while measuring the resulting current. The scan direction is then reversed to the starting voltage (swept from V_2 to V_1) and current response is measured. Depending on the experiment, either single or multiple cycles can be carried out.

The positions of the oxidation and reduction peaks (E_p^c and E_p^a) depend on the species involved in the reaction. For rapid electron transfer reactions, the forward (oxidation) and reverse
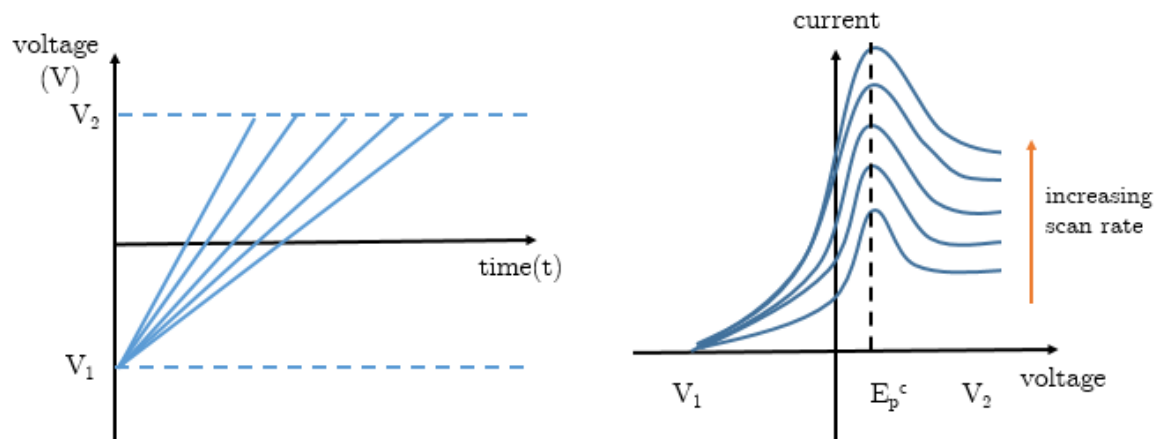
Fig. 2.7   The current response with an increase in the scan rate for linear sweep voltammetry
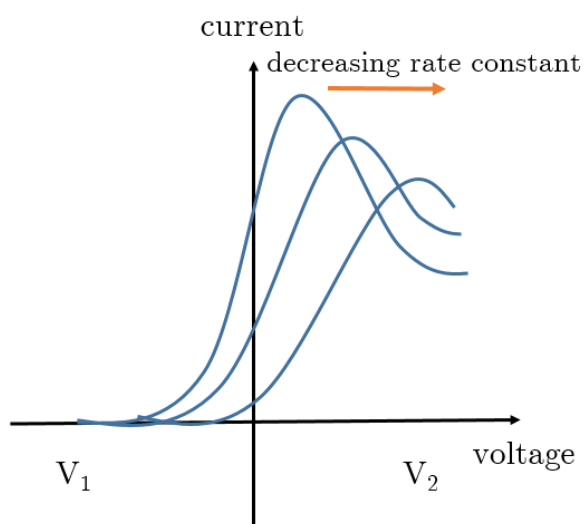

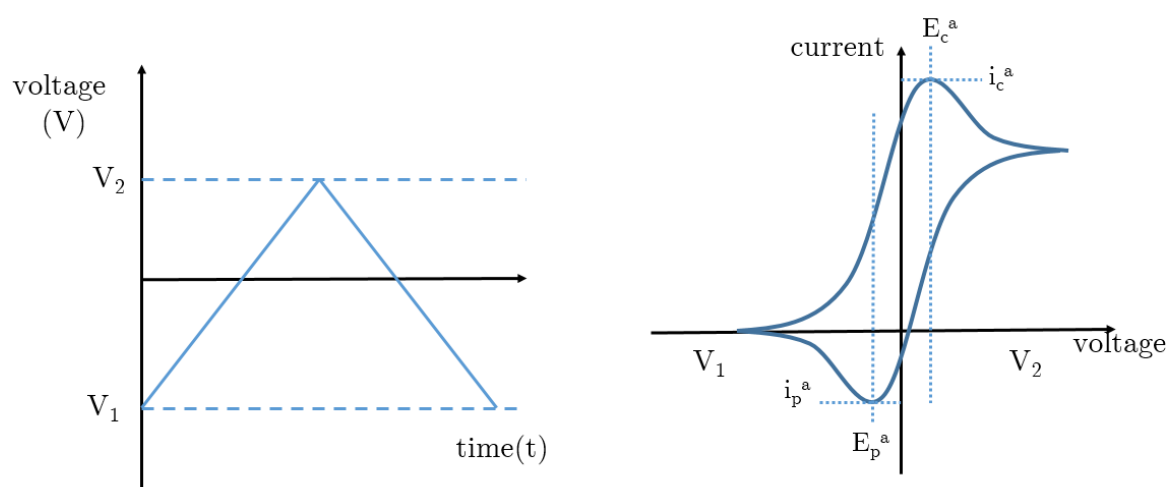**Fig. 2.8**   The current response decreasing rate constant for linear sweep voltammetry

Fig. 2.9   CV for a reversible single electrode transfer reaction for which both oxidised and reduced species are in solution
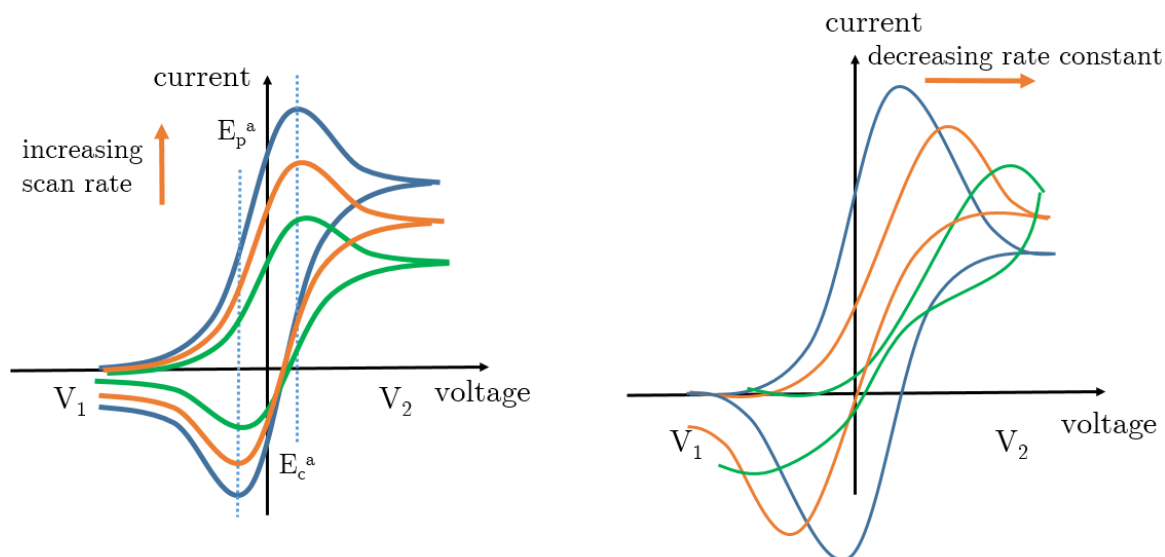
Fig. 2.10 CV for a reversible single electrode transfer reaction for which both oxidised and reduced species are in solution for multiple scan rates

(reduction) current peak ratio would be equal to 1 and separated by a potential difference (E_p^c - E_p^a) that is independent of scan rate.

$$\Delta E = E_p^c - E_p^a = \frac{59}{n}\ mV \tag{2.23}$$

The magnitude of the peak currents (i_p^c and i_p^a) are proportional to the square root of the scan rate. As with LSV the thickness of the diffusion layer increases with slower scan rates, lowering the flux at the electrode.
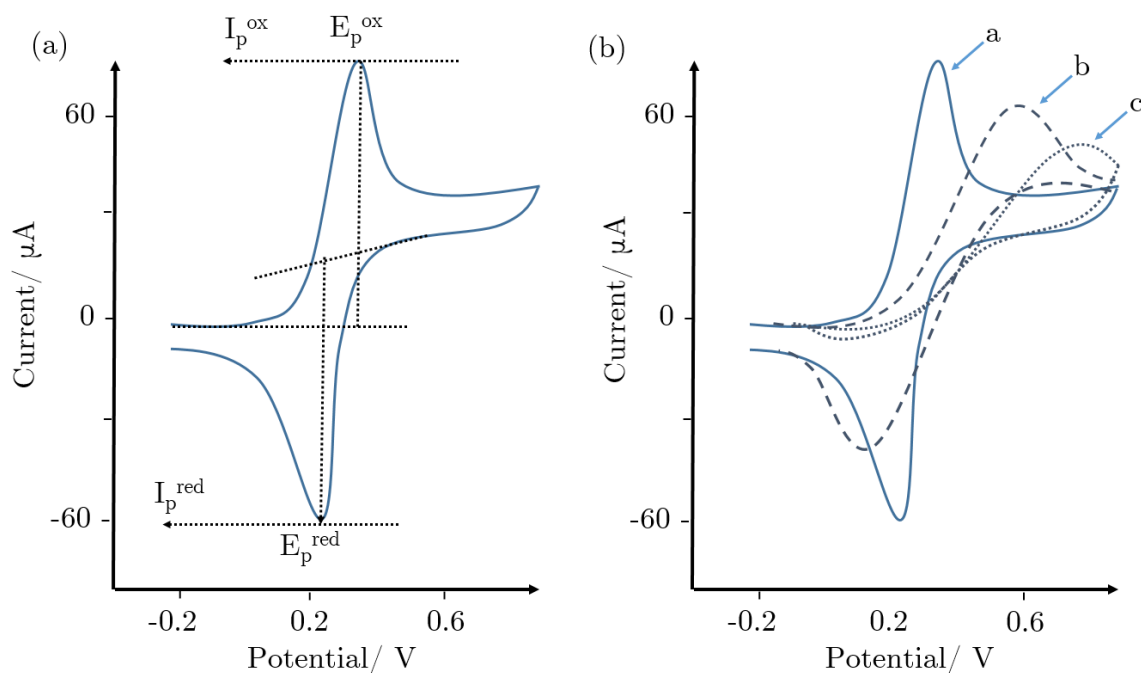

Fig. 2.11 a. Typical cyclic voltammogram depicting the peak position E_p and peak height I_p. b. Cyclic voltammograms for revsersible (a) quasi-reversible (b) and irreversible (c) electron transfer

Depending on the rate of heterogeneous electron transfer, the electrochemical responses in CV can be categorised as reversible, irreversible or quasi reversible. In each case the cyclic voltammograms would be different (Fig. 2.11).

2.1.1.5 Hydrodynamic electrodes

For electrolyte solutions if ionic migration term is neglected, there are only two major processes for mass transport: diffusion and convection. When there is no convection in the solution the thickness of the diffusion layer will increase with time. This results in a non-steady state current. Convection can control the thickness of the diffusion layer whereas diffusion controls the rate of transfer.

The rotating disk electrode is a convenient technique to control the mass transport properties of a electrodeposition system.[19] Mass transport is critical in deep eutectic solvent based systems due to high viscosity.

The working electrode is a rotating disk that drags a layer of solution causing a centrifugal force, which propels, the solution away from the centre of the disc.[18,20,21] The fluid layer removed is constantly replaced by the flow perpendicular to the electrode which creates a laminar flow across the electrode. The rate flow is governed by the electrode's angular velocity.

In RDE, the sensitivity of voltammetric response is increased because mass transport takes place by convection and diffusion. This is achieved by providing a steady supply of reactants to the electrode surface and controlling the mass transport rate by giving stable and reproducible hydrodynamic conditions near the electrode surface.[22] The main principle of this technique is the convection of electrolyte solution with the reactant at a controlled transport rate. In the experimental setup used, the convection is introduced by using a Teflon probe working electrode disc which rotates in solution.
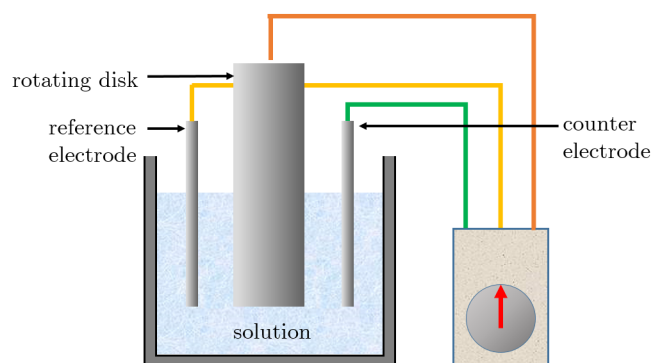

Fig. 2.12 A schematic diagram of RDE cell. The working electrode: Platinum, glassy carbon or gold disc embedded at the end of Teflon shield. The reference and the counter electrodes were a silver wire and a TiO_2 mesh respectively.

When operated within rotation speeds that give a laminar flow, the profile of the electrolyte solution is shown in Fig. 2.13 to Fig. 2.15. The flow rates closest to the electrode surface are much smaller than those further away and therefore not uniform along the x direction.
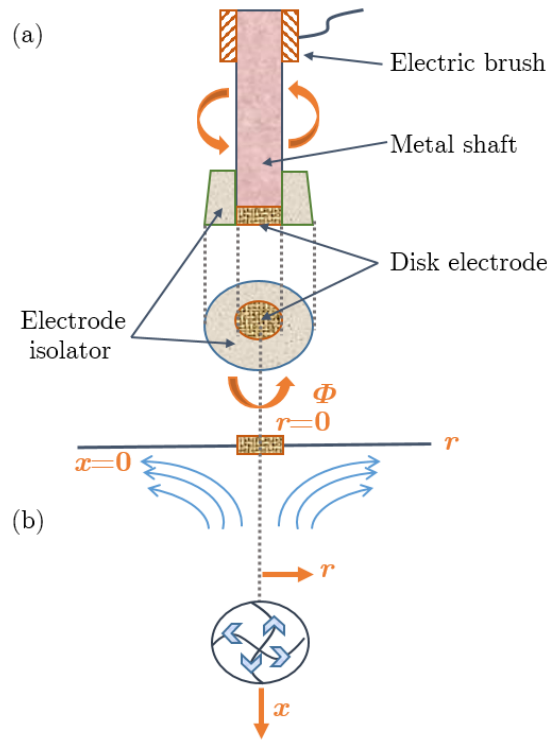
Fig. 2.13   (a) Schematic diagram of the rotating disk electrode (RDE); (b) Flow pattern near electrode surface (x is the coordinate direction perpendicular to the disk electrode surface, r is the coordinate direction parallel to the disk surface, and Φ is the coordinate direction of the electrode rotation, respectively).

However, the flow rate in y direction implies that, at the distance of δ_0 (the thickness of diffusion-convection layer), the flow rate reaches a constant flow rate v_y.
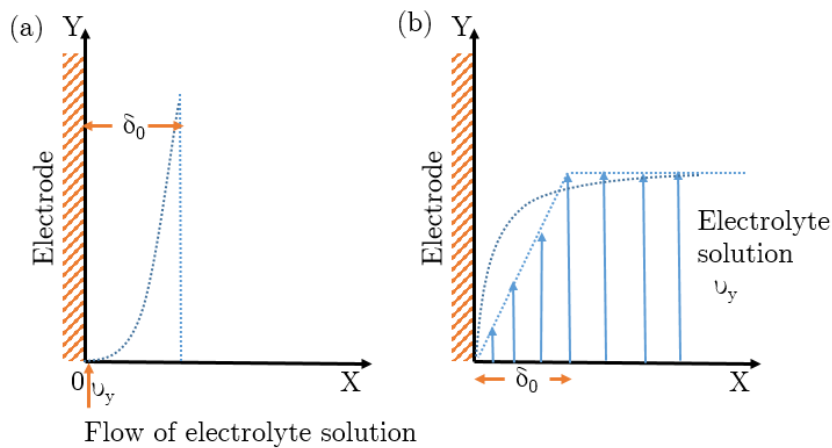

Fig. 2.14   (a) Schematic of the electrolyte solution flow along the electrode surface (b) the flow rate distribution near the electrode surface along the direction parallel to the electrode surface
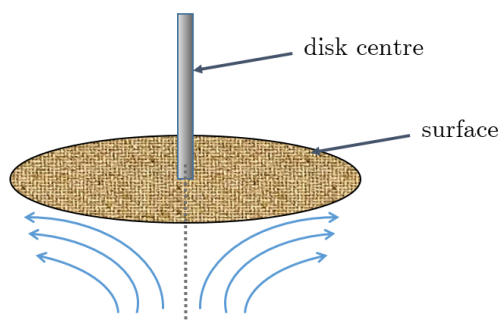
Fig. 2.15   Flow profile produced when a circular object is rotated in solution demonstrating fresh reactant being brought to the surface
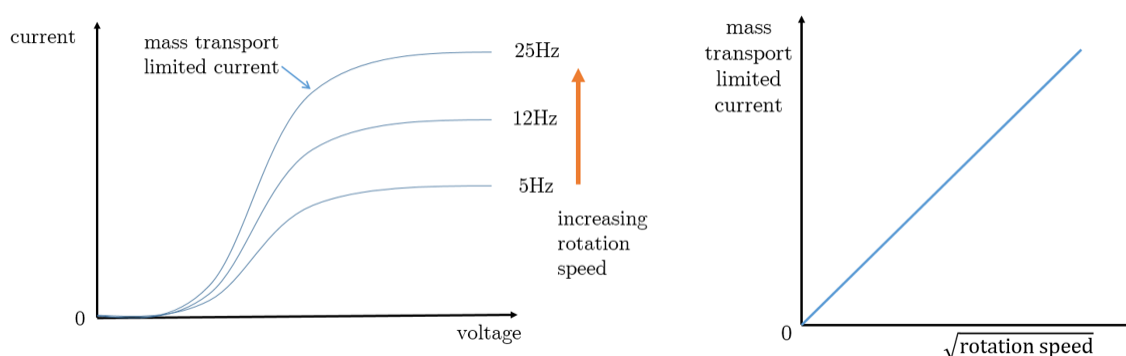

Fig. 2.16   (a) Current vs voltage for different rotation speeds (b) Mass transport limited current vs square root of rotation speed

Equation for mass transport is given by

$$\frac{\partial [C]}{\partial t} = D\frac{\partial^2 [C]}{\partial x^2} - v_x \frac{\partial [C]}{\partial x} \tag{2.24}$$

where D is the diffusion coefficient. Here both diffusion and convection terms affect the concentration of reactant at the electrode surface. Linear sweep voltammetric measurements are used with the rotating disc systems and the diagram (Fig. 2.16) depicts a reversible one electron transfer reaction at different rotation speeds.

The convection keeps the bulk solution concentration uniform. However, a stagnant thin fluid layer forms at the electrode (hydrodynamic boundary layer, δ_F) and the thickness of this layer can be given as:

$$\delta_F = 3.6 \left(\frac{\nu}{\omega}\right)^{1/2} \tag{2.25}$$

Inside the hydrodynamic boundary layer, convection becomes less important and it gives rise to a thinner diffusion only region. This layer (diffusion layer- δ_H) can be defined as:

$$\delta_H = 1.61 \, (D)^{1/3} \, \nu^{-1/6} \, \omega^{-1/2} \tag{2.26}$$

where D_F is the diffusion coefficient of the molecule (cm²s⁻¹).

Levich analysed the relationship of the mass transport limited current with the rotation speed.

$$I_L = 0.62 \, n \, F \, A \, [C]_\infty \, D^{2/3} \bar{\nu}^{-1/6} \omega^{1/2} \tag{2.27}$$

where I_L - Levich current
$\quad n$ - number of electrons transferred in the reaction
$\quad F$ - Faraday constant (96490 C mol^{-1})
$\quad A$ - universal gas constant (8.314J K^{-1} mol^{-1})
$\quad [C]_\infty$ - concentration of the bulk analyte (mol cm^{-3})
$\quad D$ - diffusion coefficient (cm^2 s^{-1})
$\quad \bar{\nu}$ - kinematic viscosity (cm^2 s^{-1})
$\quad \omega$ - angular rotation rate of the electrode (rad s^{-1})

From this we expect a linear trend for reversible reaction for plots of I$_L$ vs the square root of the rotation speed (ω).

Rearrangement of the Levich equation in terms of the reciprocal current versus the reciprocal square root of the angular rotation rate gives a Koutecky-Levich plot.

$$\frac{1}{I} = \left(\frac{1}{0.620 \, n \, F \, A \, D^{2/3} \, \nu^{-1/6} \, C} \right) \omega^{-1/2} \tag{2.28}$$

For reversible half reaction the straight trend line with an intercept at zero for $\frac{1}{I}$ vs $\omega^{-1/2}$ is expected. Non zero intercepts indicate that the half-reaction is limited by sluggish kinetics rather than by mass transport. Here the mass transport limited current plateau would be shifted further away (compared to reversible case) from the standard electrode potential since a higher overpotential would be needed to overcome the slow electron transfer rates and to reach the mass transport limited current.
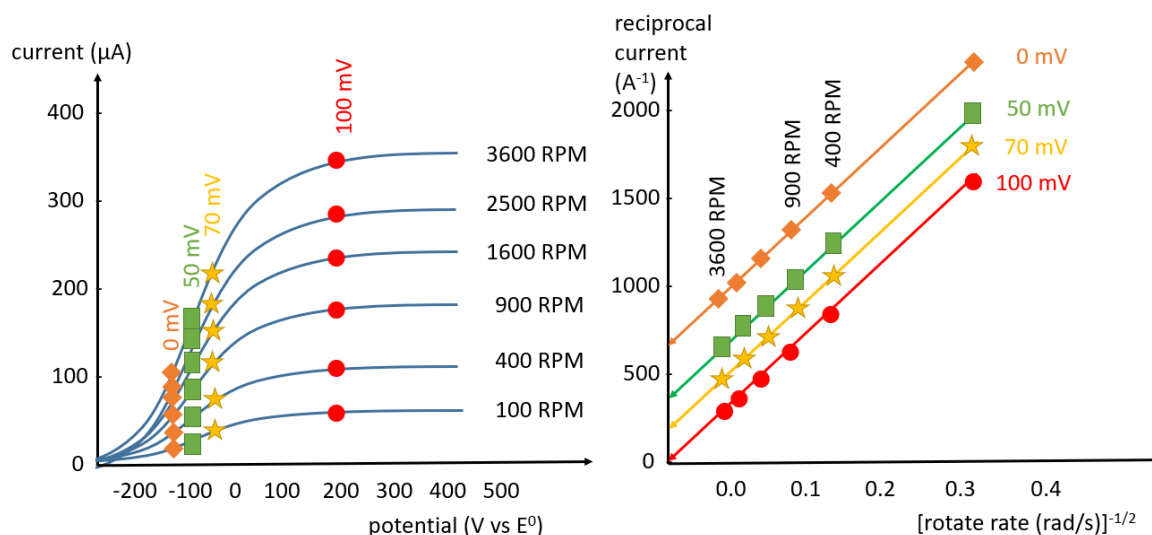

Fig. 2.17 Koutecky-Levich study

Since the limiting currents are sampled at a high enough overpotential there are no kinetic limitations and only mass transport limits the current which is proved by the line behaviour in

Levich predicted trend. These plots give an intercept which is equal to the reciprocal kinetic current ($\frac{1}{I_k}$). For the linear portion of the data on a Koutecky-Levich plot:

$$\frac{1}{I} = \frac{1}{I_k} + \left(\frac{1}{0.620 \ n \ F \ A \ D^{2/3} \ \nu^{-1/6} \ C} \right) \omega^{-1/2} \tag{2.29}$$

The kinetic current represents the current response in the absence of any mass transport limitations. From measuring the kinetic current at different overpotentials we can determine the standard rate constant for the electrochemical half reaction.[23]

The kinetic current value can be used to obtain the heterogeneous rate constant (k_H) from the expression,

$$I_k = n \ F \ A \ k_H \ C \tag{2.30}$$

where C is the concentration. The heterogeneous rate constant derived at various potentials can be used in a rearrangement of the Butler-Volmer equation to obtain the standard rate constant (k_0) and transfer coefficient (α).

$$k_H = k_0 \ exp \left(\frac{-\alpha \ F \ \eta}{R \ T} \right) \tag{2.31}$$

$$k_H = k_0 \ exp \left(\frac{1 - \alpha \ F \ \eta}{R \ T} \right) \tag{2.32}$$

$$ln \ k_H = ln \ k_0 \ + \ \left(\frac{-\alpha \ F}{R \ T} \right) \eta \tag{2.33}$$

The standard rate constant value is an indication of how fast the equilibrium of the reaction can be established. η is the overpotential which can be calculated using applied potential (E) and equilibrium potential (E_0). Thus η can be defined as:

$$\eta \ = \ \left(E - E_0 \right) \tag{2.34}$$

2.1.2 Gravimetric techniques

2.1.2.1 Quartz Crystal Microbalance

The quartz crystal microbalance (QCM) is a powerful gravimetric technique used as a mass sensitive detector and a probe for the measurement of physical properties in vacuum applications and in liquids. The principle is based upon the converse piezoelectric property (a mechanical force generated when sufficient voltage is applied) of quartz, which was discovered in 1881 by Gabriel Lippmann using a mathematical derivation. The piezoelectric word comes from the greek word "piezein" which means "to press or squeeze". This phenomenon was discovered in 1880 by the brothers Pierre Curie and Jacques Curie.[24] The applied potential across the crystal

causes surface mechanical deformation creating an acoustic wave which is propagated to the medium adjacent to the surface. When a potential is applied depending on the orientation of the crystal lattice, different types of oscillations can occur: lateral (thickness – shear and flexural), longitudinal (extensional) and torsional (twist). The quartz crystal is cut at a specific orientation at the angle of 35°15' with respect to the crystallographic axis (AT-cut) to facilitate vibrating in the thickness shear mode (TSM) which achieves highest lateral vibration at the resonant frequency of the crystal. This oscillates parallel to the electrode surface (and the deposited rigid material) synchronously with the solution immediately contacting the electrode.
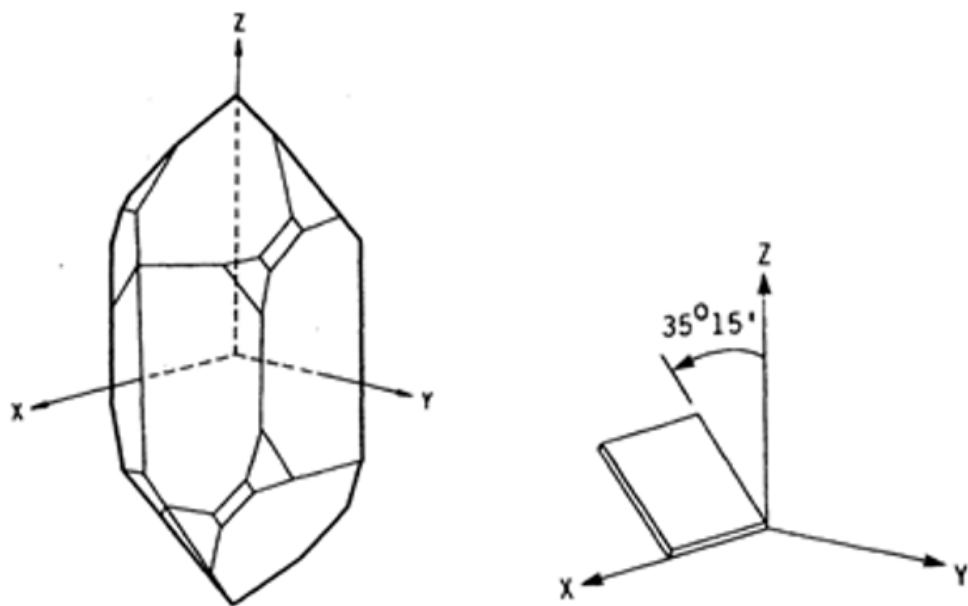

Fig. 2.18 Schematic diagram showing the assignment of the axes to a quartz block
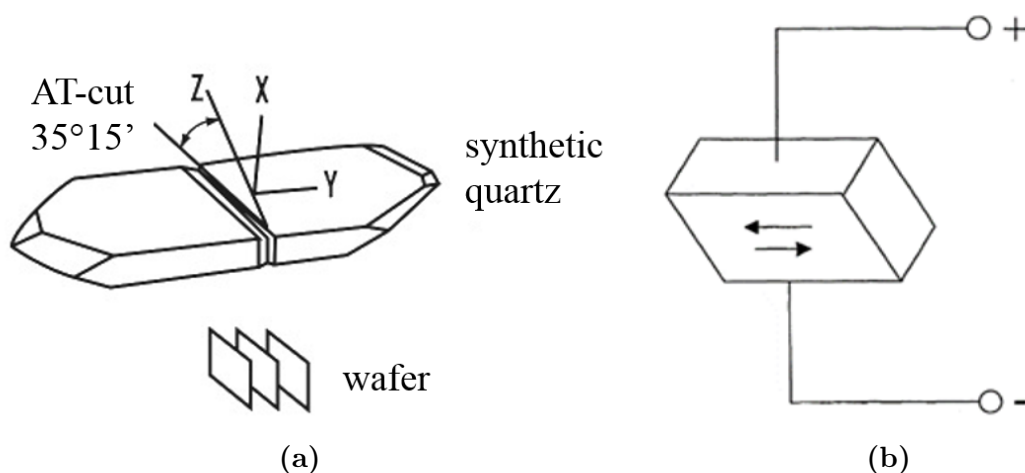

(a) (b)

Fig. 2.19 (a) Cutting angle of AT-cut quartz crystal plate (b)Lateral vibration of the crystal when a potential is applied

The combination of electrochemical and QCM techniques produces the electrochemical quartz crystal microbalance (EQCM) that can be used for monitoring mass changes of surface films during electrochemical measurements. This concept provides unparalleled sensitivity for measuring mass changes and allows simultaneous electrochemical and gravimetric analysis by EQCM. The mechanical stress causes an induction of a net dipole moment that is proportional to the electrical potential generated.[25,26]

The electrochemical deposition of metals increases the mass load on the crystal and hence a fractional change in the oscillating frequency of the crystal. The relationship between the change in mass (Δm) with the change in frequency (Δf) is given by the Sauerbrey equation,[27]

$$\Delta f = -\frac{2f_0^2}{A\sqrt{\rho_q \mu_q}}\Delta m \tag{2.35}$$

where f_0 - resonant frequency (Hz)
Δf - frequency change (Hz)
Δm - mass change (g)
A - piezoelectroctrically active crystal (area between electrode, cm^2)
ρ_q - density of quartz ($\rho_q = 2.648$ g cm^{-3})
μ_q - shear modulus of quartz for AT-cut crystal
($\mu_q = 2.947 \times 10^{11}$ g cm^{-1} s^{-2}).

The first use of EQCM for Ag deposition was published in 1981.[28] In 1985, Bruckenstein and Shay reported the first description of a practical experiment using EQCM.[29] Since then the quartz crystal resonator has been used by electrochemists due to its short data acquisition time (typically < 0.1 s) and high mass sensitivity (nanogram level). For a 10 MHz AT cut crystal, a 1Hz frequency change is approximately equivalent to 1.1 x 10^{-9} g (ca. 1 ng).

There are several limitations of the EQCM when used as a mass sensor that must be considered.[30,31] The Sauerbrey equation can only be applied to a deposited mass that moves synchronously with the quartz layer. Therefore the deposited metal film should be ca. 1% of the mass of the quartz crystal. The shear modulus and density of the film must be taken into account when the mass loaded exceeds 10% of the mass of the quartz crystal . When the mass loaded exceeds 2% of the mass of the quartz crystal, the added mass would no longer move synchronously when the crystal is excited.

The Sauerbrey equation is derived on the assumption that the frequency response is identical at the center and at the edges of the crystal although the maximum amplitude is observed at the center of the electrode. The laterally averaged values of frequency response are considered on the assumption that the film is deposited uniformly which can be validated by SEM and AFM data. Mass loading can be affected by the surface roughness of the electrode. The changes in the rigid coupled mass due to surface roughness can be assessed by AFM scans of the QCM crystal.

The temperature at which the experiments are conducted affect the resonant frequency of a quartz crystal, density and the viscosity of the medium and hence must be monitored. Attenuation of the crystal resonance in high viscous solvents can cause mechanical losses at the

crystal liquid interface and can be quantitatively analysed from calculating the Q factor for the
resonance curve.

$$Q = \frac{f_0}{W} \tag{2.36}$$

where f_0 is the resonance frequency and W is the Full Width of the peak at Half Height
(FWHH). All of the recorded spectra for frequency response (admittance spectra for QCM)
can be numerically processed using fitting procedures to calculate the peak frequency and Q
factor trends.

2.1.3   Optical techniques

2.1.3.1   Probe Beam Deflection

Importance in the field

Classical electrochemistry techniques focus on current and potential transients based on change
in electron fluxes at the electrode/electrolyte interface and have significant limitations in pro-
viding information on interfacial processes. Gravimetric sensors such as EQCM can be used
to determine mass changes on the electrode surface precisely but do not indicate the origin of
the species giving the electron flux. There are few techniques (optical interferometry,[32,33] ra-
diotracer detectors,[34] pH sensors,[35] scanning electron microscopy,[36] ring disk voltammetry,[37,38]
confocal microscopy etc.) that can determine concentration gradients for electrochemical reac-
tions. Nevertheless, their low sensitivity, complex set up and slow response have curtailed their
widespread use.

PBD techniques can be used to study ion fluxes to and from the electrode/ electrolyte inter-
face coupled to electrochemical reactions.[39–42] It helps to measure concentration gradients that
arise during an electrochemical reaction in a fast and simple manner using the optical deflec-
tion caused by refractive index gradients. The EQCM-PBD method can be used to generate
voltammetric, gravimetric and optical responses.

Optical principles

The detection in PBD involves deflection (refraction) of a beam travelling across zones with a
refractive index gradient. The speed of light is different for each part of the beam depending on
its concentration of a particular species. The deflection of a probe beam, which travels close to
an electrode along a path length l, in an electrolyte of refractive index n could be understood as
a distortion wave front of the beam. The wave speed decreases according to $v = c/n$ where v is
the speed of light in the electrolyte, c is the speed of light in the vacuum and n is the refractive
index of the medium.

In conditions of small deflection, the geometric optics approximation could be used:[40]

$$\theta(x,t) = \left(\left(\frac{l}{n} \frac{\delta n}{\delta c} \right) \left(\frac{\delta c(x,t)}{\delta x} \right) \right) \qquad (2.37)$$

where l - interaction path length
n - refractive index of the bulk
$\delta n/\delta c$ - variation of refractive index with concentration
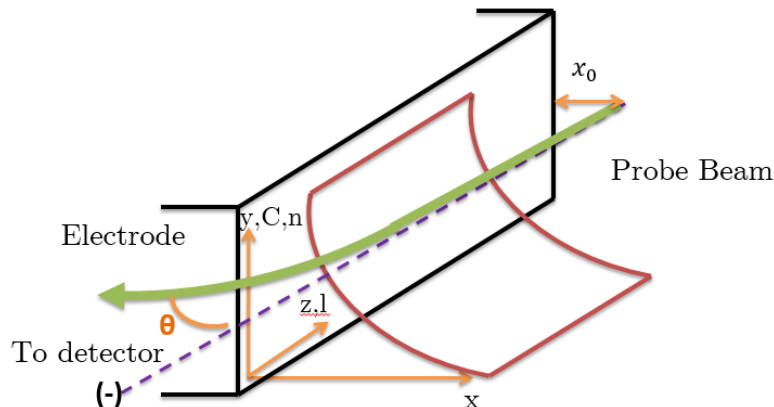x - electrode/beam distance
t - time.

Fig. 2.20   Probe beam path altered by the electrode

Factors affecting the transit times between the electrode surface and the laser beam include distance between the electrode surface and the beam, diffusion coefficient of the species and rate at which the electrochemical processes are conducted (scan rate). This can cause the half cycle to end before the product is detected, electrode reaction proceeding in the opposite direction when the product of the previous cycle is being detected or the convolution analysis not being able to detect the reaction with the potential sweep. In order to control these factors it is necessary to bring the electrode to the point where it is partly obstructing the laser beam (i.e. reducing the x) and conduct the experiment at a slower scan rate (so that the concentration gradients have time to spread out and reach the detector).

Due to this propagation delay that is caused by diffusion of exchanged species, the quantitative evaluation is not straightforward. Therefore, we use the method of temporal convolution to project the current (I) and mass (dm) to the point where optical deflection is measured.[43]

Adequate temperature control is important while conducting the experiment. This is since temperature fluctuations can generate refractive index gradients and affect the density, which would lead to convection currents within the solution. EQCM-PBD data analysis procedures allow the use of in situ optical beam deflection as a quantitative technique for studying dynamic mass exchange in complicated systems.[44]

To make the signal from the beam proportional to the refractive index gradient the beam electrode distance should be closer to zero. Beam has a cylindrical shape with fixed width waist and to avoid border effects usually beam electrode distance is kept ca. 50 μm for a 0.5 to 1 cm electrode width.

Theoretical framework

To develop a theoretical model for the application of PBD we can consider an electrochemical system consisting of a planar electrode of width w in an electrolyte solution. The diffusion of species occur in the solution layer in contact with the electrode and the diffusion layer is several orders of magnitude smaller than w (i.e. border effects are removed).
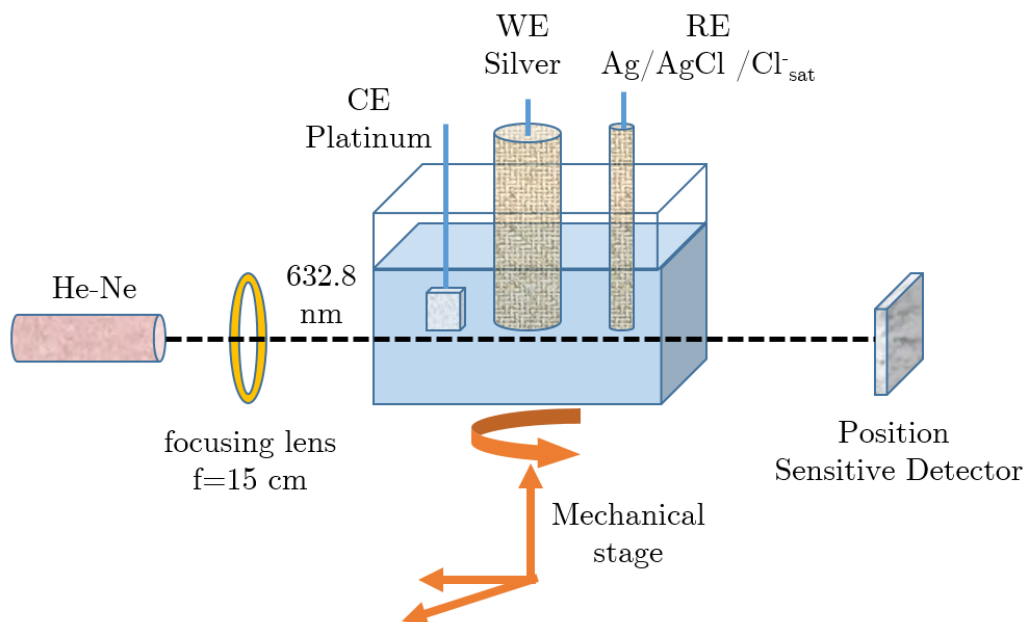

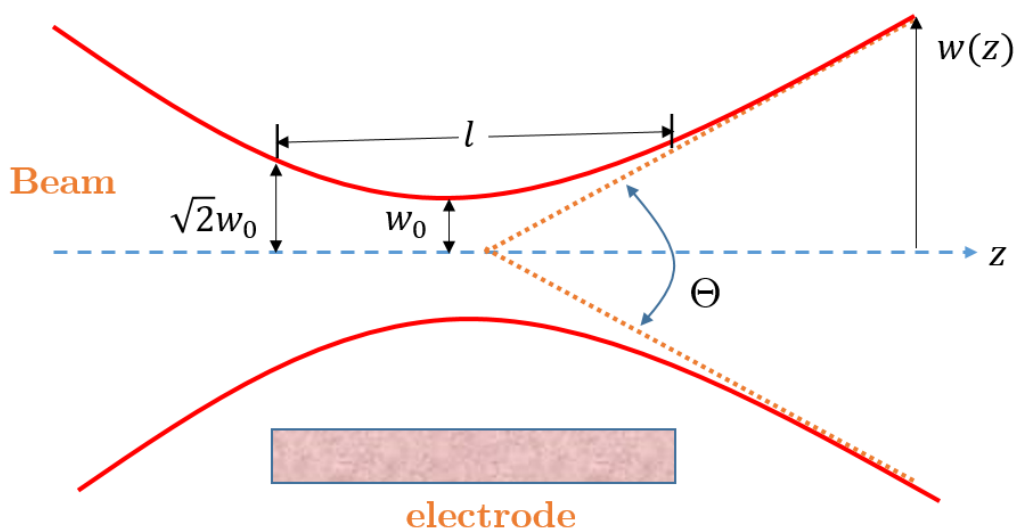**Fig. 2.21**   Probe beam path schematic

Fig. 2.22   Scheme of the probe beam shape in front of the electrode

When considering the electrode vicinity the laser beam is parallel to the electrode and length of the beam passing in the vicinity of the electrode (l) can be considered equal to (w). Electrochemical reactions takes place at the surface of the electrode and hence the distance x would be equal to zero. Therefore the mass transport equation for the diffusion of the reactant species can be represented by the following equation where x is the beam to electrode distance and t is the diffusion time.

$$\frac{\delta^2 C}{\delta x^2} = \frac{1}{D}\frac{\delta C}{\delta t} \tag{2.38}$$

The value of x, diffusion coefficient of the species (D) under study and the rate of the reaction affects the diffusional delay between the optical and electrical signal. Obtaining an optimum value for x is hence essential to reduce the diffusional delay. This can be carried out by obtaining optical deflections for a series of chronodeflectograms and comparing electrical and optical signal time scales. For less than optimum value of x the optical signal would be too small and the noise distortions influences the signal since the beam is too obstructed by the electrode. If the x value is too large the optical signal would not represent the near electrode dynamics since the beam is too far away from the electrode.

Vieil and co-workers suggested a numerical solution for the removal of diffusional delay to calculate the ion fluxes at the electrode using a convolution approach which will be described in Chapter 4.

2.2 Material characterisation

2.2.1 Characterisation methods used in the study

Microscopy and diffractometry have been used as main tools for determining the structure of electrodeposits.

2.2.2 Atomic Force Microscopy (AFM)

Surface topography features and the effect of surface forces are measured using the AFM. AFM consists of three main components: silicone or silicone nitride cantilever, sample stage and an optical detection system (Fig. 2.23). The optical detection system consists of a laser diode and four quadrant photodiode detector. The deflection of the laser due to the strength of forces between tip and the surface and is detected by the four quadrant system (Fig. 2.25). There are 3 modes of operation in AFM and the type of operational mode depend on the probe to sample distance: contact mode (the probe is in contact with the surface), non-contact mode (the probe is not in contact with the surface) and tapping mode (the probe is in contact with the surface but not continuously) (Fig. 2.24).
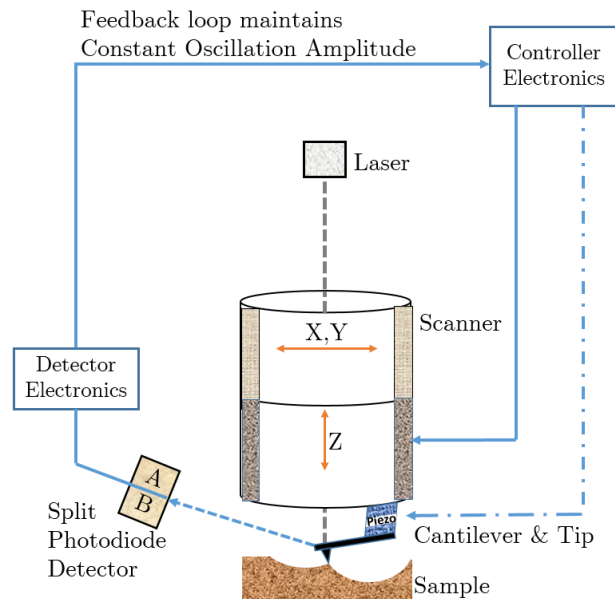
Fig. 2.23   Sketch of the AFM setup indicating positioning of the 3 dimensional scanner, detectors, cantilever and tip. The split photodiode detects the deflected beam and generates a signal which feedback in to the controlling mechanism
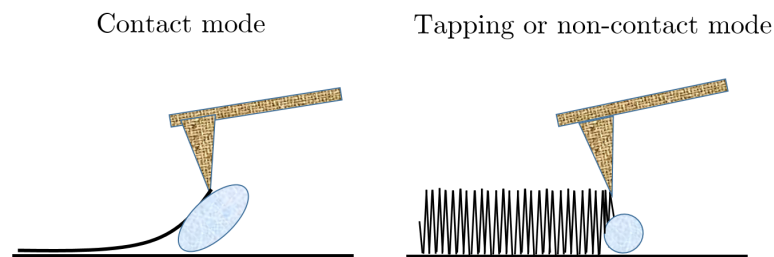

Fig. 2.24   AFM Imaging modes: (a) Cantilever tip movement in the contact mode ; (b) Cantilever tip movement in tapping/non-contact mode
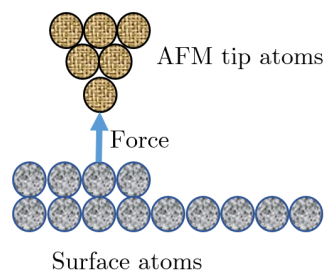

Fig. 2.25   The interaction of the tip atoms of the equipment and the surface atoms of the sample. The minute changes in the force translates in to changes in the deflected laser beam

2.2.3   Scanning Electron Microscopy (SEM)

SEM uses a beam of electrons, typically ca. $2-10$ nm in diameter, to scan in a predetermined raster pattern that cause back scattered electrons (BSEs), secondary electrons (SEs) and X-rays on impact. The scattered electrons given off are collected by a suitable detector and that information and the beam's position is combined to give a topographical, morphological and compositional information (Fig. 2.26).
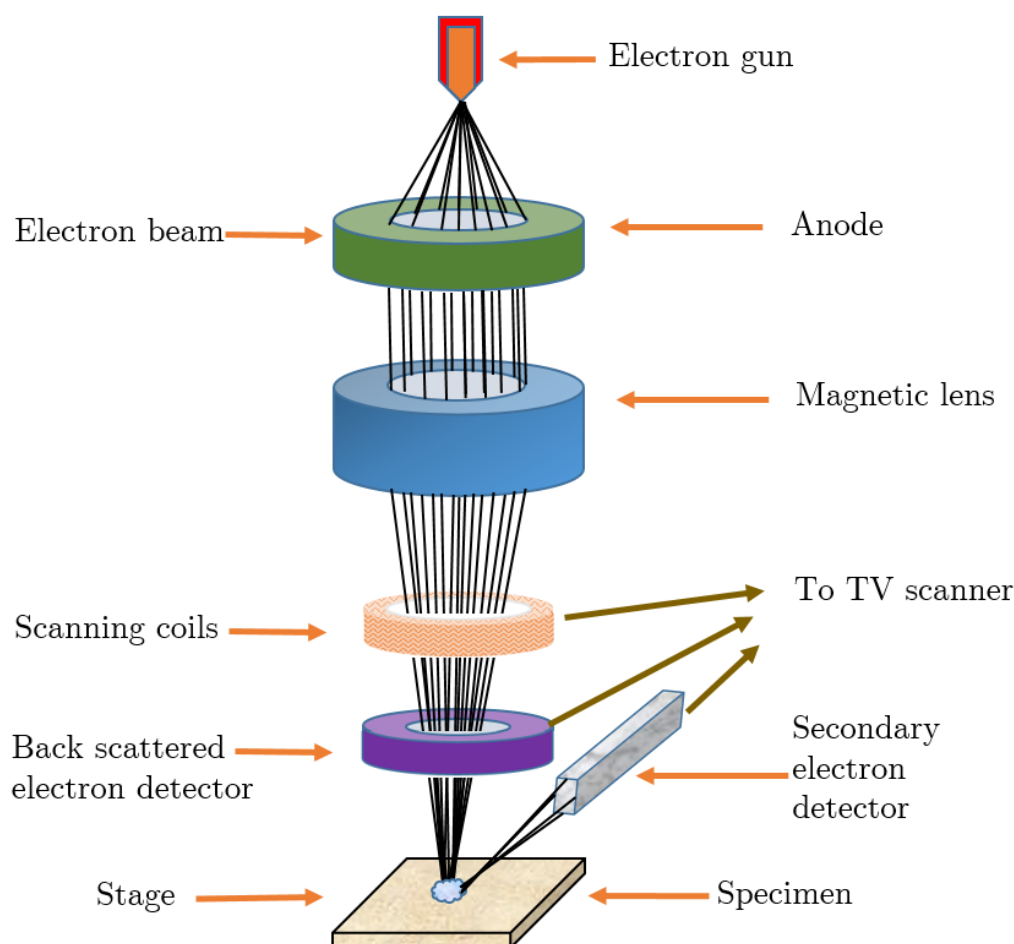

Fig. 2.26   Schematic of the scanning electron microscope setup

2.2.4   Energy-dispersive X-ray analysis (EDAX)

Energy Dispersive X-ray Spectroscopy (EDX or EDAX) is used for elemental analysis of a sample and used in conjunction with SEM.

EDX detects the X-rays produced by an electron beam and processes them into an X-ray emission spectrum, which is a unique set of peaks since each element has a unique atomic structure and the electrons ejected from the inner shell depends on the element because each element has characteristic orbital energies.

2.2.5   X-ray Diffractometry (XRD)

X-ray diffraction (XRD) is a non-destructive technique for characterising crystalline materials to derive phases, crystal orientations and structural parameters including crystallinity, grain size, strain, and crystal defects.[45] XRD is useful for characterising alloys.[46–50]

During XRD analysis, first the surface of a sample is illuminated with a monochromatic beam of X-ray radiation with a wavelength comparable to atomic spacings of the sample. The X-rays are scattered in a specular fashion by the atoms of a crystalline system.[51] Consider a set of N+1 equidistant atomic planes of spacing d, and a monochromatic X-ray falling on it at a glancing angle θ (Fig. 2.27).The scattered X-rays undergo constructive interference and remain in phase since the difference between the path lengths of the two waves is equal to an integer multiple of the wavelength. Secondly, the sample is rotated to allow data to be recorded over a wide range of angles of incidence and diffraction. Thereafter, the constructive interference data of the scattered X-rays, at specific angles from each set of lattice planes in a sample are collected.
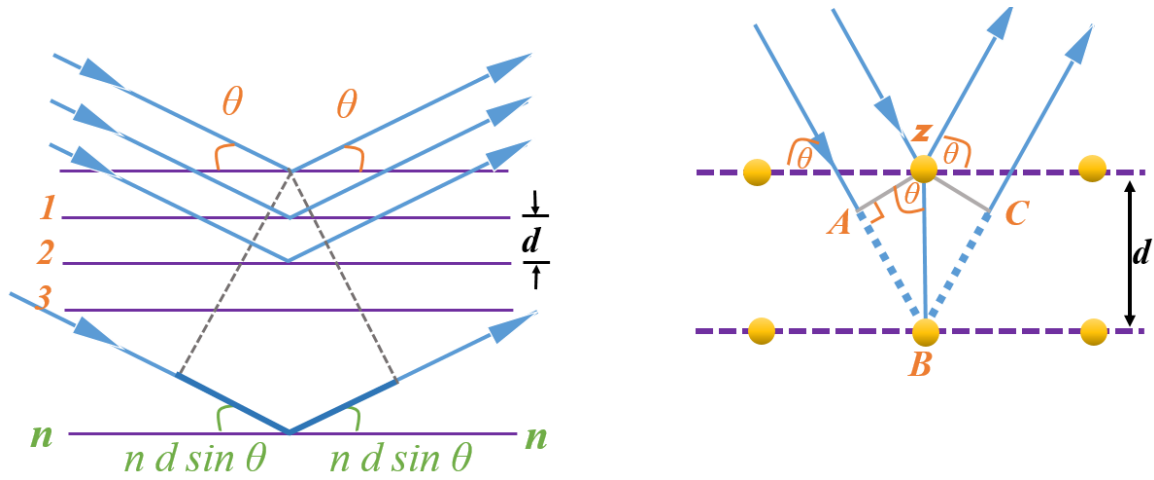

Fig. 2.27   Left panel - Bragg diffraction on a set of n atomic planes. Right panel - phenomenon of Bragg's diffraction where two beams (with same wave length and phase) approach a crystalline solid and subsequently scattered off two different atoms within the crystalline solid. The beam on the bottom travels an extra path length of $2\,d\,sin\,\theta$.

The path difference between two waves undergoing interference is given by 2d $sin\theta$, where θ is the scattering angle. This leads to Bragg's law, which describes the condition on θ for the constructive interference to be at its strongest:

$$2\,d\,sin\,\theta\,n\ =\ n\,\lambda \tag{2.39}$$

where n - a positive integer
λ - wavelength of the incident wave
θ - incident angle
d - distance between planes
$\delta n/\delta c$ - variation of refractive index with concentration

Very strong intensities known as Bragg peaks are obtained in the diffraction pattern at the points where the scattering angles satisfy the Bragg condition.

2.3 Summary

This chapter described the basic principle involved in the methods and instruments used in the study.

References

[1] R. Taylor and R. Krishna, Multicomponent Mass Transfer, John Wiley & Sons, 1993, vol. 2.

[2] S. J. Kline, W. C. Reynolds, F. Schraub and P. Runstadler, Journal of Fluid Mechanics, 1967, **30**, 741–773.

[3] What is Reynolds Number - Definition of Reynolds Number, https://www.nuclear-power.net/nuclear-engineering/fluid-dynamics/reynolds-number/.

[4] Reynolds Number, 2014, https://www.grc.nasa.gov/WWW/BGH/reynolds.html.

[5] O. Fischer and E. Fischerová, in Experimental Techniques in Bioelectrochemistry, Springer, 1995, vol. 91, pp. 41–157.

[6] S. P. Kounaves, Voltammetric Techniques, 1997.

[7] A. J. Bard and J. Ketelaar, Journal of The Electrochemical Society, 1974, **121**, 212C–212C.

[8] L.-H. L. Miaw and S. Perone, Analytical Chemistry, 1979, **51**, 1645–1650.

[9] T. M. Nahir, R. A. Clark and E. F. Bowden, Analytical Chemistry, 1994, **66**, 2595–2598.

[10] J. Heinze, Angewandte Chemie International Edition in English, 1984, **23**, 831–847.

[11] N. Elgrishi, K. J. Rountree, B. D. McCarthy, E. S. Rountree, T. T. Eisenhart and J. L. Dempsey, Journal of Chemical Education, 2017, **95**, 197–206.

[12] R. S. Nicholson, Analytical Chemistry, 1965, **37**, 1351–1355.

[13] P. T. Kissinger and W. R. Heineman, Journal of Chemical Education, 1983, **60**, 702.

[14] G. A. Mabbott, Journal of Chemical Education, 1983, **60**, 697.

[15] F. Cottrell, Z Physik Chem, 1902, **42**, 385.

[16] R. G. Compton and C. E. Banks, Understanding voltammetry, World Scientific, 2011.

[17] H. Matsuda and Y. Ayabe, Bulletin of the Chemical Society of Japan, 1955, **28**, 422–428.

[18] C. Du, Q. Tan, G. Yin and J. Zhang, in Rotating Electrode Methods and Oxygen Reduction Electrocatalysts, Elsevier, 2014, pp. 171–198.

[19] W. D. Sides and Q. Huang, Electrochimica Acta, 2018, **266**, 185–192.

[20] A. J. Bard, L. R. Faulkner et al., Electrochemical Methods, 2001, **2**, 482.

[21] Q.-X. Zha, Science Press, Beijing, 2002, 182.

[22] M. Lovrić and J. Osteryoung, Journal of Electroanalytical Chemistry and Interfacial Electrochemistry, 1986, **197**, 63–75.

[23] S. Treimer, A. Tang and D. C. Johnson, Electroanalysis, 2002, **14**, 165.

[24] J. Curie, Bull. Soc. Fr. Mineral., 1880, **3**, 90.

[25] O. Kurtz, J. Barthelmes, R. Rüther, M. Wünsche and C. Donner, Electrochemistry a. Plating Technology, 2010, **5**, year.

[26] A. R. Hillman, Journal of Solid State Electrochemistry, 2011, **15**, 1647–1660.

[27] G. Sauerbrey, Zeitschrift für physik, 1959, **155**, 206–222.

[28] T. Nomura and M. Iijima, Analytica Chimica Acta, 1981, **131**, 97–102.

[29] S. Bruckenstein and M. Shay, Electrochimica Acta, 1985, **30**, 1295–1300.

[30] K. K. Kanazawa and J. G. Gordon, Analytical Chemistry, 1985, **57**, 1770–1771.

[31] K. K. Kanazawa and J. G. Gordon II, Analytica Chimica Acta, 1985, **175**, 99–105.

[32] M. Françon, in Neutron Interferometry, 1979.

[33] P. Hariharan, Optical Interferometry, 2e, Elsevier, 2003.

[34] A. Baumann, A. Faust, M. P. Law, M. T. Kuhlmann, K. Kopka, M. Schafers and U. Karst, Analytical Chemistry, 2011, **83**, 5415–5421.

[35] P. Y. Apel, Y. E. Korchev, Z. Siwy, R. Spohr and M. Yoshida, Nuclear Instruments and Methods in Physics Research Section B: Beam Interactions with Materials and Atoms, 2001, **184**, 337–346.

[36] Y.-K. Sun, D.-H. Kim, C. S. Yoon, S.-T. Myung, J. Prakash and K. Amine, Advanced Functional Materials, 2010, **20**, 485–491.

[37] I. H. Omar, H. Pauling and K. Jüttner, Journal of The Electrochemical Society, 1993, **140**, 2187–2192.

[38] P. Andricacos, J. Tabib and L. Romankiw, Journal of the Electrochemical Society, 1988, **135**, 1172–1174.

[39] C. Barbero, M. Miras, R. Kötz and O. Haas, Solid State Ionics, 1993, **60**, 167–172.

[40] C. A. Barbero, Physical Chemistry Chemical Physics, 2005, **7**, 1885–1899.

[41] C. Barbero, M. Miras and R. Kötz, Electrochimica Acta, 1992, **37**, 429–437.

[42] L. Abrantes, M. Oliveira and E. Vieil, Electrochimica Acta, 1996, **41**, 1515–1524.

[43] A. R. Hillman, K. S. Ryder, C. J. Zaleski, V. Ferreira, C. A. Beasley and E. Vieil, Electrochimica Acta, 2014, **135**, 42–51.

[44] E. Vieil, Journal of Electroanalytical Chemistry, 1994, **364**, 9–15.

[45] P. L. Davies, U. Gather, M. Meise, D. Mergel, T. Mildenberger et al., The Annals of Applied Statistics, 2008, **2**, 861–886.

[46] V. B. Kumar, G. Kimmel, Z. Porat and A. Gedanken, New Journal of Chemistry, 2015, **39**, 5374–5381.

[47] T. Dobrovolska, I. Krastev, B. Jović, V. Jović, G. Beck, U. Lačnjevac and A. Zielonka, Electrochimica Acta, 2011, **56**, 4344–4350.

[48] S. P. Singh and B. Karmakar, Plasmonics, 2011, **6**, 457–467.

[49] V.-F. Ruiz-Ruiz, I. Zumeta-Dube, D. Díaz, M. J. Arellano-Jimenez and M. Jose-Yacaman, The Journal of Physical Chemistry C, 2016, **121**, 940–949.

[50] P. Kumar, J. Singh and A. C. Pandey, RSC Advances, 2013, **3**, 2313–2317.

[51] D. M. Moore and R. C. Reynolds, X-ray Diffraction and the Identification and Analysis of Clay Minerals, Oxford university press Oxford, 1989, vol. 322.

Chapter 3

Experimental

Contents

3.1 Introduction

This section contains descriptions of experimental work conducted in terms of instrumentation, materials and procedures for the research presented in Chapters 4 to 6. Also, the mathematical background used for convolution of the optical and gravimetric data is presented here,

3.2 Materials

Table 3.1 contains a list of chemicals used to obtain the results presented in this project. Choline chloride, ethelyne glycol, nitric acid, percholric acid (70% aq), silver nitrate, silver chloride, bismuth chloride and pottasium chloride were all supplied by Sigma Aldrich and was used as received unless specifically stated in the relevant section.

3.3 Procedures

3.3.1 Preparation of Ethaline 200 deep eutectic solvent

Choline chloride (ChCl) was added to ethyline glycol ($C_2H_5O_2$) in 1:2 molar ratio to form Ethaline 200. The resulting mixture was continually stirred in a beaker on a hot plate at 50 °C until a homogeneous and colourless liquid phase (circa 30 minutes) was formed. Once prepared, Ethaline was stored in a sealed containers in an oven at circa 50 °C until further use. Ethaline 200 was used as an electrolyte for metal deposition in chapters 4 to 7.

3.3.2 Preparation of silver nitrate in perchloric acid solution

2.14 ml of perchloric acid (70% aqueous) was mixed with 50 ml of de-ionised water in a 100 ml volumetric flask. 0.017 g of silver nitrate was added to this solution and sonicated until complete dissolution (10 minutes). The solution was topped up with de-ionised water to 100 ml and stored at 5 °C under dark conditions. The solution was filtered using 0.1 μm filters (single or multiple) before the probe beam deflection experiments to remove any insoluble particles. This solution was used for Ag deposition in aqueous media.

3.3.3 Preparation of silver chloride/ Ethaline 200 for EQCM-PBD experiments

0.14332 g of silver chloride was added to 100 ml of Ethaline 200 and the mixture was continuously stirred at 70 °C on a magnetic hot plate. Once a clear homogeneous liquid was formed, the solution was used for deposition of AgCl in DES as the metal chloride electrolyte. The solution was filtered using 0.45 μm filters (single or multiple) before the PBD experiments.

Table 3.1 List of compounds used in the studies reported in this thesis. All the chemicals were used as obtained.

Compound	Molecular weight/ g mol^{-1}	Chemical formula	Application	Purity	Supplier
Choline chloride	139.62	$C_5H_{14}ClNO$	Quaternary Ammonium salt	96%	Sigma Aldrich
Ethelyne glycol	62.07	$C_2H_6O_2$	Hydrogen bond donor	99%	Sigma Aldrich
Nitric acid	63.01	HNO_3	Cleaning agent	70%	Sigma Aldrich
Percholric acid (70% aq)	100.46	$HClO_4$	Supporting electrode	98%	Sigma Aldrich
Silver nitrate	169.87	$AgNO_3$	Metal salt	99.2%	Sigma Aldrich
Silver chloride	143.32	$AgCl$	Metal salt	99%	Sigma Aldrich
Bismuth chloride	315.34	$BiCl_3$	Metal salt	99%	Sigma Aldrich
Pottasium chloride	74.55	KCl	Electrolyte for reference electrode	99%	Sigma Aldrich

The mass of silver chloride used may differ for other studies (depending on the concentration of AgCl used) and the relevant changes will be indicated in the corresponding section.

3.3.4 Preparation of bismuth chloride/ Ethaline 200 for EQCM-PBD experiments

0.31534 g of bismuth (III) chloride was added to 100 ml of Ethaline 200 and continually stirred on a magnetic hot plate at 50 °C. Once the clear homogeneous liquid was formed the solution was stored at 50 °C. The solution was filtered using 0.45 μm filters (single or multiple) before the PBD experiments. The solution was sonicated to remove the trapped air. The mass of silver chloride used may differ for other studies (depending on the concentration of Bi(III) required) and the relevant changes in concentrations will be indicated in the corresponding section.

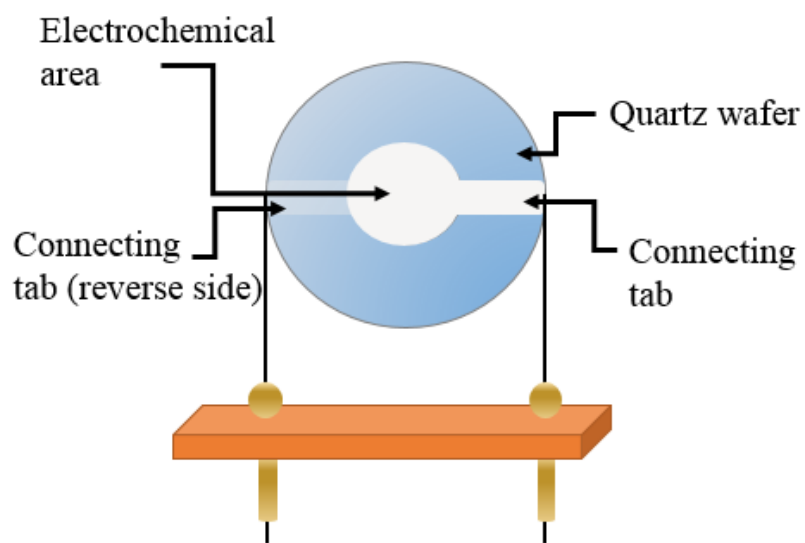### 3.3.5 Preparation of bimetal (silver/ bismuth) electrolyte solution

0.0539 g of silver chloride and 0.1596 g Bismuth (III) chloride was added to 100 ml of ethaline 200 and continually stirred on a magnetic hotplate at 50 °C. The solution was filtered using 0.45 μm filters (single or multiple) and sonicated to get rid of trapped air before each experiment. The mass of silver chloride used may differ for other studies (depending on the concentration of Ag(I)/Bi(III) required) and the relevant changes will be indicated in the corresponding section.
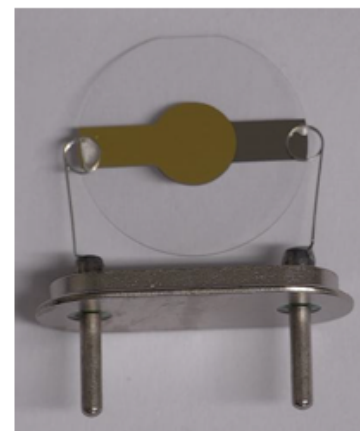
3.4 Instrumental

3.4.1 Preparation of Working Electrode

The working electrode was 10 MHz AT cut quartz crystal resonator. The crystals were supplied by International Crystal Manufacturing Co. Inc. (Oklahoma City, Oklahoma, USA). The crystal consisted of a thin wafer of AT cut quartz with vacuum deposited platinum or gold films on either sides. Piezoelectric and electrochemically active areas were 0.23 cm^2 and 0.21 cm^2 respectively (see Fig. 3.1 a, b).[1]

The working electrode was assembled by mounting a commercially available quartz resonator on a glass tube. First the quartz crystal was separated carefully from the electric lead and connected to the wires using silver conducting adhesive (supplied by Electrolube Ltd.). Then the resonator was mounted on the glass tube using RS 692-542 silicon adhesive sealant (supplied by RS Components Ltd). A minimum amount of the adhesive was carefully applied to avoid contaminating the electrode surface. The two wires were soldered to external connection and the wires were adhered to the cylindrical part of the glass tube (Fig. 3.1 c,d,e).
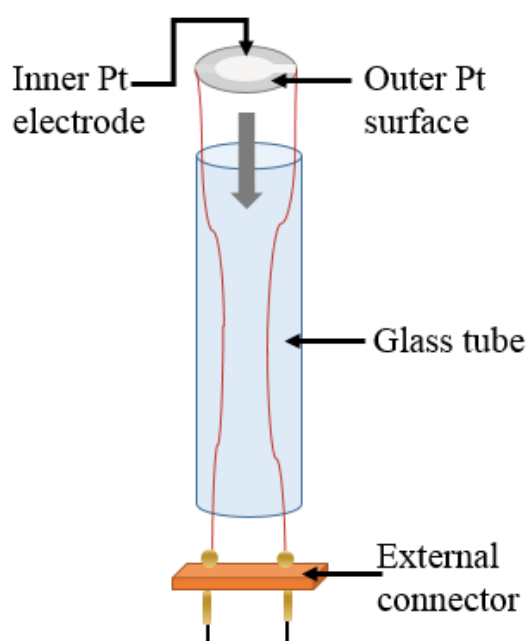
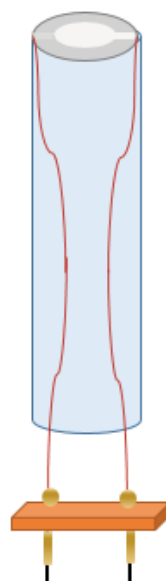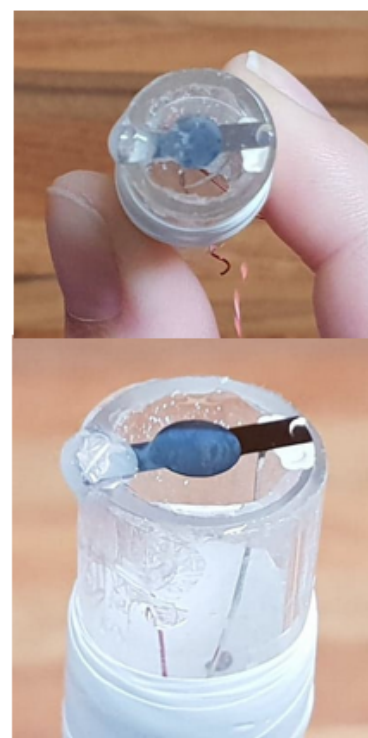**Fig. 3.1** 10 MHz AT cut platinum quartz crystal resonator (a) schematic diagram (b) actual equipment; Preparation of the working electrode for EQCM-PBD study (c)/(d) schematic diagram (e) actual equipment

3.4.2 Preparation of Counter Electrode

The counter electrode was made of IrO_2 coated Ti mesh (supplied by De Nora) and had a 2 cm^2 electroactive area. The increased electroactive area was used to overcome any CE partial blockages that might occur.[2] The electrode was bent to form 1:3 ratio 'L' shape to provide parallel/ maximum proximity to the working electrode (Fig. 3.5 (f,g)) When the working electrode and counter electrode are of similar sizes, they will influence the electrochemical response of each other.[3]

3.4.3 Preparation of the Reference Electrode

The Reference Electrode (RE) in aqueous solutions was a home-built Ag/ AgCl RE with 1 mm 99% pure Ag wire coated with a AgCl layer and saturated pottasium chloride (circa 3.5 M) (Fig. 3.2).
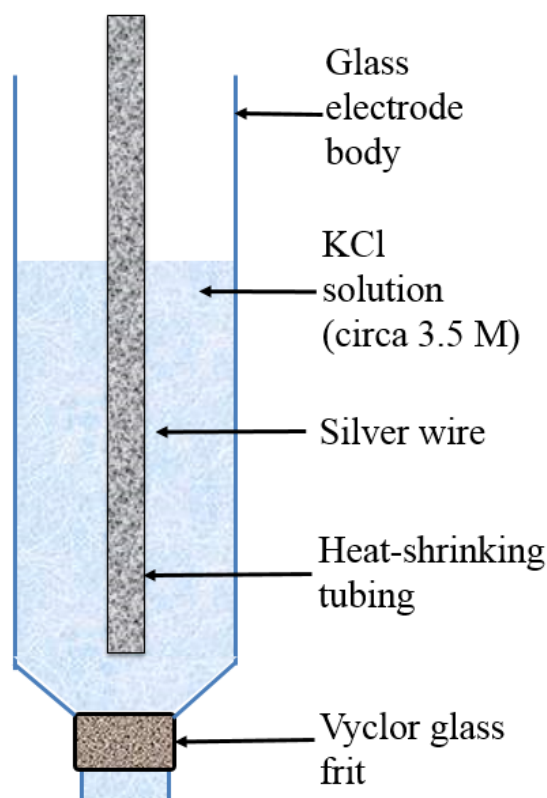
Fig. 3.2 Schematic diagram of the Ag^+/Ag in Ethaline reference electrode.

The setup was in a glass tube with a porous Vycor glass frit on the bottom. Ag/AgCl RE could not be used for DES due to the liquid junction potential because of the difference in ion mobility between aqueous and DES occurring from large vicosity differences. Quasi RE or pseudo Ag or Pt wires were used for DES in many studies[4-6] assuming that the potential does not change in experiments to create a significant change in electrode material when pseudo RE is immersed in Room Temperature Ionic Liquids (RTILs). The high concentration of Cl^- in RTIL (e.g. the concentration of Cl^- in Ethaline is circa 4.2 M) makes it possible for Ag pseudo

reference to be used.[7] Due to these reasons the Ag wire was polished with sand paper, cleaned with deionized water accetone, dried and was used as the pseudo RE.

3.4.4 Preparation of gold surface working electrodes

For some electrodeposition work, gold coated glass slides were used. The following steps were followed for this process. The glass microscope slides (Platypus technologies) were used as provided. The following 9 step process was then followed:

1. Firstly slides were cleaned by Anapol-C solution, a mixture of commercial detergents, rinsed sonicated in deionised water and dried with compressed air.

2. Secondly they were placed in a round bottom flask containing 3 vol% (3-mercaptopropyl) trimethoxy silane (MPTS) in 3 vol% deionised water and 94 vol% isopropanol (IPA)

3. The glass slides were placed on a slide holder in the solution so that the surfaces of the glass slides would not be touching; and were freely exposed to the solution.

4. The solution was then set to reflux for 20 minutes at 50 °C temperature while the large round bottom flask was covered with Al glass foil.

5. The solution was set to cool for 30 minutes and then each slide was taken out and washed with fresh IPA solution separately.

6. The glass slides were then placed again in the slide holder, immersed in fresh IPA and sonicated for 15 minutes.

7. A fresh solution of 3 vol% MPTS, 3 vol% H_2O and 94 vol% IPA was made and steps (2) to (7) were repeated two more times.

8. After iteratively drying for three times, the dried MPTS coated slides were stored in a container under vacuum and immediately used for gold coating.

9. The EMS300RT Triple target, large chamber , rotary - pumped sputter gold coater was used for this purpose. Six slides were placed at a time on the disc inside and a current of 80 μA was used for 200 seconds to achieve film of gold of uniform thickness.

MPTS is a thiol-terminated organosilane which covalantely binds to metallic nanoparticles.[8–11] MPTS has an exposed sulphur that metals like gold, silver can easily bind to facilitating gold-thiol immobolization (Fig. 3.3).[9,12–15] These slides were stored in a closed desiccator at room temperature until use.

3.4.5 Preparation of electrochemical cell for gravimetric studies

For gravimetric studies the working electrode (WE) was the EQCM crystal mounted on a polytetrafluoroethylene (PTFE) stage so that the working electrode side of it is exposed to the electrolyte and the other side is exposed to air (Fig. 3.4). The RE was a Ag wire and the CE
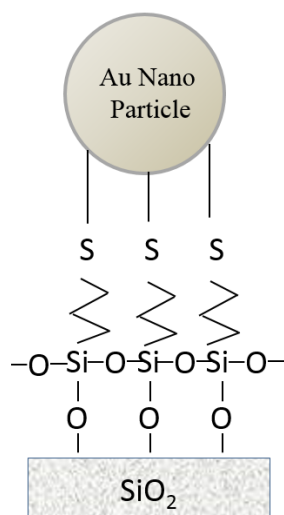
Fig. 3.3 Schematic diagram the covalent binding of gold nano particle to silicon oxide surface through MPTS.

was a IrO_2/Ti mesh. The cell was cylindrical PTFE (home made electrochemical) with external dimensions of 49 mm height, 35 mm diameter and can hold up to 20 ml electrolyte (Fig. 3.4). The electrochemical and gravimetric data were recorded simultaneously using Gamry EQCM 10 M connected to Gamry Instruments Reference 600 potentiostat. The advantage of using this was that it produced the electrochemical and gravimetric parameter outputs without requiring a separate fitting program.
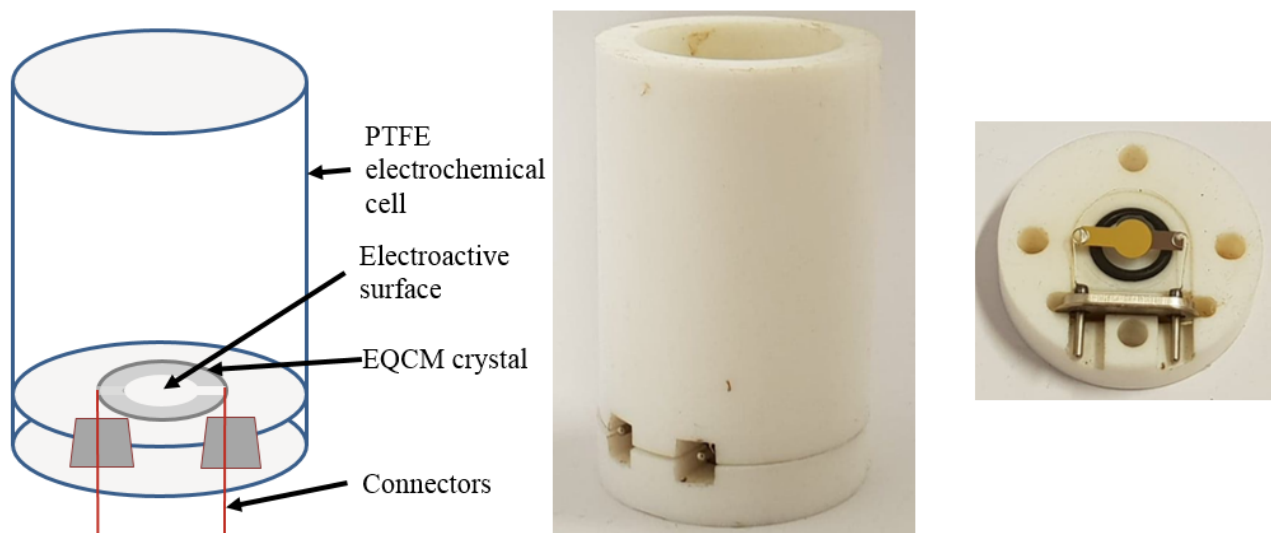

Fig. 3.4 PTFE in-house made electrochemical cell with inserted EQCM crystal schematic diagram (left) assembled electrochemical cell (middle) and quartz crystal electrode that is located within the electrochemical cell (right) (maximum electrolyte volume = 20 ml, electrolyte volume used = 10 ml).

3.4.6 Preparation of electrochemical cell for EQCM-PBD optical gravimetric studies

The cell was a glass quartz curvette (Helma Inc). The external size of this cell was 42 cm x 42 cm x 30 mm (height, breadth, width respectively). A Teflon^{TM} lid with holes for electrode inserts are used to place the electrode setup accurately. The WE was the home-built EQCM crystal electrode, RE was pseudo Ag wire and CE was IrO$_2$ coated Ti mesh.
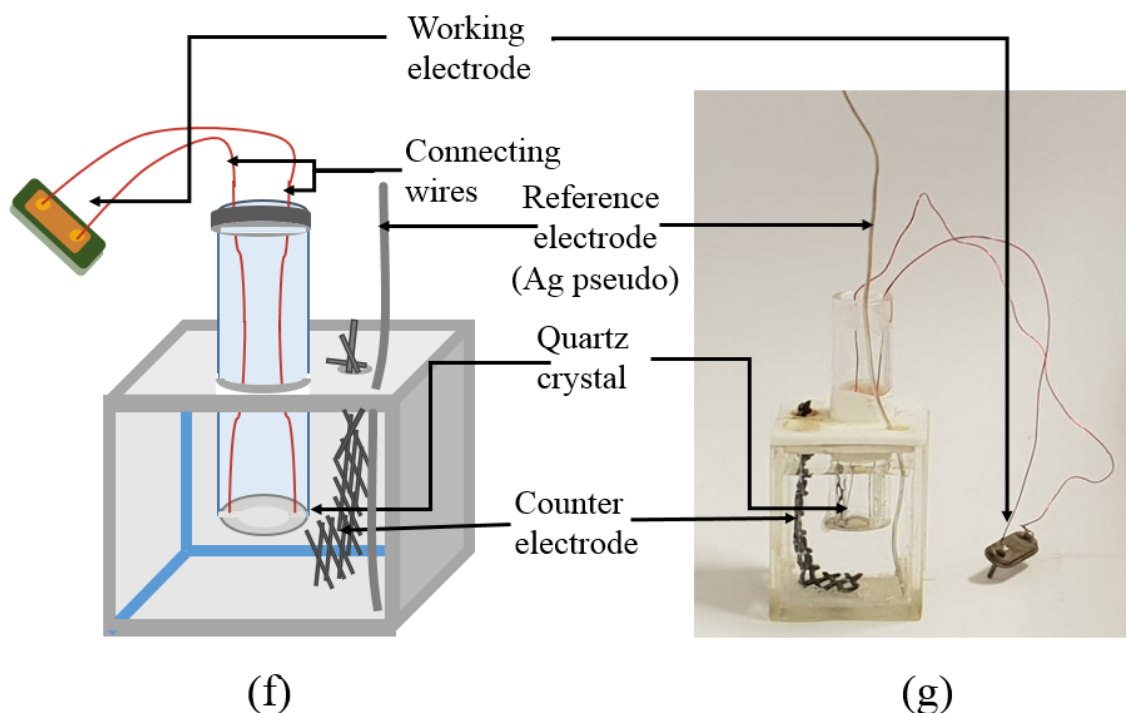
Fig. 3.5 Electrochemical cell for EQCM-PBD optical gravimetric studies(f) schematic diagram (g) actual equipment setup

3.4.7 Preparation of electrochemical cell for nucleation studies

Electrochemical methods (cyclic voltammometry, chronoamperometry) were performed using Autolab PGSTAT 12 potential controlled GPES2 software (version 4.9). For nucleation studies the electrochemical cell consisted of Pt disc (1 mm diameter) home-built working electrode, Pt flag counter electrode and pseudo Ag reference electrode.

3.4.8 Preparation of electrochemical cell for Rotating Disk Electrode

Linear sweep voltammetry experiments for Koutecky-Levich analysis were carried out using Metrohm AutoLab PGSTAT204 potentiostat with Autolab NOVA Software (version 2). The electrochemical cell consists of the RDE working electrode, a silver wire pseudo reference electrode and an IrO$_2$ coated titanium mesh counter electrode.

The RDE working electrode was a 5 mm disk electrode tip connector. Gold and platinum RDE tips have been used for the experiment in Chapter 6 (Fig. 3.6 and Fig. 3.7). The electrochemical cell used was Metroohm Autolab standard plastic cell with the stand (Fig. 3.8).

Fig. 3.6   5 mm electrode tips used with the Autolab RDE during these experiments; from (L to R): Gold and platinum electrodes. [16]

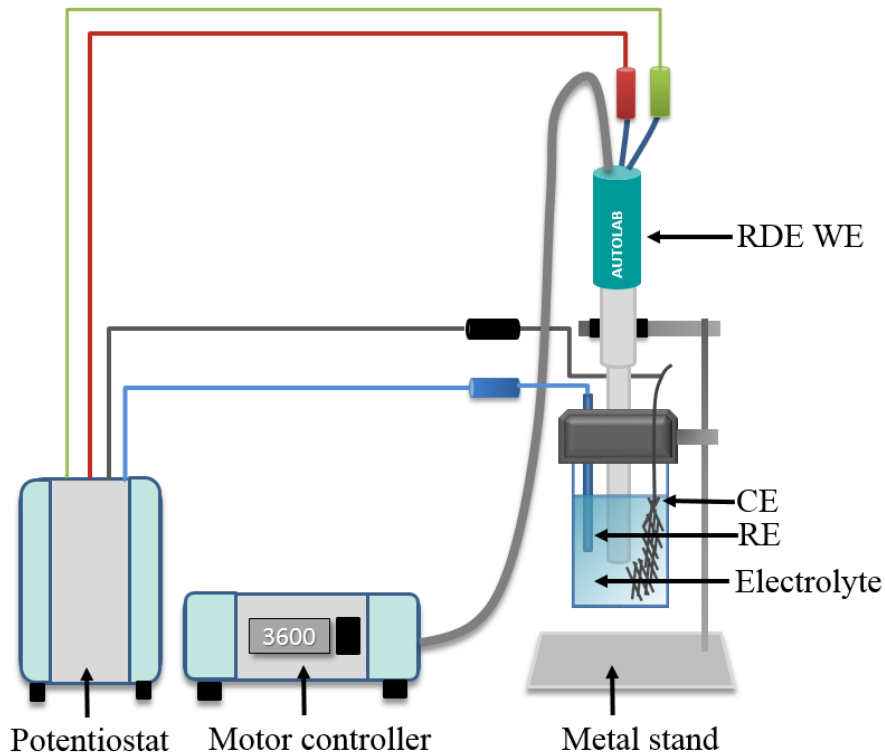

Fig. 3.7   RED working electrode. [16]

Fig. 3.8   Schematic diagram of the RDE setup

3.4.9 EQCM-PBD intrumentation

The EQCM-PBD experiments were conducted using the Gamry (poteniostat/ galvanostat/ EQCM) instrument (Gamry 600) connected to the home-built probe beam deflection instrument. The HeNe Laser (model HNL020L-EC) (provided by Thorlabs) with a wave length of 632.8 nm with 0.8 to 2 mW output power was used as the light source. Position sensing detector (PSD) (dual silicon based photodiode (Optilas model 1243) bi-cell, 2.5 mm $\times$ 2.5 mm active area, 127 m gap between the active surfaces), differential amplifier, oscilloscope and voltmeter (these were used to monitor the DC current produced by a PSD) and the x, y, z axis motorised electrochemical cell stage (these elements compromised the PBD). Set-up of the complete EQCM–PBD instrument can be seen in Fig. 3.10.
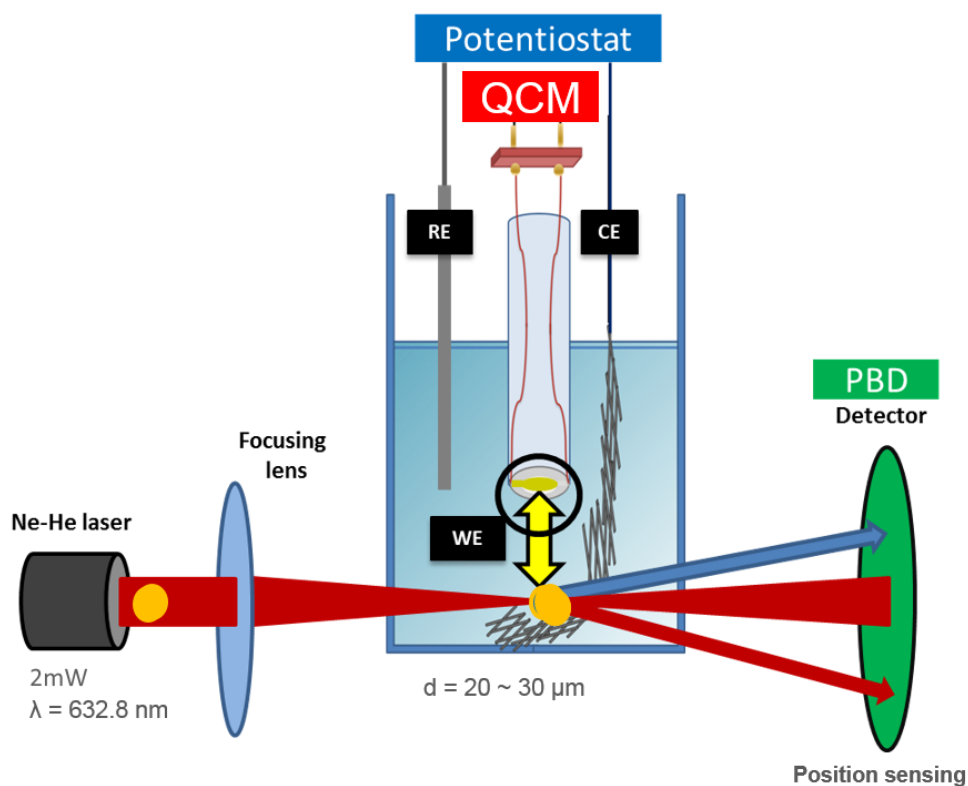
Fig. 3.9 Schematic representation of the EQCM-PBD instrument

The motorised electrochemical cell stage was remotely controlled via a Unidex 12 control unit. The electrochemical cell stage comprised an aluminium cradle mounted on a translation table allowing for vertical (x), transverse (y) and rotational (z) motion with 0.1 μm (x, y) and 0.025 arcmin (y) resolutions. These functions allowed for adjustment of the alignment, obtaining the minimum distance between the laser beam and surface of the working electrode. The intensity of the laser beam is at a maximum in the centre and the intensity can be represented by a Gaussian profile. All components of the instrument were fixed on to a steel breadboard stage and was connected to a personal computer. The Gamry software installed in the computer was used to manipulate the electrochemical parameters.

Fig. 3.10 Schematic of probe beam path alteration with respect to the working electrode used

3.4.9.1 Experimental procedure

Electrode cleaning procedures for EQCM-PBD experiments

Counter electrode was cleaned through rinsing with de-ionised water, acetone and dried in the oven (50 °C) for 60 min. Refer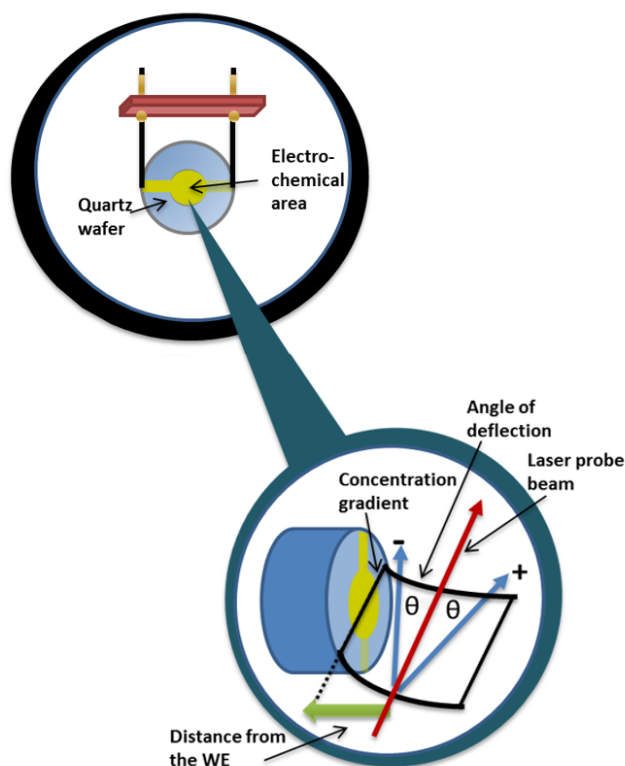ence electrode were cleaned using emerald (fine) sandpaper then washed with distilled water, acetone and dried in the oven (set to 50 °C) for the same period of time. QCM crystal working electrode were cleaned by removal of the material deposited during the experiments using cotton swabs soaked in 1:1 H_2O/HNO_3 followed by rinsing with de-ionised water, acetone and subsequent drying with compressed air. All EQCM experiments were conducted in a room with temperature maintained at 20 °C.

EQCM-PBD experimental procedure

Prior to the EQCM-PBD experiments the electrochemical cell was washed with de-ionised water, acetone, dried and washed with filtered electrolyte. All solutions used were filtered through nylon 0.1 μm or 0.45 μm or pore size filters (Cronus) prior to use in the electrochemical experiments. In order to overcome their high viscosity at room temperature all DES were hot filtered (at 60 °C), through single or multiple filters to remove impurities.

Electrodeposition of metal films

Metal deposits studied in Chapter 4-6 were electrodeposited potentiodynamically, potentio-statically or galvanostatically. Multiple trials were repetitively carried out to check for repro-ducibility and precision. The relevant electrochemical parameters used are given separately for each experiment, in the relevant section.

Calculation of laser beam diameter at the focal point

The Helium-Neon laser system used was provided by ThorLabs. The laser system provided 632.8 nm wavelength Helium-Neon gas system with output power of 2.0 mW. The beam diameter of the source was 0.63 mm ($\pm$ 3%) with beam divergence of 1.3 mrad. The beam pointing stability increases from <10 mrad to 0.02 mrad after 15 min when used from cold start. Therefore, before all experiments the beam was turned on for 15 minutes.

The major objective was to achieve minimal possible distance of approach, as the main ex-perimental objective was the observation of very small concentration gradients present during electrochemical processes conducted in ionic media. The instrumental setup should be able to detect very small gradients present during electrochemical processes conducted in RTILs. To achieve this objective, the beam diameter is an important parameter because it affects the beam to electrode distance calculations.
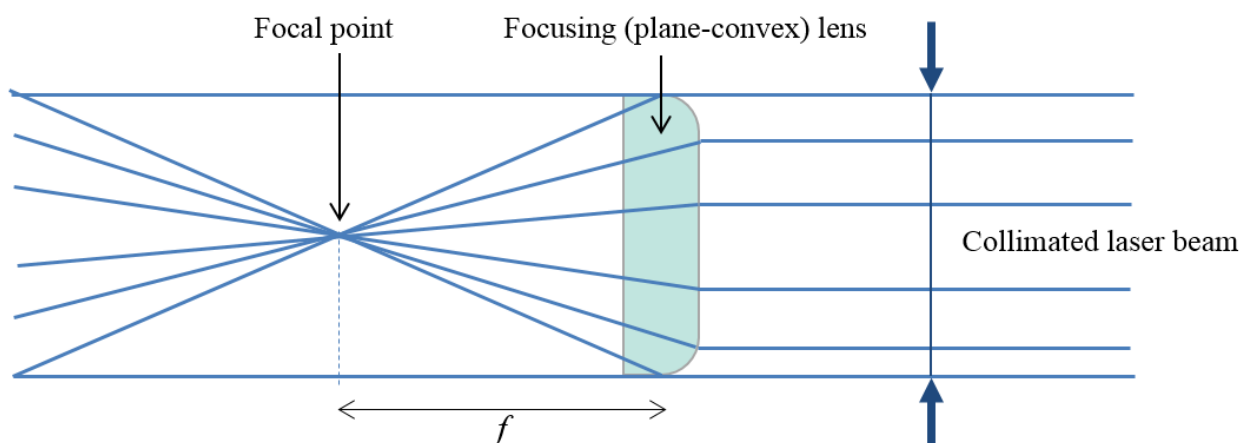

Fig. 3.11   Schematic representation of the laser beam passage prior to, at, and after the focal point

The beam diameter at the focal point, BD, was calculated using the equation:

$$BD_{fp} = 1.27 \, \frac{f}{BD} \, \lambda \tag{3.1}$$

where f = Distance between beam diameter and focal point
λ = laser wavelength (in μm)
BD = beam diameter (in μm)

For our experimental set-up, the beam diameter was calculated as 79.83 μm and the radius in the focal point was determined as 39.92 μm. These values were similar to the values reported in other PBD experimental setup.[17–20]

Calculation of the beam divergence angle

According to the manufacturer specifications provided by Thorlabs Inc., the diameter of the laser beam at the point of cavity exit was 0.63 mm and only valid for the laser beam at the point of exit from the cavity. Upon exiting the cavity the beam diverged because of the interactions between photons and air.
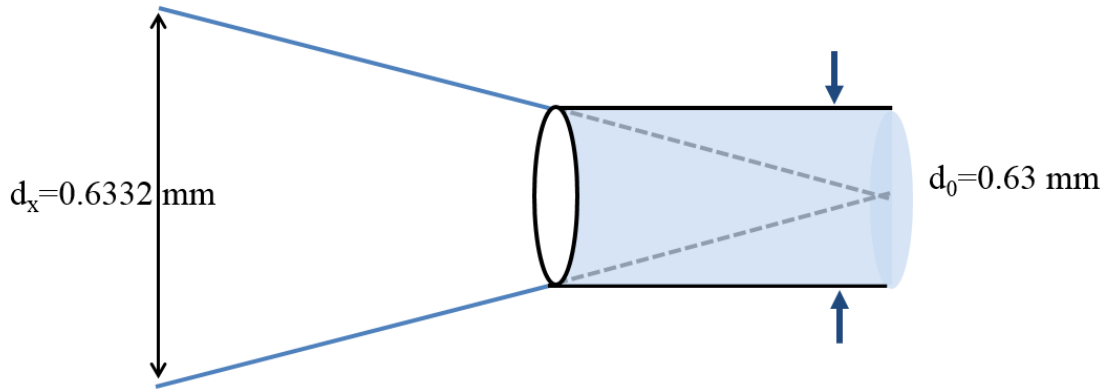
Fig. 3.12   Schematic representation of the beam divergence upon its exit from the laser cavity. x_0 is the laser beam diameter upon its exit from the laser cavity and x is the laser beam diameter at the focusing lens.

Beam divergence angle was calculated using the following equation:

$$\Theta = \frac{4}{\pi} \frac{\lambda}{d_0} \tag{3.2}$$

where Θ = beam divergence angle
d_0 = initial laser beam diameter

The calculated beam divergence angle was 1.2789×10^{-3} rad.

Calculation of the distance of minimum approach

This value determines how close to the electrode the focal point can be located. The following equation was used to determine this value:

$$\chi_{min} = \frac{S}{4} \frac{d_s}{f} \tag{3.3}$$

where S = laser beam interaction length (the WE external diameter)
d_s = distance between the laser and focusing lense

Set-up used allowed for decreasing of the minimum approach distance to 32.72 μm (measured from the centre on the focal point).

S = focal point diameter = 79.83 μm
d_s = distance between the laser and focusing lense

Focal point diameter is 79.83 μm. At the minimum distance of approach the WE would obscure circa 41 % of the beam. This is within the values reported in the literature (i.e. values of up to 70 % were reported previously).[18]
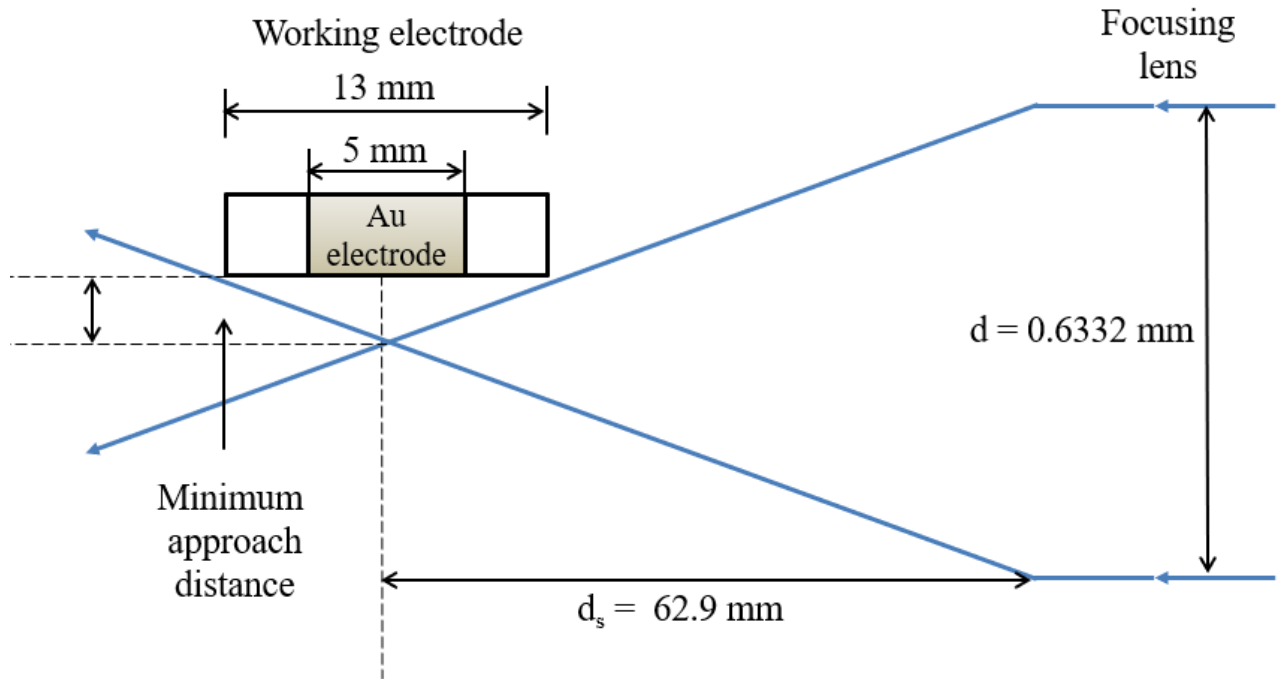
Fig. 3.13   Schematic representation of the distance of minimum approach.

Calculation of the maximum permissible deviation angle

Calculation of this value is necessary for determination of the range of deflection angles that can be recorded. Schematic representation of this is shown in figure Fig. 3.14.

Laser beam deflections exceeding this value will have low (or zero) intensity due to the laser beam being excessively obscured by the working electrode and the beam reaching the position sensing detectors has a intensity less than the lower limit of detection (LOD). From the calculations presented in the previous step the minimum distance of approach was determined as x_{min} = 32.72 μm.

The maximum angle of deflection can be calculated as:

$$\theta_{max} \approx tan(\theta_{max}) = \frac{d_s/2}{s/2} \tag{3.4}$$

$$\therefore \; \chi_{min} \approx \chi - \frac{d_s}{2} \tag{3.5}$$

Fig. 3.14   Schematic representation of the laser beam maximum permissible deviation angle.

$$\frac{ds}{2} \approx x - \left(\frac{S}{4}\frac{d}{f}\right) \tag{3.6}$$

Assuming that the electrode's surface is located 25 μm from the focal point the d s/2 = 7.72 by inference from equations 3.4, 3.5 and 3.6:

$$\theta_{max} = \frac{ds/2}{S/2} \tag{3.7}$$

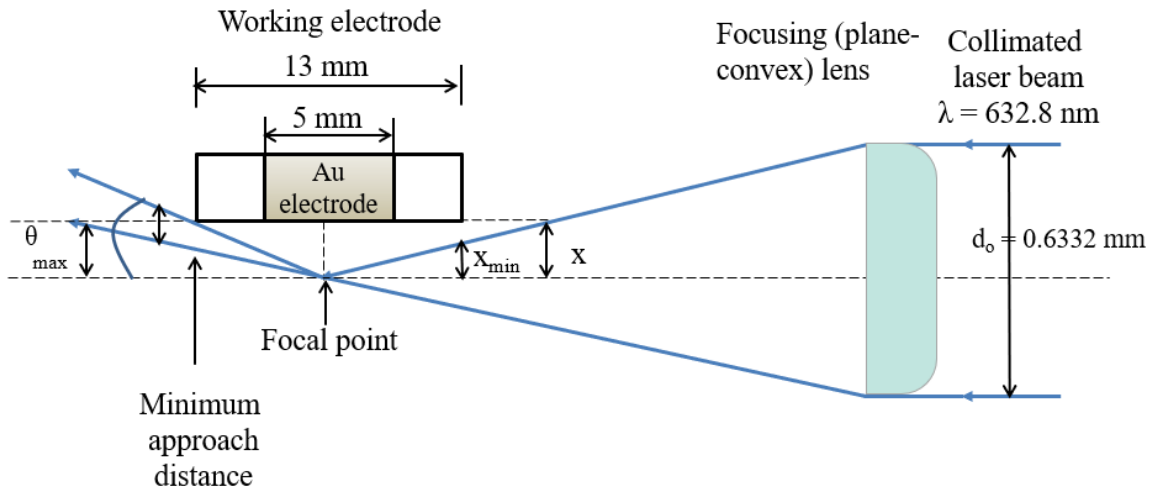Therefore, when the laser beam is positioned 25 μm from the WE, the maximum permissible angle of deflection is 1.19 mrad. At the θ_{max} values exceeding this limit, the intensity of the optical signal will decrease beyond experimentally useful values.

Translation of beam deviation into the concentration gradient

Concentration gradients created during electrochemical voltage experiments deflects the laser beam detected by the PSD and which is translated into a voltage. The voltage was then amplified and measured using a voltmeter while the potential stability was monitored by an oscilloscope. This enabled beam stability measurements prior to any electrochemical experiments. The stability readings were collected for 15 min before each experiment when the beam is passing through air (before the sample is placed) and the signal was only considered stable if the beam did not vary more than 1 to 2 mV. The laser beam monitored would give a response of approximately 0.5 V undeflected and any positive deflection of the beam (i.e. towards the WE) would yield positive signal (i.e. >0.5 V) while negative deflection (outwards from WE) would yield negative signal (i.e. <0.5 V). The signal range was measured for trial experiments so that they would be in the range of approx from -1.2V to +1.2 V.

3.4.9.2   Data analysis procedures

- **EQCM data analysis procedures**

Acquisition of the data was conducted using Gamry Analyst software and mass changes were calculated from frequency changes using the Sauerbrey equation (3.8).

$$\Delta f = \left(\frac{-2 f_0^2}{A_{pz} \sqrt{p_q \mu_q}} \right) \Delta m \qquad (3.8)$$

where f_0 - resonant frequency (Hz)
Δf - frequency change (Hz)
Δm - mass change (g)
A_{pz} - piezoelectroctrically active crystal (Area between electrode, cm^2)
ρ_q - density of quartz ($\rho_q = 2.648$ g cm^{-3})
μ_q - shear modulus of quartz for AT-cut crystal
($\mu_q = 2.947 \times 10^{11}$ g cm^{-1} s^{-2}).

The obtained mass change (Δm) was plotted versus the electrical charge passed during the experiment in order to calculate the molar mass of species exchanged (i.e the charged and non-charged species exchanged):

$$M = nF \left(\frac{dm}{dQ} \right) \qquad (3.9)$$

where M - molar mass (g mol^{-1})
n - number of electrons exchanged
dm - change in mass (g)
dQ - change in charge (C)

The mass obtained from the Saubrey equation was plotted versus charge passed (obtained from the voltammetric signal). Calculated values were then used to determine the average mass of exchanged species (M_{av}). Presence of hysteresis was assumed to result from heterogeneous mass exchange.   Therefore the final equation used was:

$$M_{av} = M_{ion} + n' \, M_{neutral} \qquad (3.10)$$

where M_{ion} - mass of the ion (this includes all positive and negative ions)
n - number of solvent molecules exchanged
$M_{neutral}$ - mass of the neutral species (from the solvent)

Since the above method was originally intended for molecular solvents it was adapted for deep eutectic solvents, with fully ionic environments in the following way:

$$M_{av} = M_{cation} + n' \, M_{anion} \text{ or}$$

$$M_{av} = M_{anion} + n' \, M_{cation}$$

This depends on whether the process was cation or anion dominated mass exchange. Further modification was necessary to measure the individual metals molar ratios upon metal co-deposition. For the system studied (i.e. simultaneous deposition and dissolution of bismuth and silver), the following method was used to obtain the mole fraction:

For the simultaneous deposition we can give the redox equations:

$$Ag^+ + e^- \rightarrow Ag^0$$
$$Bi^{3+} + 3e \rightarrow Bi^0$$
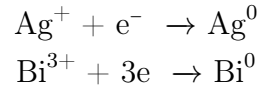
Mole fraction of Ag: χ_{Ag} and mole fraction of Bi χ_{Bi} can be given as:

$$\chi_{Ag} + \chi_{Bi} = 1 \tag{3.11}$$

Therefore,

$$\chi_{Bi} = 1 - \chi_{Ag} \tag{3.12}$$

$$masschange\ (\Delta m) = \chi_{Ag}RMM_{Ag} + \chi_{Bi}RMM_{Bi}$$

where RMM_{Ag} - Relative atomic mass of Ag (107.8682 g mol^{-1})
RMM_{Bi} - Relative atomic mass of Bi (208.9804 g mol^{-1})

$$Total\ Charge\ (Q_{Total}) = \chi_{Ag}F + \chi_{Bi}F$$

$$Q_{Total} = (1 - \chi_{Bi})F + \chi_{Bi}3F$$

$$Q_{Total} = F(1 - \chi_{Bi} + 3\chi_{Bi})$$

$$Q_{Total} = F(1 - 2\chi_{Bi})$$

$$\frac{\Delta m}{Q_{Total}} = \frac{(1 - \chi_{Bi})RMM_{Ag} + \chi_{Bi}RMM_{Bi}}{F(1 + 2\chi_{Bi})}$$

$$\chi_{Bi} = \frac{\frac{\Delta mF}{Q} - RMM_{Ag}}{RMM_{Bi} - RMM_{Ag} - 2F\frac{\Delta m}{Q_{Total}}} \tag{3.13}$$

Since RMM_{Ag}= 107.86 g mol^{-1} and RMM_{Bi}= 208.98 g mol^{-1},

$$\frac{\Delta m}{Q_{Total}} \Longrightarrow \chi_{Bi} \Longrightarrow \chi_{Ag} \text{ can be found.}$$

The calculated values were then plotted (Δ m/Q vs. mole fraction). Obtained number indicated mole fraction of individual metals in the deposited layer.

Application of convolution analysis

Application of numerical convolution protocol to process the electrochemical data is a well researched technique.[21] The technique is used for the calculation of the concentration gradients at a finite distance from the working electrode by considering the diffusional effects. Simulation of optical deflection by convolution was initially proposed by Vieil.[22] The experimental optical beam deviation is used to calculate the ionic flux at the electrode's surface which is directly compared with electrochemical current due to the diffusional gap and these two signals

are related using Fick's law. Potential window of the optical deflection signal is smaller than voltammetric one and hence observation of the electrode processes at the extreme potentials might not be achievable.

Convolution of current

The main objective of this operation is to derive the metal cation flux (in metals redox chemistry) from the ionic flux (optical deflection signal). Beam deflection (θ/μrad) and current generated electrochemically (i/ μA) are used as input values for the convolution software. Using the following set of assumptions:

1. Electron flux results from ionic flux

2. Electrode processes result in simultaneous ion and electron exchange

3. Analysed process is instantaneous (i.e. electrode ion exchange is rapid in comparison to diffusional delay).

The mathematical treatment is as follows. The total cationic ionic flux (f_{PBD}) is a sum of fluxes towards and outwards from the electrode and this can be represented as:

$$f_{PBD} = \frac{\theta^+}{\theta^- + \theta^+} \tag{3.15}$$

where θ^+ - deflection from positive ions and θ^- - deflection from negative ions

Projection of current and mass signal from the electrode surface into the electrolyte require fulfillment of several assumption.

1. The electroactive deposit on the electrode has act as an ideal transducer between the electrical input and the ionic output.

2. The species propagation delay has to be negligible.

Based on these assumptions, the measured current i_t can be treated as being proportional to the total flux of charged species and is described by the equation:

$$i_{(t)} = F A \sum \left(z_\gamma J_\gamma \right)_{(0,t)} \tag{3.16}$$

where

$\gamma = C^+$ or A⁻ (i.e. charges of cation C, anion A)

$J_{(0,t)}$ = species flux at the film electrode interface (where the distance is zero)

The convolution analysis uses the extrapolation of the flux measurements from the electrode surface (distance = 0) to a focal point (distance = (x), which is the actual physical distance between the electrode and laser beam). The optical deflection measurements (i.e. refractive index changes) are collected at distance (x). The convolution analysis is based on the following:

$$J_{C^+A^- (x,t)} = F_{(x,t)} \times J_{C^+A^- (0,t)} \tag{3.17}$$

where $F_{(x,t)}$ is the convolution factor. This factor is based on the assumption of mass transfer

being a semi-infinite diffusion in the dimension perpendicular to the electrode surface. Then, the Fick's law application allows relating the flux of species to be related to the concentration gradient:

$$J_{(x,t)} = -D \left(\frac{\delta c_{(x,t)}}{\delta x} \right) \tag{3.18}$$

Combination of equations 3.16, 3.17 and 3.18 reveals the convolution factor as a function of diffusion:

$$F_{(x,t)} = \left(\frac{x}{2\sqrt{\pi D t^3}} \right) e^{\frac{-x_{pd}^2}{4D t_{pd}}} \tag{3.19}$$

where

D = diffusion constant

t_{pd} = propagation delay

x_{pd} = propagation distance

The relationship between the optical deflection and concentration gradient then becomes:

$$\theta = -\frac{1}{n_R} \frac{\delta n_R}{\delta C} \frac{1}{D} J_{(0,t)} \tag{3.20}$$

Eqn. 3.20, when expressed as function of the electrode current develops into Eqn. 3.21. This equation directly relates the species flux with optical deflection:

$$\theta_{(x,t)} = -\frac{h_k L}{z_\gamma F A_{pz}} F_{(x,t)} \times i_t \tag{3.21}$$

where $h_k = \frac{\delta n_R}{\delta C 4} \frac{1}{D}$ and it is a constant for a given electrolyte. This approach eliminates the need for measurement $\frac{\delta n_R}{\delta c}$ (which would otherwise have to be conducted prior to the experiment). The convolution software thus removes the propagation delay effectively extrapolating the optical deflection signal from distance x_0 to the electrode surface and compares it to the experimental electrical signal (i). The convolution of these signals derives the value $x/\sqrt{D}$ which is compared with the diffusion coefficient values calculated from Randles-Sevcik equation. The result was the convolved current (i.e. current measured in the focal point). This value and the value of $x/\sqrt{D}$ were recorded and stored for further calculations.

Convolution of mass

The objective of this operation is to derive mass flux of the individual species from the experimental optical deflection. Recorded beam deflection and gravimetrically determined mass changes are used as the input parameters for the convolution software. The following set of assumptions are being used:

1. Ionic flux is accompanied by a solvent (or neutral species) flux

2. Ionic flux does and solvent flux does not result in formation of a concentration gradient

3. Mass flux is instantaneous

Optical deflection and current densities are related to each other via mass flux (via Faraday's Law). The mathematical treatment is as follows:

Current density: $\quad \frac{i}{A_z F} = z_{C^+} J_{C^+(x,t)} + z_{C^-} J_{C^-(x,t)}$

Optical deflection: $\quad \theta_{(x,t)} = L \left(h_{C^+} J_{C^+(x,t)} + h_{C^-} J_{C^-(x,t)} \right)$

Mass flux: $\quad \frac{dM_{(x,t)}}{dt} = m_{C^+} J_{C^+(x,t)} + m_{A^-} J_{A^-(x,t)} + m_N J_{N(x,t)}$

The above approach allows for determination of individual contributions of cations, anions and solvent to the overall dynamics of the analysed system. In order to apply the convolution protocol gravimetric mass signal was converted to charge and then to current. The obtained mass-derived-current was then the input value for the convolution software. $x/\sqrt{D}$ factor was used and current convolution was applied.

The resulting convolved current and convolved masses were used for the subsequent ion and/or solvent flux calculations. As it can be seen above, this step required gravimetrically and electrochemically derived assumptions about the dopant ion identity of ions. Identity of ions was deduced from the gravimetric and voltammetric signals.

Calculation of the qualitative ionic and solvent (neutral species) contributions

To achieve this objective prior to the separation of the cation, anion and solvent individual contributions the following assumptions were formed:

1. Experimental deflection signal represents the total flux of electroactive as well as non-electroactive species.

2. Convolved current represents exclusively the mobile active ion flux.

3. Convolved mass represents the total mass flux of counter and co-ion.

4. Any part of the experimental optical signal which does not represent anion or cation flux is the solvent flux.

The generic protocol (for a solvent based, anion doped) system is presented below:

$$\theta - \left(\frac{i_{(x,t)} hL}{zFA} \right) = C^+ \tag{3.22}$$

$$\left(\frac{i_{(x,t)} hL}{zFA} \right) = A^- \tag{3.23}$$

$$\left(\frac{dM_{(x,t)}}{dt} \right) \left(\frac{zFAhL}{RMM} \right) - \left(\frac{i_{(x,t)} hL}{zFA} \right) = (C^+ + N) \tag{3.24}$$

$$\left(\left(\frac{dM_{(x,t)}}{dt} \right) \left(\frac{zFAhL}{RMM} \right) - \left(\frac{i_{(x,t)} hL}{zFA} \right) - \left(\theta - \left(\frac{i_{(x,t)} hL}{zFA} \right) \right) \right) = N \tag{3.25}$$

where θ is the optical deflection $\left(\frac{i_{(x,t)} hL}{zFA} \right)$ is projected current, $\left(\frac{dM_{(x,t)}}{dt} \right) \left(\frac{zFAhL}{RMM} \right)$ is projected mass flux and RMM is the dopant ion molar mass. C^+, A^- and N are contribution of of cation, anion and neutral species respectively. Convolution methodology returns solvent flux

contribution. In DES case, this contribution is assumed to be composed of equal amounts of anions and cations. Thus, solvent flux is partitioned into anion and cation transfers. These in turn are added to separately determine ion fluxes obtained using the convolution software. Therefore, N contribution is not present in convolution products of DES experimental data.

Calculation of the quantitative ionic and solvent contributions

Integration of the differential responses obtained in the previous phase returns the quantitative results of the anion, cation and solvents fluxes. The mathematical operation used can be given as:

$$\frac{\theta}{h} \times dt \times \left(\frac{RMM}{F}\right) = \theta_{quant} \tag{3.26}$$

$$\left(\frac{\frac{dM_{(x,t)}}{dt}\frac{zFAhL}{RMM}}{h}\right) \times dt \times \left(\frac{RMM}{F}\right) = \left(\frac{dM_{(x,t)}}{F}\right)\left(\frac{zFAhL}{RMM}\right)_{quant} \tag{3.27}$$

where *quant* adjectives the quantitative level of response. The obtained signals are individual mass fluxes (n mol^{-1}) of each species. A more detailed study into the principle used in convolution is beyond the scope of this study.

3.4.9.3 Atomic force microscopy (AFM)

Silver, bismuth and silver-bismuth morphologies were observed by Atomic Force Microscopy using Digital Instruments, Dimensions^{TM} 3100 microscope. Microscope was coupled to Nanoscope Dimension^{TM} 3100 controller and Nanoscope Scanning Probe Microscope Controller. The entire instrument is controlled through Nanoscope software (version 6.1).

Measurements were made ex situ in tapping mode. Silicon nitride (Si_3N_4) tips were used. Materials analysed were deposited on Au-plated quartz slides (1.75 cm^2 electroactive area and total area 3 cm^2). Surface roughness and depth of deposition was measured for minimum of 5 sample areas for all the deposited samples and the average was used.

3.4.9.4 Scanning electron microscopy (SEM/ EDAX)

Surfaces of metals deposited were analysed for the grain structure and metal percentage using scanning electron microscopy (SEM) and energy dispersive spectrocopy (EDAX) respectively. SEM and EDAX elemental analysis was carried out under vacuum using a Philips XL30 scanning electron microscopy instrument with voltage between 15 - 20 KeV giving an average beam current of circa 120 μA.

3.4.9.5 X-ray diffractometry

The surface structure was characterised using X-ray diffraction (XRD). Characterisation was done using a Rigaku Smartlab at ISIS Neutron and Muon Source located at the STFC Ruther-

ford Appleton Laboratory (Oxfordshire). The scan range used was from 22 to 86 degrees at scan rate of 0.01 sec/step. The material was characterised in continuous scanning mode using K-Alpha1 (radiation wavelengths 1.54059 Å and 1.54441 Å). The raw data was analysed using Match! Powder Diffraction Phase Identification software (version 3.6) from Crystal Impact GbR. The software was used to remove background noise and to identify the peaks. The peaks were then compared against entries in the Crystallographic Open Database.[23] Position and intensity of the peaks were used to ascertain the crystalline phases in the thin films. The Crystallographic Open Database ID was used to retrieve further information (using http://www.crystallography.net/cod/search.html) .

References

[1] M. A. Skopek, M. A. Mohamoud, K. S. Ryder and A. R. Hillman, Chemical Communications, 2009, 935–937.

[2] R. G. Compton and C. E. Banks, Understanding voltammetry, World Scientific, 2011.

[3] C. J. Zaleski, Ph.D. thesis, University of Leicester, 2015.

[4] U. Schröder, J. D. Wadhawan, R. G. Compton, F. Marken, P. A. Suarez, C. S. Consorti, R. F. de Souza and J. Dupont, New Journal of Chemistry, 2000, 24, 1009–1015.

[5] D. MacFarlane, S. Forsyth, J. Golding and G. Deacon, Green Chemistry, 2002, 4, 444–448.

[6] B. Huber and B. Roling, Electrochimica Acta, 2011, 56, 6569–6572.

[7] A. Yavuz, Ph.D. thesis, University of Leicester, 2015.

[8] V. Colvin, A. Goldstein and A. Alivisatos, Journal of the American Chemical Society, 1992, 114, 5221–5230.

[9] I. U. Vakarelski, C. E. McNamee and K. Higashitani, Colloids and Surfaces A: Physicochemical and Engineering Aspects, 2007, 295, 16–20.

[10] M. B. Ali, F. Bessueille, J.-M. Chovelon, A. Abdelghani, N. Jaffrezic-Renault, M. Maaref and C. Martelet, Materials Science and Engineering: C, 2008, 28, 628–632.

[11] A. Kaminska, O. Inya-Agha, R. J. Forster and T. E. Keyes, Physical Chemistry Chemical Physics, 2008, 10, 4172–4180.

[12] K. C. Grabar, K. J. Allison, B. E. Baker, R. M. Bright, K. R. Brown, R. G. Freeman, A. P. Fox, C. D. Keating, M. D. Musick and M. J. Natan, Langmuir, 1996, 12, 2353–2361.

[13] K. C. Grabar, P. C. Smith, M. D. Musick, J. A. Davis, D. G. Walter, M. A. Jackson, A. P. Guthrie and M. J. Natan, Journal of the American Chemical Society, 1996, 118, 1148–1153.

[14] J. A. Harnisch, A. D. Pris and M. D. Porter, Journal of the American Chemical Society, 2001, 123, 5829–5830.

[15] O. Seitz, M. M. Chehimi, E. Cabet-Deliry, S. Truong, N. Felidj, C. Perruchot, S. J. Greaves and J. F. Watts, Colloids and Surfaces A: Physicochemical and Engineering Aspects, 2003, 218, 225–239.

[16] J. Coenen, RDE2 User Manual, Metrohm Autolab B.V., Utrecht, The Netherlands, 2nd edn., 2007.

[17] M. J. Henderson, A. R. Hillman, E. Vieil and C. Lopez, Journal of Electroanalytical Chemistry, 1998, **458**, 241–248.

[18] C. Barbero and M. Miras, Journal of the Argentine Chemical Society, 2003, pp. 1–40.

[19] C. Barbero, M. Miras and R. Kötz, Electrochimica Acta, 1992, **37**, 429–437.

[20] A. R. Hillman, K. S. Ryder, C. J. Zaleski, V. Ferreira, C. A. Beasley and E. Vieil, Electrochimica Acta, 2014, **135**, 42–51.

[21] G. G. Láng and C. A. Barbero, Laser techniques for the study of electrode processes, Springer Science & Business Media, 2012.

[22] E. Vieil, Journal of Electroanalytical Chemistry, 1994, **364**, 9–15.

[23] S. Gražulis, A. Daškevič, A. Merkys, D. Chateigner, L. Lutterotti, M. Quiros, N. R. Serebryanaya, P. Moeck, R. T. Downs and A. Le Bail, Nucleic acids research, 2011, **40**, D420–D427.

Chapter 4

Application of the combined EQCM-PBD technique for Ag, Bi and Ag-Bi in DES

Contents

4.1 Introduction

The main objective of this chapter is to investigate the metal ions speciations and ionic fluxes present during deposition of silver and bismuth individually and during co-deposition of silver/ bismuth in DES. The Electrochemical Quartz Crystal Microbalance (EQCM), in its most commonly used mode, is a gravimetric probe with high sensitivity to the deposition and dissolution of heavy species such as metals. The Probe Beam Deflection (PBD) technique deals with gradients of refractive index, so it is sensitive to fluxes of species present in solution, for example generated by interfacial proton transfers. Coupling of these methodologies is especially advantageous as it exploits PBD sensitivity with the reliability of EQCM.[1] A larger part of application of EQCM-PBD techniques has been focused on electroactive polymer films. Hillman and coworkers have researched on the applicability of EQCM-PBD to metal deposition using silver, lead,[1] tin[2] and copper deposition, in addition to redox chemistry of nickel hydroxide in LiOH[3] whilst Abrantes et al. studied oxidation of hypophosphite on nickel electrodes.[4]

A comprehensive study of copper deposition has been conducted by Eriksson from an aqueous solution and proved that PBD can resolve concentration profiles down to 1 mmol dm^{-3}.[5] Despite electrolytic/ electroless deposition of metals from room temperature ionic liquids (RTIL) being a rapidly growing field, optical analysis of metal deposition/ dissolution from ionic liquids has been reported only twice.[2,6,7]

In electrocrystallisation processes, metal ions in aqueous solutions are stabilised through the formation of the solvation shell. In ionic liquids, metal ions are assumed to have no solvent molecules to coordinate. Their stability depends upon surrounding counter ions in the solvent (metals are generally complexed by anions e.g. Cl$^-$ ions which are present at high concentrations). In order to investigate the electrode/electrolyte interfacial kinetics during the metal deposition/dissolution processes in fully ionic environments, we need an understanding of movement of ionic fluxes in the near electrode area.

The EQCM[8,9] and PBD[10–12] techniques have been used independently and have proven extremely useful for interfacial processes such as electropolymerization,[13–17] electrocrystallisation,[18] adsorption,[19,20] absorption,[21] underpotential deposition (UPD),[22,23] and electroactive film redox switching.[14,24–31] As explained in Chapter 2, the E in EQCM refers to the electrochemical measurements in a typical EQCM-PBD experiment i.e. current (or charge). Mass and optical deflection are measured simultaneously with current. Their combined outputs are used for resolving the transfers of up to three species: anion, cation and solvent.[32,33] This novel optical deflection technique which combines optical, gravimetric, electrochemical measurements has been used to accomplish this task.

Optical deflection originates due to refractive index gradients generated by concentration gradients of ion complexation resulting from electrochemical reactions. Each ion complexation has a distinct refractive index making the EQCM-PBD an ideal tool for real-time, non-invasive, quantitative detection of the number and amount of the metal complexation species present

during the electrodeposition. Fully ionic environments such as ionic liquids or their subclass Deep Eutectic Solvents (DES) represent a significant challenge in terms of optical analysis. If the concentration of the medium is very high, as it is in DES, the difference in concentrations between the bulk electrolyte and the electrolyte near the electrode does not differ significantly. This in turn causes smaller deflections compared to dilute electrolytes. The concentration near the electrode will also depend on rate of diffusion of the species concerned. The rates of diffusion in DES are orders of magnitude lower than that of aqueous or organic electrolytes.

Table 4.1 Diffusion coefficients calculated by Zaleski et al.[34] at 25 °C

Electrolyte	Diffusion coefficient
Ag^+ in aqueous medium	$2.83 \times 10^{-5} cm^2 s^{-1}$
$CuCl_2^-$ in Ethaline 200	$3.01 \times 10^{-7} cm^2 s^{-1}$

Due to these reasons fully ionic environments (in this case) DES would face significant challenges in terms of optical analysis.[7] On the other hand most common methods of ionic species elucidation such as mass spectrometry can cause species fragmentation during the ionization process.[35] Due to the bond instability of ionic species formed by dissolution of metal salts (in DES) these methods do not generate conclusive results for these ionic species.[35]

In constrast, the combined optical-gravimetric measurements provide a non-invasive, affordable technique to gain a unique insight into the electroplating of metals in DES. The associated optical deflection signal has a displacement spatially (circa 50 μm) from the electrode surface which causes it to be temporally separated from the electrode surface. As the diffusion of the species is subjected to a (viscosity controlled) propagation delay there is a significant temporal separation of signals which causes a problem for quantitative PBD analysis in these ionic media. This inherent delay between the electrochemical reaction at the electrode surface and its detection by the probe beam increases if the beam is positioned further away from the electrode surface. This also results in distortion of the optical signal.

For accurate, quantitative analysis of the EQCM-PBD data it is important to remove the effects of diffusional delay. This is achieved in two ways: by minimising the beam – electrode distance and by digital numeric simulation or convolution of the experimental optical signal. In order to adjust the beam-electrode distance it is imperative to have a method of measuring beam deflection with beam electron distance. In the experimental set-up (see Chapter 2) used it was impossible to do so in real-time.

To overcome this issue a series of chronodeflectometry (CD) experiments were carried out using the electrolyte (e.g. $AgNO_3/HClO_4$) and the QCM electrode with the same conditions (current, time settings and temperature) for varying beam-electrode distances (x). At the optimum beam-electrode distance the optical signal bore closest possible resemblance to the electrical signal hence would show lowest propagation delay and lowest signal distortion. The optimal distance measured was denoted x_0. The optical signal intensity was very low when the working electrode was obscuring a greater part of the laser beam (at low x values) and it lost sensitivity to the electrode reaction when the beam electrode distance was too high due to

diffusion barrier effects (at high x values).

Another method of removal of the diffusional delay is either by digital numeric simulation or convolution of the experimental optical signal. For numeric simulation ion fluxes at the electrode are calculated using PBD experimental data and species diffusion coefficients. Numerical convolution proposed by Vieil and coworkers[26] is the most popular method to quantify PBD data. This approach involves calculating the electrochemical species flux at the x distance and comparing the calculated signal with the experimental optical signal (see Chapter 2). The numerical convolution method has the advantage that both diffusion coefficients and beam-electrode distance can be evaluated from simple chronodeflectometric experiments conducted at variable x distances.

To obtain the beam-electrode distance, chronodeflectometric experiments are repeated at several distances using the optimal beam electrode distance as the initial value of x. The value of x is changed in an increasing sequence $(+10, + 20, +30~\mu m)$ and then a decreasing sequence $(-10, -20, -30~\mu m)$ to obtain optical deflection profiles. The raw data from the experiments were used to obtain the D parameter from the convolution software. When these x results are plotted versus the $x/\sqrt{D}$ parameter, a linear plot is obtained. The gradient of the plot can be used to determine the diffusion coefficient of the electroactive species involved in the experiment. The diffusion coefficient values obtained from other experiments (e.g. Cottrell plots) are then compared to this value to validate the convolution protocol used. The extrapolated trend line can be used to find the absolute beam-electrode distance (x_0).

The main objective of this chapter was to investigate the metal ions speciations and ionic fluxes present during deposition of silver and bismuth individually and during co-deposition of silver/ bismuth in DES. The optical deflection technique provides circumstantial, rather than factual, evidence since it is not a structural probe. Previous work carried out by Hartely et al. demonstrated the difference in metal speciation in Ethaline compared to aqueous systems.[36] For aqueous systems formal electrode potentials can be measured with respect to the saturated calomel electrode and for Ethaline systems they have been measured with respect to a silver pseudo reference electrode.[36] Hartley has given a graphical representation as to how these values vary (see Fig. 4.1). The line shown in the center of the graph is the line of equivalence (i.e. point at which potentials are the same in both aqueous and ionic solutions and can be used as a comparison for the eye). Therefore, the line demonstrates the stability of metal oxidation state in Ethaline. The oxidation states below the line are more stable compared to oxidation states above the line. Kekesi et al. demonstrated that there is a correlation between metal ion speciation and the properties of the deposit upon electrodeposition.[37]
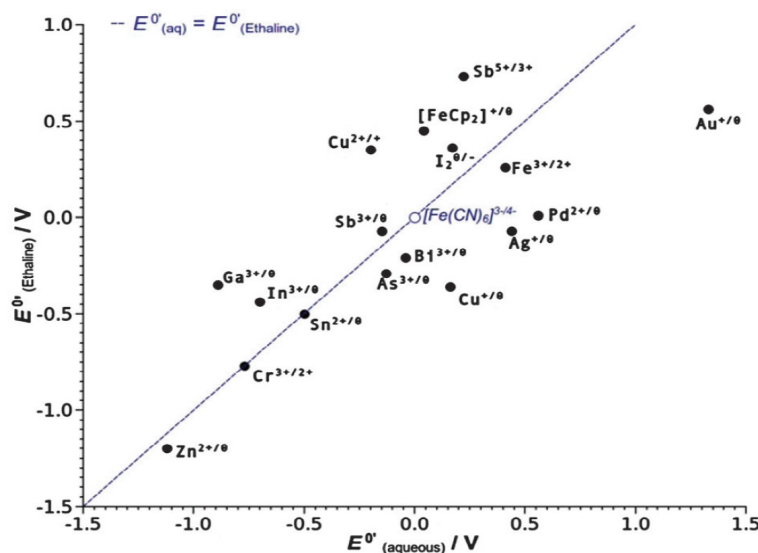
Fig. 4.1 Formal electrode potentials of metals are given above comparing metal speciation in an aqueous solution with that in an Ethaline solution. Potentials in an aqueous solution were measured versus saturated calomel electrode; potentials in figure used with permission from reference.[36] Potentials in Ethaline were measured against Ag pseudo reference electrode

4.2 Application of EQCM-PBD in electrodeposition of metal deposits

General experimental procedures have been discussed in Chapter 3. Specific details that are applied to this experiment are given here. The working electrode was cleaned using dilute HNO_3 (1:1 molar ratio of HNO_3 and H_2O), deionized water, acetone and air dried. The quartz cuvette was cleaned using deionized water, acetone and air dried. All solutions were filtered before they were used in the PBD experiments. 0.1 μm filters (single or multiple) were used to filter the aqueous solutions whereas 0.45 μm filters (single or multiple) were used for Ethaline 200 solutions. Metal deposition experiments were done potentiodynamically at scan rates varying from 5 mV s^{-1} to 0.0625 mV s^{-1} within the potential window of 0.2 V to -0.3 V. Three cyclic voltammetry experiments were conducted for each scan rate studied, with the third data set used for the analysis of optical response and the voltage-current response.

4.3 Results and discussion

4.3.1 Study of mass transport during the electrodeposition/ dissolution of silver from $AgNO_3$ in $HClO_{4(aq)}$

Silver deposition/ dissolution in aqueous solutions of perchloric acid was selected as the calibration system due to its mechanistically simple nature. A solution of 0.001 M $AgNO_3$ in 0.2 M $HClO_4$ was used for this purpose. Silver deposition/dissolution in an aqueous solution of perchloric acid[36] has an uncomplicated redox chemistry ($Ag^+ \rightarrow Ag^0$). Also, silver benefits from

having high refractivity, a high molar mass and its ease of plating makes it an'ideal candidate to be used as a calibration system. Henderson and coworkers have demonstrated clearly that Ag^+ is the only significant charge carrier and that current (i), mass (Δm), optical deflection (θ) signals data are fully consistent with that.[1] Zaleski and coworkers proved that reducing the distance between beam and electrode can be used to overcome the propagation delay problems.[3] It was imperative to repeat Henderson's original study with a reduced electrode-beam distance as a proof of method before using an ionic liquid as solvent which would be more viscous and hence difficult to configure. Current, mass and optical deflection (θ) measured during these experiments were plotted separately against the voltage applied (Fig. 4.2).

The reversible redox process (Ag^+/Ag^0) is shown by the current response and the Ag^+ reduction can be seen from 0 to -0.3 V. The mass changes were calculated using the Sauerbrey equation (assuming the rigidity of the deposited metal)[38] and the Δm vs E plot indicated a steady increase in the difference of the mass of the QCM crystal during reduction. The changes in the mass can be determined from the frequency change using the Sauerbrey equation:

$$\Delta f = \left(\frac{-2f_0^2}{A\sqrt{p_q\mu_q}}\right)\Delta m \tag{4.1}$$

where f_0 - resonant frequency (Hz)
   Δf - frequency change(Hz)
   Δm - mass change(g)
   A - piezoelectrically active crystal area (cm^2)
   ρ_q - density of quartz (ρ_q = 2.648 g cm^{-3})
   μ_q - shear modulus of quartz for AT-cut crystal (2.947 x 10^{11} g cm^{-1}s^{-2})

The mass change (Δm) was plotted against the electrical charge passed during the experiment in order to calculate the molar mass of the species exchanged (i.e. the charged and non-charged species exchanged)

$$M = zF\left(\frac{dm}{dQ}\right) \tag{4.2}$$

where M - molar mass
   z - number of electrons exchanged
   dm - change in mass
   dQ - change in charge

dm/dQ was obtained from the the gradient of the Δm vs Q graph. Mass obtained from gravimetric signal was plotted versus charge passed (obtained from voltammetric signal). Calculated values were then used to calculate average mass of exchanged species. Heterogeneous mass exchange was seen to be followed by hysteresis.

The deposition seemed to be a mass transport controlled continuous process, which continued even in the positive scan up to the potential of -0.05 V where dissolution of the Ag film began and continued rapidly until 0.07 V (Fig. 4.2). Subsequently the current and mass signals decayed to their initial values. Furthermore, the single peak observed for optical deflection in the anodic sweep (dissolution) indicates that only one metal ion species is present in the electrolyte (see bottom panel of Fig. 4.2).
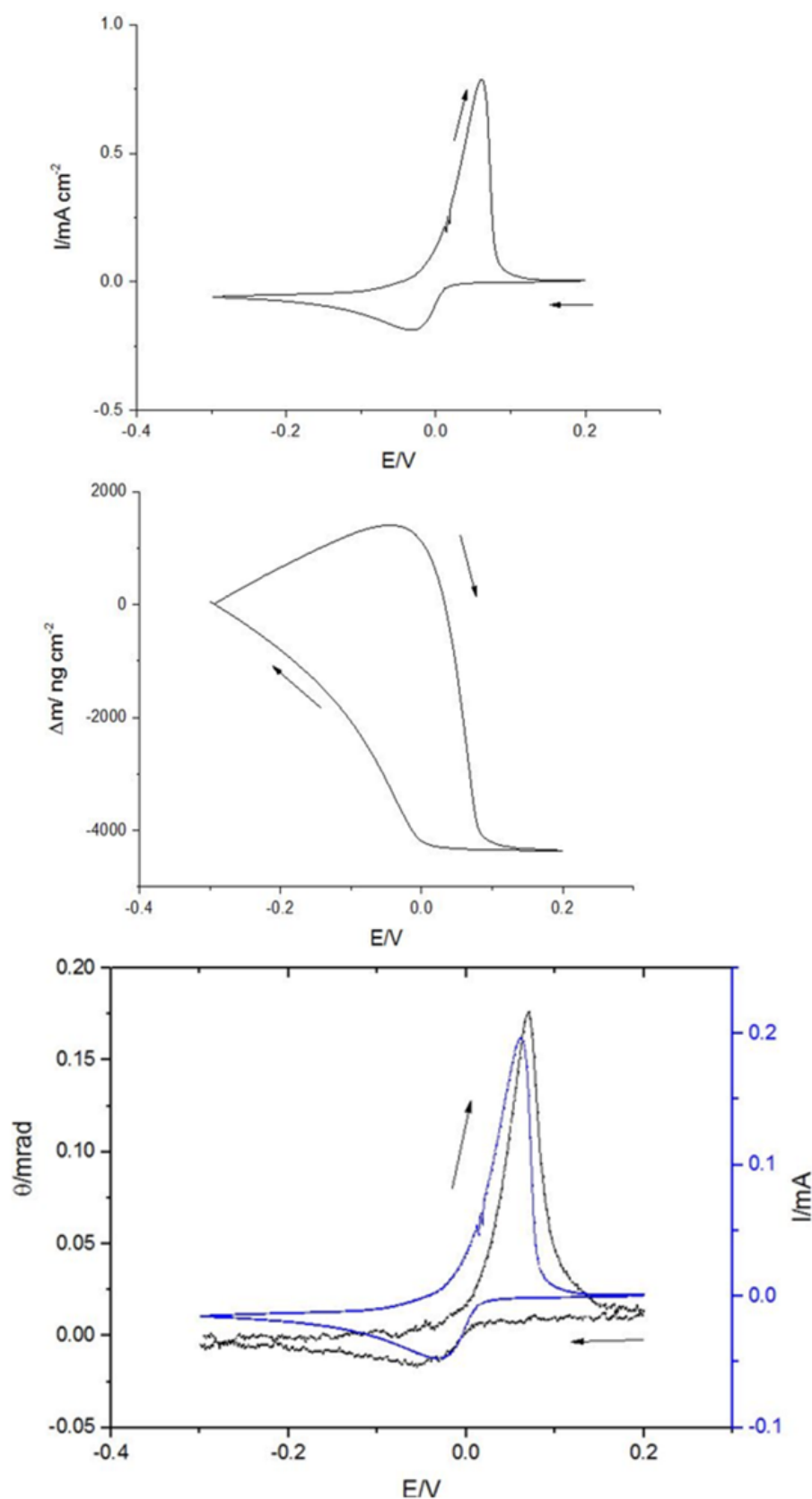
Fig. 4.2 The current(I) (top panel), mass change (Δm) (middle panel) and optical response (θ) (bottom panel) plots for the cyclic voltammogram recorded during deposition and dissolution of elemental Ag from 0.001 M AgNO$_3$ in 0.2 M HClO$_{4(aq)}$ Scan rate = 5 mV s^{-1}. To aid comparison, the current trace from the top panel is also superimposed with the optical response in the bottom panel.
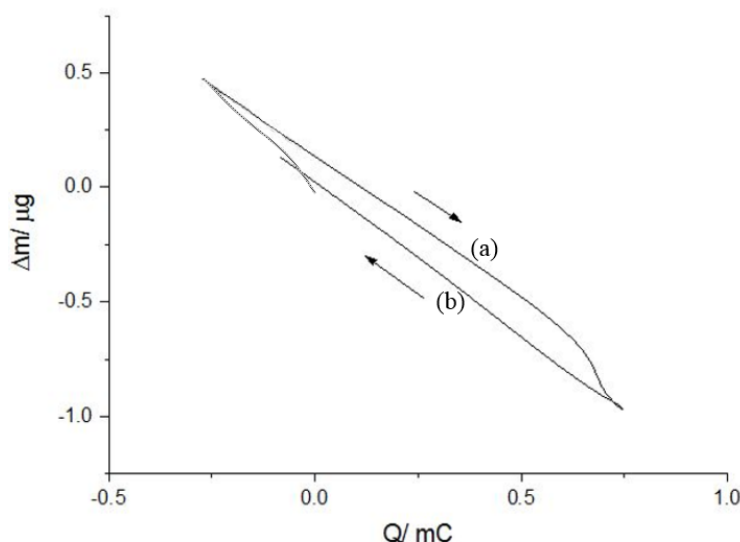
Fig. 4.3 Mass change (Δm) versus charge (Q) plot for the cyclic voltammogram (in Fig. 4.2) recorded during deposition and dissolution of elemental Ag from 0.001 M AgNO$_3$ in 0.2 M HClO$_{4(aq)}$. Scan rate = 5 mV s^{-1}.

The thickness of the deposit was circa 2.5 μm (calculated using density and mass of silver). The average roughness of the AT-cut Pt plated polished quartz electrode is on the order of 1 μm.[39] Therefore we can assume that the morphology of the deposit will closely follow the underlying substrate.

The probe beam deflection optical response (Fig. 4.2 bottom panel), showed a symmetrical deflection profile during silver deposition/dissolution. The negative deflection trend at the start was due to the decrease in Ag$^+$ concentration at the electrode surface. The plateau observed at circa 165 mrad indicate that the deposition reaction is a continuous mass transport process. The positive deflection trend observed during oxidation (anodic stripping process) continued indicating the increasing concentration of Ag$^+$ in the near electrode area. The 1 second delay between the current signal and optical beam deviation can be attributed to the propagation delay caused by electrode–beam distance used in instrumentation (in comparison to the instantaneous electric and gravimetric signals).

An exchange of a single metal ion will always result in linearity of a Δm vs Q profile according to Faraday's law. This was proved by the Δm vs Q profile for the exchange of a single ion Ag$^+$ (Fig. 4.3). Any deviations from this would have given evidence for other contributing species. The gradient of Δm vs Q plot allowed for the calculation of the mass of the mobile species (M$_{MS}$) for two segments of the line. The curve (a) in Fig. 4.3 corresponds to a molar mass of 122.4 $\pm$ 0.1 gmol^{-1} where as curve (b) in the same figure corresponds to a molar mass of 134.4$\pm$0.1 gmol^{-1}. This is in reasonable agreement with the molar mass of silver (107.2 gmol^{-1}).

The hysteresis seen can be because of the movement of the other species present (H$^+$, NO$_3^-$ and ClO$_4^-$) in the electrolyte. According to previous research carried out by Henderson and coworkers the hysteresis present may also be due to the local density changes in the electrolyte. The metal ions released during the oxidation increases the concentration and liquid density within
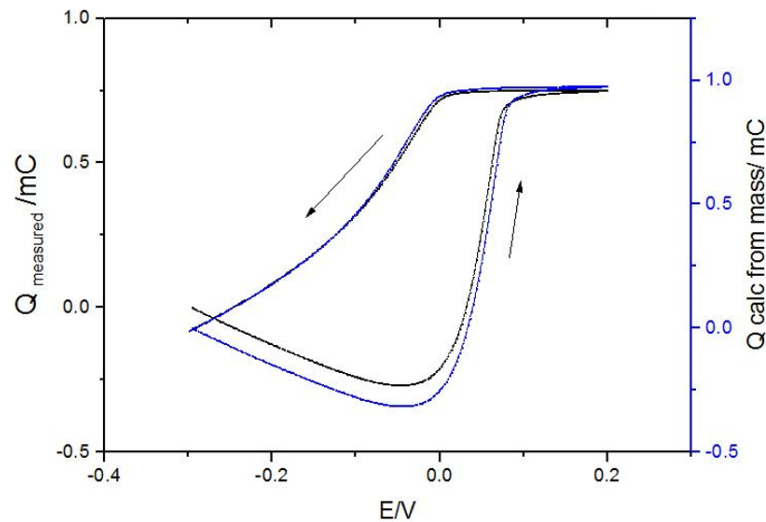
Fig. 4.4 Comparison of the measured electrochemical charge to the charge calculated from the mass (versus potential) for data in Fig 4.2

the acoustic wave penetration depth (Eqn. 4.3). The increase in density and hence the viscosity, changes the oscillation frequency of the resonator and causes "damping" of the oscillation frequency. The penetration depth would be circa 178 nm for a 10MHz resonator in a solution of 1 cP.

$$Depth = \sqrt{\frac{\bar{\nu}_L}{\pi f_0}} \tag{4.3}$$

where

$\bar{\nu}_L$ = kinematic viscosity of the solution (i.e. viscosity multiplied by density)

f_0 = quartz resonator initial frequency.

Assuming $f_0 = 10$ MHz and viscosity 1 cP, the Eqn. 4.3 returns the value of the penetration depth as circa 178 nm. The propagation delay can be corrected by the convolution analysis which uses experimental optical response (from PBD), the gravimetric data (from QCM) and charge passed during the redox process (from the potentiostat). The measured electrochemical charge from the potentiostat and charge calculated using mass (from EQCM) through Sauerbrey equation (Eqn. 2.30) demonstrated good correlation over the potential range studied (Fig. 4.4).

The convolution analysis relates the flux of the Ag^+ species in the optical deflection zone, where the beam is located ($J_{Ag^+_{(x,t)}}$) to the Ag^+ flux at the electrode ($J_{Ag^+_{(0,t)}}$) by applying the convolution product with the transfer function of the mass transport (Eqn. 4.6). Using convolution the concentration gradients at a finite distance from working electrode can be found. Ionic (metal cationic) flux at the electrode is compared with the electrochemical current (i.e. electron flux). We assume that electron flux is generated only by the metal ion flux, metal ion and electron exchange is simultaneous and the electrode ion exchange is instantaneous compared to the diffusional delay. The total ionic flux (f_{PBD}) is the sum of all the fluxes towards and away from the electrode. The measured current $i_{(t)}$ is proportional to the total flux of the charged species and can be represented by

$$i_{(t)} = FA \sum (Z_K J_K)_{(0,t)} \tag{4.4}$$

where K represents cation or anion and $J_{K_{(0,t)}}$ represents the cationic or anionic flux at the

electrode at a given time when $x = 0$. The distance x is the beam electrode distance (distance between electrode and the focal point of the laser beam). At the focal point, refractive index gradients result in an optical deflection which is measured and the convolution extrapolates the flux measurements from focal point to the electrode surface. The convolution analysis based at the focal point can be represented as

$$J_{C^+A^-_{(x,t)}} = F_{(x,t)} \times J_{C^+A^-_{(0,t)}} \tag{4.5}$$

$$J_{Ag^+NO_3^-_{(x,t)}} = F_{(x,t)} \times J_{Ag^+NO_3^-_{(0,t)}} \tag{4.6}$$

It is assumed that mass transfer is by semi-finite diffusion perpendicular to the electrode surface and hence $F_{(x,t)}$ is the convolution factor.

From application of Fick's law of diffusion,

$$J = -D\frac{dC_i}{dx} \tag{4.7}$$

where J = molar flux (mol m^{-2} s^{-1}) of species i
D_i = diffusion coefficient of species i (m^2 s^{-1})
c_i = concentration of species i (mol m^{-3})
x = position (m)

Molar flux in this equation is proportional to the concentration gradient. Therefore relating flux of the species to concentration gradient at time t,

$$J_{(x,t)} = -D\left(\frac{\partial C_{(x,t)}}{\partial x}\right) \tag{4.8}$$

The convolution factor is given as

$$F_{(x,t)} = \left[\frac{x}{2\sqrt{\pi Dt^3}}\right]e^{-\frac{x^2}{4Dt}} \tag{4.9}$$

where D = diffusion coefficient of transferred mobile specie
t = propagation delay time
x = propagation distance

Beam deflection induced by concentration gradient can be given as

$$\theta = -\frac{\partial n}{\partial C}\frac{1}{D}J_{(x,t)} \tag{4.10}$$

where θ is beam deviation. The experimental setup used is programmed to give positive deflection for the decay of the concentration profile resulting from dissolution of metal. The negative deviation indicated an increase in concentration profile due to metal deposition i.e. concentration of Ag$^+$ decreasing at the electrode compared to electrolyte at x. The electrochemical current can be related to species flux and optical deflection by

$$\theta_{(x,t)} = \frac{h_K L}{Z_K F A}F_{(x,t)} \times i_{(t)} \tag{4.11}$$

where $h_K = -\left[\frac{1}{n}\frac{\partial n}{\partial c}\frac{1}{D}\right]$ named convolution factor and is a constant for a given electrolyte. This eliminates the need to calculate $\frac{\partial n}{\partial c}$. L is the path length (electrode diameter).

For a successful quantitative optical analysis the electrochemically generated current must resemble the optical deflection. This was evident in this study and hence the comparison of convolved current and mass variations were analysed (Fig. 4.5).
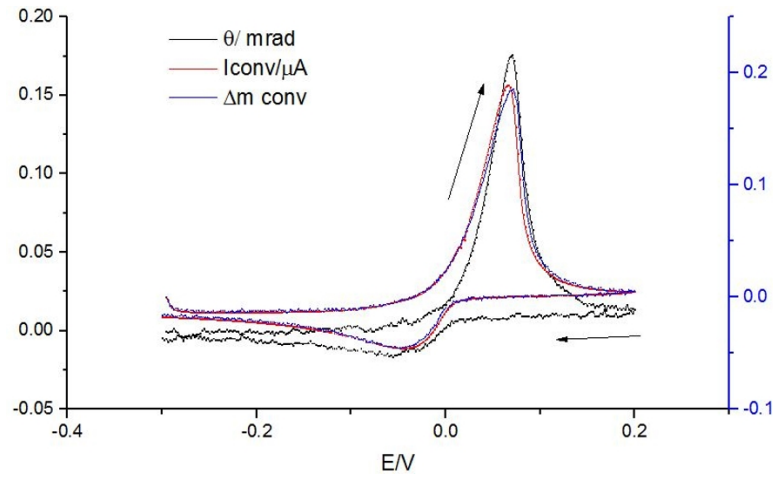
Fig. 4.5   Comparison of experimental beam deflection (θ), convolved current ($i_{(x,t)}\frac{hL}{zFA}$) and convolved mass variation ($\left(\frac{dM_{(x,t)}}{dt}\right)\frac{zFAhl}{m_{Ag+}}$) versus potential recorded for data in Fig. 4.2.

Convolved current deviates from θ during the deposition process but follows θ closely in disso-lution. The closed form of optical signal indicates that optical signal was successfully measured and the beam-electrode distance is fairly low. For convolved mass, the deviation can be ex-plained by the influence of $HClO_4$, the supporting electrolyte.[36]

To find individual contributions for the optical deflection the following were assumed:

1. The optical deflection signal is generated by total flux of species which is electroactive and non-electroactive.

2. The convolved current represents the cationic ion flux

3. Convolved mass represents the total mass flux for counter and co-ion

4. The remaining optical signal after deducting the cation and anion contributions represent the solvent flux.

According to Lang and Barbero,[12] the general representation of contributions of cation, anion and neutral species (C^+, A^- and N) can be given by the following equations, where θ is the optical deflection, $\frac{i_{(x,t)}hL}{ZFA}$ is projected current, $\frac{dM_{(x,t)}}{dt}\left(\frac{ZFAhL}{RMM}\right)$ is projected mass, RMM is dopant ion molar mass.

$$\theta - \left(\frac{i_{(x,t)}hL}{zFA}\right) = C^+ \tag{4.12}$$

$$\left(\frac{i_{(x,t)}hL}{zFA}\right) = A^- \tag{4.13}$$

'

$$\left(\frac{dM_{(x,t)}}{dt}\right)\left(\frac{zFAhL}{RMM}\right) - \left(\frac{i_{(x,t)}hL}{zFA}\right) = (C^+ + N) \tag{4.14}$$

$$\left(\left(\frac{dM_{(x,t)}}{dt}\right)\left(\frac{zFAhL}{RMM}\right) - \left(\frac{i_{(x,t)}hL}{zFA}\right) - \left(\theta - \left(\frac{i_{(x,t)}hL}{zFA}\right)\right)\right) = N \tag{4.15}$$
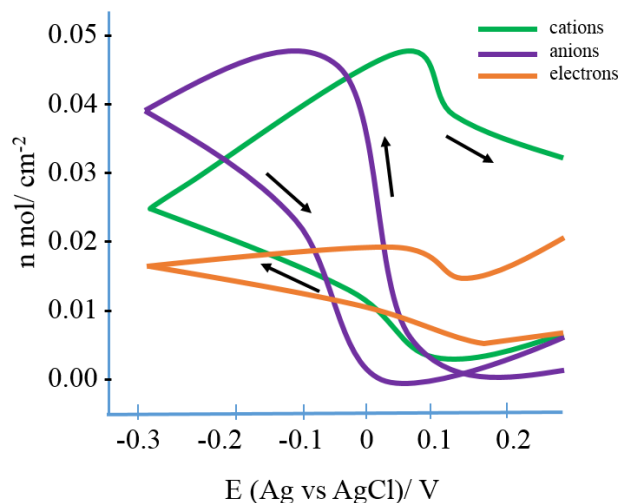

Fig. 4.6 Comparison of convolved signal integrals recorded during deposition and dissolution of elemental Ag from 0.001 M AgNO$_3$ in 0.2 M HClO$_{4(aq)}$. Scan rate = 5 mV s^{-1}

The cationic, anionic and electron contributions that were calculated are given in Fig. 4.6. The metal ions and electrons show equal but opposing responses in direction to confirm overall reaction as Ag$^+$ + e $\rightarrow$ Ag^0 . For convolution analysis, the contribution from NO$_3^-$ was not used as the concentration of NO$_3^-$ was 200 times lower than that of ClO$_4^-$ (HClO$_4$ = 0.2 M, ClO$_4^-$ = 0.001 M). The graph of $x/\sqrt{D}$ vs distance is given (Fig. 4.7). These represent the $x/\sqrt{D}$ value calculated at 10 μm increments and decrements from optimum electrode beam distance. From this plot the beam electrode distance was calculated to be 40 μm which was lower than that of previous studies (Fig. 4.7). [40]
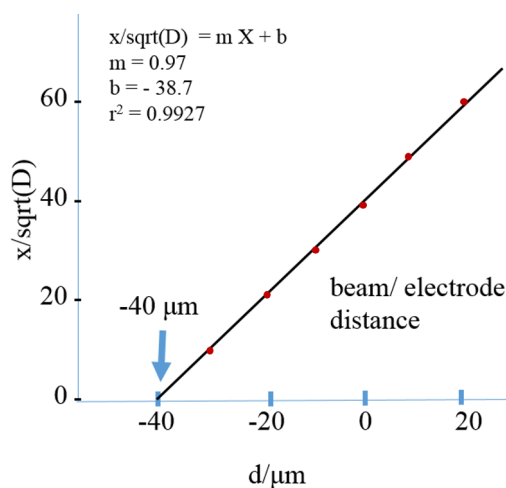

Fig. 4.7 Plot of the convolution parameter $x/\sqrt{D}$ expressed as a function of the relative beam distance

The diffusion coefficient of Ag^+ was found by the gradient to be 3×10^{-5} cm^2 s^{-1} which was in reasonable agreement with values in literature.[36,41]

The importance of this experiment was that it proved that the experimental protocol used in this study is consistent with the original study conducted by Henderson et al.[1]

4.3.2 EQCM-PBD study of Ag deposition/ dissolution in Deep Eutectic Solvent - Ethaline 200

The protocol used for preparing electrodes, solutions and experimental setup was discussed in Chapter three. Ionic liquids have high viscosity and low diffusivity compared to aqueous systems and this can pose a challenge for optical deflection studies in DES.[42] Zaleski et al. showed that this can be overcome by using low scan rates to account for slow optical sampling rates.[2] AgCl was selected instead of $AgNO_3$ as AgCl is not readily soluble in DES. High viscosity of DES slows down the mass transport rate compared to molecular solvents.[43] In order to get a good agreement between optical deflection data and electrochemical response, the following has been proven suitable:

- low beam - electrode distance

- low reaction rate to keep up with lag in optical deflection signal (low scan rate)

A series of chronodeflectograms were carried out to achieve a beam electrode distance of 47.9 μm (Fig. 4.8) and to identify the highest possible scan rate achievable at this distance.
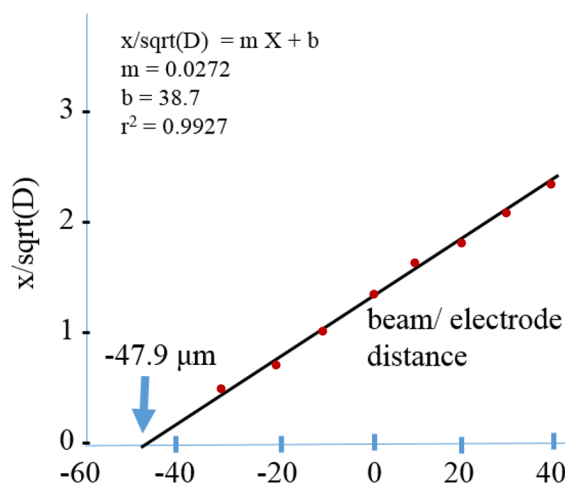

Fig. 4.8 Plot of the convolution parameter $x/\sqrt{D}$ expressed as a function of the relative beam distance.

Cyclic voltammograms of Ag deposition and dissolution were achieved at 0.5 mV s^{-1}, 0.25 mV s^{-1}, 0.125 mV s^{-1}, 0.0625 mV s^{-1}. As shown by Zaleski et al. the lowest scan rates were more successful in giving the optimal results. Cyclic voltammograms and cyclic deflectograms were recorded for deposition and dissolution of Ag in Ethalene 200.

The potential window applied was 0.2 V to -0.3 V and the potential scan rate (optimal scan rate) was set to be 0.0625 mV s^{-1} (Fig. 4.9). The reversible redox process (Ag$^+$/Ag^0) is shown by the current response and the Ag$^+$ reduction can be seen from 0.02 V to -0.3 V. The mass changes were calculated using the Sauerbrey equation[38] (Eqn. 4.1).
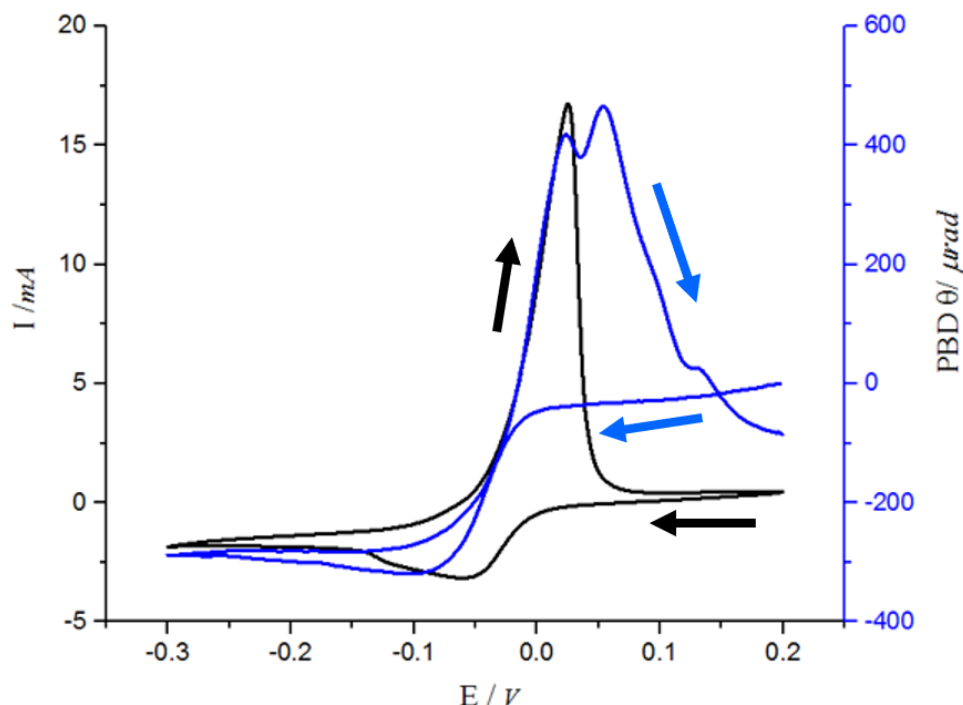

Fig. 4.9 The (a) current (I) black trace, optical response (θ) blue trace for the cyclic voltammograms recorded during deposition an dissolution of elemental Ag from 0.01 M AgCl in Ethaline 200 at scan rate ($\nu = 0.0625$ mV s^{-1} within the applied potential window applied $0.2\,V \rightarrow -0.3\,V \rightarrow 0.2\,V$ (against Ag pseudo reference electrode)

The Δm-E plot for data in Fig. 4.9 left panel indicated a steady increase from 0.01 V and continue even in the anodic scan up to 0 V where dissolution of the Ag starts and continued rapidly until 0.05 V (Fig. 4.10). The current decayed to its initial value but mass (Δm) did not reach the initial value leaving a 1 μg deficit (hysterisis effect). In the anodic sweep insoluble layers form at the electrode surface and super saturation can occur due to lack of suitable ligands (chloride) to complex the dissolving silver.[44] The solubility of the complex that forms between silver and chloride will depend on the solvation and the overall charge of the complex species where the overall charge for silver complex can be either -1 or -2.

The solubility depends on the ion ligand combination which in turn varies depending on the coordination number and the availability of the chloride ligand. In Ethaline, the chloride ion associates with ethelene glycol, reducing the availability of chloride, to complex with the silver cation. Insoluble film formation can hinder the mass transport causing a drop in anodic current affecting dissolution of silver. Since this is an unstirred solution, the Cl$^-$ ligand transport is diffusion limited. This effect together with the viscosity effect would slow down Ag$^+$ ion diffusion. The QCM resonator is capable of identifying this event in the form of a deficit in mass loss. As the voltage sweeps from -0.3 V to 0.3 V in the anodic regime, two clear peaks
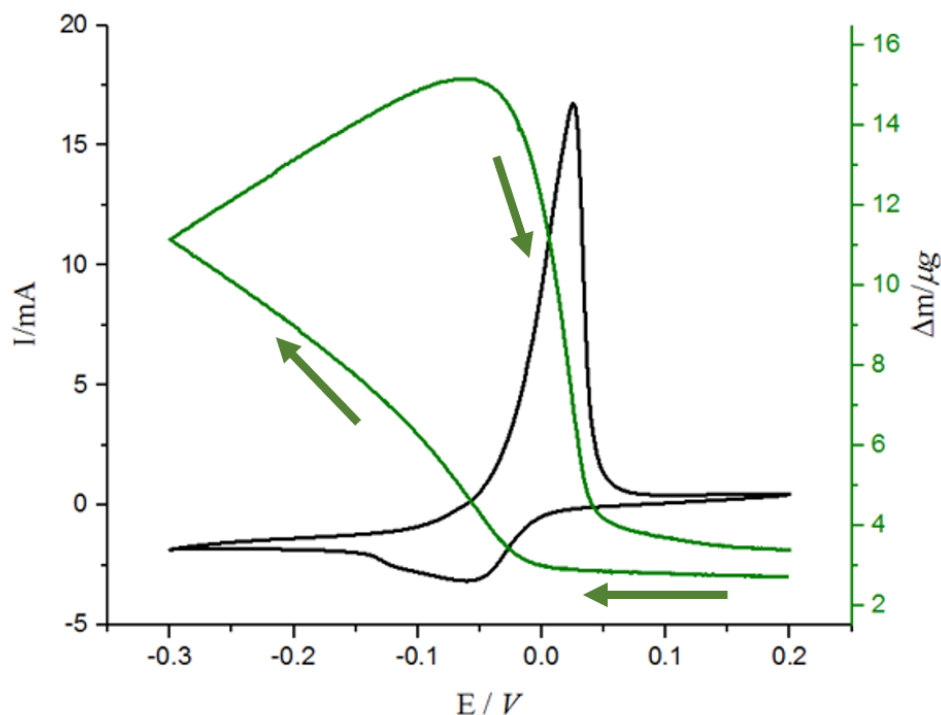
Fig. 4.10 The current (I) black trace, mass change (Δm) green trace plots for the cyclic voltammograms recorded during deposition an dissolution of elemental Ag from 0.01 M AgCl in Ethaline 200 at scan rate ($\nu = 0.0625$ mV s^{-1} within the applied potential window applied $0.2\ V \to -0.3\ V \to 0.2\ V$ (against Ag pseudo reference electrode)

can be seen for dissolution of Ag. These have been identified as peaks due to $AgCl_2^-$ and $AgCl_3^{2-}$ during EXAFS studies conducted by Abbott et al.[45] Also integration of peaks can be used to find the ratio of $AgCl_2^-$ and $AgCl_3^{2-}$ speciations to be 1:1.15 and can be explained by the Cl$^-$ concentration drop as Ag$^+$ is released to the medium.[3]

The gradient of Δm vs Q plot allowed calculation of the mass of the mobile species (M_{MS}) for two segments of the line. The curve (a) in Fig. 4.19 corresponds to a molar mass of 85.1 gmol^{-1} whereas curve (b) in the same figure corresponds to a molar mass of 96.4 gmol^{-1}. This latter value is in reasonable agreement with the molar mass of silver (107.2 gmol^{-1}).

Silver was electrodeposited on a glass slide under the same conditions to measure the thickness. Atomic force microscopy (AFM) was used to measure the thickness of the layer. The thickness of the silver deposit was found to be 5.6 μm. This was an increase of 2.5 μm from the value calculated using silver density and change in mass data (from QCM response). The lower than expected value calculated for the molar mass of the mobile species and the increase in thickness confirms the morphology of Ag to be nanoporous. This observation agrees with the results obtained by Abbott et al. for studies involving silver deposition using DES.[46,47] The nanoporous morphology may also indicate the reason for the molar mass calculated in dissolution being 93 gmol^{-1} compared to 107.6 gmol^{-1} expected for Ag. Nanoporous structure of Ag indicates Ag as a good alloying metal for metals like Bi and Sn. Loose packing layer morphology of silver was confirmed from AFM studies (See Chapter 5).

The convolved mass variation and convolved current variation showed good agreement with
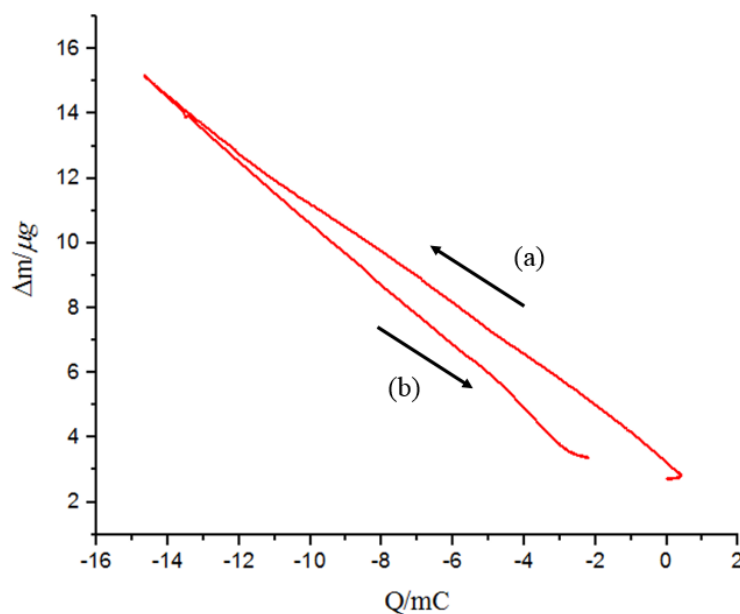
Fig. 4.11   Mass change (Δm) versus charge (Q) plot for the cyclic voltammogram recorded during deposition and dissolution of elemental Ag from 0.01 M AgCl in Ethaline 200 at scan rate (ν) = 0.0625 mV s^{-1} within the applied potential window applied $0.2\ V \rightarrow -0.3\ V \rightarrow 0.2\ V$ (against Ag pseudo reference electrode)

the deflectogram (Fig. 4.12, Fig. 4.13,). There was a larger propagation delay compared to the aqueous system which was expected from DES but less than that of previous studies. The absence of double peaks in the convolved graphs indicates that the signal obtained was a cumulative one and does not differentiate between two species.
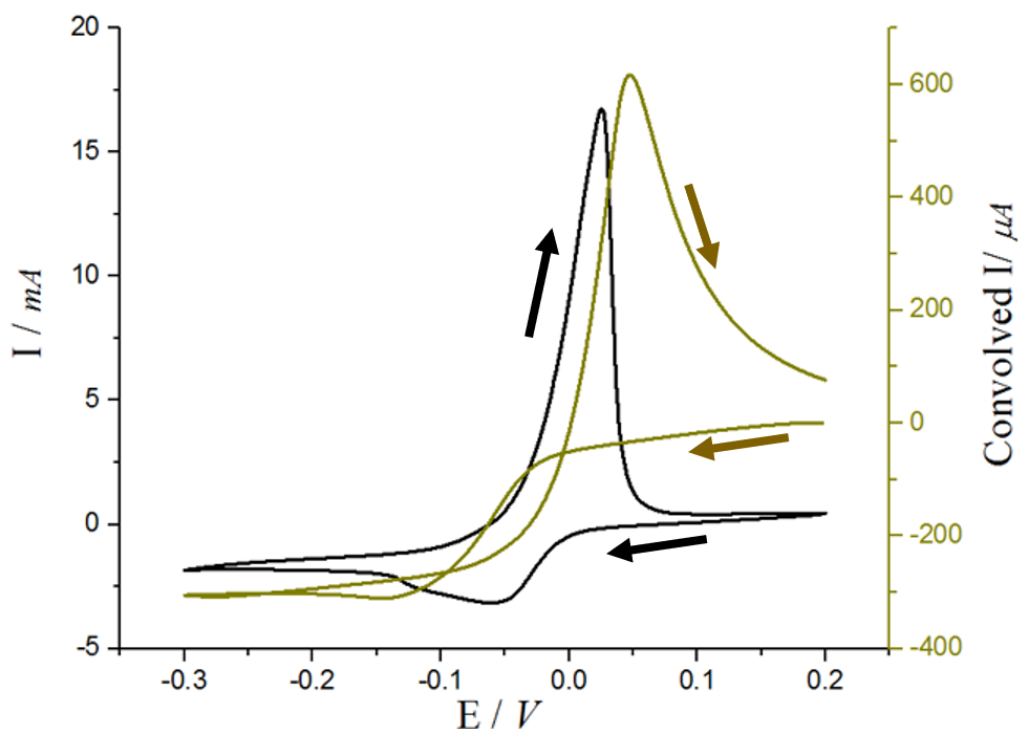
Fig. 4.12   Current (black trace), convolved current (yellow trace) during deposition and dissolution of elemental Ag from 0.01 M AgCl in Ethaline 200 at scan rate ($\nu = 0.0625$ mV s^{-1} within the applied potential window applied $0.2\ V \rightarrow -0.3\ V \rightarrow 0.2\ V$ (against Ag pseudo reference electrode)
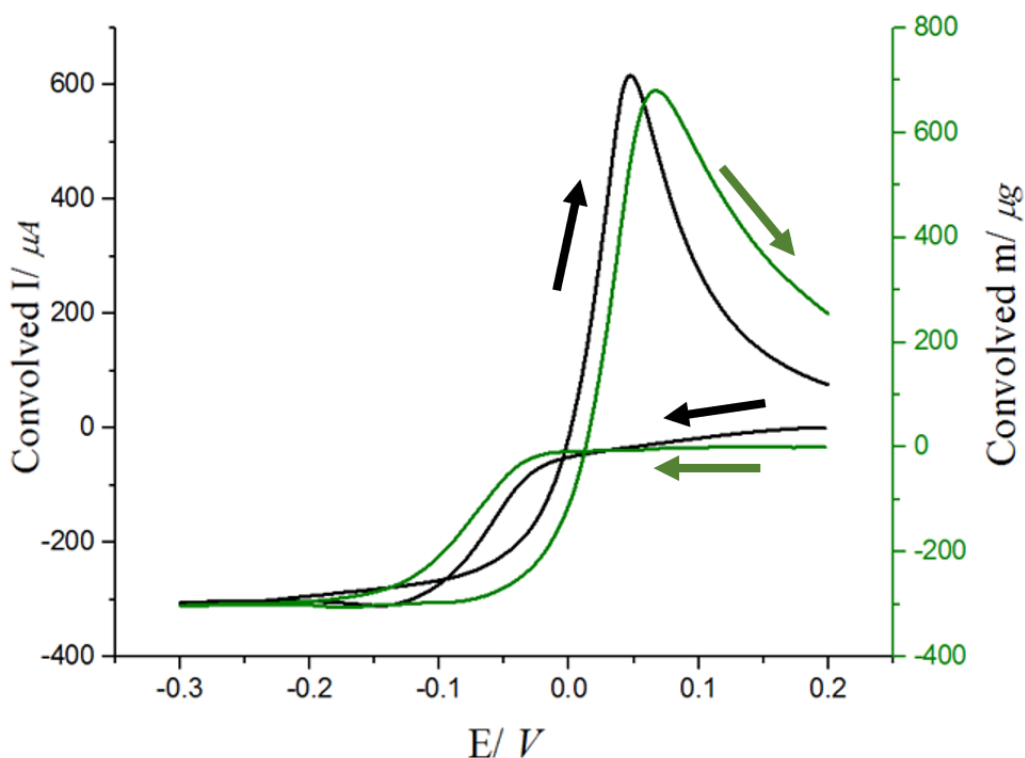

Fig. 4.13   Convolved mass (green trace) vs potential recorded during deposition and dissolution of elemental Ag from 0.01 M AgCl in Ethaline 200 at scan rate ($\nu = 0.0625$ mV s^{-1} within the applied potential window applied $0.2\ V \rightarrow -0.3\ V \rightarrow 0.2\ V$ (against Ag pseudo reference electrode)

Using Randles-Sevcik equation,

$$I_p = 0.4436 \, nFAC\sqrt{\frac{nF}{RT}\nu D} \tag{4.16}$$

where n - number of electrons transferred in the redox event
$\quad\quad F$ - Faraday constant (C mol^{-1})
$\quad\quad A$ - electrode area (cm^2)
$\quad\quad C$ - concentration (mol/cm^3)
$\quad\quad R$ - gas constant (J K^{-1}mol^{-1})
$\quad\quad T$ = temperature (K)

The graph of $x/\sqrt{D}$ vs distance is shown in Fig. 4.8. From this plot the beam electrode distance was calculated to be 47.9 μm.

The diffusion coefficient obtained from $x/\sqrt{D}$ vs distance graphs was 4.3 x 10^{-7} cm^2 s^{-1} which was higher than that from Randles-Sevcik equation (2.2 x 10^{-6} cm^2 s^{-1}) (see Chapter 5). The linearity of I$_p$ vs $\nu^{1/2}$ indicates diffusion control mass transport in both deposition and dissolution of Ag in DES.

4.3.3 EQCM-PBD study of Bi deposition/ dissolution of Ethaline 200

As discussed in Chapter 1, bismuth electrodeposition has many advantages. Underpotential deposition (UPD) of bismuth in aqueous media has been investigated as far back as the 1930s. Hartley et al. studied bismuth trichloride dissolved in Ethaline 200[36] and deduced that UPD occurs in cycling of bismuth film in Ethaline 200.

Cyclic voltammograms, deflectograms for deposition-dissolution of elemental bismuth from 0.01 mol dm^{-3} BiCl$_3$ in Ethaline 200 were analysed for scan rates ranging from 0.5 mV s^{-1}, 0.25 mV s^{-1}, 0.125 mV s^{-1} and 0.0625 mV s^{-1} all with a potential window of 0.4 V to - 0.6 V.

The cyclic voltammogram shown in (Fig. 4.14) has two deposition peaks. The deposition at -0.13 V corresponds to the bulk deposit of Bi on the electrode and the peak at positive potential regime (0.062 V) corresponds to underpotential deposition. The Bi deposition and dissolution process at electrode can be given as:

$$\text{Bi}^{3+} + 3\,\text{e} \rightleftharpoons \text{Bi}$$
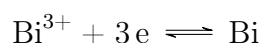
The equilibrium potential where deposition/ dissolution of bulk metal phase given by Nernst eqation.

$$E_{eq} = E^{\ominus}\frac{RT}{nF}ln\frac{a_{Bi(III)}}{a_{Bi(0)}} \tag{4.17}$$

where E_{eq} - equilibrium potential
$\quad\quad E^{\ominus}$ - standard potential
$\quad\quad a$ - activity and $a_{Bi(0)} = 1$
$\quad\quad n$ - number of electrons involved in the reaction
$\quad\quad R$ - gas constant (J K^{-1}mol^{-1})
$\quad\quad F$ - Faraday constant (96490 C mol^{-1})

Metal deposition happens in two stages, the first of which happens at a potential higher than the Nernst potential during which a monolayer of metal atoms is formed on the electrode surface. Studies conducted by Gewirth et al. on electrodepositing a Bi monolayer on Au electrodes provided evidence that there are two distinct underpotential deposited Bi adlattice structures. According to these studies in the 250 - 190 mV region, Bi formed (2 x 2)-Bi structures with 25% coverage.[48–52] These structures are described as open and low in coverage and found to be stabilised by coadsorption of anions or by Coulombic repulsion due to partial charge remaining on Bi adatoms. Bi electrodeposition from chloroaluminate ionic liquids ($BuPyCl-AlCl_3$[53] and $MBIC-AlCl_3$[54]) had shown two distinct processes. Pan et al. demonstrated that these processes take place at 1.2 V and 0.9 V (with respect to an Al quasi-reference electrode) with two different morphologies.[54] The study of bismuth in $AlCl_3-N(n-butyl)$ pyridinium chloride ionic liquid done by Heerman and D'Oileslager concluded that the electrochemical reduction of Bi^{3+} forms Bi_5^{3+} cluster ion which is an unstable intermediate before the formation of Bi^0 metal.[53] The Δm vs E plot of this process shows a mass change with two distinct slopes indicating that this theory is applicable to the deposition from Ethaline as well (Fig. 4.14). The corresponding deflectogram shows two areas of small positive deflection confirming that the concentration of the metal species has decreased in two distinct steps (Fig. 4.15).

The valancies for electrosoption may range from 2.6 to 3 in this region.[55] The coverage of the electrode surface (Au(111)) has increased when the potential becomes more negative and it has been found that (2x2) structure is replaced by uniaxially commensurate ($p \times \sqrt{3}$) Bi adlayer.[48–52] Bulk deposition happens on ($p \times \sqrt{3}$) layer and therefore understanding UPD is important for understanding growth. Mao et al. have investigated UPD during deposition of Bi from $BMIBF_4$ (1-Butyl-3-methylimidazolium tetrafluoroborate) ionic liquid.[56] They report that $BiCl_3$ neutral molecules (in ionic liquid) form an adsorbed monolayer on the Au electrode surface and these are reduced to a UPD layer. The $BiCl_3$ adsorbed layer formation can be explained by the strong ionic strength of $BMIBF_4$ ionic liquid.

Henderson et al. conducted a UPD study using PBD and prove that PBD can be used to probe into the UPD process.[1] Deep eutectic media are media of highly coordinating components and therefore we expect different behaviour compared to UPD in ionic liquids studied by Mao et al.[56] Also $BiCl_3$'s ability to readily dissolve in Ethaline 200 makes it an ideal candidate for this study. For the application of convolution analysis, we assume that Bi^{3+} is the only charge carrier since it was demonstrated in a previous study.[34] Assuming Bi^{3+} as the only species that is exchanged between electrode surface/ electrolyte the reaction can be described as follows:

$$Bi^{3+} + 3\,e \longrightarrow Bi^0 \text{ and}$$

$$Bi^0 + 4\,Cl^- \longrightarrow BiCl_4^- + 3\,e$$
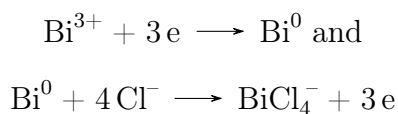
Nevertheless, we are not able to deduce the exact identity and origin of the UPD species forming the monolayer. The majority of Cl^- in the DES Ethaline gives a high Cl^- ion concentration near the electrode area. Therefore the formation of chloro complexes would be considered as
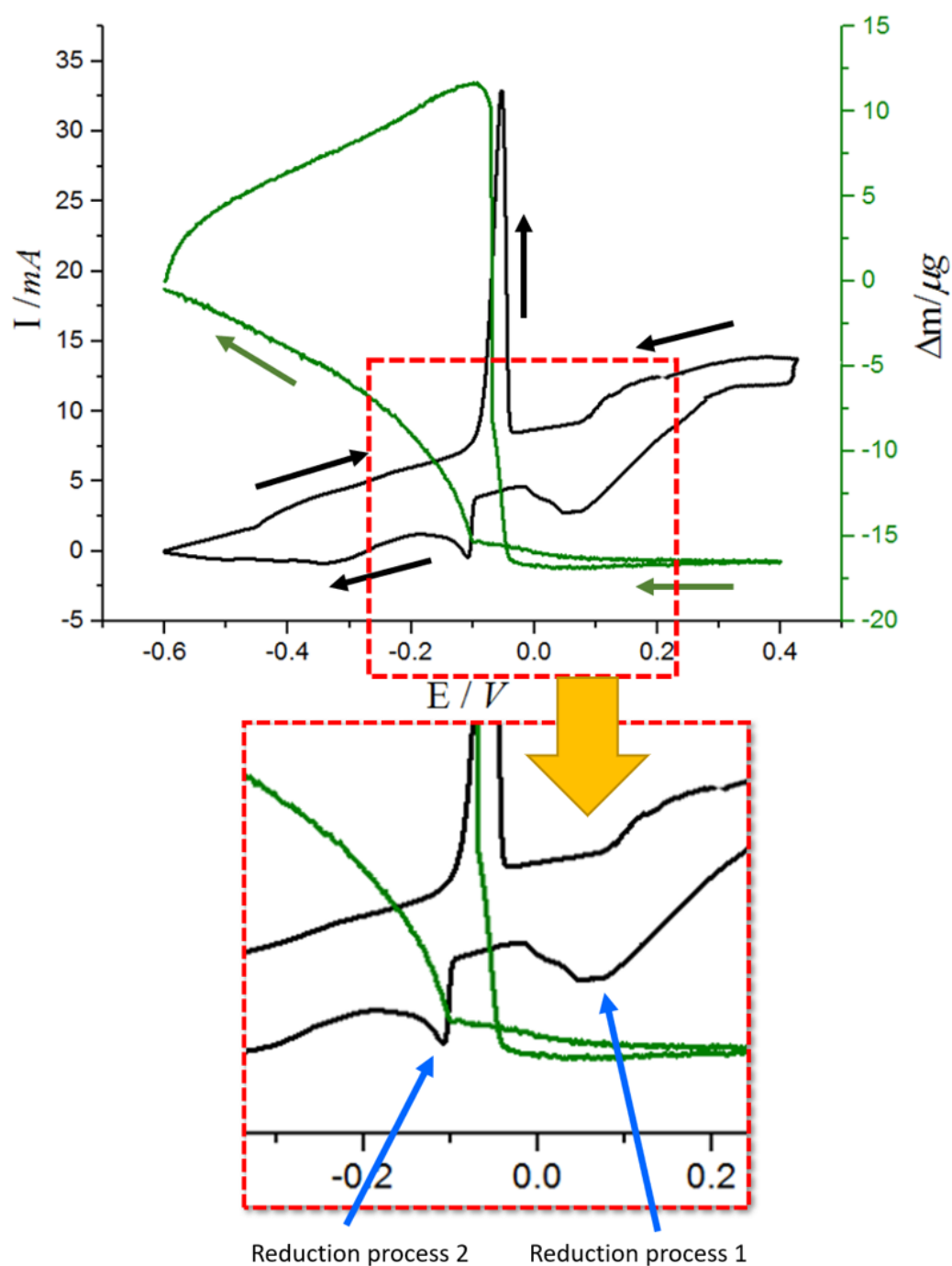
Fig. 4.14 The current (I) black trace, mass change (Δm) green trace plots for the cyclic voltammograms recorded during deposition and dissolution of elemental Bi from 0.01 M BiCl$_3$ in Ethaline 200 at scan rate ($\nu = 0.0625$ mV s^{-1} within the applied potential window applied $-0.6\,V \rightarrow 0.4\,V \rightarrow -0.6\,V$ (against Ag pseudo reference electrode)

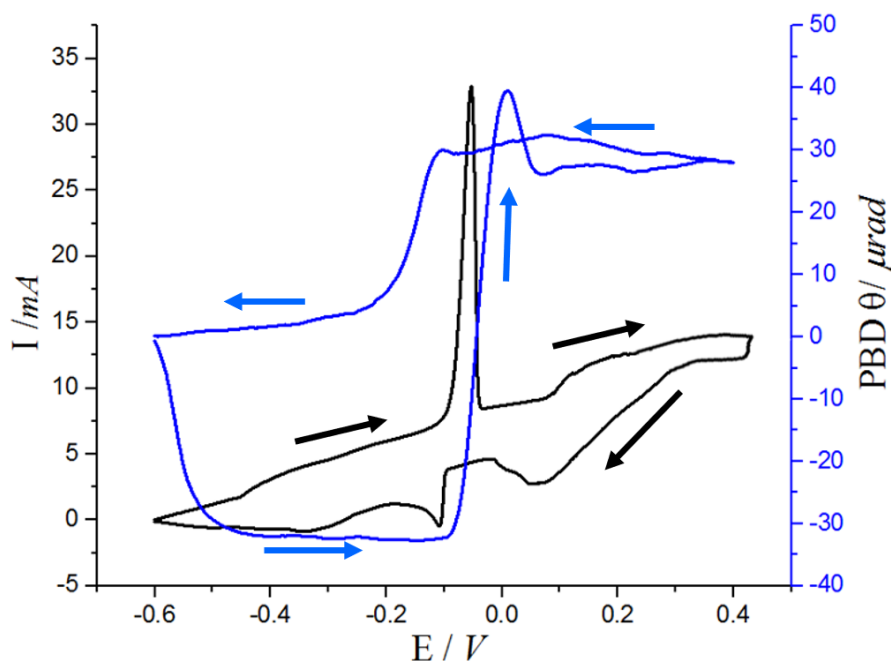**Fig. 4.15** The current (I) black trace, optical response (θ) blue trace and plot for the cyclic voltammograms recorded during deposition and dissolution of elemental Bi from 0.01 M BiCl$_3$ in Ethaline 200 at scan rate ($\nu = 0.0625$ mV s^{-1} within the applied potential window applied $-0.6\ V \rightarrow 0.4\ V \rightarrow -0.6\ V$ (against Ag pseudo reference electrode)

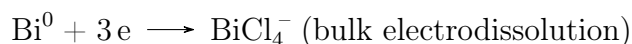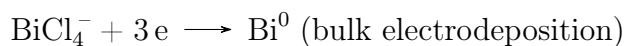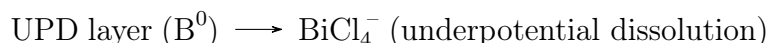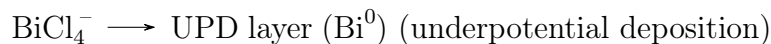an ideal assumption under this circumstance. We are able to make an initial assumption that Bi^{3+} ions get adsorbed, with their Cl$^-$ coordinating spheres, to the electrode surface resulting in the formation of a monolayer. The monolayer increases in coverage with the cathodic scan and transforms into a bulk deposit. This process can be represented as:

$$BiCl_4^- \longrightarrow UPD\ layer\ (Bi^0)\ (underpotential\ deposition)$$

$$UPD\ layer\ (B^0) \longrightarrow BiCl_4^-\ (underpotential\ dissolution)$$

$$BiCl_4^- + 3\,e \longrightarrow Bi^0\ (bulk\ electrodeposition)$$

$$Bi^0 + 3\,e \longrightarrow BiCl_4^-\ (bulk\ electrodissolution)$$

In order for this assumption to be true we should have 1:3 electron/cation ratio. This agreed with the calculated 1:2.4 ratio observed between the convolved signals (Fig. 4.16).

Hepel et al[57] studied insitu underpotential deposition of Pb using EQCM studies and found that the adsorption of Pb(II) complexes to the working electrode in the positive potential regime. As the Pb was reduced to Pb(0), the acetates adsorbed were rejected and affected mass difference observed was the net effect of Pb deposition and removal of acetate groups. Here we observed a similar scenario due to the high chloride ion concentration in the media. The bismuth forms [BiCl$_4$]$^-$ complexes in Ethaline 200 DES medium and the negative complexes are adsorbed to the electrode when the potential is swept from $0V \rightarrow 0.4V \rightarrow 0V$. When the Bi(III) is reduced to Bi(0) the observed mass change is due to the removal of the chloride ions (of the complex) and the deposition of bismuth. Since there is a loss of four chloride ions for each bismuth (0) deposited the net change of mass would be small (i.e. expected mass change for Bi deposition
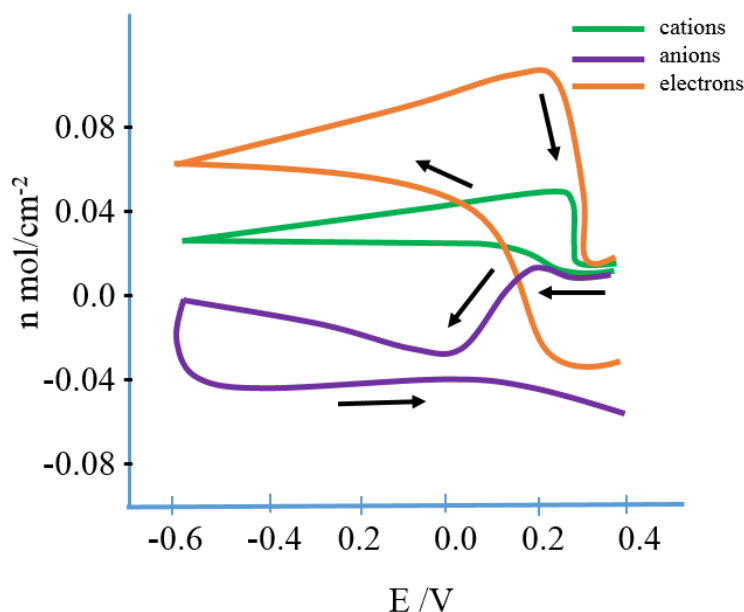
Fig. 4.16 Comparison of convolved signal integrals recorded during deposition and dissolution of elemental Bi from 0.01 M BiCl$_3$ in Ethaline 200 at scan rate ($\nu = 0.0625$ mV s^{-1} within the applied potential window applied $-0.6\ V \rightarrow 0.4\ V \rightarrow -0.6\ V$ (against Ag pseudo reference electrode)

$\propto$ to 208.9 gmol^{-1} whereas the net change $\propto$ 66.9 gmol^{-1}.

The cyclic voltammogram has a single clear peak at -0.052 V for dissolution and a slightly elevated curve in the potential range 0.0125 V - 0.25 V which may be for underpotential dissolution. This is clearly supported by the optical signal deflection (Fig. 4.15). In the deflectogram there is a very high positive deflection which is an increment of 40.5 μrad. The positive deflection is a consequence of the decreasing ion concentration at the electrode and the beam deviation reaches a maximum at 31.9 μrad after which it decreases by 3 μrad to again have a increment of 4.5 μrad. This clearly demonstrates a sudden release of ions to the medium by underpotential dissolution which cannot be identified so easily by cyclic voltammogram or massogram. This dissolution trend continues even during the reverse scan until the voltage becomes approx. +0.2 V due to the deposition of bulk deposition of Bi on to the electrode.

Convolution analysis of UPD processes is not straightforward as shown by Henderson et al.[1] The convolution was carried out and the convolved mass and convolved current signals are shown in Fig. 4.17 and Fig. 4.18. The convolved current followed the experimental current response and optical signal to a good extent. However, the same cannot be assumed for the comparison of convolved mass with optical signal. In the convolved mass there is a lack of superimposition for bulk deposition region between -0.4 V to -0.5 V.
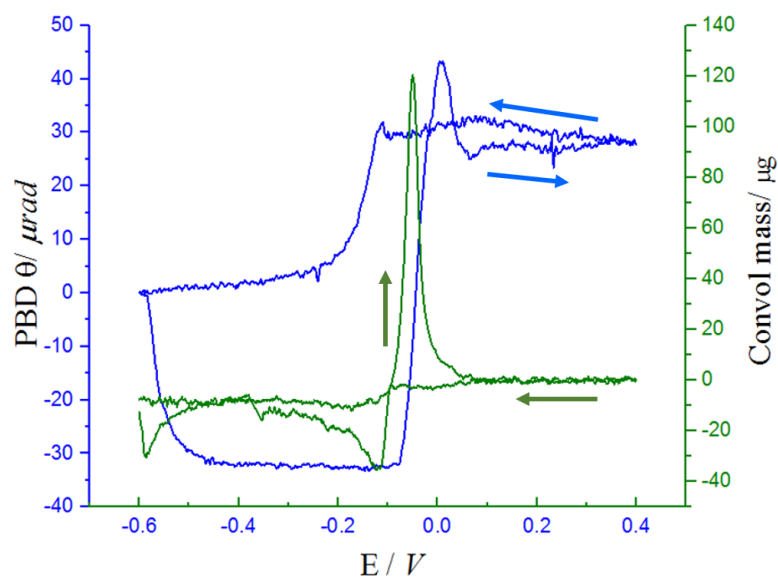
Fig. 4.17   Convolved mass (green trace) with respect to the PBD deflection signal (blue trace) recorded during deposition and dissolution of elemental Bi from 0.01 M $BiCl_3$ in Ethaline 200 at scan rate ($\nu = 0.0625$ mV s^{-1} within the applied potential window applied $-0.6\ V \rightarrow 0.4\ V \rightarrow -0.6\ V$ (against Ag pseudo reference electrode)
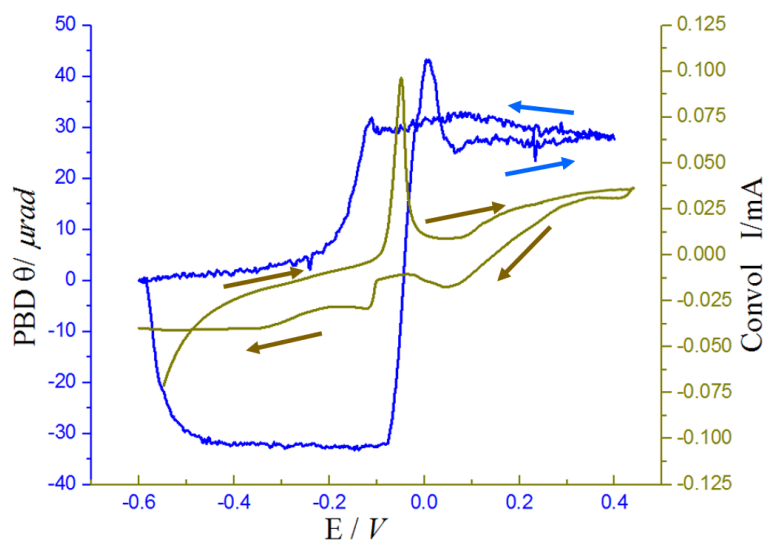

Fig. 4.18   Convolved current (light green trace) with respect to the PBD signal (blue trace) recorded during deposition and dissolution of elemental Bi from 0.01 M $BiCl_3$ in Ethaline 200 at scan rate ($\nu = 0.0625$ mV s^{-1} within the applied potential window applied $-0.6\ V \rightarrow 0.4\ V \rightarrow -0.6\ V$ (against Ag pseudo reference electrode)

The analysis of Δm vs Q graph demonstrate that the overall process can be separated into five distinct regions (Fig. 4.19).
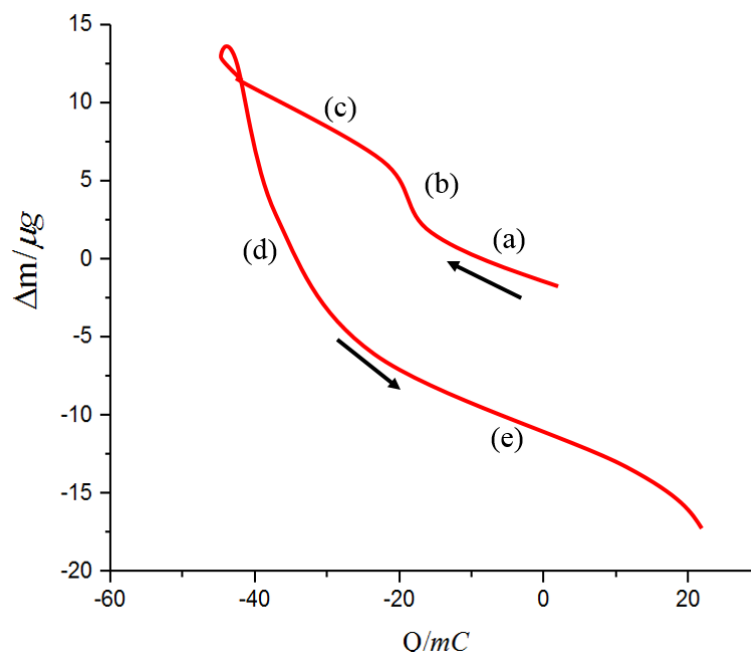

Fig. 4.19   Mass change (Δm) versus charge (Q) plot for the cyclic voltammogram recorded (Fig. 4.12) during deposition and dissolution of elemental Bi from 0.01 M BiCl$_3$ in Ethaline 200 at scan rate (ν) = 0.0625 mV s^{-1} within the applied potential window applied $-0.6\ V \rightarrow 0.4\ V \rightarrow -0.6\ V$ (against Ag pseudo reference electrode) using data obtained from plot shown in Fig. 4.18

Table 4.2   Analysis of Q plot for deposition and dissolution of elemental Bi

Curve region	Potential region / V	Gradient (μg/mC)	Effective molar mass calculated when z=1 /gmol^{-1}	Effective molar mass calculated when z=3 /gmol^{-1}
(a)	0 to -0.25	0.83	77.1±0.1	231.5 ±0.1
(b)	-0.25 to -0.62	2.3	221.4 ±0.1	665.7±0.1
(c)	-0.6 to -0.125	0.92	86.8±0.1	260.5 ±0.1
(d)	-0.125 to -0.0625	3.01	280.4 ±0.1	868.4±0.1
(e)	-0.0625 to +0.4	0.9	77.8±0.5	233.4 ±0.5

- The region (a) which represents points from 0 V to -0.25 V for cathodic electrodeposition gives the mass of mobile species (M$_{MS}$) as 231.5 gmol^{-1} for z=3 value. This is in reasonable agreement with Bi molar mass of 208.98 gmol^{-1}. This is also congruent with the large mass increase in this region and the optical deflection signal.

- The region (b) which represents points from -0.25V to -0.6 V shows a M$_{MS}$ of 665.7 gmol^{-1}. This is an extraordinary increase from the expected value of 208.98 gmol^{-1}. This region shows a significant change in mass (17 μg) without a significant change in current output. This indicates that the Bi reduction may not happen as previously predicted. The M$_{MS}$ calculated with a z=1 for this region gives 221.9 gmol^{-1} which is in agreement

with Bi molar mass indicating that the mobile ion involved might be Bi^+. Further studies using EXAFS would be necessary to prove or disprove this assumption. Furthermore, to support the argument that the mass increase is solely due to $Bi^{3+} \longrightarrow Bi^0$ in the -0.25 V to -0.6 V region, the current output and optical deflection signal should support the QCM output of mass (for which is missing in this process). The EQCM-PBD output corroborating the claim that the mass increase is due to $Bi^{3+} \longrightarrow Bi^0$ in the -0.25 V to -0.6 V region is not seen in the deflectogram. Also M_{MS} can be influenced by factors other mobile species being Bi^{3+}. The co-flux of the anion species (choloro complexes) can be expected to influence the calculated M_{MS} value. Fig. 4.16 where ionic contributions are plotted supports this assumptions. So in region (b) it is fair to assume that partial reduction of Bi or co-flux of anions are affecting $\Delta m/Q$ values.

- The region (c) represents points from -0.6 V to -0.125 V where the $\Delta m/Q$ gradient 0.9 gmol^{-1} agrees with (260.5 gmol^{-1}) the redox reaction being Bi(III) → Bi(0) which corresponds to the 15 μg mass difference in the Δm vs E plot.

- The region (d) the range from -0.125 V to +0.0625 V shows a M_{MS} of 280.47 gmol^{-1} for z=1 and 868.4 gmol^{-1} for z=3. The optical deflection signal shows a positive deviation of ca. 10 μrad in this region and the Δm vs E plot shows mass drop ca. 2 μg . This indicates a large amount of bulk Bi deposit dissolving and going in to the electrolyte near the electrode. This corresponds to 1.2×10^{-8} mol of Bi released to this volume. Analysing the variation of I_p(peak cathodic and anodic current observed) for Bi deposition/dissolution from 0.01 M BiCl$_3$ in Ethaline 200 with different scan rates (see Chapter 5) demonstrates that diffusion coefficient for Bi^{3+} ions in Ethaline DES is $1.9 - 2.4 \times 10^{-7}$ cm^{2}s^{-1}. This indicates that diffusion of Bi^{3+} is very slow in Ethaline due to its high viscous nature. Also solubility of the complex formed between bismuth and chloride will depend on the Cl$^-$ ion concentration available for ion-ligand combination. Also Abbott et al. demonstrated that Cl$^-$ ion interacts with ethylene glycol in unstirred solutions reducing the availability of Cl$^-$ ions further,[44] since Cl$^-$ ion transport is diffusion limited in unstirred solutions. This causes the insoluble film formation on the electrode and blocking the electrode from the electrolyte. These reasons explain the lower than expected positive deflection in optical signal, unexpected value of M_{SM} derived from $\Delta m/Q$ graph and the drop in Δm vs E plot.

- The region (e) corresponding to +0.0625 V to +0.4 V voltage regime. $\Delta m/Q$ gradient (0.9) indicates M_{SM} value of 233.4 for z=3 charge. The Δm vs E graph shows a slight decrease (1 μg) in this region which is corroborated by a slight increase in optical signal. There is an increase in current output around 0.2 V and this is in agreement with data reported by Hartley who attributed this second oxidation peak to the dissolution of under-potentially deposited Bi layer. As the potential is swept further into the positive regime the dispersion of Bi ions from the electrode and influx of Cl$^-$ ions towards the electrode surface is increased. Therefore, the M_{SM} value observed may explain this phenomenon.

The beam-electrode distance derived from a series of deflectograms is shown in Fig. 4.20. From

the plot of $x/sqrt(D)$ vs d the beam electrode distance has been shown to be 48.9 μm which proves the setup that was used for analysis was successful and the diffusion coefficient calculated by the gradient (2.20×10^{-7} cm^2 s^{-1}) agreed with the values derived from Cottrell equation (2.7×10^{-7} cm^2 s^{-1}) and Koutecky Levich study (1.50×10^{-7} cm^2 s^{-1}).
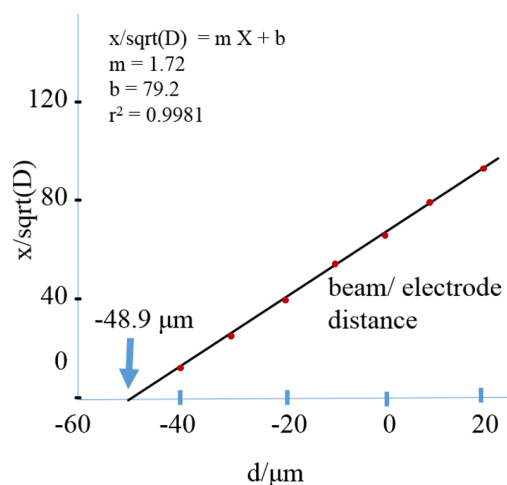

Fig. 4.20 Plot of the convolution parameter $x/\sqrt{D}$ expressed as a function of the relative beam distance

4.3.4 EQCM-PBD study of co-deposition/ dissolution of silver and bismuth in Ethaline 200

Co-electrodeposition of silver and bismuth to form silver/ bismuth intermetallics is proven to alleviate low hardness and wear resistance of silver. silver/ bismuth intermetallics electrode-posited using alkaline solutions have been shown to form segregated phases in the coating and lower wear resistance properties although complexing agents such as KCN have proven to improve micro-hardness.[58] Silver/ bismuth alloy electrodes have been used to detect trace metals and have proven to have high overpotential for hydrogen evolution depending on the incorporated bismuth percentage.[59,60]

The same protocol (used previously for Ag/ Ethaline and Bi/ Ethaline) was used for preparing electrodes, solutions and experimental setup (see Chapter 3). A series of deflectograms were carried out to calculate beam-electrode distance and diffusion coefficient from $x/\sqrt{D}$ plots (Fig. 4.25). The optically determined diffusion coefficient value derived for a co-deposition/ dissolution process must be treated as an average of the values of individual diffusion coefficient values (i.e. $D_{AgCl_2^-}$ and $D_{BiCl_4^-}$).

Cyclic voltammograms of silver/ bismuth deposition/dissolution were carried out at 0.5 mV s^{-1}, 0.25 mV s^{-1}, 0.125 mV s^{-1} and 0.0625 mV s^{-1}. The lowest scan rates were proven more successful due to slow diffusion rates of DES. At slow scan rates the optical signal measurement can keep up with the half cycle time even with slow transit times.

The potential window of +0.25 mV to +0.15 was used and AgCl:BiCl$_3$ concentration was mainly kept at 1:1 ratio (e.g. 0.005 M: 0.005 M or 0.01 M: 0.01 M). The obtained current,

optical deflection, and mass response are given in Fig. 4.21 and Fig. 4.22. The only charge carrying species were assumed to be Ag(I) and Bi(III).
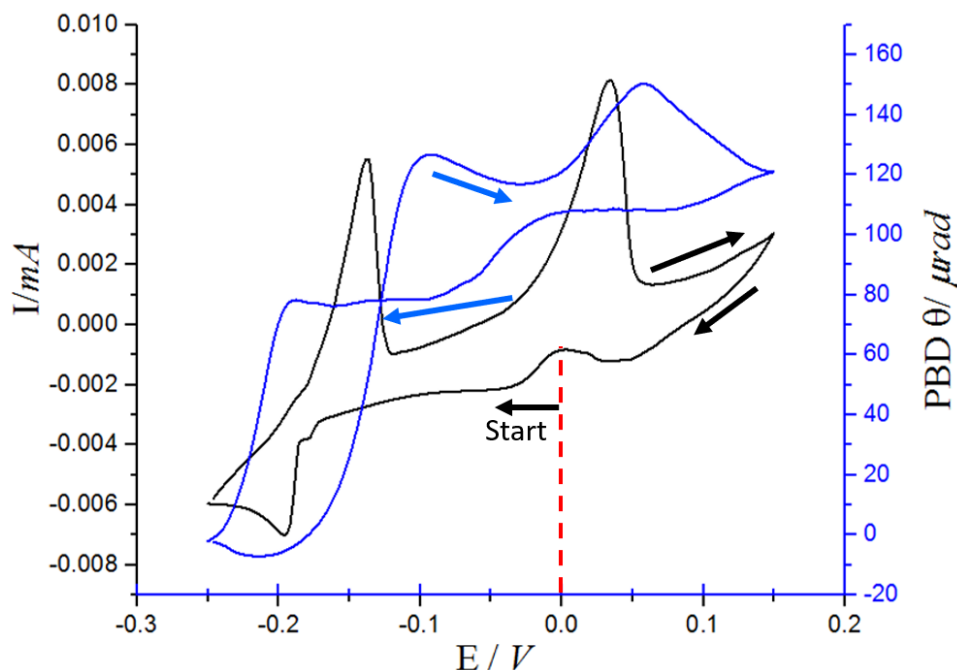

Fig. 4.21 The current (I) (black trace), optical response (θ) (blue trace) vs potential plot for the cyclic voltammograms recorded during deposition and dissolution of elemental Bi from 0.01 M BiCl$_3$ in Ethaline 200 at scan rate $\nu = 0.0625$ mV s^{-1} within the applied potential window (against Ag pseudo reference electrode)
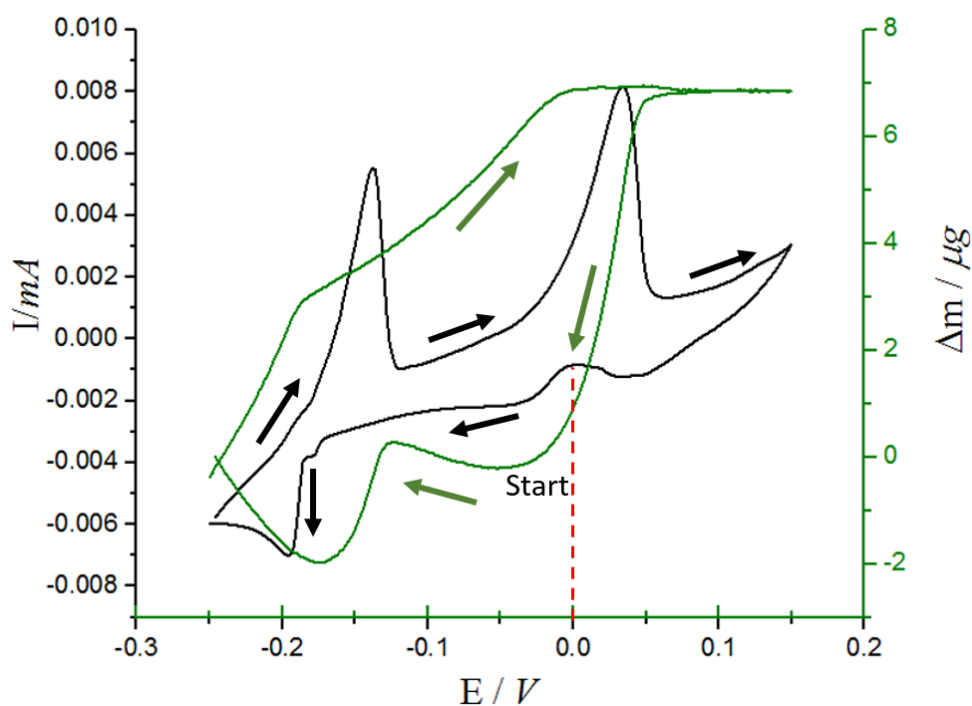

Fig. 4.22 The current (I) (black trace), mass change (Δm) (green trace) plots for the cyclic voltammograms recorded during deposition and dissolution of elemental Bi from 0.01 M BiCl$_3$ in Ethaline 200 at scan rate $\nu = 0.0625$ mV s^{-1} within the applied potential window applied $-0.6V \rightarrow 0.4V \rightarrow -0.6V$ (against Ag pseudo reference electrode)

Several cyclic voltammograms were recorded (3 or 4) in AgCl:BiCl$_3$ in Ethaline at 20 °C for each scan rate and the third data set was used for the analysis of optical, voltage and current response. These were compared to the cyclic voltammograms acheived for Ag/ Ethaline and Bi/ Ethaline separately (Fig. 4.9,Fig. 4.10 Fig. 4.15 and Fig. 4.14). There are clearly 4 deposition areas in the cyclic voltammograms at +40 mV, -32 mV, -178 mV and -196 mV. The voltage was scanned in the order of $0V \rightarrow -250mV \rightarrow +50mV \rightarrow 0V$. The feature at -32 mV (see Fig. 4.22) can be assigned to the Ag deposition as Ag/Ethaline system showed this peak at -25 mV. The feature at -178 mV should correspond to a Bi deposition on the Ag substrate (see Fig. 4.22). For Bi only systems there were three significant areas of deposition and the main Bi deposition peak was at -125 mV (see Fig. 4.12) with another significant deposit around -312 mV. This clearly indicates that the reduction potential for Bi has shifted to more negative values for co-deposition of Ag/Bi. It has been shown that when Ag/Bi is co-deposited on Pt in aqueous medium, they form a Ag-Bi solid solution with an additional pure Bi phase at more negative potentials. Here we can assume that Bi is forming two different phases which may or may not be two different solid solutions or metallic phases at -178 mV and -196 mV (see Fig. 4.22). This was further analysed by simultaneous thickness electrochemical potential method (see section on STEP methodology in Chapter 6) and proved to consist of several intermetallic phases. In the anodic regime there were two clear peaks, at -138 mV and +35 mV. The peak at -138 mV could correspond to Bi and Ag co-dissolution while the peak at +35 mV could correspond to Ag dissolution.
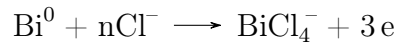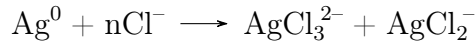
As the voltage is scanned from +150 mV to 0 mV, there is a small broad feature in the region of +100 mV to 0 mV with the clear deposition around +40 mV. This deposition can be attributed to underpotential deposition of Bi which shows a 20 mV negative shift from Bi/ Ethaline system (i.e. 62 mV). When comparing the Δm vs E graph response with the current response (in Fig. 4.22) around 40 mV the mass gain is non-existent, supporting the theory of Bi UPD. Furthermore, in the deflectogram (Fig. 4.19), this is indicated as a slight negative deflection (circa 5 μrad). From 0 mV to 150 mV, Ag deposition is indicated as a prominent negative deflection in the deflectogram (circa 30 μrad).

In the reverse scan, starting from -250 mV to +150 mV, the deflectogram has two positive deflection peaks for the dissolution of Ag-Bi phase and Ag deposit. It is quite evident from the 125 μrad deflection for the first peak that the bulk of the deposit has been dissolved during the first anodic peak region (see Fig. 4.19 - blue trace) which would be circa 4 μg of Bi, Ag dissolving according to the Δm vs E graph. For the second peak, the difference in Δm vs E graph is about 3 μg which is in agreement with the small positive optical deflection. Based on the above observations for the convolution process, the following assumptions were made:

Bi^{3+} and Ag^+ are the only charged species exchanged between electrode/ electrolyte. So the simplified redox reaction can be given as:

$$Ag^+ + Bi^{3+} + 4\,e \longrightarrow Ag^0 + Bi^0$$

and

$$Ag^0 + nCl^- \longrightarrow AgCl_3^{2-} + AgCl_2^-$$

$$Bi^0 + nCl^- \longrightarrow BiCl_4^- + 3\,e$$

The flux of the species at the electrode J_{Total} is due to both species involved,

$$J_{Total_{(x,t)}} = F_{(x,t)} \times J_{Ag^+Cl^-/Bi^{3+}+nCl^-_{(0,t)}}$$

Here the convolution factor F would involve two diffusion coefficients to represent $AgCl_2^-/$ $AgCl_3^{2-}$ (D_{AgCl}) and $BiCl_4^-$ (D_{BiCl_3}). It can be assumed that $AgCl_2^-$ would be the main contributing species due to the lack of availability of chloride ions.

The convolved current (μA) (Fig. 4.24) showed a qualitatively similar trend to the optical deflection θ (μrad) (Fig. 4.23) values proving the convolution process was successful.
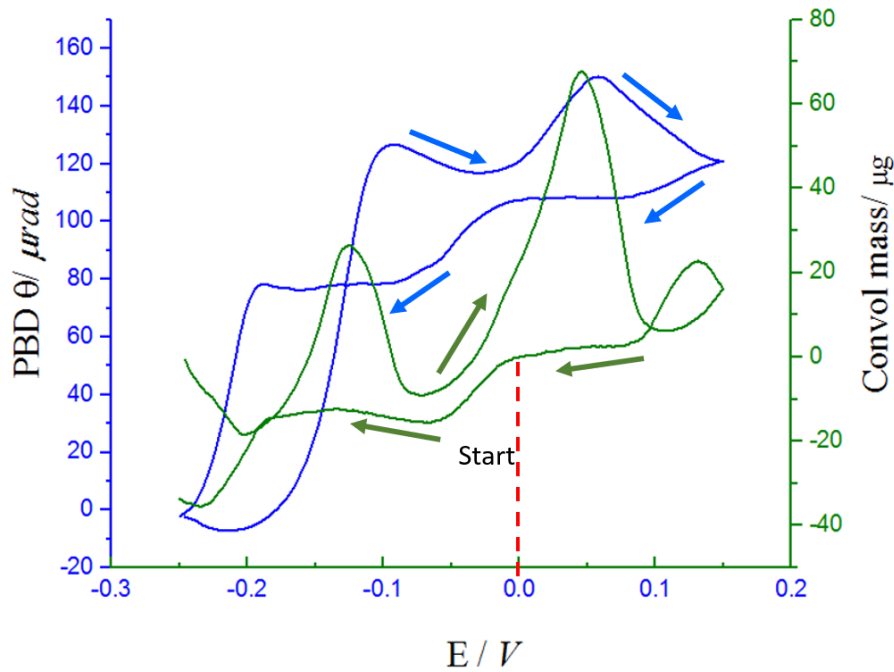

Fig. 4.23   Convolved mass (green trace) with respect to the PBD signal (blue trace) recorded during deposition and dissolution of elemental Bi from 0.01 M $BiCl_3$ in Ethaline 200 at scan rate (ν) = 0.0625 mV s^{-1} within the applied potential window (against Ag pseudo reference electrode).
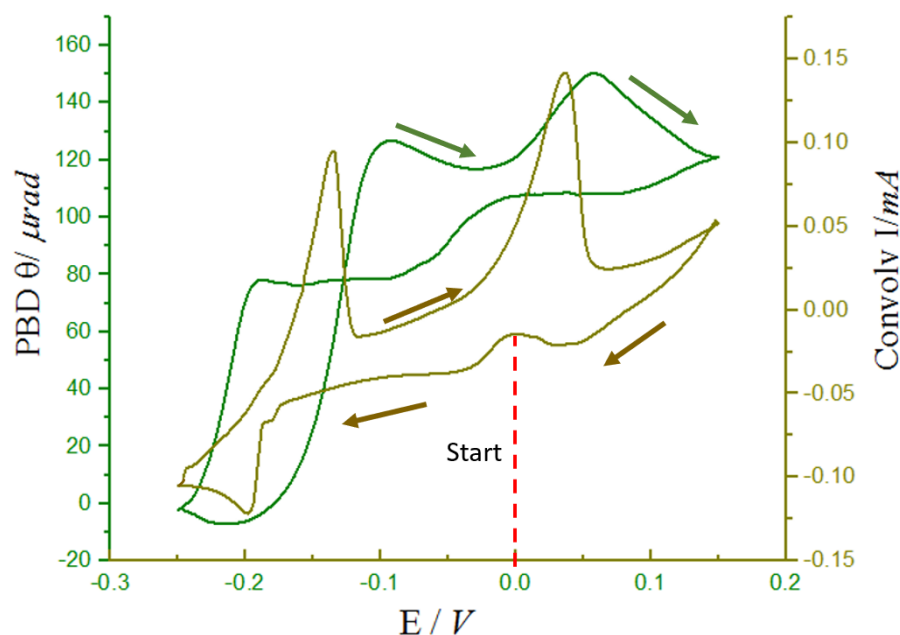
Fig. 4.24 Convolved current (yellow grey trace) with respect to the PBD signal (green trace) recorded during deposition and dissolution of elemental Bi from 0.01 M BiCl$_3$ in Ethaline 200 at scan rate (ν) = 0.0625 mV s^{-1} within the applied potential window (against Ag pseudo reference electrode)

The convolved mass deviated from optical deflection (see Fig. 4.21) in the -250 mV to -200 mV region which may be due to the complexity of bulk metal (Ag$^+$ and Bi^{3+}) deposition in this region. Analysis of the integrated form of the convolved signal is used to calculate the ratio of electron:cations in the process, which was found to be circa 1:1. Analysis of the Δm/Q gradient values and the regions given in Table 4.3 represents the regions marked in Fig. 4.25.

Table 4.3 Analysis of Q plot for deposition and dissolution of elemental AgBi (EMM - Effective Molar Mass)

Region	Potential Range / (mV)	dm/Q value calculated / (μg/mC)	EMM z=1 (gmol^{-1}) ±0.1	EMM z=2 (gmol^{-1}) ±0.1	EMM z=3 (gmol^{-1}) ±0.1	EMM z=4 (gmol^{-1}) ±0.1
(a)	-0.25 to -0.17	0.46	44.96	89.93	134.89	**179.86**
(b)	-0.17 to +0.05	2.07	**200.51**	401.01	601.52	802.02
(c)	+0.05 to +0.08	0.02	2.03	4.05	6.08	8.11
(d)	+0.08 to -0.13	0.55	53.17	106.33	**159.50**	**212.66**
(e)	-0.13 to -0.19	0.90	86.91	173.82	**260.73**	347.63
(f)	-0.19 to -0.25	0.39	38.19	76.38	114.57	**152.76**

To calculate the contribution of each metal the following method was used. In this co-deposition process of Ag/Bi the charge carriers would be Ag$^+$ and Bi^{3+}. For the simultaneous deposition we can give the redox equations:
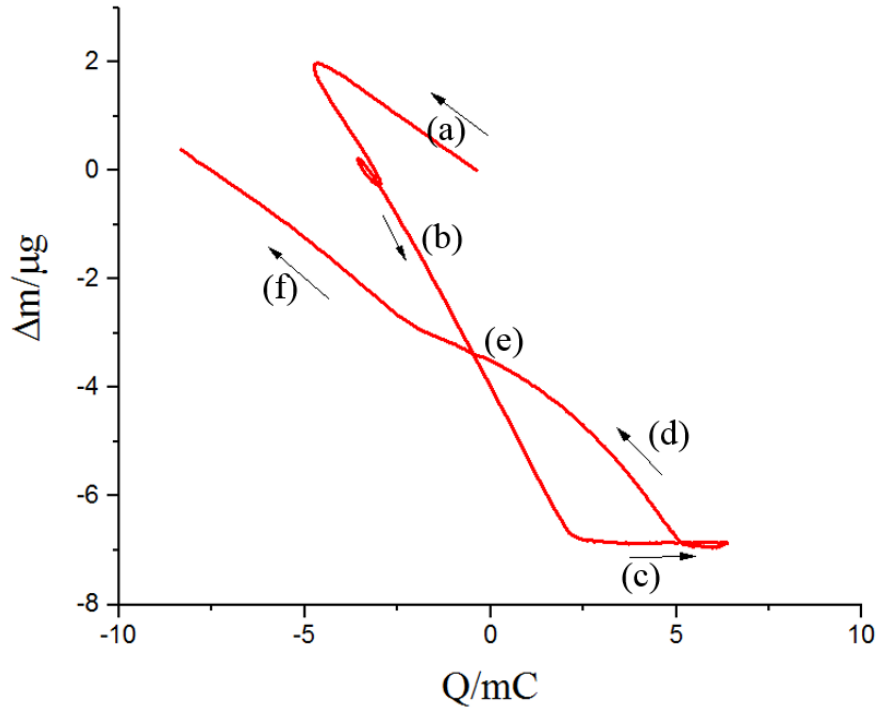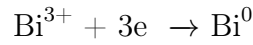
$$Ag^+ + e \rightarrow Ag^0$$
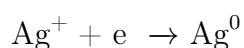
Fig. 4.25   Mass change (Δm) versus charge (Q) plot for the cyclic voltammogram (Fig. 4.23) recorded during deposition and dissolution of elemental AgBi from 0.01 M $BiCl_3$ in Ethaline 200 at a scan rate (ν) = 0.0625 mV s^{-1} within the applied potential window (against Ag pseudo reference electrode).

$$Bi^{3+} + 3e \ \rightarrow Bi^0$$

Mole fraction of Ag (χ_{Ag}) and mole fraction of Bi (χ_{Bi}) can be given by:

$$\chi_{Bi} = \frac{\frac{\Delta mF}{Q} - 107.86}{101.12 - 2F\frac{\Delta m}{Q}}$$

(4.18)

$$\chi_{Ag} = 1 - \chi_{Bi}$$
(4.19)

By substituting the value of $\frac{\Delta m}{Q}$ values for χ_{Bi}, χ_{Ag} can be found. The full method is given in Chapter 3.

χ_{Bi} and χ_{Ag} values were tabulated for each region in Fig. 4.25. Table 4.4 combines these values with potential region and $\frac{\Delta m}{Q}$.

The mole fractions calculated for Ag-Bi are all circa 1:1. The interpretation for each region can be given as follows:

- The region (a) (250 mV to -170 mV): The M_{MS} is 179.86 gmol^{-1} which is in agreement with bulk Bi deposition since 179.86 gmol^{-1} is in the acceptable range with molar mass of bismuth (208 gmol^{-1}) but the circa 28 gmol^{-1} deficit may be due to the Ag-Bi metal solution formation. Also this agrees with the integrated convolved signals for cation flux.

- The region (b) (-170 mV to -50 mV) gives M_{MS} 200.51 gmol^{-1} for mobile species mass (for

Table 4.4   Analysis of Q plot for deposition and dissolution of elemental Ag/Bi

Region	$\Delta m/Q$ value calculated	X_{Bi} calculate	X_{Ag} calculated	Ratio of Bi:Ag	Potential Range/ mV
a	0.466	0.499	0.500	1:1.00	-0.25 to -0.17
b	2.078	0.499	0.500	1:1.00	-0.17 to +0.05
c	0.021	0.485	0.514	1:1.05	+0.05 to +0.08
d	0.551	0.499	0.500	1:1.00	+0.08 to -0.13
e	0.900	0.499	0.500	1:1.00	-0.13 to -0.19
f	0.395	0.499	0.500	1:1.00	-0.19 to -0.25

z=1) which shows a large deviation from circa 107 gmol^{-1} expected for Ag deposition. This value may be explained by co-flux of other neutral species (chloro complexes are the most probable candidate). z= 2, 3 or 4 cannot be taken as probable values.

- The region (c) (+50 mV to +80 mV) shows 2.03 gmol^{-1} for z=1 and 6.08 gmol^{-1} for z=3. The expected molar mass of Bi (208 gmol^{-1}) is not compatible with the value observed.

- The region (d) (+80 mV to -130 mV) has a M_{MS} value of 159.50 gmol^{-1} for z=3 and 212.66 gmol^{-1} for z=4 indicates that both Ag and Bi maybe mobile species in this region as dissolution of deposited Ag and Bi can be assigned to these values.

- In the region (e) (-130 mV to -190 mV) has M_{MS} value of 260.73 gmol^{-1} for z=3 which suggests dissolution of Bi deposit from the electrode (Bi(0) → Bi(III)).

- The region of (f) (-190 mV to -250 mV) M_{MS} has value of 152.76 gmol^{-1} for z=4 suggests that Ag/Bi co-deposition may be taking place.
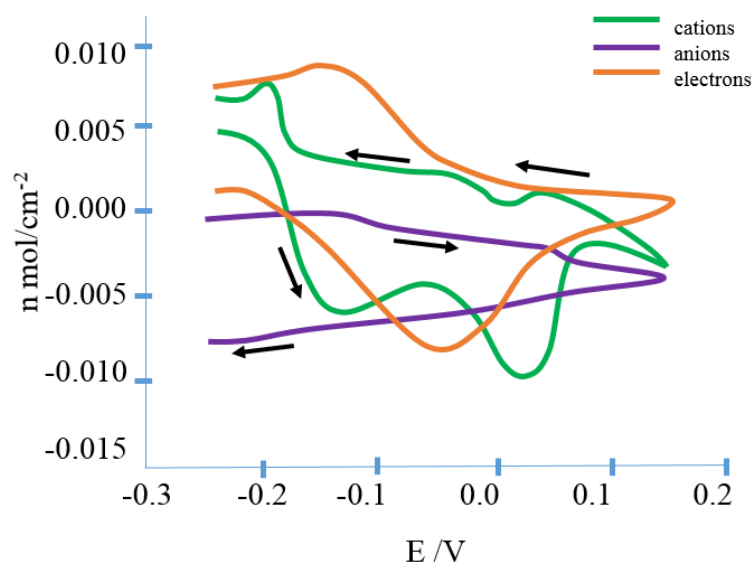
Fig. 4.26   Comparison of convolved signal integrals recorded during deposition and dissolution of elemental AgBi from 0.01 M BiCl$_3$ in Ethaline 200 at scan rate = 0.0625 mV s^{-1} within the applied potential window (against Ag pseudo reference electrode)

From the Δm vs E plot (Fig. 4.22) change in mass was used to calculate the thickness of the silver/ bismuth coating (by using density of silver and bismuth).The value derived was in

the range of 40-42 nm. A series of chronodeflectograms were used to find the beam-electrode distance for the setup used for the experiment and the diffusion coefficient (Fig. 4.27).
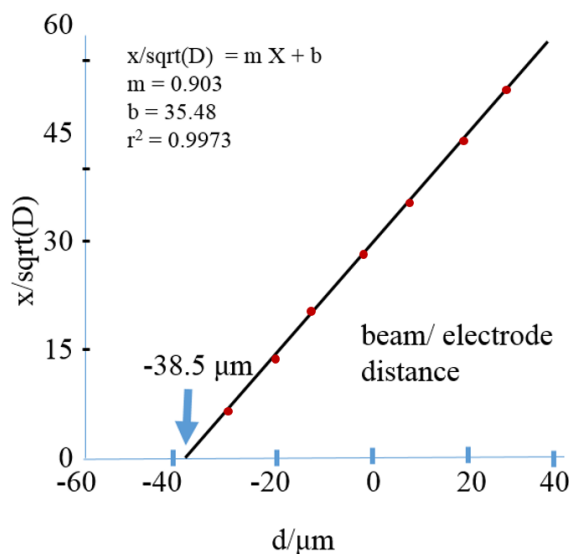

Fig. 4.27 Plot of the convolution parameter $x/\sqrt{D}$ expressed as a function of the relative beam distance

The beam-electrode distance was calculated to be 38.5 μm. Diffusion coefficient measured by optical deflection contains contributions from both metals and therefore needs to be treated as an average of individual diffusion coefficients (D_{AgCl} and D_{BiCl_3}). The diffusion coefficient value obtained (i.e. $D = 1.65 \times 10^{-7}$ cm^2 s^{-1} for each species involved) was compared to that from the Randles-Sevcik plots for individual metal ions (see Chapter 6) and was found to be similar (3.57×10^{-7} cm^2 s^{-1}).

The comparison of peak potentials observed for deposition and dissolution of silver/ bismuth system in Ethaline (Fig. 4.28) demonstrated that peaks for underpotential deposition/ dissolution that is clearly visible for Bi in DES.[61–63] UPD related peaks were less prominent for Bi deposition in aqueous systems and completely absent in organic solvents.

4.4 Summary

The main objective of this chapter was to use EQCM-PBD technique to understand the fundamentals of redox chemistry and mass transport during deposition and dissolution of silver and bismuth separately and then simultaneously in Ethaline 200 deep eutectic solvent which was successfully achieved. The main challenge of diffusional barrier effects caused by high viscosity of DES have been overcome by reducing beam-electrode distance and using slow scan rates. We were able to reduce the beam electrode distance significantly (ca. 40 μm) and find the optimum scan rate (0.0625 mV s^{-1}) to avoid diffusional delays. Optical methods are not commonly used for investigation of interfacial mass transport and redox chemistry. In this study, the novel technique of EQCM-PBD was applied successfully to study these aspects of bismuth and

Medium [contributor]	Medium composition	Deposition or Dissolution	Potential at maximum peak observed/ mV		
			Ag	Bi	Ag/Bi
Aqueous medium Alkaline thiocyanate tartarate [Valkova2002][59]	KAg(CN)$_2$, NaBiO$_3$, KSCN, KNaC$_4$H$_4$.4H$_2$O, KOH	Deposition	-750 -1150	-770 -1300	-800(Ag) [a] -900(Codep) [b]
		Dissolution	-440 +90	+530 Small feature at positive potential	+50[c] -500[d]
Aqueous medium Alkaline cyanide tartarate [Krastev2003][60]	KAg(CN)$_2$, BiNO$_4$, KNaC$_4$H$_5$O$_6$.4H$_2$O, KSCN, KCN, NaOH	Deposition	-550 -750	-820 -930	-800(Ag)[a] -600(Codep)[b]
		Dissolution	-445 +60	-550	450(Codep)[d] +200(Ag) [c]
Organic medium [Gaoren 2006][61]	Bi(NO$_3$)$_3$, AgClO$_4$, LiClO$_4$, DMSO	Deposition	-204	-413	-203 (Ag) [a] -386 (Bi on Ag)[b]
		Dissolution	+181	-19	-4 (Bi) [c] +89 (Ag-Bi alloy)[d]
Deep eutectic solvent [Present study 2018]	AgCl, BiCl$_3$, Ethaline 200 - Etgl:ChCl = 1:1	Deposition	-25	-312 -125 +62[UPD]	+40 -32 -178 -196
		Dissolution	+25	-62 +125[UPD]	-138 +35

a - Ag deposition on Pt   b - Codeposition of Bi & Ag on Ag deposit

c - Dissolution of Bi   d - Co-dissolution of Ag and Bi

Fig. 4.28 Comparison of potential at maximum peak observed for studies investigating AgBi deposition/dissolution

silver bismuth deposition in DES. The original silver deposition/ dissolution study in aqueous and ionic media was reproduced to validate the procedures and to achieve a decreased beam-electrode distance.This method was successfully applied to the metal systems: silver and bismuth and to determine the following:

1. Speciation of metal ions at the near electrode area during the deposition/ dissolution of metals are different for DES than for aqueous electrolytes. For bismuth, it was found that Bi(III) and Bi(I) to be the mobile species depending on the potential region. For silver, it was $AgCl_2^-$ and $AgCl_3^{2-}$ depending on the availability of the chloride ions. For silver/ bismuth co-deposition only, one silver speciation was seen which was predicted to be $AgCl_2^-$ and $BiCl_4^-$.

2. The deposition of Bi system included distinct underpotential and bulk deposit regions. The thickness of the UPD confirmed that it is greater than a monolayer. This dissolution of Bi gave rise to insoluble metal layers as suggested by Abbott et al.[44] Identifying underpotential deposition occurring in bismuth deposition and the potential range and localised effects of dissolution for the UPD layer.

3. The co-deposition of silver/ bismuth was studied with EQCM-PBD and the optical response was explained using Δm vs E plots and electrical parameters. Fundamental electrochemical parameters such as diffusion coefficients for species involved and mole fractions of mobile species at the electrode has been analysed. Mole ratios of involved species in silver/ bismuth deposition were calculated.

4. The calculated values of diffusion coefficients for silver and bismuth agreed with the values derived from other techniques (Cottrell study- Chapter 5, Randle-Sevcik study- Chapter 5 and Levich study- Chapter 6.

The novel technique of EQCM-PBD has been used to successfully study mass transport and redox chemistry of metal deposition dissolution in deep eutectice solvents.

References

1 M. J. Henderson, E. Bitziou, A. R. Hillman and E. Vieil, Journal of the Electrochemical Society, 2001, **148**, E105–E111.

2 A. R. Hillman, K. S. Ryder, C. J. Zaleski, V. Ferreira, C. A. Beasley and E. Vieil, Electrochimica Acta, 2014, **135**, 42–51.

3 H. M. French, M. J. Henderson, A. R. Hillman and E. Vieil, Solid State Ionics, 2002, **150**, 27–37.

4 L. Abrantes, M. Oliveira and E. Vieil, Electrochimica Acta, 1996, **41**, 1515–1524.

5 R. Eriksson, Electrochimica Acta, 1996, **41**, 871–878.

6 A. R. Hillman, K. S. Ryder, C. J. Zaleski, C. Fullarton and E. L. Smith, Zeitschrift für Physikalische Chemie, 2012, **226**, 1049–1068.

7 A. R. Hillman, K. S. Ryder, V. C. Ferreira, C. J. Zaleski and E. Vieil, Electrochimica Acta, 2013, **110**, 418–427.

8 D. Johannsmann, Physical Chemistry Chemical Physics, 2008, **10**, 4516–4534.

9 A. R. Hillman, Journal of Solid State Electrochemistry, 2011, **15**, 1647–1660.

10 C. Barbero, M. Miras, R. Kötz and O. Haas, Solid State Ionics, 1993, **60**, 167–172.

11 C. A. Barbero, Physical Chemistry Chemical Physics, 2005, **7**, 1885–1899.

12 G. G. Láng and C. A. Barbero, Laser techniques for the study of electrode processes, Springer Science & Business Media, 2012.

13 S. Servagent and E. Vieil, Journal of Electroanalytical Chemistry and Interfacial Electrochemistry, 1990, **280**, 227–232.

14 N. Lassalle, A. Roget, T. Livache, P. Mailley and E. Vieil, Talanta, 2001, **55**, 993–1004.

15 O. Schneider, A. Bund, A. Ispas, N. Borissenko, S. Zein El Abedin and F. Endres, The Journal of Physical Chemistry B, 2005, **109**, 7159–7168.

16 M. A. Mohamoud and A. R. Hillman, Journal of Solid State Electrochemistry, 2007, **11**, 1043–1050.

[17] M. Skompska and A. Tarajko-Wazny, Electrochimica Acta, 2011, **56**, 3494–3499.

[18] H. Gomez, R. Henrıquez, R. Schrebler, G. Riveros and R. Cordova, Electrochimica Acta, 2001, **46**, 821–827.

[19] Z. Jusys, H. Massong and H. Baltruschat, Journal of the Electrochemical Society, 1999, **146**, 1093–1098.

[20] P. Kern and D. Landolt, Electrochimica Acta, 2001, **47**, 589–598.

[21] A. Glidle, A. R. Hillman, K. S. Ryder, E. L. Smith, J. M. Cooper, R. Dalgliesh, R. Cubitt and T. Geue, Electrochimica Acta, 2009, **55**, 439–450.

[22] M. Hepel, S. Bruckenstein and K. Kanige, Journal of the Chemical Society, Faraday Transactions, 1993, **89**, 251–254.

[23] M. Santos, M. Cabral and S. Machado, Electrochimica Acta, 2011, **58**, 1–5.

[24] A. R. Hillman, D. C. Loveday and S. Bruckenstein, Journal of Electroanalytical Chemistry and Interfacial Electrochemistry, 1989, **274**, 157–166.

[25] A. R. Hillman, M. J. Swann and S. Bruckenstein, Journal of Electroanalytical Chemistry and Interfacial Electrochemistry, 1990, **291**, 147–162.

[26] E. Vieil, Journal of Electroanalytical Chemistry, 1994, **364**, 9–15.

[27] J. Bacskai, K. Martinusz, E. Czirok, G. Inzelt, P. Kulesza and M. Malik, Journal of Electroanalytical chemistry, 1995, **385**, 241–248.

[28] A. Bund and S. Neudeck, The Journal of Physical Chemistry B, 2004, **108**, 17845–17850.

[29] A. R. Hillman, S. J. Daisley and S. Bruckenstein, Electrochemistry Communications, 2007, **9**, 1316–1322.

[30] L. T. T. Kim, C. Gabrielli, H. Perrot, J. Garcia-Jareno and F. Vicente, Electrochimica Acta, 2012, **84**, 35–48.

[31] H. J. Salavagione, J. Arias-Pardilla, J. Pérez, J. Vázquez, E. Morallon, M. C. Miras and C. Barbero, Journal of Electroanalytical Chemistry, 2005, **576**, 139–145.

[32] L. Abrantes and J. Correia, Electrochimica Acta, 1999, **44**, 1901–1910.

[33] J. P. Correia, E. Vieil and L. M. Abrantes, Journal of Electroanalytical Chemistry, 2004, **573**, 299–306.

[34] C. J. Zaleski, Ph.D. thesis, University of Leicester, 2015.

[35] A. P. Abbott, G. Capper, D. L. Davies, R. K. Rasheed and V. Tambyrajah, Chemical Communications, 2003, 70–71.

36 J. Hartley, Ph.D. thesis, University of Leicester, 2013.

37 T. Kekesi and M. Isshiki, Journal of Applied Electrochemistry, 1997, **27**, 982–990.

38 G. Sauerbrey, Zeitschrift für physik, 1959, **155**, 206–222.

39 S. Bruckenstein, A. Fensore, Z. Li and A. R. Hillman, Journal of Electroanalytical Chemistry, 1994, **370**, 189–195.

40 M. J. Henderson, A. R. Hillman, E. Vieil and C. Lopez, Journal of Electroanalytical Chemistry, 1998, **458**, 241–248.

41 C. Barbero, M. Miras and R. Kötz, Electrochimica Acta, 1992, **37**, 429–437.

42 Q. Zhang, K. D. O. Vigier, S. Royer and F. Jérôme, Chemical Society Reviews, 2012, **41**, 7108–7146.

43 A. R. Hillman, S. J. Daisley and S. Bruckenstein, Electrochimica Acta, 2008, **53**, 3763–3771.

44 A. P. Abbott, G. Frisch, J. Hartley, W. O. Karim and K. S. Ryder, Progress in Natural Science: Materials International, 2015, **25**, 595–602.

45 J. M. Hartley, C.-M. Ip, G. C. Forrest, K. Singh, S. J. Gurman, K. S. Ryder, A. P. Abbott and G. Frisch, Inorganic chemistry, 2014, **53**, 6280–6288.

46 A. P. Abbott, G. Capper, K. J. McKenzie and K. S. Ryder, Journal of Electroanalytical Chemistry, 2007, **599**, 288–294.

47 A. P. Abbott, K. El Ttaib, G. Frisch, K. S. Ryder and D. Weston, Physical Chemistry Chemical Physics, 2012, **14**, 2443–2449.

48 C. H. Chen and A. A. Gewirth, Journal of the American Chemical Society, 1992, **114**, 5439–5440.

49 B. K. Niece and A. A. Gewirth, Langmuir, 1996, **12**, 4909–4913.

50 C. H. Chen, K. D. Kepler, A. A. Gewirth, B. Ocko and J. Wang, The Journal of Physical Chemistry, 1993, **97**, 7290–7294.

51 C. A. Jeffrey, D. A. Harrington and S. Morin, Surface Science, 2002, **512**, L367–L372.

52 K. Tamura, J. Wang, R. Adžic and B. Ocko, The Journal of Physical Chemistry B, 2004, **108**, 1992–1998.

53 L. Heerman and W. D'Olieslager, Journal of The Electrochemical Society, 1991, **138**, 1372–1376.

54 G.-B. Pan and W. Freyland, Electrochimica Acta, 2007, **52**, 7254–7261.

55 G. R. Stafford and U. Bertocci, The Journal of Physical Chemistry B, 2006, **110**, 15493–15498.

56 Y.-C. Fu, Y.-Z. Su, H.-M. Zhang, J.-W. Yan, Z.-X. Xie and B.-W. Mao, Electrochimica Acta, 2010, **55**, 8105–8110.

57 M. Hepel, K. Kanige and S. Bruckenstein, Journal of electroanalytical chemistry and interfacial electrochemistry, 1989, **266**, 409–421.

58 I. Krastev, T. Valkova and A. Zielonka, Journal of Applied Electrochemistry, 2004, **34**, 79–85.

59 S. M. Skogvold, Ø. Mikkelsen and K. H. Schrøder, Electroanalysis: An International Journal Devoted to Fundamental and Practical Aspects of Electroanalysis, 2005, **17**, 1938–1944.

60 Ø. Mikkelsen and K. H. Schrøder, Analyst, 2000, **125**, 2163–2165.

61 T. Valkova and I. Krastev, Transactions of the IMF, 2002, **80**, 13–15.

62 I. Krastev, T. Valkova and A. Zielonka, Journal of Applied Electrochemistry, 2003, **33**, 1199–1204.

63 G. Li, L. Kay, G. Liu, P. Liu and Y. Tong, Electrochemical and solid-state letters, 2006, **9**, C32–C35.

Chapter 5

Electrochemical study of silver, bismuth and silver-bismuth codeposition

Contents

5.1 Introduction

This chapter focuses on the fundamental aspects of electrodeposition of silver, bismuth and co-deposition of silver/ bismuth with particular reference to nucleation and growth under room temperature (20 °C) conditions in the choline chloride based ionic liquid Ethaline 200 (1:2 ChCl:EG). Preparation methods are given in Chapter 3. The investigation was carried out by using electrochemical methods (i.e. cyclic voltammetry, chronoamperometry) and acoustic impedance spectroscopy.

5.2 Cyclic voltammetry

Cyclic voltammetry (CV) was used to define the redox properties of silver and bismuth and co-deposition of silver/ bismuth processes. Fig. 5.1 shows the cyclic voltammograms of pure silver, pure bismuth and co-deposition of silver/ bismuth onto a platinum disk electrode from Ethaline 200. Electrode preparation methods and solution preparation methods were discussed in Chapter 2 and 3 respectively. The voltage scan was driven from 0 $\rightarrow$ –0.75 mV $\rightarrow$ 0.75 mV $\rightarrow$ 0 mV in a cyclic manner. During these experiments 25 mmoldm^{-3} silver chloride, 25 mmoldm^{-3} bismuth chloride were used for silver and bismuth deposition whereas 1:1 ratio of bismuth chloride and silver chloride (i.e. 25 mmoldm^{-3} silver chloride, 25 mmoldm^{-3} bismuth chloride) were used for co-deposition. The three electrode system, Pt disk (diameter = 2 mm) working electrode, IrO$_2$ coated Ti mesh counter electrode and silver pseudo reference electrode. was used and the voltammograms curves obtained are given in Fig. 5.1.

Fig. 5.1 shows a single broad wave for reduction of Ag (I) to Ag (0) peak at (a: –0.068 ±0.001 V) and sharper almost symmetrical wave for oxidation of Ag (0) to Ag (I) at (b:0.085 ±0.001 V). The cyclic voltammogram of bismuth (Fig. 5.1) indicates a broad peak for Bi(III) to Bi(0) at (e: –0.220 ±0.001 V) and a sharper symmetrical wave (f: 0.023 ±0.001 V) followed by two other broad peaks (g and h) for Bi (0) to Bi (III). The AgCl−BiCl$_3$ cyclic voltammogram in Fig. 5.1 shows two broad reduction peaks for (j: -0.074 V), (i: –0.268 ±0.001 V) and a broad peak for combined oxidation at (k: 0.103 ±0.001 V) in Ethaline 200.

A series of cyclic voltammograms at different scan rates ranging from 5 mV s^{-1} to 100 mV s^{-1} for 100 mmoldm^{-3} silver chloride, 25 mmoldm^{-3} bismuth chloride, silver chloride:bismuth chloride (ration of 25 mmoldm^{-3}:25 mmoldm^{-3}) concentrated solutions in Ethaline 200 were obtained. The observed curves are shown in Fig. 5.2 to Fig. 5.4. When the scan rate is fast the diffusion layer thickness will decrease, increasing the supply of reactant and hence the current.[1]
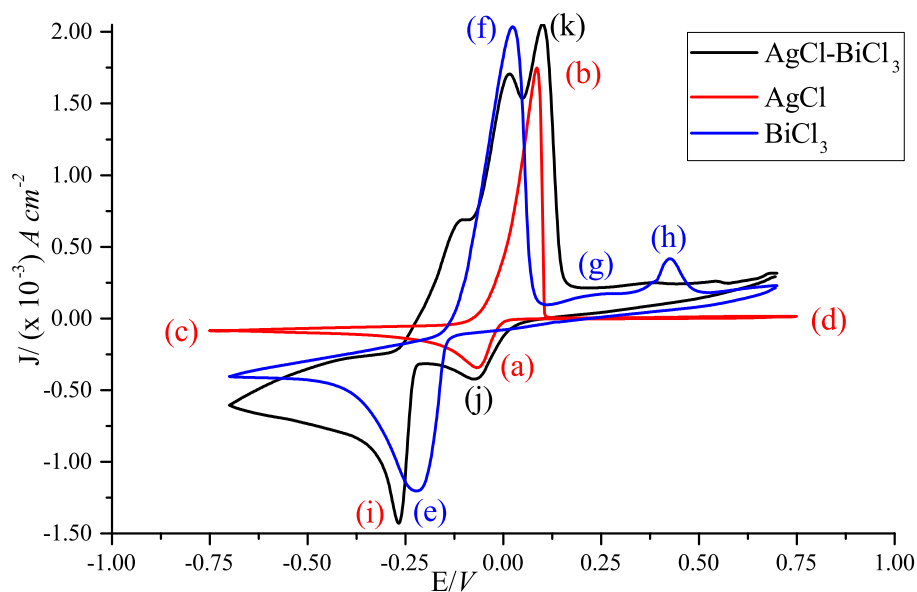
Fig. 5.1 Cyclic voltammogram of 25 mmoldm^{-3} AgCl, 25 mmoldm^{-3} BiCl$_3$ and 25:25 mmoldm^{-3} BiCl$_3$:AgCl in Ethaline 200 obtained at 10 mV s^{-1} scan rate at 20 °C using 2 mm Pt disc working electrode (WE), IrO$_2$ coated Ti mesh counter electrode (CE) and Ag pseudo reference electrode (RE) were used. The important features marked (a) to (k) are discussed in text.

Fig. 5.2 Current density vs potential for 25 mmoldm^{-3} AgCl in Ethaline 200 at different scan rates at 20 °C using 2 mm Pt disc working electrode (WE), IrO$_2$ coated Ti mesh counter electrode (CE) and Ag pseudo reference electrode (RE) as the three electrode system.
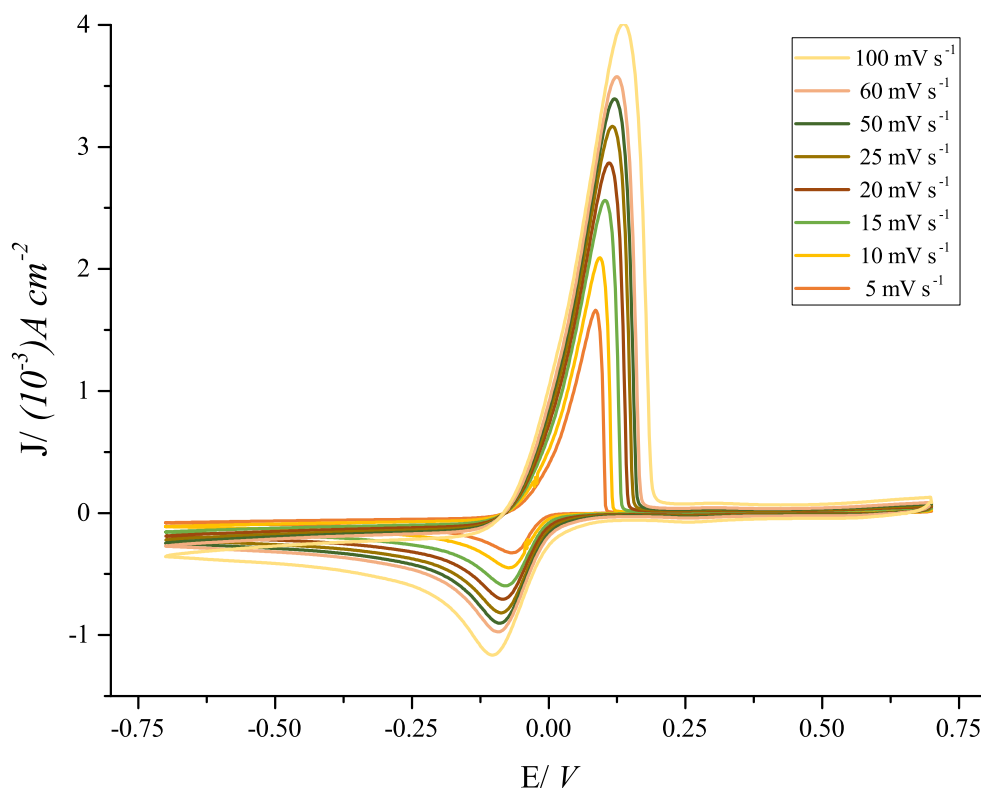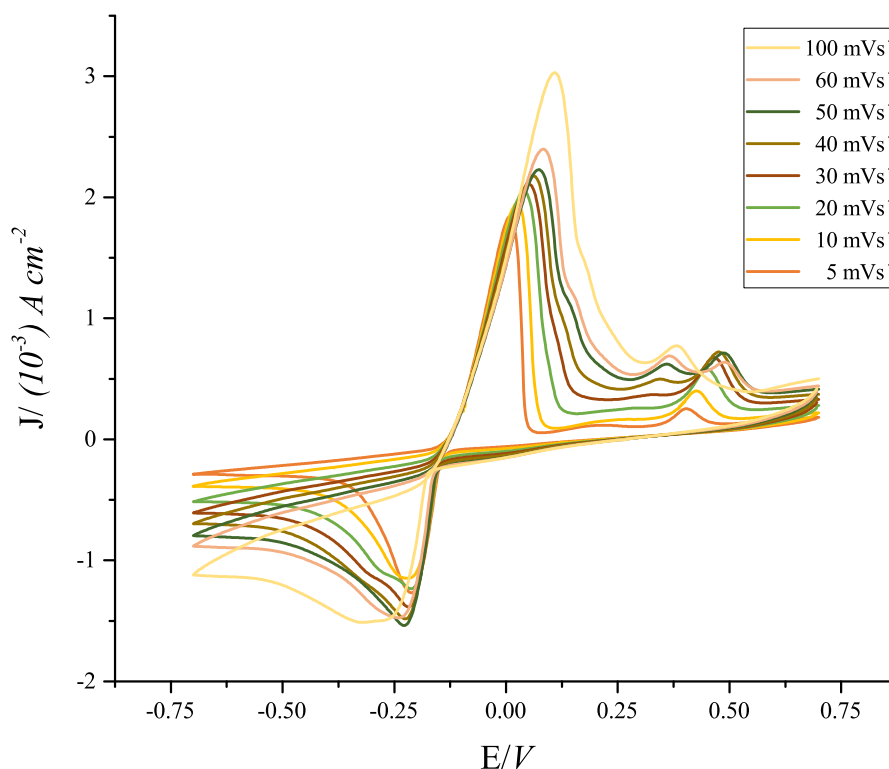
Fig. 5.3 Current density vs potential for 25 mmoldm^{-3} BiCl$_3$ in Ethaline 200 at different scan rates at 20 °C using 2 mm Pt disc working electrode (WE), IrO$_2$ coated Ti mesh counter electrode (CE) and Ag pseudo reference electrode (RE) as the three electrode system.

Fig. 5.4 Current density vs potential for 20 mmoldm^{-3}: 20 mmoldm^{-3} AgCl:BiCl$_3$ respectively in Ethaline 200 at different scan rates at 20 °C. 2 mm Pt disc working electrode (WE), IrO$_2$ coated Ti mesh counter electrode (CE) and Ag pseudo reference electrode (RE) as the three electrode system.
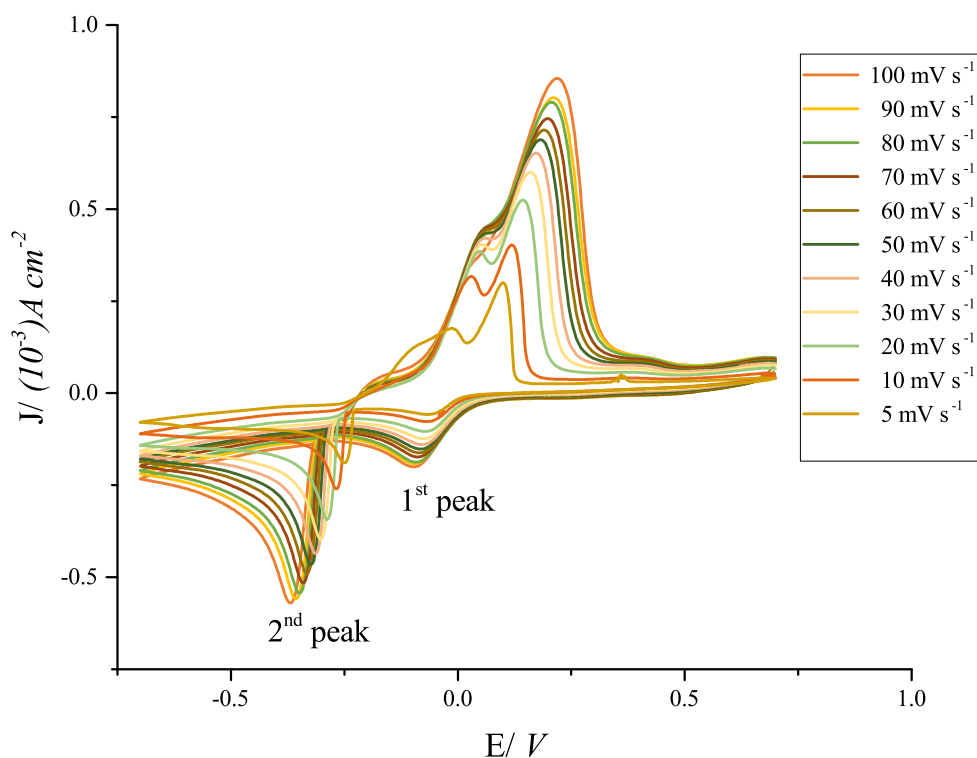
The current decreases as the scan rate is decreased in the series of cyclic voltammograms for silver chloride (Fig. 5.2), due to the diffusion layer growing further from the electrode and decreasing the flux of ions coming towards the electrode. Since the electrolytic current is small, the effect of ohmic drop on the peak potential is assumed to be negligible. The cathodic peak potential has shifted to more negative values with increasing scan rate. This suggests that reduction of Ag(I) and oxidation of Ag(0) is electrochemically quasi-reversible (i.e. electron transfer is slow compared to the voltage scan rate, causing the peak to shift unlike in rapid electron transfer reactions). Peak separation (ΔE_p) was in the range of ca. 0.24 - 0.55 V.

The series of cyclic voltammograms for the bismuth chloride system (Fig. 5.3) exhibits almost the same peak potential (ca. -0.23 V ± 0.02 V) for cathodic deposition at all scan rates. This indicates that even when the scan rate is increased (i.e. available time scale for electron transfer is shorter), the equilibrium can keep up and deliver the current at the same potential i.e. reduction Bi(III) $\longrightarrow$ Bi(0) is almost reversible. The current decreased after the peak because of the increasing thickness of the diffusion layer which causes the arrival of reactants at the electrode to become slow. The deposition peak current increased with increasing scan rate due to the thinner diffusion layer which increases the concentration gradient and hence the current (according to Fick's law). The anodic peaks demonstrate a similar trend. Anodic peak position shifted to more positive values with increasing scan rate due to sluggish charge transfer and a peak separation of ca. 0.22 - 0.43 V is observed. At higher scan rates three peaks were observed.

According to Figure 5.3 and 5.4, when bismuth metal is involved in the metal system, a complex set of anodic stripping peaks are seen. This can be explained using pseudo passivation of electrode surface and saturated layer effects[2] which have been studied by Abbott et al. Metal dissolution depends on metal speciation which is different in ionic media compared to aqueous media. It also depends on mass transport and solubility. In metal dissolution, the metal is oxidised, interacts with one or more types of ligands to form a metal ion complex. The solubility of the complex depends upon the solvation and overall charge. In an ionic liquid, the anion of the ionic liquid will be the dominant ligand. In this case, chloride ion is a strongly coordinating ligand and the rate of anodic processes depend on the activity of the ligand and the viscosity of the ionic liquid. The chloride salts of metals generally have a high solubility in Ethaline. According to Abbott et al., there is an additional layer of complexity, introduced by the structure of the double layer and the availability of chloride ions to complex with metals. In ethaline, chloride anions interact with ethyline glycol and reduce the availability of chloride ions to form complexes with the metal cation. From the probe beam studies (see chapter 4), it was proven that bismuth dissolution involves multiple oxidation states of bismuth. We can assume (since there are no studies done in to the specific dissolution rates for bismuth) that the solubility of Bi(I) and Bi(III) complexes to be different. Also, from investigations carried out by Abbott et al., it is evident that, even for generally soluble halide complexes, the insoluble film formation can block the electrode surface, leading to a decrease in the anodic current (pseudo passivation). This affects the even dissolution of the metal and is prevalent in

unstirred solutions.

In the series of cyclic voltammograms for AgCl/BiCl$_3$ (Fig. 5.4), all anodic and cathodic peaks have shifted to more positive and more negative values respectively, indicating that rates of co-deposition/ dissolution of silver and bismuth are limited by rate of charge transfer. The range for first peak separation and second peak separation was seen to be ca. 0.03 - 0.009 V and ca. 0.49 V. This indicates that the first peak of deposition (which we can reasonably assume to be silver) has moved to a more positive potential value compared to the pure silver deposition system. The second peak potential for bismuth deposition has moved to a more negative potential value compared to the pure bismuth case. The number of anodic peaks for dissolution of silver and bismuth co-deposits have decreased with increasing scan rates. The multiple peaks observed at lower scan rates have been replaced by a broader larger peak (merged peak) at high scan rates.

5.2.1   Silver redox system

For electrochemically reversible electron transfer processes the peak current (i_p) variation with scan rate (ν) for a freely diffusing redox species is given by Randles-Sevcik equation,

$$i_p = 0.446 \, n \, F \, A \, C^\circ \left(\frac{n \, F \, D}{RT} \right)^{1/2} \nu^{1/2} \qquad (5.1)$$

where F - Faraday constant (96490 C mol^{-1})
$\quad\quad\;\; A$ - electrode surface area (0.22 cm^{-2})
$\quad\quad\;\; D$ - diffusion coefficient
$\quad\quad\;\; R$ - gas constant (8.314 J K^{-1} mol^{-1})
$\quad\quad\;\; T$ - temperature (293 K)
$\quad\quad\;\; n$ - number of electrons
$\quad\quad\;\; C^\circ$ - bulk concentration of analyte (mol cm^{-3})

According to the above equation i_p shows a linear relationship to $\nu^{1/2}$ if the reaction has fast kinetics. Fig. 5.5 shows that cathodic peak potentials shifted to more negative values with increasing scan rate and suggests that the deposition process is limited by the charge transfer rate. Therefore reduction of Ag(I) $\rightarrow$ Ag(0) and oxidation of Ag(0) $\rightarrow$ Ag(I) are electrochemically quasi-reversible.
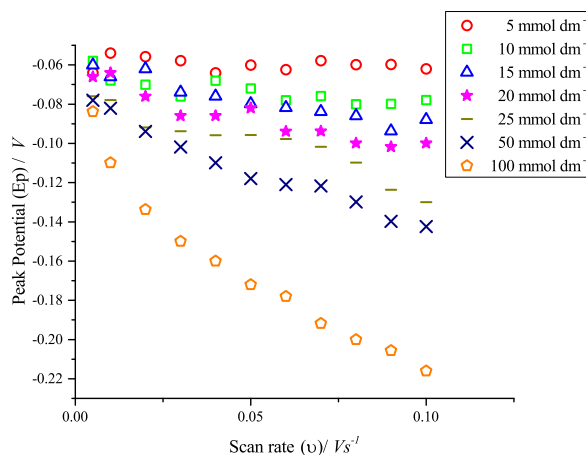
Fig. 5.5 Correlation of peak potential with scan rate for different concentrations of AgCl in Ethaline 200 at 20 °C using 2 mm Pt disc working electrode (WE), IrO$_2$ coated Ti mesh counter electrode (CE) and Ag pseudo reference electrode (RE)

Fig. 5.6 Correlation of peak separation for reduction with the scan rate (Left panel)and and peak broadening with scan rate (Right panel) for different concentrations (5 mmoldm^{-3} to 100 mmoldm^{-3}) of AgCl in Ethaline 200 at 20 °C using 2 mm Pt disc working electrode (WE), IrO$_2$ coated Ti mesh counter electrode (CE) and Ag pseudo reference electrode (RE)
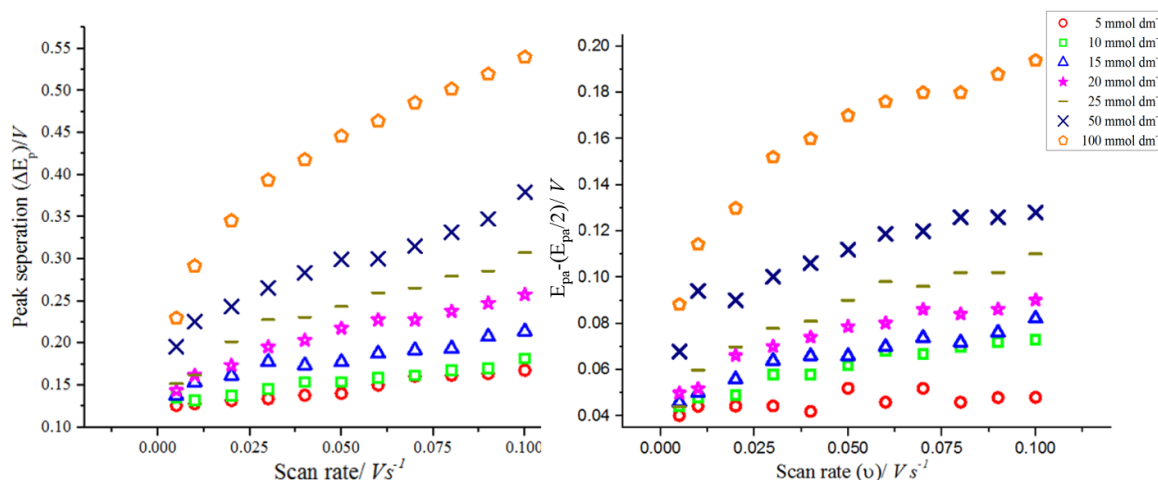
The peak separation for oxidation and reduction (Fig. 5.6 left panel), the peak potential - half peak potential separation $\left[E_p^{Ox} - E_{p/2}^{Ox} \right]$, increases with scan rate (Fig. 5.6 right panel). Even at the lowest scan rate, $[E_p^{Ox} - E_p^{Red}]$ is larger than 0.059 V, the expected potential separation for reversible one electron electrode process. All these observations suggest that there is some kinetic limitation of the phase formation or quasi-reversibility of the Ag(I) $\rightarrow$ Ag(0) charge transfer. Fig. 5.7 shows that cathodic and anodic peak currents are proportional to the square root of the scan rate. Since the reactant is already on the surface of the electrode, diffusion should not have a effect on the current. Therefore, this was an unexpected observation.

Using Randles-Sevcik equation (Eqn. 5.1) the diffusion coefficient of silver ($D_{Ag(I)}$) was calculated by using cyclic voltammograms for different concentrations and the data of Fig. 5.7.

$$i_p = 0.446 \, n \, F \, A \, C \left(\frac{nFD_0}{RT} \right)^{1/2} \nu^{1/2} \tag{5.2}$$
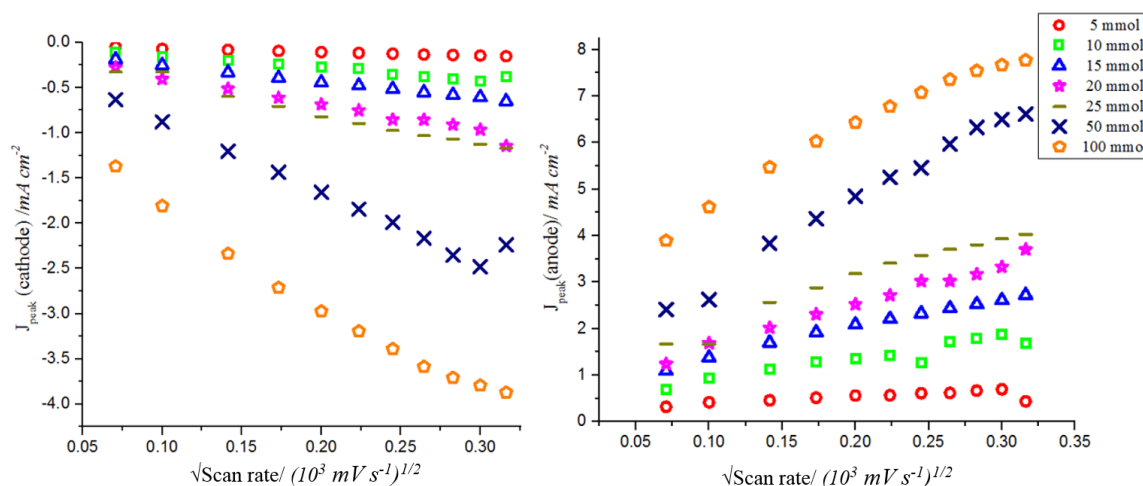
Fig. 5.7   Correlation of peak current density of cathode (left panel) and anode (right panel) with the square root of scan rate for different concentrations (5 mmoldm^{-3} to 100 mmoldm^{-3}) of AgCl in Ethaline 200 at 20 °C using 2 mm Pt disc working electrode (WE), IrO$_2$ coated Ti mesh counter electrode (CE) and Ag pseudo reference electrode (RE)

where $F =$ Faraday constant (96490 C mol^{-1})
$\quad\quad\quad A = 0.22$ cm^2
$\quad\quad\quad C = (5, 10, 15, 20, 25, 50, 100) \times 10^{-6}$ mol cm^{-3}
$\quad\quad\quad R = 8.314$ J K^{-1} mol^{-1}
$\quad\quad\quad T = 293$ K

The slope was found to be $0.617286 \times C° \times D^{1/2}$. From substituting for the concentrations, D values were found and tabulated in Table 5.1 at T= 20°C.

Table 5.1   Diffusion coefficient in different concentrations of AgCl$_2^-$ in Ethaline 200 calculated for reduction process

Concentration of AgCl/ Ethaline 200 (x 10^{-6} mol cm^{-3})	R^2 of the trend line	Diffusion Coefficient (D) calculated (cm^2 s^{-1})
5	0.99	(7.65 ±0.01) ×10^{-8}
10	0.95	(1.90 ±0.01) ×10^{-7}
15	0.99	(1.70 ±0.01) ×10^{-7}
20	0.97	(2.82 ±0.01) ×10^{-7}
25	0.98	(2.45 ±0.01) ×10^{-7}
50	0.97	(2.55 ±0.01) ×10^{-7}
100	0.98	(1.99 ±0.01) ×10^{-7}

The average D was found to be (2.02 ±0.01) ×10$^{-7} cm^2 s^{-1}$

5.2.2   Bismuth redox system

Analysis of the cyclic voltammogram for bismuth chloride was used to correlate cathodic peak potential vs square root of scan rate (Fig. 5.8 left panel), peak separation vs scan rate (Fig. 5.8 right panel), peak broadening vs scan rate (Fig. 5.9 left panel), peak current density vs scan

rate (Fig. 5.9 right panel) for 5, 10, 15, 20 and 25 mmoldm^{-3} concentrated bismuth chloride in Ethaline solutions. Relevant procedures for solution preparation are given in Chapter 3.

Fig. 5.8 shows the peak potential shifting to more negative values with increasing scan rates suggesting sluggish kinetics. Although this was previously seen for silver deposition, here the variation is very small suggesting faster electron transfer compared to the silver systems. Similar to the silver system, the peak separation and the $E_p^{Ox} - E_{p/2}^{Ox}$ increased with scan rate. However, $E_p^{Ox} - E_p^{Red}$ value exceeded 0.019 V expected for reversible three electron process suggesting quasi-reversibility of electron transfer for bismuth deposition or limitations in phase formation.
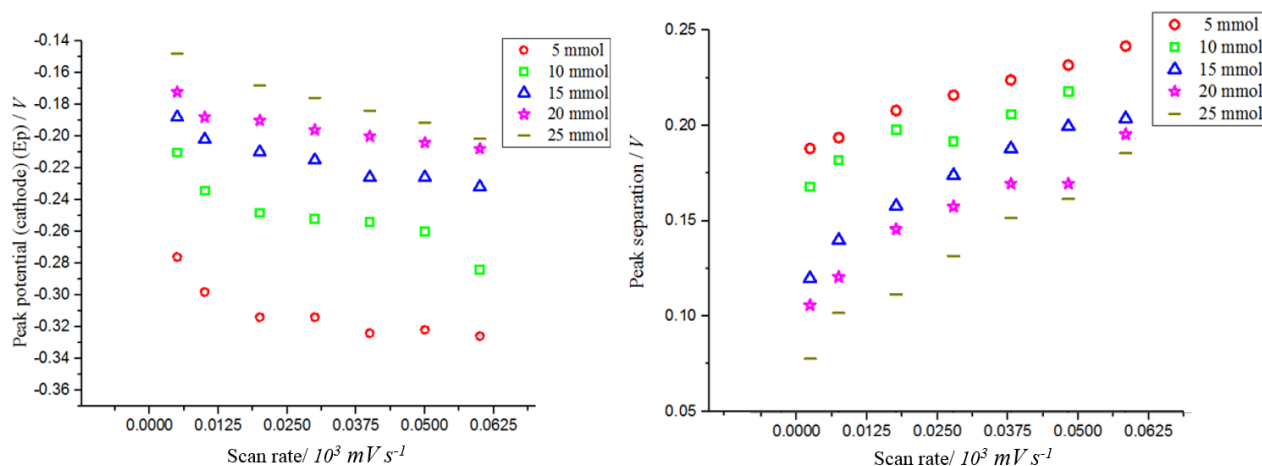

Fig. 5.8 Correlation of reduction peak potential with the scan rate (left panel) and peak separation with scan rate (right panel) for different concentrations (5, 10, 15, 20, 25 mmoldm^{-3}) of BiCl$_3$ in Ethaline 200 at 20 °C using 2 mm Pt disc working electrode (WE), IrO$_2$ coated Ti mesh counter electrode (CE) and Ag pseudo reference electrode (RE)

The cathodic peak current density versus square root of scan rate (Fig. 5.9 right panel) was used to calculate diffusion coefficient for bismuth (Table 5.2) and the trend indicated that growth is diffusion controlled.
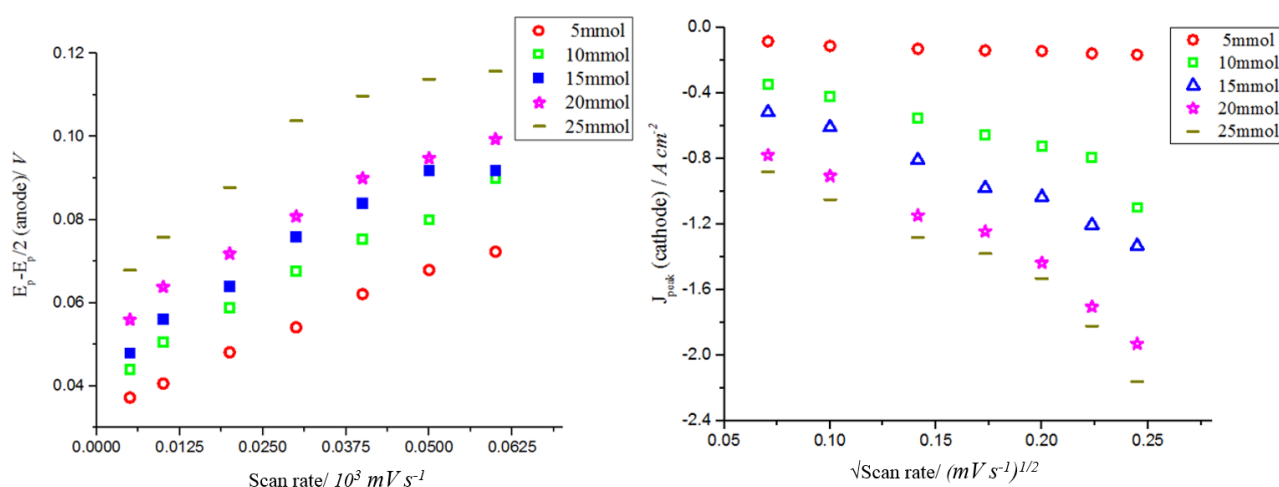

Fig. 5.9 Peak broadening with the scan rate (left panel) and current density with scan rate (right panel) for different concentrations (5, 10, 15, 20, 25 mmoldm^{-3}) of BiCl$_3$ in Ethaline 200 at 20 °C using 2 mm Pt disc working electrode (WE), IrO$_2$ coated Ti mesh counter electrode (CE) and Ag pseudo reference electrode (RE)

Using Randles-Sevcik equation (Eqn. 5.1) the diffusion coefficient of bismuth was calculated using cyclic voltammograms for different concentrations and the data of the plot shown in the right panel of Fig. 5.9.

$$i_p = 0.446 \, n \, F \, A \, C^{\circ} \left(\frac{nFD_0}{RT} \right)^{1/2} \nu^{1/2} \tag{5.3}$$

For the graph of i_p/A vs $\nu^{1/2}(\text{Vs}^{-1})^{1/2}$ when $n = 3$,

F = Faraday constant (96490 C mol^{-1})
$A = 0.22$ cm^{-2}
C°=(5, 10, 15, 20, 25) x 10^{-6} mol cm^{-3}
$R = 8.314$ J K^{-1} mol^{-1}
T=293 K

slope $= 0.32074 \times C^{\circ} \times D^{1/2}$

From substituting for the concentrations, D values were found and tabulated in Table 5.2. The average D value was found to be 1.65 ±0.05 x 10^{-7} cm^2 s^{-1}.

Table 5.2 Diffusion coefficient in different concentrations of BiCl$_4^-$ in Ethaline 200 for reduction data

Concentration of Bi(III)/ Ethaline 200 (x 10^{-6} mol cm^{-3})	R^2 of the trend line	Diffusion Coefficient (D) calculated (cm^2 s^{-1})
5	0.862	(2.77 ±0.01) x 10^{-5}
10	0.963	(5.35 ±0.05) x 10^{-7}
15	0.918	(1.45 ±0.06) x 10^{-7}
20	0.580	(4.83 ±0.04) x 10^{-7}
25	0.998	(1.46 ±0.04) x 10^{-7}

5.2.3 Silver/bismuth redox system

Cyclic voltammograms (Fig. 5.4) for 1:1 mixture of bismuth chloride and silver chloride were used to correlate cathodic peak potential with scan rate (Fig. 5.10), peak separation with scan rate (Fig. 5.11) and peak current density with square root of scan rate (Fig. 5.12). Concentration ratios 5:5, 10:10, 15:15, 20:20, 25:25 (all mmoldm^{-3}) for bismuth chloride: silver chloride in Ethaline solutions at 20 °C were used. Relevant procedures for solution preparation are given in Chapter 3.

Peak potentials shift to more negative values with increasing scan rates for both cathodic peaks (peak 1 and peak 2). This shift is more prominent in peak 2 (ca. 0.15 V change is seen). The peak separation between cathodic peak 1 and main anodic peak, the peak separation between cathodic peak 2 and main anodic peak, increased with increasing scan rate. These observations indicate the co-deposition of silver/bismuth having slow kinetics. Furthermore, the significant shift in cathodic peak 2 can be attributed to change in substrate (silver) compared to that for peak 1 (platinum). The peak current density shows a linear relationship with square root of scan rate indicating the process is diffusion controlled. For peak 1 the substrate was a polished
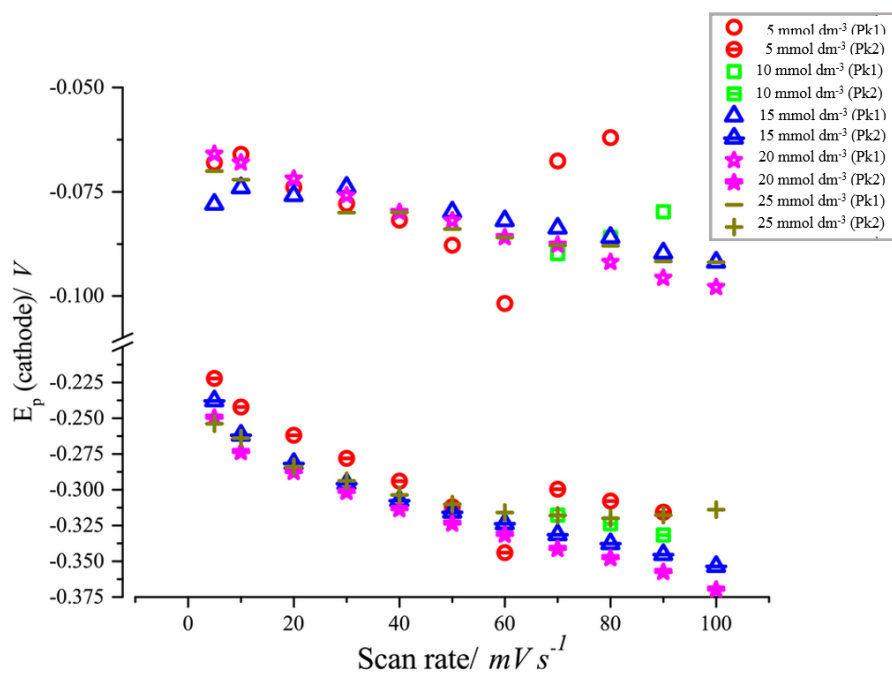
Fig. 5.10 Correlation of reduction peak potential with the scan rate for different concentrations of silver/ bismuth in Ethaline 200. Pk 1 corresponds to peak 1 of Fig. 5.4 whereas Pk 2 corresponds to peak 2 of Fig. 5.4
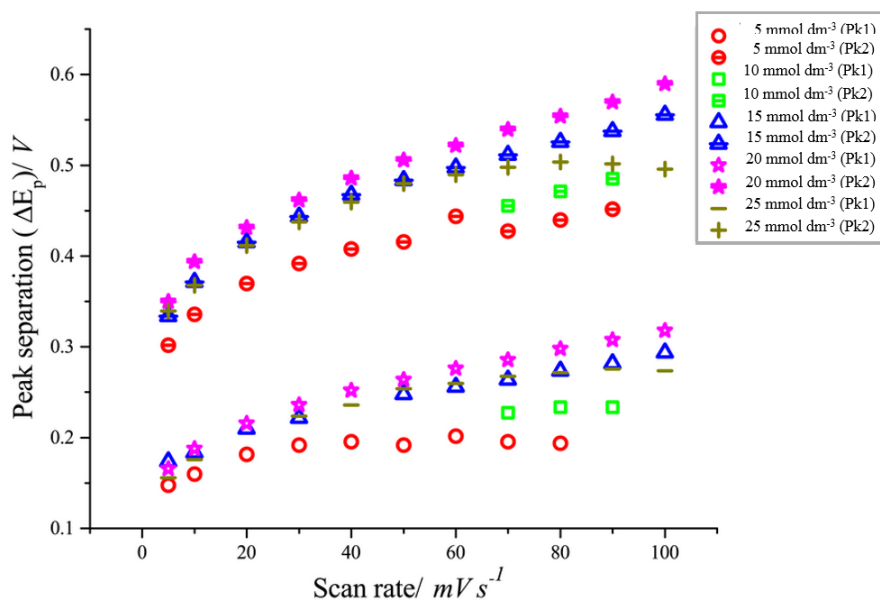

Fig. 5.11 Correlation of reduction peak separation with the scan rate for different concentrations of AgCl/BiCl$_3$ in Ethaline 200. Pk 1 corresponds to peak 1 of Fig. 5.4 whereas Pk 2 corresponds to peak 2 of Fig. 5.4

Fig. 5.12 Correlation of reduction peak current density of the cathode with the square root of scan rate for different concentrations of AgCl/BiCl$_3$ in Ethaline 200. Pk 1 corresponds to peak 1 of Fig. 5.4 whereas Pk 2 corresponds to peak 2 of Fig. 5.4
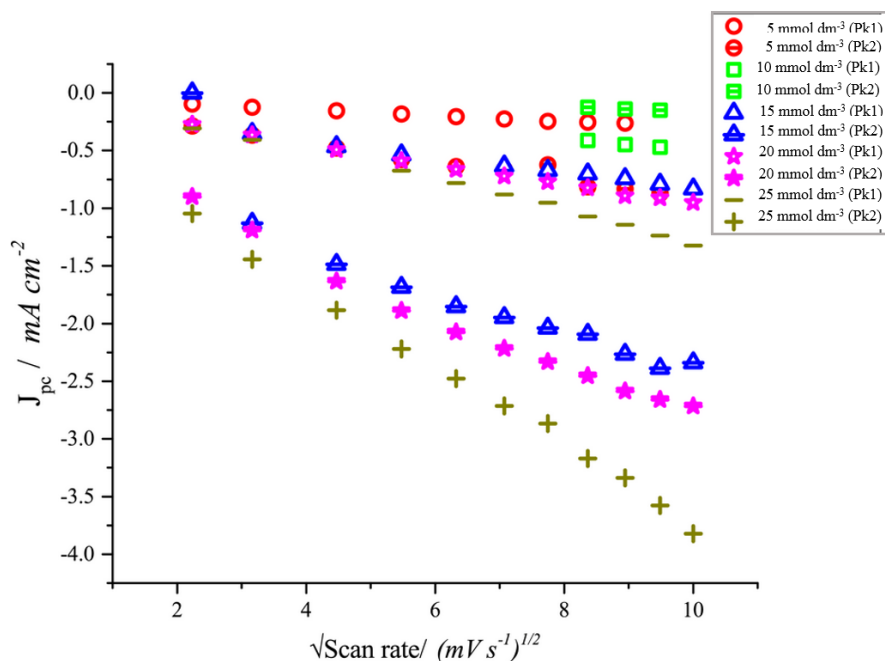
platinum surface while for the peak 2 the platinum surface may have a porous (proven by AFM: see Chapter 6) silver layer making the substrate silver instead of platinum.

Using Randles-Sevcik equation (Eqn. 5.1) the diffusion coefficients of AgCl$_2^-$ and BiCl$_4^-$ were calculated using cyclic voltammograms for different concentrations and the data of Fig. 5.12.

$$i_p = 0.446 \, n \, F \, A \, C \left(\frac{nFD_0}{RT} \right)^{1/2} \nu^{1/2} \tag{5.4}$$

For the graph of i_p/A vs $\nu^{1/2}$(V s^{-1})$^{1/2}$ when $n = 1$ for AgCl$_2^-$ and $n = 3$ for BiCl$_4^-$,

F = Faraday constant (96490 C mol^{-1})
A = 0.22 cm^2
C=(5:5, 10:10, 15:15, 20:20, 25:25) x 10^{-6} mol cm^{-3}
R = 8.314 J K^{-1} mol^{-1}
T=293 K

By substituting values to the equation corresponding to AgCl$_2^-$ and BiCl$_4^-$ obtained from the two cathodic peaks in the cyclic voltammograms, the D values for the two cases were determined. These D values are tabulated in Table 5.3. The average D value was found to be 3.09 ±0.08 x 10^{-7} cm^2 s^{-1} for AgCl$_2^-$ and 2.10 ±0.07 x 10^{-7} cm^2 s^{-1} BiCl$_4^-$.

Table 5.3 Diffusion coefficient in different concentrations of $AgCl_2^-$ and $BiCl_4^-$ in Ethaline 200 for reduction data

Concentration of $AgCl_2^-:BiCl_4^-$ in Ethaline 200 ($\times 10^{-6}$ mol cm^{-3})	Diffusion Coefficient (D_{Ag}) calculated (cm^2 s^{-1})	Diffusion Coefficient (D_{Bi}) calculated (cm^2 s^{-1})
5:5	$(9.57 \pm 0.06) \times 10^{-7}$ (R^2=0.36)	$(4.13 \pm 0.07) \times 10^{-7}$ (R^2=0.95)
10:10	$(1.83 \pm 0.05) \times 10^{-7}$ (R^2=0.97)	$(3.03 \pm 0.02) \times 10^{-7}$ (R^2=0.98)
15:15	$(1.97 \pm 0.08) \times 10^{-7}$ (R^2=0.12)	$(3.34 \pm 0.02) \times 10^{-7}$ (R^2=0.83)
20:20	$(1.30 \pm 0.08) \times 10^{-7}$ (R^2=0.99)	$(4.64 \pm 0.02) \times 10^{-7}$ (R^2=0.97)
25:25	$(8.14 \pm 0.08) \times 10^{-8}$ (R^2=0.17)	$(1.10 \pm 0.03) \times 10^{-7}$ (R^2=0.99)
[Average]	$(3.09 \pm 0.08) \times 10^{-7}$	$(2.10 \pm 0.07) \times 10^{-6}$

5.3 Effect of concentration

5.3.1 Silver redox system

The effect of change in concentration was studied for AgCl in Ethaline 200 using cyclic voltammograms. The concentration of AgCl was varied in the range 5 - 100 mmoldm^{-3} to compare the results at a range of scan rates at 20 °C. The current and peak voltage were found to vary with the concentration of Ag(I) in the electrolyte solution.

The position of the cathodic peak was shifted to more negative potential values with increasing concentration (Fig. 5.13). At high concentrations the voltammetric peaks broaden.
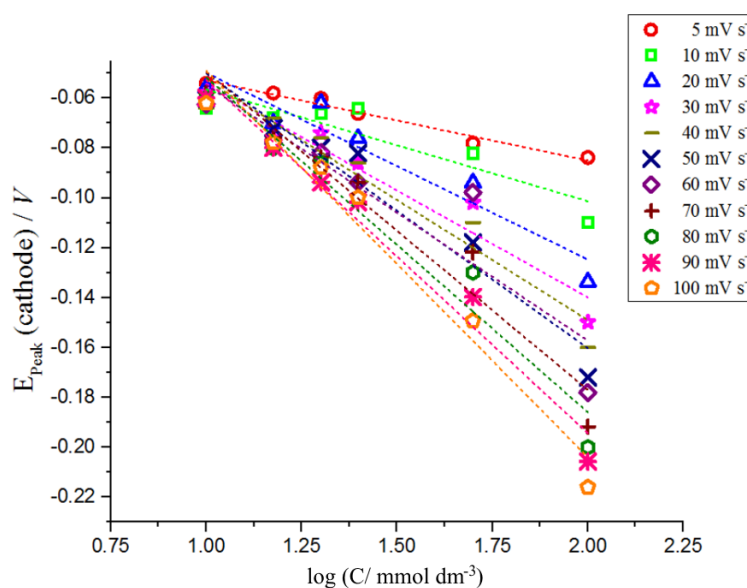

Fig. 5.13 Cathodic peak potential vs log of concentration of AgCl in Ethaline 200 at various scan rates at 20 °C using 2 mm Pt disc working electrode (WE), IrO$_2$ coated Ti mesh counter electrode (CE) and Ag pseudo reference electrode (RE)

The linear relationship between logarithm of current density ($\log J_P$) and $\log C$ indicates that the reduction process is diffusion controlled (Fig. 5.14).
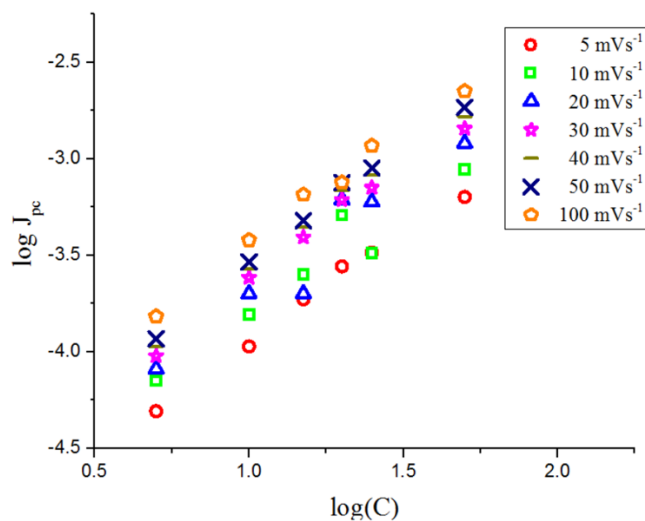

Fig. 5.14   Log of cathodic peak current density vs log of concentration of AgCl ($\log C$) in Ethaline 200 at various scan rates at 20 °C using 2 mm Pt disc working electrode (WE), IrO_2 coated Ti mesh counter electrode (CE) and Ag pseudo reference electrode (RE)

5.3.2   Bismuth redox system

Similar experiments were conducted for $BiCl_3$ in Ethaline 200, where $BiCl_3$ concentration was varied in the range 5 - 25 mmoldm^{-3}.

The current magnitude and peak potentials varied with the concentration of Bi(III) in the deposition bath. Cathodic peak potential increased to more positive values with increasing concentration (Fig. 5.15). At high concentrations the voltammetric peaks broadened.

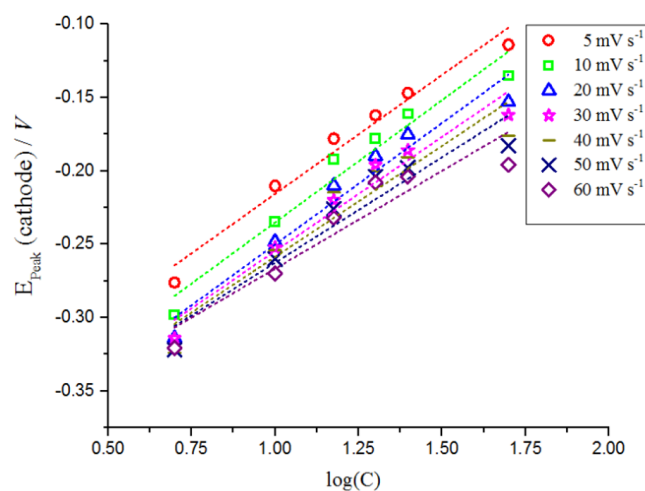**Fig. 5.15**   Cathodic peak potential vs log of concentration of $BiCl_3$ in Ethaline 200 at various scan rates at 20 °C using 2 mm Pt disc working electrode (WE), IrO_2 coated Ti mesh counter electrode (CE) and Ag pseudo reference electrode (RE)

The linear relationship between log J_p vs log $C_{Bi(III)}$ indicates that the reduction process is diffusion controlled (Fig. 5.16).
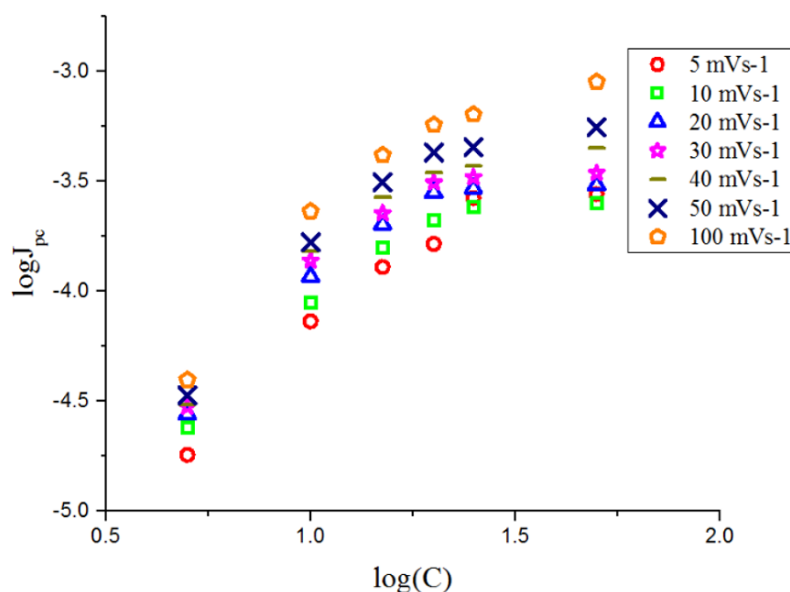

Fig. 5.16 Log of peak current density vs log of concentration of $BiCl_3$ in Ethaline 200 at various scan rates at 20 °C using 2 mm Pt disc working electrode (WE), IrO_2 coated Ti mesh counter electrode (CE) and Ag pseudo reference electrode (RE)

5.4   Bulk deposition and stripping efficiency

The efficiency of deposition and stripping of silver and bismuth separately, and silver/ bismuth together in more than monolayer amounts can be studied by integrating current corresponding to the reduction and oxidation sweeps in cyclic voltammograms. For this purpose cyclic voltammograms were conducted sequentially by using more negative switching potentials each time for the forward scan.

Cyclic voltammograms were obtained at different switching potentials (for the forward scan) for Ag(I) concentrations 5, 10, 15, 20, 25, 50, 100 mmoldm^{-3} using 10 mV s^{-1} scan rate. The same method was applied to $BiCl_3$ in Ethaline solutions with Bi(III) concentrations in the range 5 - 25 mmoldm^{-3} and for $AgCl/BiCl_3$ with 5:5, 10:10, 15:15, 20:20, 25:25 (mmoldm^{-3}:mmoldm^{-3}) Ag(I): Bi(III) ratios. Representative results are given in figs. Fig. 5.17, Fig. 5.19 and Fig. 5.21.

The two potential limits (for cyclic voltammograms) V_1 to V_2 were used for silver, bismuth and silver/ bismuth systems in Ethaline. The potential was swept (in Volts) in ranges: (-0.1 →0.7), (-0.2 →0.7), (-0.3 →0.7), (-0.4 →0.7), (-0.5 →0.7), (-0.6 →0.7) and (-0.7 →0.7).

5.4.1   Silver deposition and dissolution

Crossover potentials (i.e. the potential at which the current changes the sign) shifted negatively as the negative potential limit became more negative Fig. 5.17.[3] Also, the anodic stripping curve became more symmetric as the potential was scanned more negatively. The shape of stripping curve depends on the amount of metal deposited on the electrode surface and for more positive switching potential values the symmetric wave represents less deposition.

Fletcher et al. studied the effects of triangular scans of potentials for nucleation, growth processes using deposition of many metals including silver and bismuth on glassy carbon electrodes.[3] They used scanning electron microscopy and current time transients with potential steps. Both methods derived the same results.

The current maximum observed during the reverse triangular scan of potentials indicated that growth rate of crystals are not an exponential function of potential. The rate was concluded to be controlled by interfacial kinetics or hemispherical diffusion.

Fig. 5.17   Cyclic voltammograms obtained at different switching potentials in forward scan for 10 mmoldm^{-3} AgCl in Ethaline 200 at 20 °C using 2 mm Pt disc working electrode (WE), IrO$_2$ coated Ti mesh counter electrode (CE) and Ag pseudo reference electrode (RE)

The plot of charge of silver stripping with charge of silver deposition was obtained by integrating current responses from cathodic and anodic scans (Fig. 5.18). If the calculated stripping

efficiency is 100%, then all the deposited material during the cathodic sweep should be oxidised during the anodic sweep. The red solid line in Fig. 5.18 represents this case. For the example shown here, the stripping efficiency was found to be $92\pm1\%$. Analogous measurements across a range of concentrations were taken. All the results were in 80-90% range. However, the results did not vary systematically. The mean stripping efficiency calculated was ca. $89\pm1\%$.
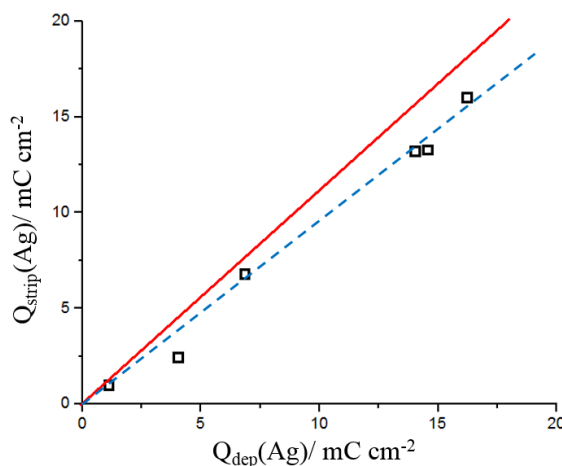
Fig. 5.18   Plot of charge for silver metal deposition vs metal stripping constructed from the data in Fig. 5.17. Unit slope, passing through the origin, is used as a guide to the eye. Dashed line is the line obtained from linear regression for data values.

5.4.2   Bismuth deposition and dissolution

The current density responses for bismuth are shown in Fig. 5.19. Crossover potentials (i.e. the potential at which the current changes the sign) have shifted negatively as the potential reversal became more negative due to diffusion control.

The anodic stripping curve shape varies with the switching potentials. As the switching potential swept more negatively the anodic peaks became more prominent and the size of the peak became larger (except for the –0.7 switching potential). However, the stripping efficiency was lower than for silver indicating that there may be layer effects (dissolved Bi(III) making insoluble complexes near the electrode surface blocking the diffusion process).[2]

For the example shown here stripping efficiency was found to be $74\pm1\%$ (Fig. 5.19, Fig. 5.20). Analogous measurements across a range of concentrations were taken and all the results were in 60-80% range. However, the results did not vary systematically so a trend could not be found.
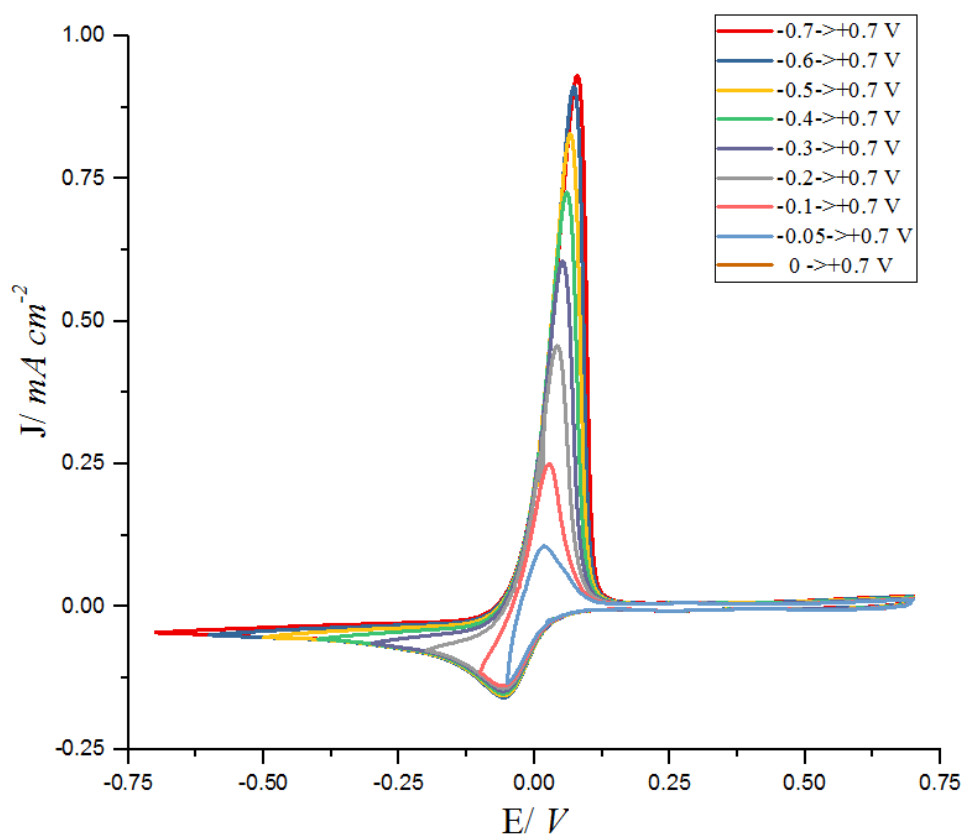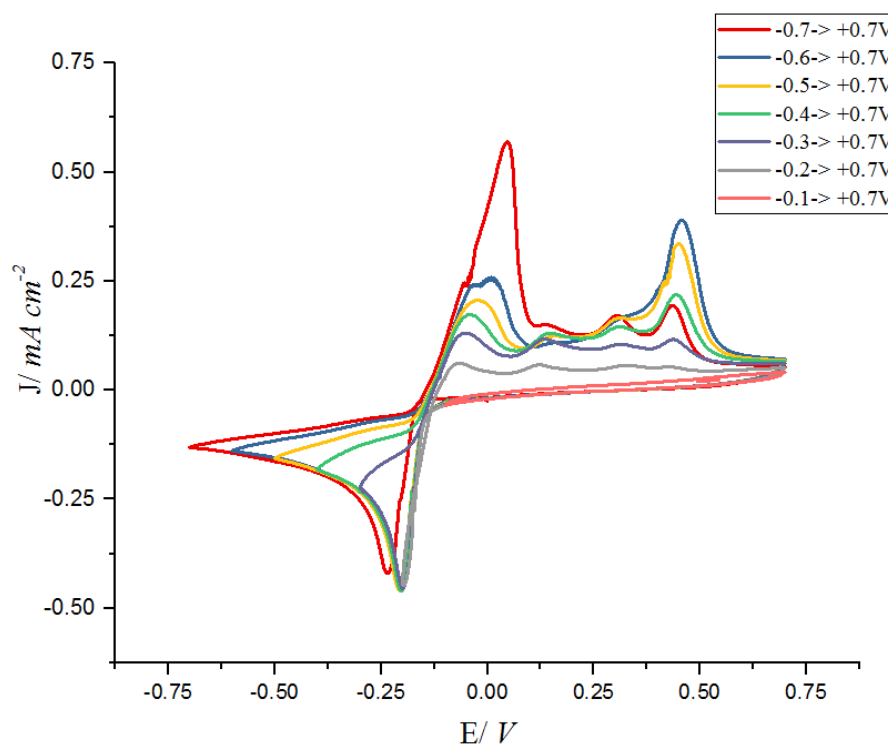
Fig. 5.19 Cyclic voltammograms obtained at different switching potentials in forward scan for 10 mmoldm^{-3} BiCl$_3$ in Ethaline 200 at 20 °C using 2 mm Pt disc working electrode (WE), IrO$_2$ coated Ti mesh counter electrode (CE) and Ag pseudo reference electrode (RE)

Fig. 5.20 Plot of charge for bismuth metal deposition vs metal stripping constructed from the data in Fig. 5.19. Unit slope, passing through the origin, is used as a guide to the eye. Dashed line is the line obtained from linear regression for data values.

5.4.3   Silver/bismuth co-deposition and dissolution

The same set of experiments and analysis were carried out for silver/ bismuth mixture in Ethaline 200 (Fig. 5.21).
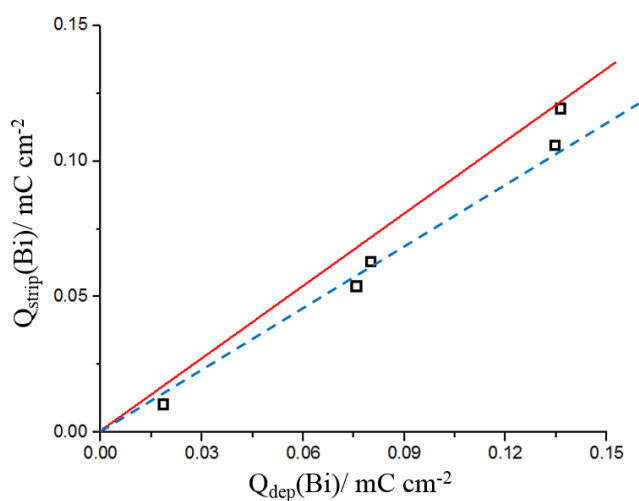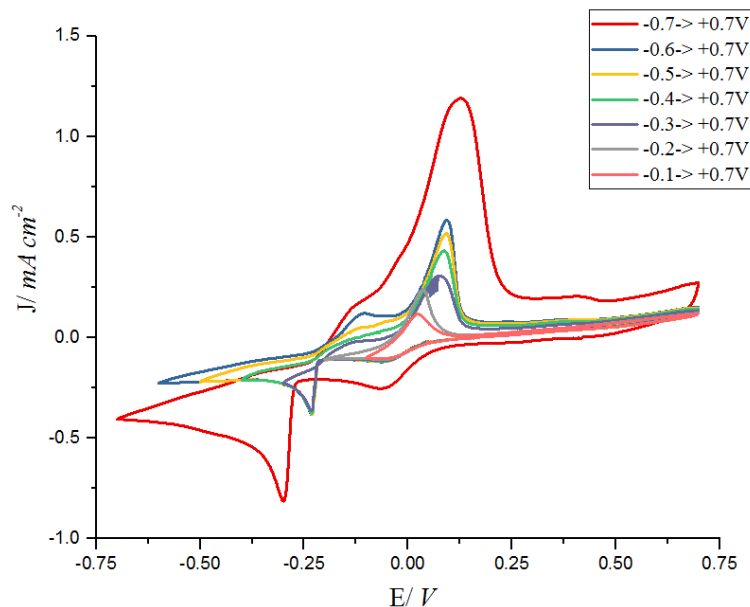

Fig. 5.21   Cyclic voltammograms obtained at different switching potentials in forward scan for 5 mmoldm^{-3}: 5 mmoldm^{-3} AgCl:BiCl$_3$ in Ethaline 200 at 20 °C using 2 mm Pt disc working electrode (WE), IrO$_2$ coated Ti mesh counter electrode (CE) and Ag pseudo reference electrode (RE)

The stripping efficiency of this process had a very low value of 50–80%. Crossover potentials (i.e. the potential at which the current changes the sign) shifted negatively as the potential reversal became more negative as in silver and bismuth systems. For the example shown here, stripping efficiencies were ca. $36 \pm 4\%$ (Fig. 5.22). Analogous measurements across a range of concentrations were taken. All the results show poor stripping efficiencies. This may be due to the insoluble film formation that blocks the electrode surface from the near electrode solution leading to a decrease in anodic current (see explanation in section 5.2))

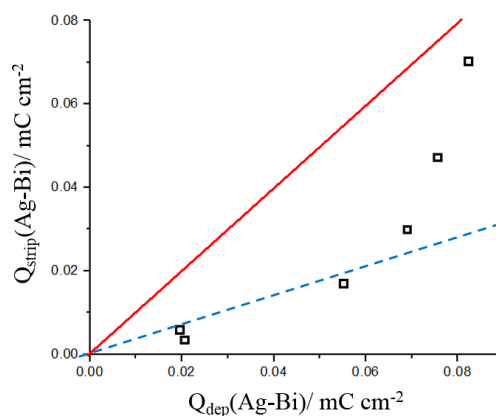**Fig. 5.22**   Plot of charge for silver/ bismuth metal deposition vs metal stripping constructed from the data in Fig. 5.21. Unit slope, passing through the origin, is used as a guide to the eye. Dashed line is the line obtained from linear regression of data values. Mean stripping efficiency calculated was $(60 \pm 5\%)$.

5.5   Gravimetric analysis

The deposition and dissolution of the metal systems have been studied using the electrochemical quartz crystal microbalance (EQCM). The EQCM is an extremely sensitive probe to measure in situ processes at the electrode/electrolyte interface with sub-monolayer resolution.[4-8] This technique was described in Chapter 2 and the experimental set up was given in Chapter 3. The deposited mass of metal (e.g. silver, bismuth or silver/ bismuth) is measured via the variation of the resonant frequency of a Pt coated quartz crystal working electrode. The Q factor of the resonance curve, which is a measure of rigidity (Eqn 2.23), was calculated in each case to investigate the validity of Sauerbrey's equation (Eqn 2.22). Solution preparation techniques and electrode setup were discussed in Chapter 3.

The change in resonance was judged by calculation of a Q factor during experiments and the change was found to be less than ca. $(\pm 5\%)$ for all experiments.

5.5.1   Current efficiency

The current efficiency is defined by two methods according to Bard et al[9]. If two or more faradaic reactions occur simultaneously at an electrode, the fraction i_i of the total current i_{total} involved in the xth process is defined as instantaneous current efficiency and denoted by i_i/i

Although it is desirable for bulk electrodeposition processes to be carried out with high values of current efficiency it is practically not possible due to side reactions that take place (due to the other redox process involving solvent, supporting electrolyte, electrode material or impurities). In order to prevent this situation, the working electrode potential and other conditions can be selected so that no side reactions may occur. However, for electrogravimetric methods, as long as the side reactions do not produce insoluble products that deposit on the electrode, 100% current efficiency is not needed. In most electrodeposition studies, the current efficiency can

be calculated from the ratio between apparent molar mass calculated from EQCM data and molar mass of the metal. For co-deposition of metals apparent molar mass depends on the mole fraction of each metal involved. Fig. 5.23 and Fig. 5.24 indicates the plots of silver and bismuth deposited as a function of charge passed for 15 - 100 mmol dm^{-3} Ag(I) in Ethaline 200 and 15 - 25 mmoldm^{-3} Bi(III) in Ethaline 200.

Fig. 5.23 Mass of the silver deposited as function of charged passed from silver in Ethaline 200 at 20 °C using 2 mm Pt disc working electrode (WE), IrO$_2$ coated Ti mesh counter electrode (CE) and Ag pseudo reference electrode (RE). a, b, c represent data for three separate experiments (Table 5.4)
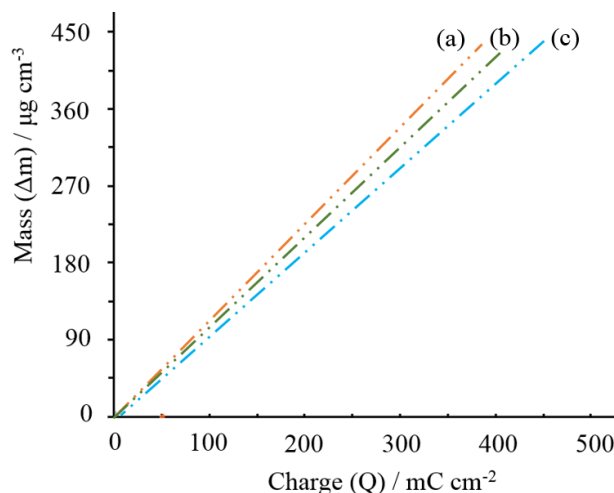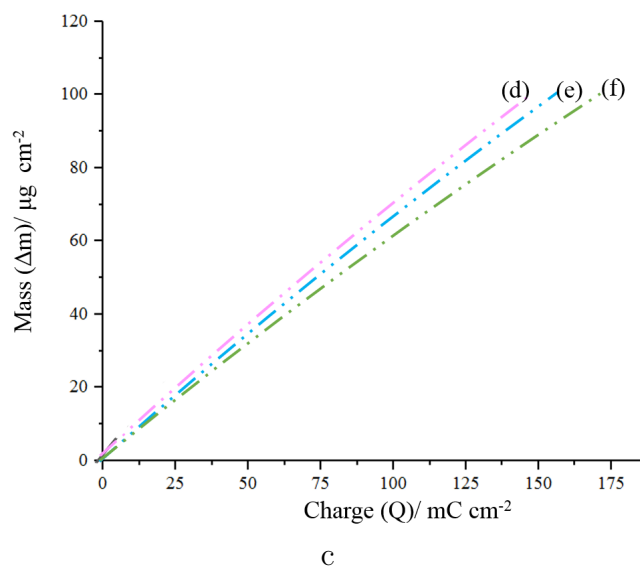

c

Fig. 5.24 Mass of the bismuth deposited as function of charged passed from silver in Ethaline 200 at 20 °C using 2 mm Pt disc working electrode (WE), IrO$_2$ coated Ti mesh counter electrode (CE) and Ag pseudo reference electrode (RE). d, e, f represent data for three separate experiments (Table 5.4)

The apparent molar mass M (g mol^{-1}) is related to slope of these graphs (i.e. change in mass (Δm) / change in charge (ΔQ)) by the following equation,

$$M = n \, F \, \frac{\Delta m}{Q} \tag{5.5}$$

where

n - number of electrons involved (Ag: n = 1; Bi: n = 3)

F - Faraday's constant (96490 C mol^{-1})

The current efficiencies and apparent molar masses that were found are given in Table 5.4. No significant correlations between current efficiencies with concentration were found. For bismuth deposition there is a current efficiency decrease with time; but this trend was not seen for silver.

Table 5.4   Calculation of the current efficiency for plots in Fig. 5.23 and Fig. 5.24

Metal system	Plot No	$\Delta m/Q$ gradient (μg cm^{-2}/ mC cm^{-2})	M_{calc} (g mol^{-1})	Current efficiency/%
Silver	(a)	1.10	106.13	98.3
Silver	(b)	1.01	97.45	90.3
Silver	(c)	0.99	107.10	88.5
Bismuth	(d)	0.61	176.57	84.4
Bismuth	(e)	0.62	180.91	86.5
Bismuth	(f)	0.66	192.49	92.1

5.6   Potentiostatic study of metals in DES

In metal film formation, the nucleation and diffusion controlled growth can take place by instantaneous or progressive nucleation mechanisms.[10] In instantaneous nucleation, the rate of nucleation is faster than the rate of subsequent growth of nuclei. In progressive nucleation, the rate of nucleation is comparable to the subsequent growth rate. Sharifker and Hills model for the nucleation and growth is the most successful physical model developed to date.[11-13] (see Chapter 1) This method was used to study the deposition of silver, bismuth and co-deposition of silver/ bismuth under diffusion controlled mode. Electrochemical measurements were obtained from the three electrode set up (Pt disk working disk electrode, IrO$_2$ coated Ti mesh electrode and Ag reference electrode) using Ag(I), Bi(III) and a mixture of Ag(I)/Bi(III) chloride salts dissolved in Ethaline 200 at 20 °C. The concentrations used for each system are given in Table 5.5. Preparation methods were discussed in Chapter 3.

Chronoamperometry was used to obtain current transient curves for electrochemical deposition of metals on 1 mm Pt disk electrodes. The Pt working electrode was cleaned using 0.3 μm alumina paste mixed with acetone, rinsed with acetone and dried with compressed N$_2$ each time before use. An equilibrium potential was maintained at the Pt working electrode for 120 s prior to each chronoamperometry experiment. These measurements were carried out by stepping the

Table 5.5   Concentration of metal chlorides in Ethaline 200 used to study nucleation

Metal chlorides	Concentration (mmoldm^{-3})
AgCl in Ethaline 200	10, 14, 20, 25, 50, 100
BiCl$_3$ in Ethaline 200	10, 15, 20, 25
AgCl:BiCl$_3$ in Ethaline 200	5:5, 10:10, 15:15, 20:20, 25:25

potential from the equilibrium potential (e.g. 200 mV for Ag system) vs Ag pseudo reference to different potentials between 50 mV and 200 mV vs silver pseudo reference electrode. The equilibrium potential is the initial potential where no metal reduction takes place. The time duration for conducting chronopotentiaometry was decided depending on the t_{max} observed. The time durations for the experiments were few multiples of t_{max}. Step potentials of −50, −60, −70, −80, −90, −100, −110 and −120 mV were applied for the silver system. For the bismuth system, the step potentials of −10, −20, −30, −40, −50, −60, −70 and −80 mV were used. These measurements were carried out by stepping the potential from 700 mV vs Ag (as initialisation step where no Bi reduction takes place) to different potentials between −50 mV and −120 mV against the silver pseudo reference electrode. The time duration for conducting chronopotentiometry experiments was decided depending on the t_{max} observed (t_{max} is the time observed at which the maximum current density is observed). The time duration for the experiments were few multiples of t_{max}.

The experiments were conducted for AgCl, BiCl$_3$ and AgCl/BiCl$_3$ mixtures (Table 5.5) in quiscent solutions. The current transient curves obtained showed a similar trend with well defined current maxima regardless of the applied potential or concentration for the solution.

5.6.1   Analysis of silver deposition current transients

Each current density curve can be divided into 4 segments (t_1, t_2, t_3, t_4 as shown in Fig. 5.25). At the initial potential (200 mV), since the potential is more positive than the equilibrium reduction potential of Ag(I), no nucleation can occur. Therefore, the observed abrupt rise in current density and the sudden exponential decay corresponds (t_1) to double layer charging (non Faradaic or capacitance current).

The second segment (t_2) is the induction period which may be attributed to adsorption-desorption of silver ions. This period is very short in this case and the rising current represents the increase in size of isolated nuclei (or increase in the number of nuclei) and therefore the increase in electroactive surface. The growth of nuclei can take place by hemispherical diffusion of electroactive species (see region t_3) in the diffusion zone which has developed around each nucleus. When the individual hemispherical diffusion zones around nuclei overlap hemispherical diffusion gives away to linear planar diffusion which gives rise to a maximum current density J_{max} that takes place at t_{max}.

In the next region (t_4) the growth of crytallites is governed by linear diffusion to a planar surface
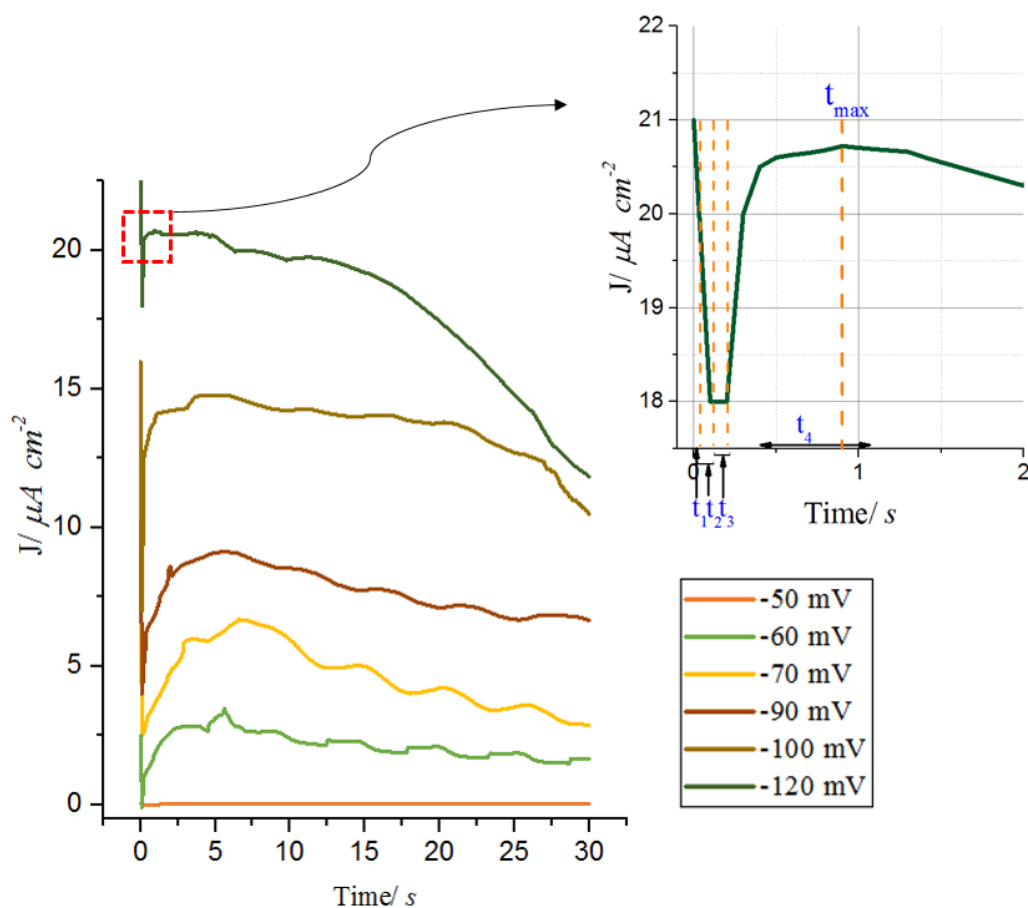
Fig. 5.25   These are several representative chronoamperometric current density vs time data graph for the reduction of silver on Pt electrode where Ag(I) concentration is 20 mmoldm^{-3} in Ethaline 200 at 20 °C

of the electrode. Therefore, after the current maximum, the Faradaic current decreases and the different responses merge into a potential independent curve. For higher applied voltage the reaction rate is increased and hence the drop of current density in the diffusional area is steep.

The current transients at a range of step potentials for different concentrations were analysed (Fig. 5.26 - left panel).

The graph shape in Fig. 5.8 was similar for all step potentials indicating a similar mechanism. The J_{max} values for the lower concentrations (e.g. 20 mmoldm^{-3} in Fig. 5.26 - right panel) was 10 times lower than that for 100 mmoldm^{-3} solutions. The t_{max} values were also 10 times lower than that for 100 mol dm^{-3} solutions.

At short time intervals the concentration of metal ions near the electrode can be considered to be high and hence the current observed would be kinetically controlled. So the current will depend on the applied potential. A drop in current density with the decrease in step potential is observed. Furthermore the electrochemical rate constant depends on the potential and for small changes in potential a significant variation in current is observed. At longer times when the reaction has consumed the metal ions near the electrode surface then the rate of reaction depends on the diffusion of metal ions to the electrode i.e. the rate of the reaction (measured as
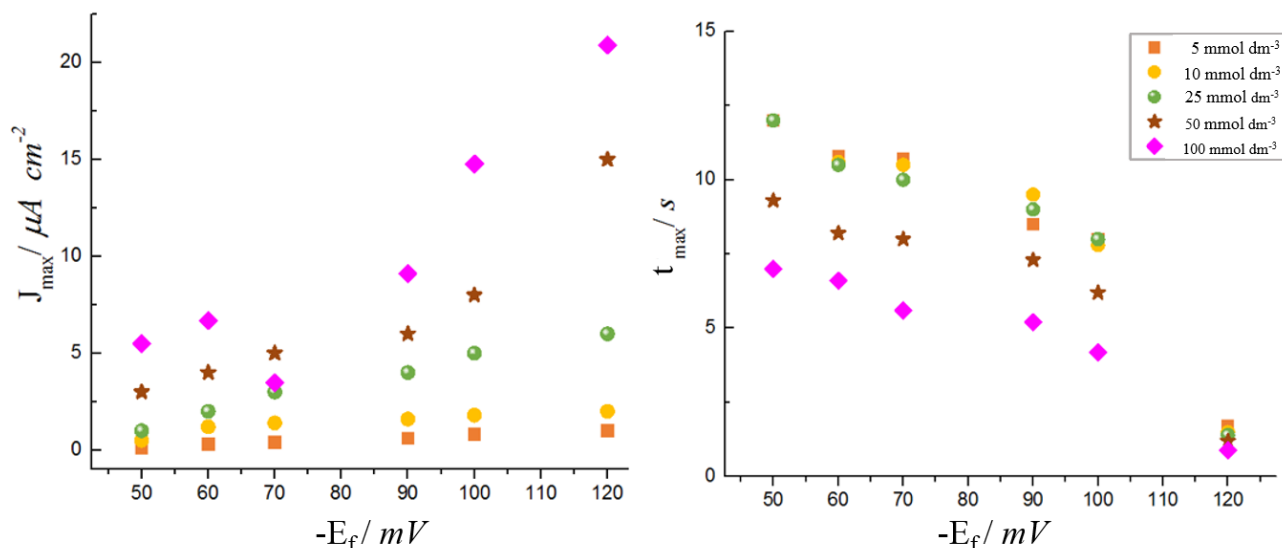
Fig. 5.26 E_f is the final potential to which E_i is changed to with respect to the silver pseudo reference electrode. The plot (left panel) shows the maximum current density (J_{max}) at t_{max} as a function of E_f for different concentrations of AgCl in Ethaline 200. The plot in (right panel) shows the t_{max} values as a function of $-E_f$ for the same concentrations as in the left panel.

current) would depend on diffusion coefficient. For higher step potentials the reaction is faster and hence the drop in diffusional area is steep.

The nucleation process at low step potentials is sensitive to Ag(I) concentration while at more negative potentials it becomes more insensitive to Ag(I) concentration (see Fig. 5.26). J_{max} increases linearly with more negative step potentials as a function of Ag(I) concentrations (see Fig. 5.26). This data was consistent with data from cyclic voltammetry and EQCM study.

All the current transients in Fig. 5.27 present a typical response of 3D nucleation and diffusion controlled growth and were analysed by using Sharifker and Monstany[12] and Hills et al. models.[11,14] The theories and models describe the kinetics of electrodeposition at early stages from nucleation to subsequent growth or phase formation (see Chapter 1). The diffusion of the depositing species from bulk solution to the depositing site on the electrode surface is considered as the rate determining step for both models. These diffusion layers are considered to form diffusion zones which overlap, forming columnar diffusion.[11,12,14]

According to the above mentioned models, the current transients correspond to two extreme nucleation modes:

1. Instantaneous nucleation mode

2. Progressive nucleation mode

The two nucleation modes can be analysed by the following equation (see Chapter 1).

For progressive nucleation:

$$J = zFC\left(\frac{D}{\pi t}\right)^{1/2}\left[1 - exp\left(-\frac{A_n}{2}\pi k'Dt^2\right)\right]$$ (5.6)

where

> z - equivalent mole^{-1}
> F - Faraday constant (96490 C mol^{-1})
> C - bulk concentration (mol cm^{-3})
> D - diffusion coefficient (cm^2 s^{-1})
> A_n - nucleation rate (cm^{-2} s^{-1})
> t - time (s)

The k'' in the equation is defined as,

$$k'' = \frac{4}{3}\left(\frac{8\pi CM}{\rho}\right)^{1/2}$$ (5.7)

where

> M - Molar mass
> ρ - density of the deposited material

For instantaneous nucleation:

$$J = zFC\left(\frac{D}{\pi t}\right)^{1/2}\left[1 - exp(N\pi kDt)\right]$$ (5.8)

where N is the number density of active sites.

The k in the equation is defined as,

$$k = \left(\frac{8\pi CM}{\rho}\right)^{1/2}$$ (5.9)

To classify nucleation process as instantaneous or progressive equations, Eqn.5.6 and 5.8 can be represented in terms of reduced variables J/J_{max} and t/t_{max} after normalising with time (t_{max}) and current density (J_{max}). J_{max} is the current density observed at t_{max}.

$$\left[\frac{J}{J_{max}}\right]^2 = 1.9542\left[\frac{t}{t_{max}}\right]^{-1}\left\{1 - exp\left[-1.2564\left[\frac{t}{t_{max}}\right]\right]\right\}^2$$ (5.10)

$$\left[\frac{J}{J_{max}}\right]^2 = 1.2254\left[\frac{t}{t_{max}}\right]^{-1}\left\{1 - exp\left[-2.3367\left[\frac{t}{t_{max}}\right]^2\right]\right\}^2$$ (5.11)

According to the models, the theoretical model can be described using the following regions.

1. Formation and growth of nuclei on the electrode ($\frac{t}{t_{max}} < 1$)

2. Physical coalescence of nuclei that are growing and the overlap of their diffusion zones ($\frac{t}{t_{max}} = 1$)

3. The growth process of the new phase of metal layer ($\frac{t}{t_{max}} > 1$)

Therefore for better clarity an initial time period was selected for graphical analysis that includes the above mentioned stages. The experimental data and theoretical data curves (Eqn. 5.10 and Eqn. 5.11) were compared to analyse the nucleation mechanism pathway. The current transients for theoretical and experimental data are given in Fig. 5.27 using non-dimensional plots for 100 mmoldm^{-3} AgCl/ Ethaline system.
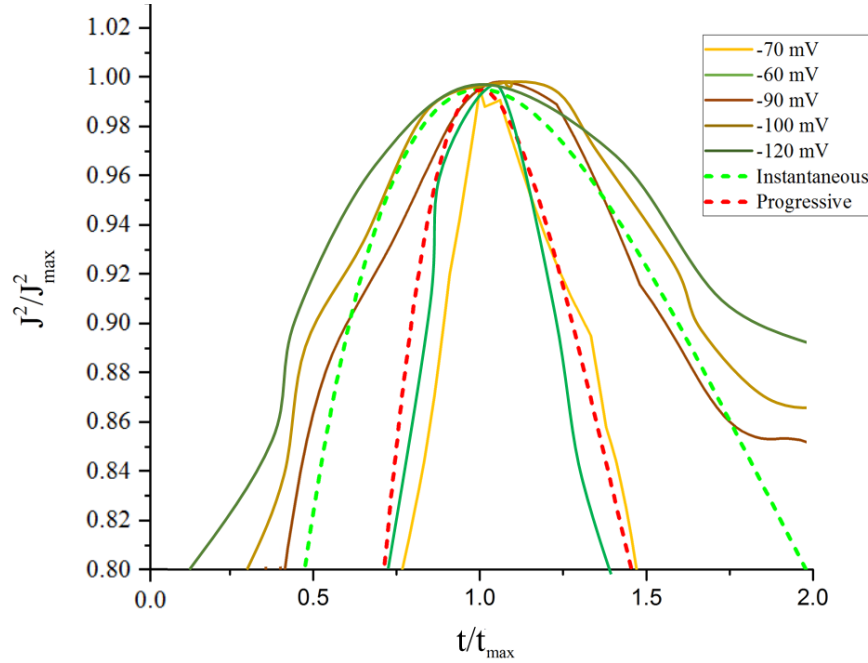

Fig. 5.27 Reduced variable plot for the current transients of 20 mmoldm^{-3} AgCl in Ethaline 200 on Pt working electrode at 20 °C. For classification of the nucleation process i.e. 3D instantaneous and 3D progressive theoretical curves have been shown.

A good agreement was observed between experimental curves for –120 mV, –100 mV and –90 mV step potentials and the theoretical instantaneous nucleation curve. The experimental curves for –60 mV, –70 mV had a good agreement with theoretical progressive nucleation curves. This indicated that higher overpotentials facilitate instantaneous nulceation.

The initial rising part of the current transient (t$_3$ range of J vs t plot in Fig. 5.25) was used to distinguish the nucleation and growth mechanism. The right rectangular cone[15] explains that 3D nucleation is limited by lattice incorporation of adatoms. This can be explained using nucleation under diffusion controlled growth when n=1/2 or n=3/2 as following[11]

For instantaneous nucleation from eqn.5.6:

$$J(t) = \frac{z\ F\ D^{1/2}\ C}{\pi^{1/2}t^{1/2}}\left[1\ -\ exp(-N\ \pi\ k''\ D\ t)\right] \tag{5.12}$$

$J(t)$ - current density at time t

Considering current transient data at early stage (t$_3$ in Fig. 5.25) we can assume that at short times: $N\ \pi\ k''\ D\ t\ <<\ 1$;
therefore, $1\ -\ exp\left(-N\ \pi\ k''\ D\ t\right) \approx N\ \pi\ k\ D\ t$ and the equation 5.12 can be simplified to:[10]

$$J(t) = z\ F\ D^{3/2}\ C\ \pi^{1/2}\ k''\ D\ t^{1/2} \tag{5.13}$$

By a similar argument for progressive nucleation:

$$1 \; - \; exp\left(-A \, N_\infty \, \pi \, k'' \, D \, t/2\right) \approx A_\infty \, \pi \, k \, D \, t^2/2$$

Therefore, for progressive nucleation,

$$J(t) = \frac{z \, F \, D^{1/2} \, C}{\pi^{1/2} t^{1/2}} \left[1 \; - \; exp(N_\infty \, \pi \, k'' \, D \, t^{1/2}/2) \right] \tag{5.14}$$

becomes

$$J(t) \; = \; \frac{1}{2} \, z \, F \, D^{3/2} \, C \, \pi^{1/2} \, N_\infty \, k' \, t^{3/2} \tag{5.15}$$

According to equation 5.13, the plot of J vs $t^{1/2}$ should be linear for instantaneous nucleation and according to equation 5.15, the plot of J vs $t^{1/2}$ should be linear for progressive nucleation. So current transient curves for t_3 segment (Fig. 5.25 was analysed for different final potentials (E_f)).
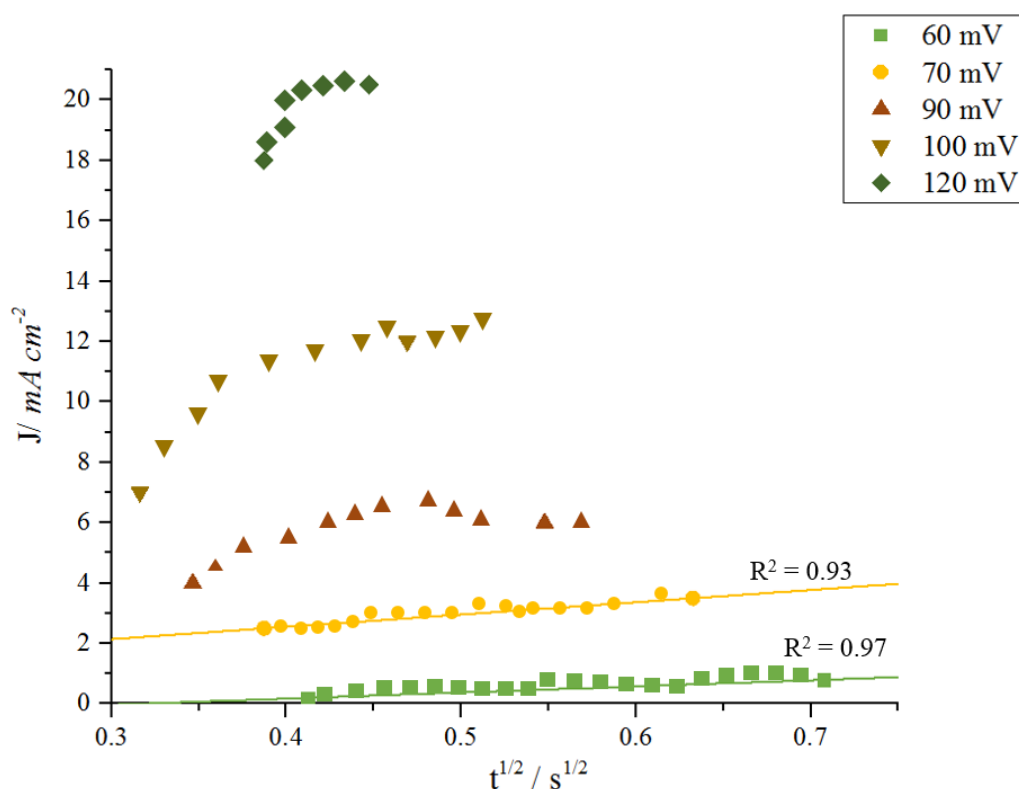

Fig. 5.28 J vs. $t^{1/2}$ plot for the rising part of the current transients for 20 mmoldm^{-3} AgCl in Ethaline 200 at 20 °C using 2 mm Pt disc working electrode (WE), IrO$_2$ coated Ti mesh counter electrode (CE) and Ag pseudo reference electrode (RE)

The analysis of Fig. 5.28 and Fig. 5.29 indicated at high negative step potentials I vs $t^{1/2}$ displayed more linear trendlines (Fig. 5.28: $R^2 > 0.9$) indicating at high overpotentials instantaneous nucleation is favoured. However at all potentials (except for −120 mV, −100 mV) I vs $t^{3/2}$ displayed linear behaviour (R^2 is more than 0.9) indicating that at low negative overpotentials progressive nucleation is favoured. When this behaviour was compared to similar system at different concentrations of Ag(I) (e.g. 5 mmoldm^{-3}, 10 mmoldm^{-3}, 25 mmoldm^{-3}, 50 mmoldm^{-3}), it was evident that the nucleation and growth mechanism was not effected by the
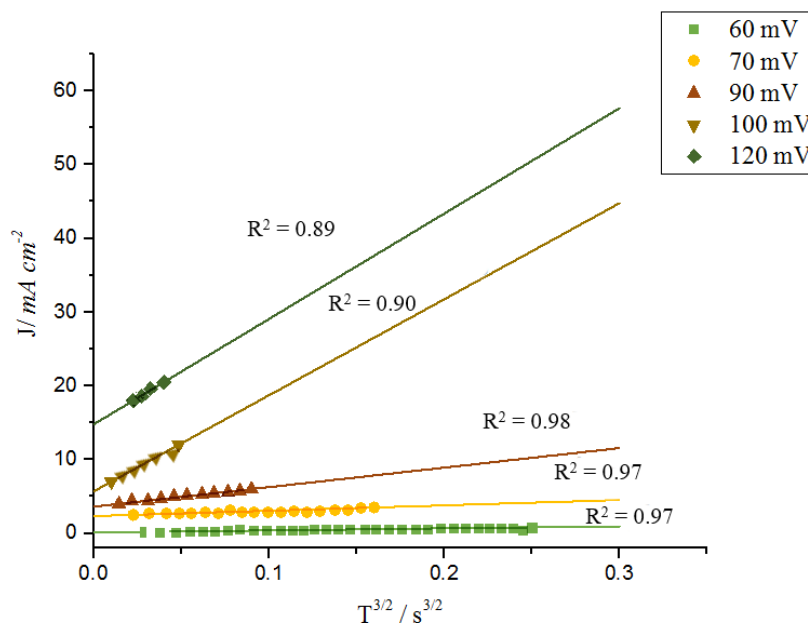
Fig. 5.29   J vs. t$^{3/2}$ plot for the rising part of the current transients for 20 mmoldm^{-3} AgCl in Ethaline 200 at 20 °C using 2 mm Pt disc working electrode (WE), IrO$_2$ coated Ti mesh counter electrode (CE) and Ag pseudo reference electrode (RE)

concentration. This was in agreement with work done by Abbott et al. at high temperatures.[16] This indicated that the nucleation and growth was independent of concentration or temperature but dependent on overpotential. The falling of some of the experimental non-dimensional current transient between theoretical instantaneous and theoretical progressive indicate that the nucleation is slow with diffusional controlled growth only for some cases. The plots (Fig. 5.28, Fig. 5.29) can be taken as reliable evidence since the R^2 values were closer to 1.

A further expression has been derived which relates maximum current density (J$_{max}$) to the time taken to reach the maximum current density (t$_{max}$) with the diffusion coefficient of electroactive metal ion.[11,17]

For instantaneous nucleation the expression is:

$$J_{max}^2 t_{max} = 0.1629(z\ F\ C)^2\ D \tag{5.16}$$

and for progressive nucleation it becomes:

$$J_{max}^2 t_{max} = 0.2598(z\ F\ C)^2\ D \tag{5.17}$$

where

z - equivalent mole^{-1}
F - Faraday constant (96490 C mol^{-1})
C - bulk concentration (mol dm^{-3})
D - diffusion coefficient (cm^2 s^{-1})

All the terms in the right hand side of the above equation (i.e. z, F, c, D) are independent of the overpotential or applied potential. Therefore, the product $J_{max}^2 t_{max}$ should be independent of mechanism and growth.
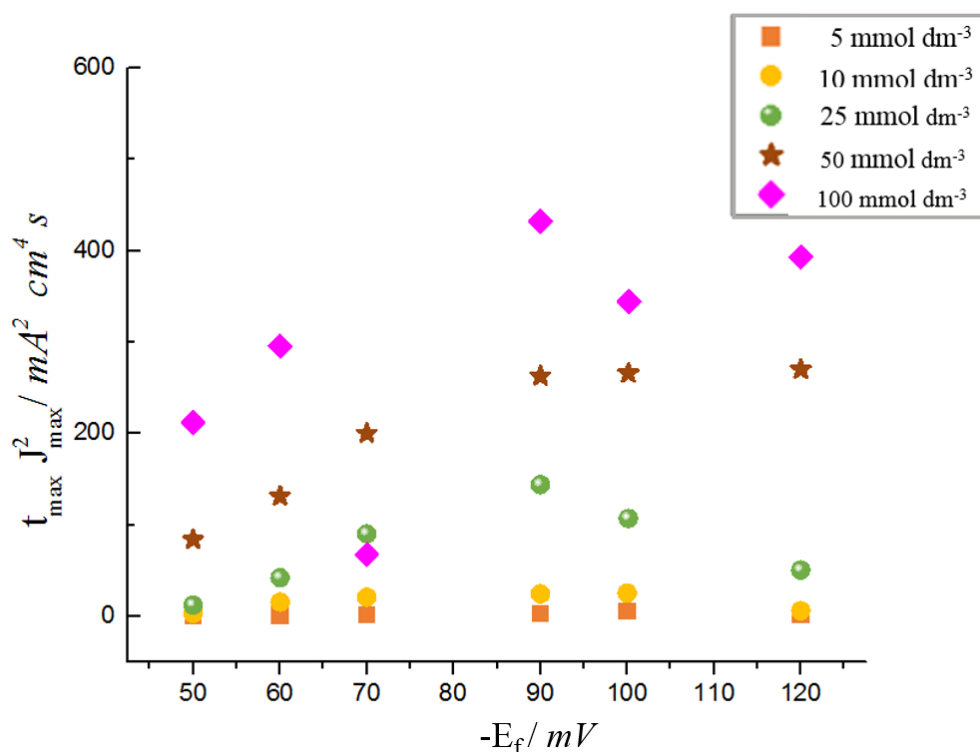
Fig. 5.30 $J_{max}^2 t_{max}$ plot for deposition of 20 mmoldm^{-3} AgCl in Ethaline 200 at 20 °C using 2 mm Pt disc working electrode (WE), IrO$_2$ coated Ti mesh counter electrode (CE) and Ag pseudo reference electrode (RE)

Fig. 5.30 shows that $J_{max}^2 t_{max}$ of AgCl for different concentrations and its value did not vary significantly with the applied potential for lower concentrations. However, there is an indication that $J_{max}^2 t_{max}$ model is not applicable for higher concentrations for the AgCl in Ethaline 200 (since $J_{max}^2 t_{max}$ values varied significantly depending on the concentration of Ag(I)).

Diffusion coefficient calculated using current transients

The region of the current transients after J_{max} was used to calculate diffusion coefficient values using the Cottrell equation.[9]

$$J(t) = \frac{n \ F \ D^{1/2} \ C}{\pi^{1/2} \ t^{1/2}} \tag{5.18}$$

where z - equivalent mole^{-1}
F - Faraday constant (96490 C mol^{-1})
C - bulk concentration (mol cm^{-3})
D - diffusion coefficient (cm^2 s^{-1})

Plot of J vs t$^{-1/2}$ were drawn for the decaying portions (t>t$_{max}$ of the current transients (Fig. 5.31).

The data from Cottrell plots were used to calculate diffusion coefficient values that were averaged (D = 2.16×10^{-7} cm^2 s^{-1}). These compared with diffusion coefficient value from cyclic voltammetry using Randles-Sevcik equation (2.01×10^{-7} cm^{2}s^{-1}) and probe beam data using chrono-deflectometry (4.3×10^{-7} cm^{2}s^{-1}). The value calculated here is higher that the values calculated by other methods.
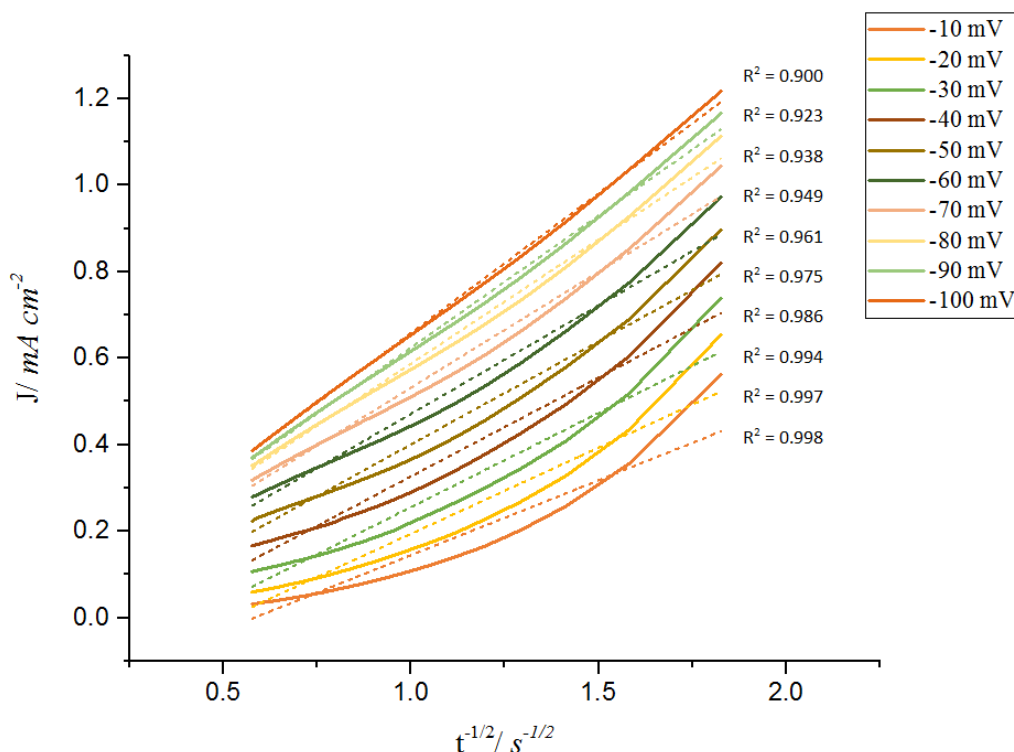
Fig. 5.31 J vs. $t^{1/2}$ plot for the decaying part of the current transients Fig. 5.25 for 20 mmoldm^{-3} AgCl in Ethaline 200 at 20 °C using 2 mm Pt disc working electrode (WE), IrO$_2$ coated Ti mesh counter electrode (CE) and Ag pseudo reference electrode (RE)

5.6.2   Analysis of bismuth deposition current transients

Chronoamperometry was used to obtain current transient curves for electrochemical deposition of bismuth on platinum electrodes. The potential was stepped from 200 mV (vs Ag pseudo reference to) potentials between −10 mV to −80 mV. The time duration for chronoamperometry was taken as ca. 50 times of t$_{max}$ for the lowest potential step. The same experiment was repeated for 5, 10, 15, 20 and 25 mmoldm^{-3} in the quiescent solution. All current transients had the same shape with well defined current maxima denoted by J$_{max}$. Several representative current transient curves are shown in Fig. 5.32 for 20 mmoldm^{-3} BiCl$_3$ in Ethaline 200.

Four segments of time which was used to analyse silver current transients were used to analyse bismuth deposition as well. The current transients for a range of step potentials for different concentrations were analysed and the graph shape was seen to be similar indicating that they have a similar mechanism. J$_{max}$ values for lower concentrations (10 mmoldm^{-3}) were 6 times lower than that for 20 mmoldm^{-3} solutions for same step potentials. Maximum current density decreased with decreasing step potential since the electrochemical rate constant depends on the applied potential at first and thereafter rate of reaction (measured as current) depended on diffusion. At higher step potentials, the reaction rate depended on diffusion (Fig. 5.33 left panel).

At higher step potentials, the fast reaction rate causes the high consumption of ions for deposition and displays a steep drop in current which is clearly seen in the graph(Fig. 5.32). Fig. 5.33
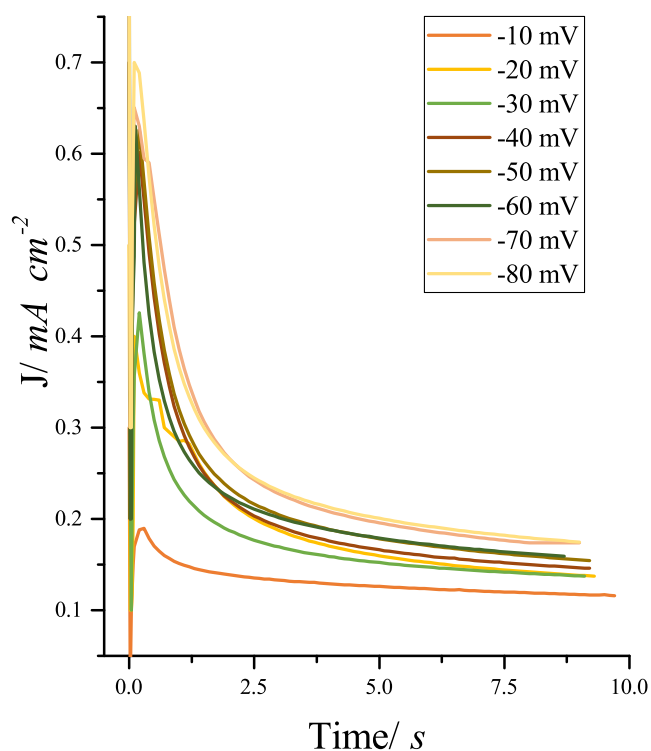
Fig. 5.32   Current density vs time plot for 20 mmoldm^{-3} BiCl$_3$ in Ethaline 200 at 20 °C using 2 mm Pt disc working electrode (WE), IrO$_2$ coated Ti mesh counter electrode (CE) and Ag pseudo reference electrode (RE)

Fig. 5.33   Maximum current density(J$_{max}$)(left panel) and t$_{max}$ vs E$_f$ for different concentrations of BiCl$_3$ in Ethaline 200 at 20 °C using 2 mm Pt disc working electrode (WE), IrO$_2$ coated Ti mesh counter electrode (CE) and Ag pseudo reference electrode (RE).
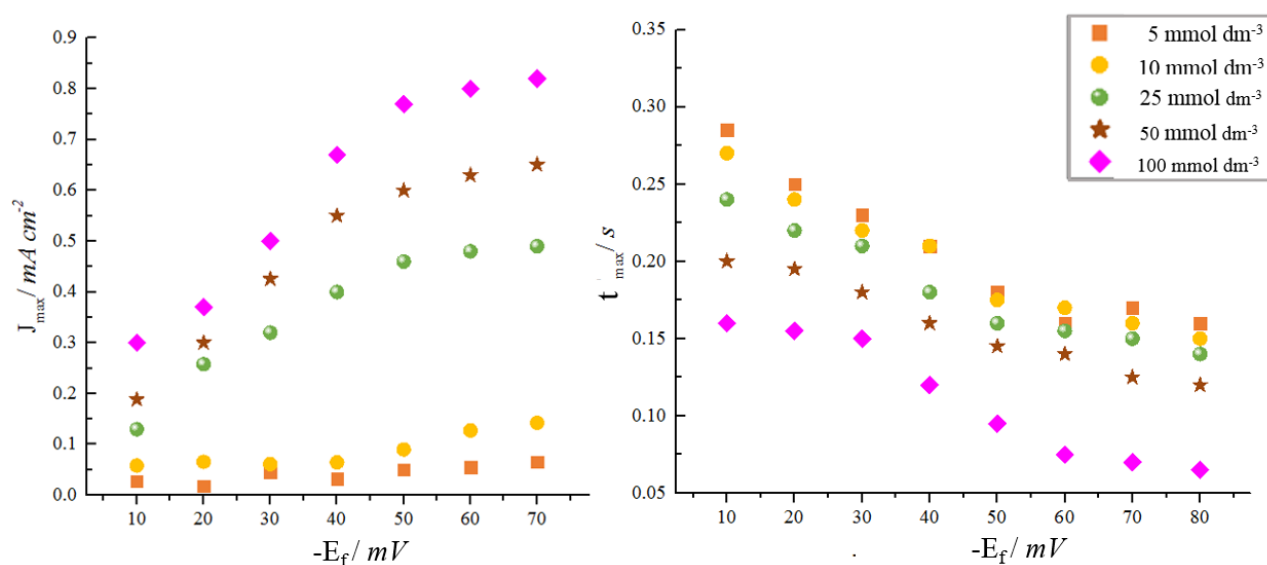
(right panel) shows the t_{max} as a function of concentration and step potential. t_{max} value decreased with increasing concentration and increasing negative step potentials. J_{max} (Fig. 5.33 left panel) increased with concentration and negative potential applied. The positive deviation seen was more significant for higher concentration and for high negative potentials.

From −50 mV to −80 mV, the increase in J_{max} was significant compared to the lower negative voltages for all concentrations, indicating that the nucleation process at high concentrations is more sensitive to applied potentials. The models put forward by Sharifker and Mostany[11] and Hills et al.[13] were used to analyse the current transients (Eqns. 5.6, 5.7, 5.8, 5.9). To classify the nucleation processes normalised reduced variable plots i.e. J^2/J^2_{max} vs t/t_{max} were used (Fig. 5.34).
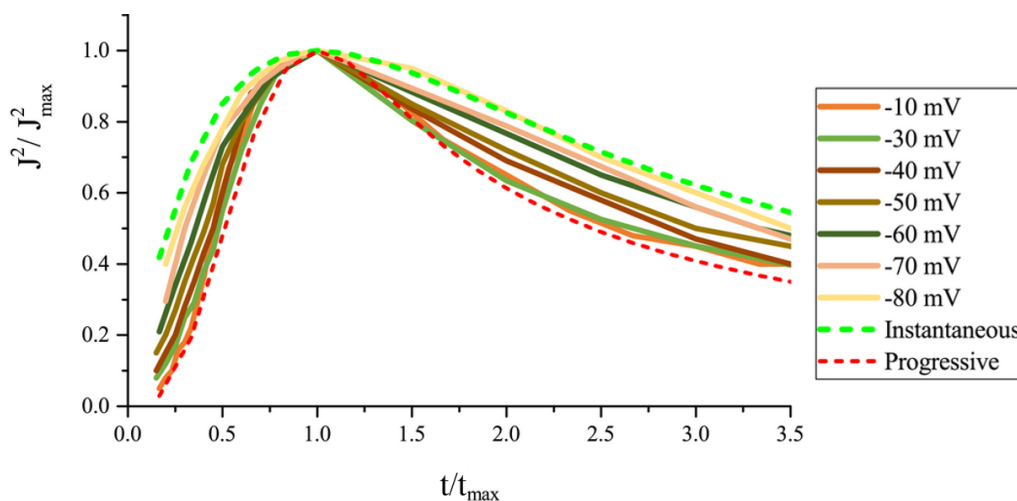

Fig. 5.34 Reduced variable plots for current transients in Fig. 5.32 to compare with limiting cases i.e. instantaneous and progressive nucleation

These transients for experimental data were compared with theoretical curves derived from (Eqns. 5.6, 5.8). All reduced variable plots fell between theoretical instantaneous and theoretical progressive curves. As the applied potential was increased the curves move towards instantaneous (theoretical) curve. This provided evidence that when the applied overpotential is higher, nuclear overpotential is achieved favouring new nuclei formation during the first few seconds. This trend is seen for both $t/t_{max} < 1$ and $t/t_{max} > 1$ regions in the normalised plot. As explained for silver in section 5.7.1, the initial rising part can be analysed by equations 5.11 and 5.10. A significant range of current transient curve for J vs $t^{1/2}$ were linear indicating that nucleation was instantaneous (Fig. 5.35). The data appears to deviate from the mathematical model for instantaneous and progressive nucleation. According to Palomar-Pardave et al. this trend may include additional effects from faradaic processes occurring on the nucleation surfaces of the metal. It has been shown that the small amount of residual water in the DES was reduced during metal deposition. This may have happened in the present system.[18]

The expressions 5.18 and 5.19 were used to analyse the current transients (Fig. 5.36). The calculated $J^2_{max}t_{max}$ values (averaged) and expected theoretical values (for both instantaneous and progressive cases) are given in Table 5.6. The results from this analysis were inconclusive (since the theoretical instantaneous and progressive data were significantly different to the
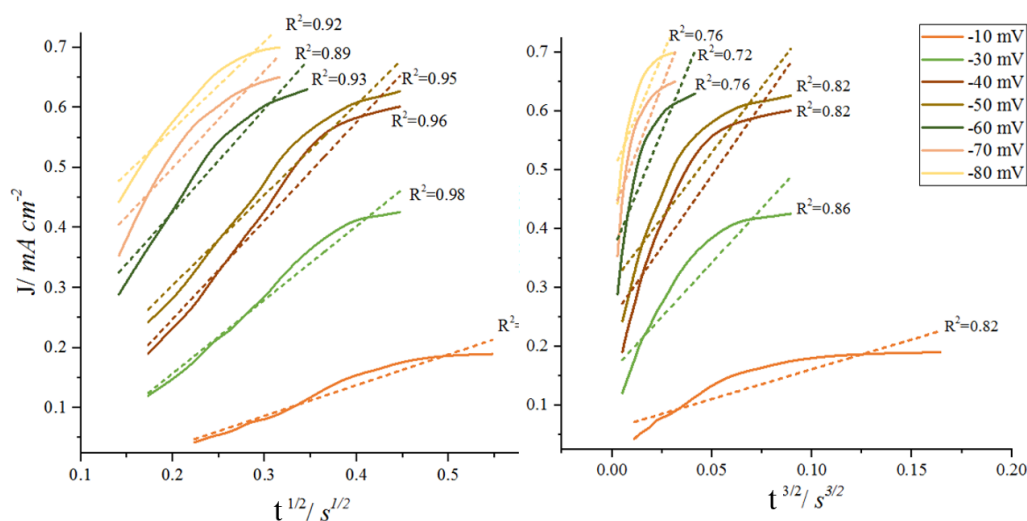
Fig. 5.35   J vs $t^{1/2}$ and J vs $t^{3/2}$ plots for modification of rising part of the current transient for 20 mmoldm^{-3} BiCl$_3$ in Ethaline 200 at 20 °C using 2 mm Pt disc working electrode (WE), IrO$_2$ coated Ti mesh counter electrode (CE) and Ag pseudo reference electrode (RE). Dashed lines represent linear regression fitted for data points.

experimental values).   Therefore, expressions 5.18 and 5.19 cannot be used to analyse the bismuth system in this context.
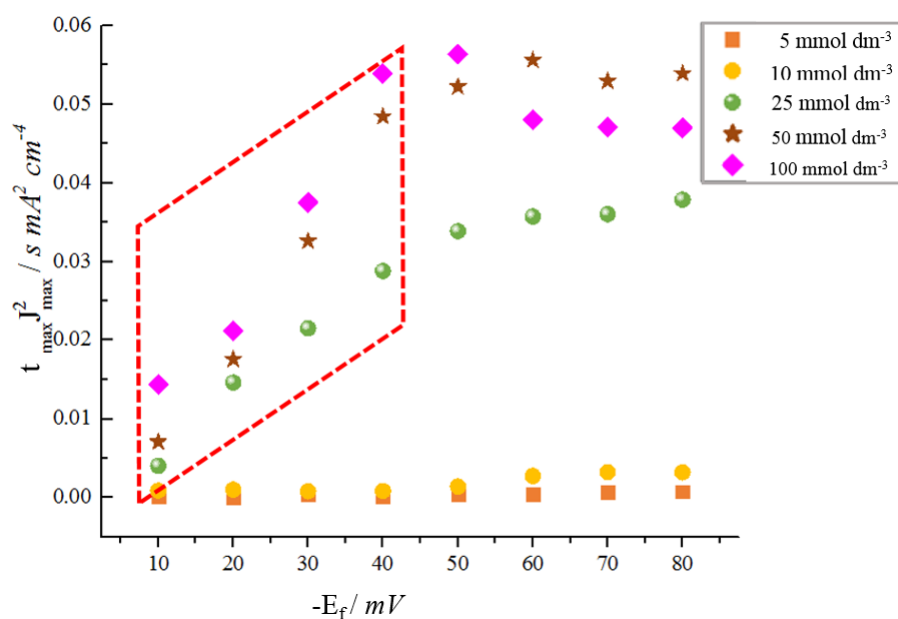

Fig. 5.36 $t_{max}J_{max}^2$ vs overpotential of 20 mmoldm^{-3} BiCl$_3$ in Ethaline 200 at 20 °C using 2 mm Pt disc working electrode (WE), IrO$_2$ coated Ti mesh counter electrode (CE) and Ag pseudo reference electrode (RE). -10 mV $\rightarrow$ -40 mV window is highlighted in the figure to indicate variations from the expected constant values.

Table 5.6 Analysis of $J_{max}^2 t_{max}$ to determine bismuth nucleation mechanism using eqns. 5.19 and 5.20 using data from Fig. 5.36

Concentration (mmoldm^{-3})	$J_{max}^2 t_{max}(mA^2\ cm^{-4}\ s)$ (calculated)	Instantaneous (theoretical)	Progressive (theoretical)
5	4.23×10^{-4}	8.19×10^{-8}	1.31×10^{-7}
10	1.79×10^{-3}	3.28×10^{-7}	5.22×10^{-7}
15	1.34×10^{-2}(-10 to -30 mV)	7.37×10^{-7}	1.18×10^{-6}
	3.44×10^{-2}(-40 to -80 mV)	7.37×10^{-7}	1.18×10^{-6}
20	1.91×10^{-2}(-10 to -30 mV)	1.31×10^{-6}	2.09×10^{-6}
	5.26×10^{-2}(-40 to -80 mV)	1.31×10^{-6}	2.09×10^{-6}
25	2.44×10^{-2}(-10 to -30 mV)	2.05×10^{-6}	3.27×10^{-6}
	5.04×10^{-2}(-40 to -80 mV)	2.05×10^{-6}	3.27×10^{-6}

Thereafter, expression 5.21 (Cottrell equation) was used to analyse the decaying part of the current transients. The derived plot is given in Fig. 5.37. The diffusion coefficient values found for each step potential was averaged to be $D = 2.4 \times 10^{-7}$ cm^2 s^{-1}. This was compared to the diffusion coefficient values derived from cyclic voltammetry (1.77×10^{-7} cm^2 s^{-1}) and probe beam data (2.2×10^{-7} cm^2 s^{-1}). The value calculated here was lower than those derived from previous methods.
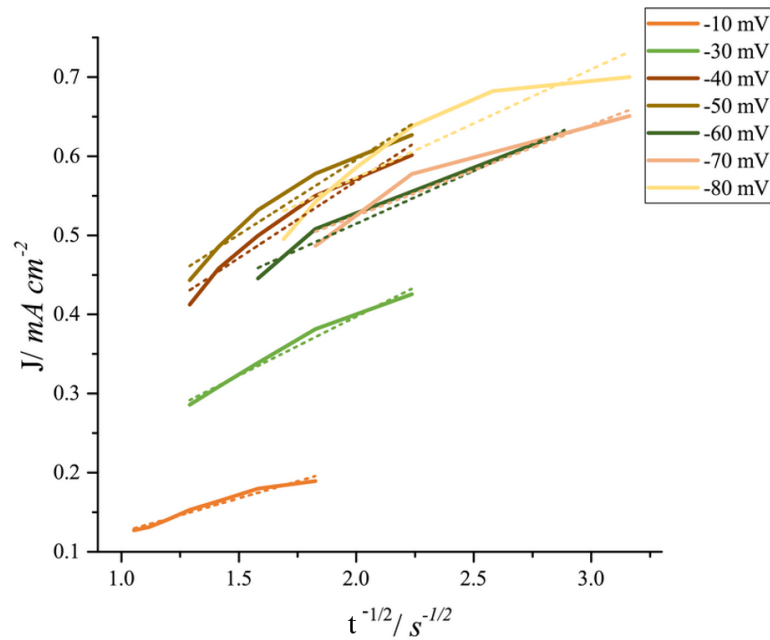

Fig. 5.37 J vs t$^{-1/2}$ plot of decaying portions of the current transients for 20 mmoldm^{-3} BiCl$_3$ in Ethaline 200 at 20 °C using 2 mm Pt disc working electrode (WE), IrO$_2$ coated Ti mesh counter electrode (CE) and Ag pseudo reference electrode (RE)

5.6.3   Analysis of silver/ bismuth co-deposition current transients

Chronoamperometry was used to obtain current transients for simultaneous electrodeposition of silver and bismuth on platinum electrodes. Potential steps applied varied from -10 mV to -100 mV vs silver pseudo reference electrode. The time duration for each scan was ca. 10 seconds. The experiments were repeated for the following $AgCl:BiCl_3$ concentration ratios in Ethaline 200.

Table 5.7 $AgCl:BiCl_3$ concentrations used

[AgCl] (mmoldm^{-3})	[BiCl$_2^-$] (mmoldm^{-3})
5	5
10	10
15	15
20	20
25	25

All current transients showed well defined current maxima J_{max} and a similar shape (Fig. 5.38) indicating similar mechanism of nucleation. Similar to the two previous cases (silver and bismuth) J_{max} vs step potential (-E_f) and t_{max} vs step potential (-E_f) variations were analysed for each concentration (Fig. 5.39). t_{max} decreased with increasing step potentials and increasing concentrations.
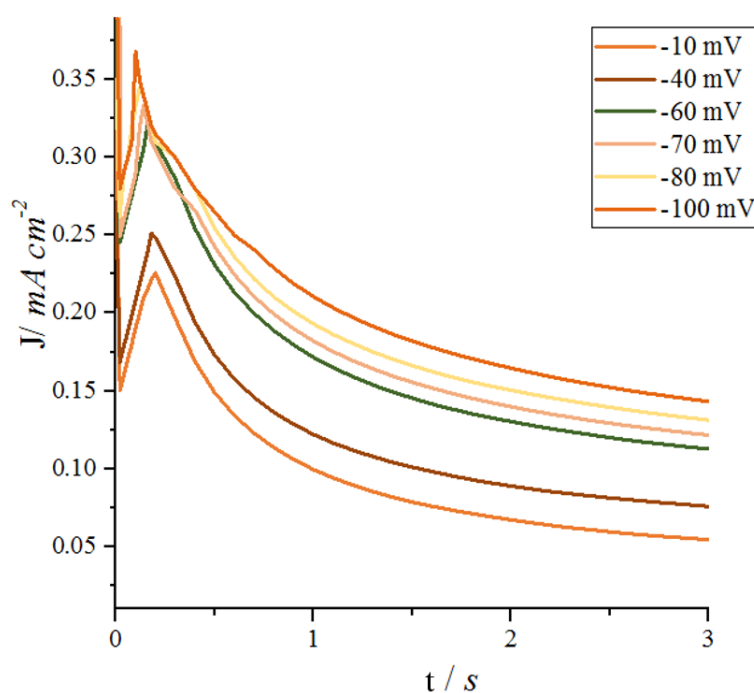

Fig. 5.38   A representative chronoamperometric current density vs time plot for the reduction of Bi(III) and Ag(I) on Pt electrode where Ag(I):Bi(III) concentration ratio is 25 mmoldm^{-3}: 25 mmoldm^{-3} in Ethaline 200 at 20 °C using 2 mm Pt disc working electrode (WE), IrO$_2$ coated Ti mesh counter electrode (CE) and Ag pseudo reference electrode (RE)

Fig. 5.39   Representative J_{max} vs $-E_f$ and t_{max} vs $-E_f$ plots for the reduction of silver/ bismuth mixtures on Pt electrode where Ag(I):Bi(III) concentrations are varied in Ethaline 200 at 20 °C using 2 mm Pt disc working electrode (WE), IrO_2 coated Ti mesh counter electrode (CE) and Ag pseudo reference electrode (RE)
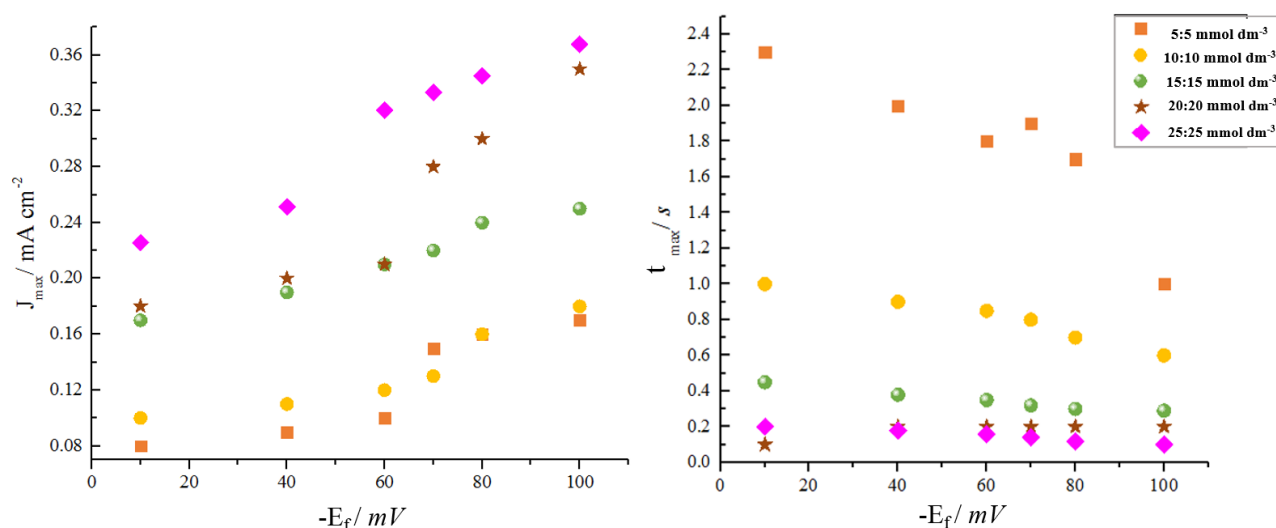
The variations were clear for samples with higher concentrations. We can assume that the error in measurement for J_{max} at low values to be a significant contribution. Sharifker-Mostany and Hills models were used to analyse the nucleation mechanism of this system. Reduced variable plots were used to compare experimental data with theoretical curves for progressive and instantaneous nucleation (Fig. 5.40). Reduced variable plots fell between theoretical instantaneous and progressive lines only in the $t/t_{max} < 1$ region (Fig. 5.40). In this region all current transients closely followed the instantaneous nucleation curve indicating that during initial stages instantaneous nucleation is favoured. The current transients did not give conclusive evidence for the type of mechanism for the $t/t_{max} > 1$ region.

The initial rising part was then analysed with equation 5.13 and 5.14. The outcome is presented in Fig. 5.41. According to these plots, it is clear that J vs $t^{1/2}$ shows a linear trend indicating that nucleation is instantaneous.
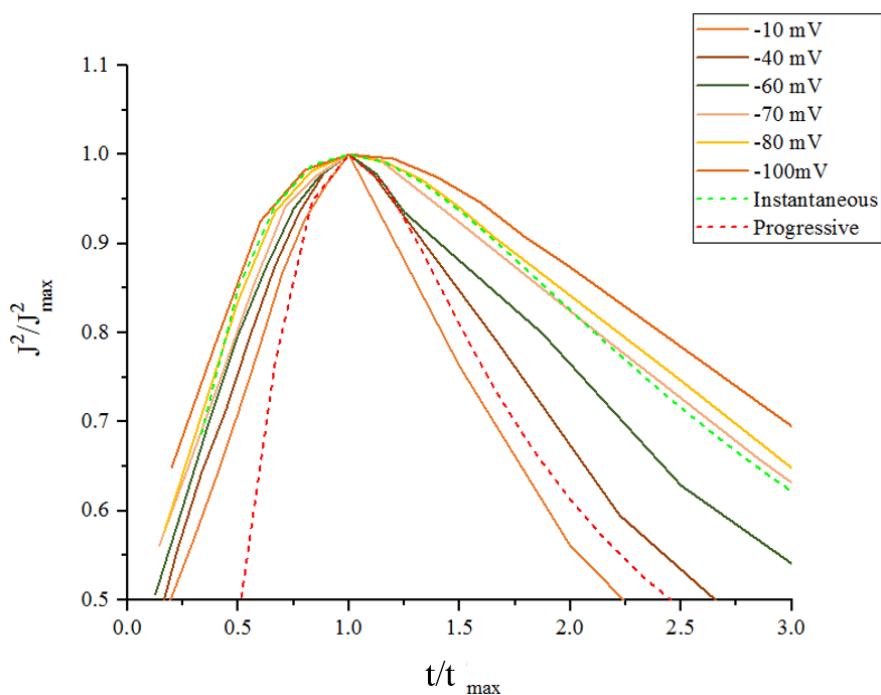
Fig. 5.40   Reduced variable plot for the current transients of 25 mmoldm^{-3}: 25 mmoldm^{-3} AgCl:BiCl$_3$ in Ethaline 200 on Pt working electrode at 20 °C using 2 mm Pt disc working electrode (WE), IrO$_2$ coated Ti mesh counter electrode (CE) and Ag pseudo reference electrode (RE). For classification of the nucleation process i.e. instantaneous and progressive theoretical curves have been shown

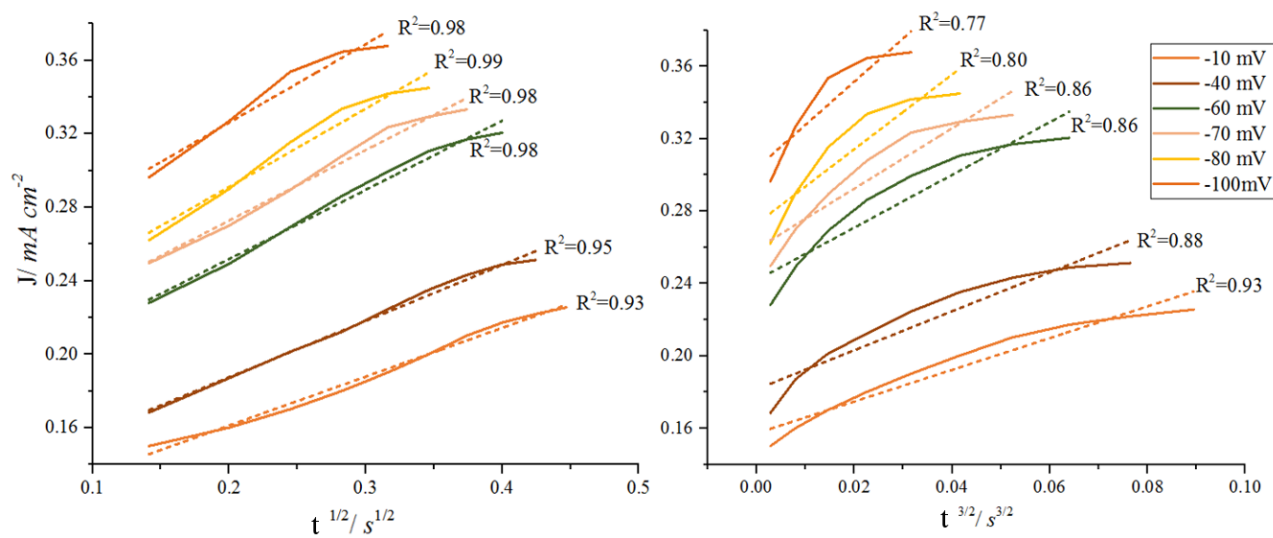**Fig. 5.41**   J vs. t$^{1/2}$ and J vs. t$^{3/2}$ plots for the rising part of the current transients for 25 mmoldm^{-3}: 25 mmoldm^{-3} AgCl:BiCl$_3$ in Ethaline 200 at 20 °C using 2 mm Pt disc working electrode (WE), IrO$_2$ coated Ti mesh counter electrode (CE) and Ag pseudo reference electrode (RE)

To gain further insights, the current transients were further analysed by eqns. 5.18 and 5.19. The calculated $J_{max}^2 t_{max}$ vs step potential graph is given in Fig. 5.42 and $J_{max}^2 t_{max}$ were compared to theoretically derived values (Table 5.8). The comparison did not give conclusive evidence for the type of mechanism since the calculated values were significantly different to predicted theoretical (progressive and instantaneous) values.
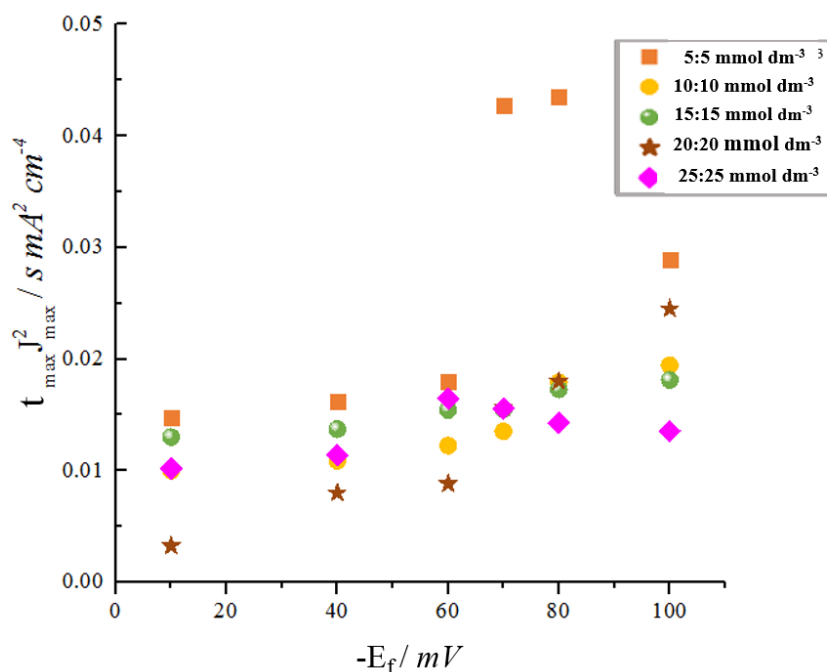

Fig. 5.42 $t_{max} J_{max}^2$ vs E_f of 25 mmoldm^{-3}: 25 mmoldm^{-3} AgCl:BiCl$_3$ in Ethaline 200 at 20 °C using 2 mm Pt disc working electrode (WE), IrO$_2$ coated Ti mesh counter electrode (CE) and Ag pseudo reference electrode (RE).

Table 5.8 Analysis of $J_{max}^2 t_{max}$ to determine nucleation mechanism using eqns. 5.18 and 5.19

Concentration (mmoldm^{-3})	$J_{max}^2 t_{max} (mA^2\ cm^4\ s)$ (calculated)	Instantaneous (theoretical)	Progressive (theoretical)
5	1.95×10^{-2}	2.17×10^{-6}	3.45×10^{-6}
10	1.40×10^{-2}	8.66×10^{-6}	1.38×10^{-5}
15	1.55×10^{-2}	1.95×10^{-5}	3.11×10^{-5}
20	1.50×10^{-2}	3.47×10^{-5}	5.53×10^{-5}
25	1.42×10^{-2}	5.41×10^{-5}	8.64×10^{-5}

Further analysis of the decaying part of the chronoamperometry current transients with Cottrell equation (eqn 5.21) was used to derive diffusion coefficient values for the silver/ bismuth system assuming that it would give the average value of individual diffusion coefficients. The average value for the diffusion coefficient was 5.34×10^{-7} cm^2 s^{-1}. This value was compared to the values derived from Randles-Sevcik equation (where combined diffusion coefficient was found to be 3.57×10^{-7} cm^2 s^{-1}) by cyclic voltammetry and probe beam method (1.65×10^{-7} cm^2 s^{-1} for each species) by chronodeflectometry. The diffusion coefficient derived from Cottrell equation was found to be higher compared to the values derived by the other methods and non-acceptable

compared to the values in literature. The value may have deviated due to the curvature of the plots (see Fig. 5.43) being higher, making the linear regression very small.
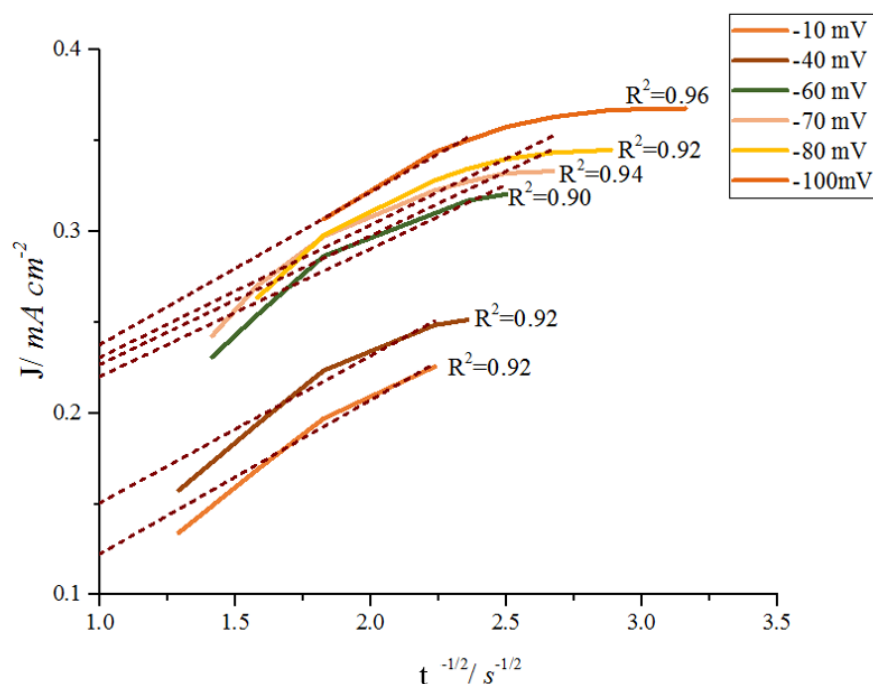

Fig. 5.43   J vs. $t^{-1/2}$ plot for the decaying part of the current transients for 25 mmoldm^{-3}:25 mmoldm^{-3} AgCl:BiCl$_3$ in Ethaline 200 at 20 °C using 2 mm Pt disc working electrode (WE), IrO$_2$ coated Ti mesh counter electrode (CE) and Ag pseudo reference electrode (RE)

5.7   Summary

The electrodeposition of Ag(I), Bi(III) and mixture of Ag(I) and Bi(III) are currently carried out in aqueous media; due to the availability of the wealth of knowledge, academic insight which enables control over deposit morphology, composition and kinetic factors. Here we explore the deposition of these metal systems using deep eutectic solvent, Ethaline 200 (which has many advantages over aqueous solvents).

We were able to deduce diffusion coefficients, mechanism of nucleation and growth (for initial stages) using widely accepted models developed by Sharifker, Hills and Monstany for deposition of silver, bismuth and co-deposition of silver/ bismuth in choline chloride based deep eutectic solvent Ethaline 200.

Silver, bismuth and silver/ bismuth systems were quasi-reversible and their diffusion coefficients were calculated by the Randles-Sevcik equation and the Cottrell equation, and were averaged (see below).

		Randles-Sevcik study		Cottrell study	Stripping efficiency
Ag (I)	:	2.01×10^{-7} cm^{2}s^{-1}	:	2.16×10^{-7} cm^{2}s^{-1}	89%
Bi (III)	:	1.65×10^{-7} cm^{2}s^{-1}	:	2.40×10^{-7} cm^{2}s^{-1}	74%
Combined values for Ag(I), Bi (III)	:	3.57×10^{-7} cm^{2}s^{-1}	:	5.35×10^{-7} cm^{2}s^{-1}	36%

The stripping efficiencies for each metal system were calculated and silver/ bismuth showed poor stripping efficiencies (see above). The application of reduced non-dimensional nucleation and initial growth models showed (eqn 5.11 and eqn 5.12) that nucleation of silver was instantaneous at high overpotentials but became progressive at lower overpotentials. The same trend was seen for bismuth nucleation as well. However, for co-deposition of silver/ bismuth, the nucleation mechanism showed instantaneous behaviour only during $t/t_{max} < 1$ region. The theoretical model was not able to give conclusive evidence for $t/t_{max} > 1$ region and may have a combination of instantaneous and progressive nucleation. The nucleation in this region may be further complicated by availability of multiple species. e.g. $[AgCl_2]^-$, $[AgCl_2]^{2-}$, $[BiCl_4]^-$

The nucleation processes for these metal systems were further analysed by using eqn 5.14 and eqn 5.16 models for the initial rising part. According to these models for silver, nucleation was instantaneous at high overpotentials but progressive for lower overpotentials. However, this model derived instantaneous nucleation for bismuth and silver/ bismuth systems for the whole potential range which was contrary to that predicted by the previous method (eqn 5.11 and eqn 5.12). The model $t_{max}J_{max}^2$ used for the same purpose did not give conclusive evidence due to the unexpected variance it with the concentration. Therefore the non-dimensional reduced plots can be considered as the most suitable model to analyse the nucleation of silver and bismuth in DES.

References

1 N. Elgrishi, K. J. Rountree, B. D. McCarthy, E. S. Rountree, T. T. Eisenhart and J. L. Dempsey, Journal of Chemical Education, 2017, **95**, 197–206.

2 A. P. Abbott, G. Frisch, J. Hartley, W. O. Karim and K. S. Ryder, Progress in Natural Science: Materials International, 2015, **25**, 595–602.

3 S. Fletcher, C. Halliday, D. Gates, M. Westcott, T. Lwin and G. Nelson, Journal of Electroanalytical Chemistry and Interfacial Electrochemistry, 1983, **159**, 267–285.

4 D. Buttry, In Electroanalytical Chemistry; Bard, AJ, Ed, 1991.

5 M. R. Deakin and D. A. Buttry, Analytical Chemistry, 1989, **61**, 1147–1154.

6 A. Bund, Journal of Solid State Electrochemistry, 2004, **8**, 182–186.

7 A. P. Abbott, S. Nandhra, S. Postlethwaite, E. L. Smith and K. S. Ryder, Physical Chemistry Chemical Physics, 2007, **9**, 3735–3743.

8 A. R. Hillman, I. Efimov and M. Skompska, Journal of the American Chemical Society, 2005, **127**, 3817–3824.

9 A. J. Bard, L. R. Faulkner, J. Leddy and C. G. Zoski, Electrochemical methods: fundamentals and applications, wiley New York, 1980, vol. 2.

10 A. Mashreghi and H. Zare, Current Applied Physics, 2016, **16**, 599–604.

11 B. Scharifker and G. Hills, Electrochimica Acta, 1983, **28**, 879–889.

12 B. Scharifker and J. Mostany, Journal of Electroanalytical Chemistry and Interfacial Electrochemistry, 1984, **177**, 13–23.

13 G. Hills, D. Schiffrin and J. Thompson, Electrochimica Acta, 1974, **19**, 657–670.

14 G. Gunawardena, G. Hills, I. Montenegro and B. Scharifker, Journal of Electroanalytical Chemistry and Interfacial Electrochemistry, 1982, **138**, 225–239.

15 M. Abyaneh and M. Fleischmann, Journal of Electroanalytical Chemistry and Interfacial Electrochemistry, 1981, **119**, 187–195.

16 A. Abbott, M. Azam, K. Ryder and S. Saleem, Transactions of the IMF, 2018, **96**, 297–303.

17 G. Oskam, J. Long, A. Natarajan and P. Searson, Journal of Physics D: Applied Physics, 1998, **31**, 1927.

18 M. Palomar-Pardavé, B. Scharifker, E. Arce and M. Romero-Romo, Electrochimica Acta, 2005, **50**, 4736–4745.

Chapter 6

Rotating disk electrode study and analysis of silver-bismuth thin films

Contents

6.1 Introduction

The study of nucleation, growth kinetics, electrochemical investigations involves the analysis of consumption of the reactants during electrodeposition of metals(Chapter 5). They do not investigate products which can be either individual metals, composites, intermetallics or alloys. The Simultaneous Thickness and Electrochemical Potential measurement (STEP) experiments on the other hand would indicate whether the metals form intermetallics. X-ray diffractometry (XRD) would assist in identification of these news alloy phases.

Chapter 6 also investigates application of Hydrodynamic electrodes (mainly RDE) for the study of the deposition of silver, bismuth and silver-bismuth systems. Further details of this method were given in Chapter 2.

6.2 Application of rotating disc electrode (RDE) in deep eutectic solvents (DES)

The application of RDE methods to DES can be difficult due to high viscosity of DES. To overcome this and to achieve steady state conditions, high rotation speeds and lower scan rates were used.[1] Despite this drawback there have been several applications of RDE for metal electrodeposition in ionic liquids and deep eutectic solvents. A summary of reported applications of RDE in DES is given in Table 6.1.

Overall RDE has shown as a good method for the study of electrodeposition in DES. However, bismuth (with particularly Pt and Au working electrodes), silver and bismuth-silver systems have not been studied before using RDE. Therefore, it is important to further the understanding of the electrochemical behaviour of these systems for successful electrodeposition.

The experimental setup of RDE and the theory of hydrodynamic electrodes have been discussed in Chapter 2. The procedures for preparing solutions were given in chapter 3. Rotating discs were used as working electrodes (WE). The disc electrodes used were made of platinum (diameter = 3mm) and gold (diameter = 3mm).The electrode surfaces were polished to a mirror finish with alumina powder (0.3 μm), rinsed with deionised water, acetone and dried with compressed nitrogen prior to each experiment. All experiments were carried out at room temperature (20 °C). Iridium oxide coated titanium mesh counter electrode and silver pseudo reference electrode were used as the other two electrodes in the three electrode setup for all the experiments. Linear sweep voltammetry (LSV) was conducted for all systems separately using +0.7 V to −0.7 V as the potential range and 100 to 3600 (RPM) rotation speeds. The experiments were repeated for two scan rates and two concentrations for each system (see Table 6.2). For each metal system discussed here, multiple experiments were carried out for each type of working electrode (i.e. Pt and Au) to check for reproducibility of results.

Table 6.1   Applications of RDE in DES reported to date

Metal deposited	Metal salt used	System temperature /°C	Solvent	Reference electrode	Working electrode	Reference publication
Ga and Cu-Ga alloys	Anhyd. $CuCl_2$ Anhyd. $GaCl_3$	60	Reline 200	Ag	Mo	Steichen et al.[2]
Zn	$ZnCl_2$	30	Ethaline 200	Zn	Glassy carbon	Vieira et al.[3]
Cu	Anhyd. $CuCl_2$	25-35	Ethaline 200	Pt	Pt	Lloyd et al.[4,5]
Zn	$ZnCl_2$	30	Ethaline 200	Zn	Glassy carbon, stainless steel, Au, Pt, Cu, Zn	Vieira et al.[6]
Mn	$MnCl_2 \cdot H_2O$	80	Reline 200	Ag	Pt	Sides er al.[1]
Cu-In alloy	Anhyd. CuCl Anhyd. $InCl_3$	60	Reline 200	Ag	Mo	Malaquias et al.[7]
Sn, Bi, Sn-Bi alloy	[NnBu₄][a][SnCl₃] [NnBu₄][a][BiCl₄]	20	Ethaline 200	Not given	Glassy carbon	Vieira et al.[8]

[a]Tetrabutyl ammonium chloromalate salt $[(CH_3CH_2)_3]_4^{-}[N^{+}-Cl^{-}$

Table 6.2 The RDE experiments conducted for the systems under investigation

Experiments	Scan rate = 5 mVs⁻¹		Scan rate = 10 mVs⁻¹	
100 mmol dm-3 AgCl/ Ethaline 200	Au	Pt	Au	Pt
50 mmol dm-3 AgCl/ Ethaline 200	Au	Pt	Au	Pt
5 mmol dm-3 BiCl3/ Ethaline 200	Au	Pt	Au	Pt
10 mmol dm-3 BiCl3/ Ethaline 200	Au	Pt	Au	Pt
5:5 mmol dm-3 AgCl:BiCl3/ Ethaline 200	Au	Pt	Au	Pt
10:10 mmol dm-3 AgCl:BiCl3/ Ethaline 200	Au	Pt	Au	Pt

Key: Au - gold RDE working electrode and Pt - platinum RDE working electrode.

6.2.1 Current transients for silver, bismuth deposition and co-deposition of silver-bismuth

Firstly, hydrodynamic voltammetry was carried out and the current transients were plotted (I/mA vs E/V) for each rotation speed. The limiting currents observed (I_L) was plotted with the square root of rotation speed ($\omega^{1/2}$) for each system to derive Levich plots (see Chapter 2) and calculate the diffusion coefficient for each mobile species. Secondly, Koutecky – Levich plots for all systems were drawn using the rising portion of the exponential curves obtained from LSV and I_K (current at which no mass transfer effects exist) was calculated from the intercept of these plots for each selected potential. Thirdly, using the relationship $I_K = nFAk_HC$ and substituting values for each applied potential k_H (heterogeneous rate constants) were found. Thereafter by using the relationship: $\ln k_H = \ln k_0 + (\alpha F/RT) \eta$ and plotting $\ln k_H$ vs. η for each system the transfer coefficient (α) and the standard rate constant (k_0) for each metal deposition system were found. More details on these parameters were given in Chapter 2. Finally, the values calculated were tabulated for comparison purposes. For the ease of explanation, the graphs for each system for each electrode are grouped and specific comments for each system are given separately. All experiments were conducted at 20 °C.

6.2.2 Analysis of silver deposition

In these experiments the forced convection is applied by RDE that spins the solution away from the electrode while drawing the fresh reactants towards the electrode surface. This ensures the swift removal of product formed (if the product is soluble) and the steady supply of new reactants to the electrode. As discussed in the second chapter, knowing whether a laminar flow is maintained is an important aspect for RDE analysis and this can be done by calculation of Reynolds number for the system. For the current study the Reynolds number was calculated using Eqn 6.1 and the value obtained (i.e. 3301 for highest rotation rate) was less than 1×10^5

hence the flow was deemed as laminar.

$$Re = \frac{r^2\,\omega}{\bar{\nu}}$$

(6.1)

where r - radius of the electrode (5×10^{-3} m)

ω - speed of rotation (3600 rad s^{-1})

$\bar{\nu}$ - kinematic viscosity (2.726×10^{-5} m^{2}s^{-1})

The convection of the solution maintains uniform concentration in the bulk of solution. However the layer that is formed in the near electrode volume (hydrodynamic boundary layer) tend to rotate with the electrode. From the frame of reference of the electrode this layer appears stagnant. The convection control mass transport occurring in the bulk solution becomes less important in the stagnant hydrodynamic boundary layer. This creates a layer where diffusion becomes the dominant mass transport method. The thickness of this smaller diffusion layer is ca. 20 times thinner than that of the stagnant layer.

For the RDE experiments, the linear sweep experiments were conducted from $+0.7$ V to -0.7 V for different rotation rates. When the working electrode is stationary the current reaches a peak at which the mass transport becomes limited and the current starts to decay (Chapter 5). However, the RDE exhibits a different current response and a limiting current plateau is observed. Another feature to notice is the increase in this current plateau with the increase in rotation rates. This indicates that the increase in rotation speed (hence convection mass transport) increase the current response by replenishing the electrode surface faster with fresh reactants.

Fig. 6.1 and Fig. 6.2 shows results obtained from the linear sweep voltammogram for different rotation rates for reduction of Ag(I) to Ag(0) in 0.01 mol dm^{-3} AgCl in Ethaline 200, at 10 mVs^{-1} scan rate, at 20 °C with platinum RDE. Analysis using Levich plot of limiting current (I) versus rotation rate ($\omega^{1/2}$) from data (Fig. 6.3), Koutecký-Levich plot (Fig. 6.4),plot of overpotential (η) vs ln k$_H$ that was used to calculate k$_0$ and α (Fig. 6.5) are also given.

Fig. 6.6 and Fig. 6.7 shows results obtained from the linear sweep voltammogram for different rotation rates for reduction of Ag(I) to Ag(0) in 0.01 mol dm^{-3} AgCl in Ethaline 200, at 10 mVs^{-1} scan rate, at 20 °C with gold RDE. Analysis using Levich plot of limiting current (I) versus rotation rate ($\omega^{1/2}$) from data (Fig. 6.8), Koutecký-Levich plot (Fig. 6.9),plot of overpotential (η) vs ln k$_H$ that was used to calculate k$_0$ and α (Fig. 6.10) are also given.
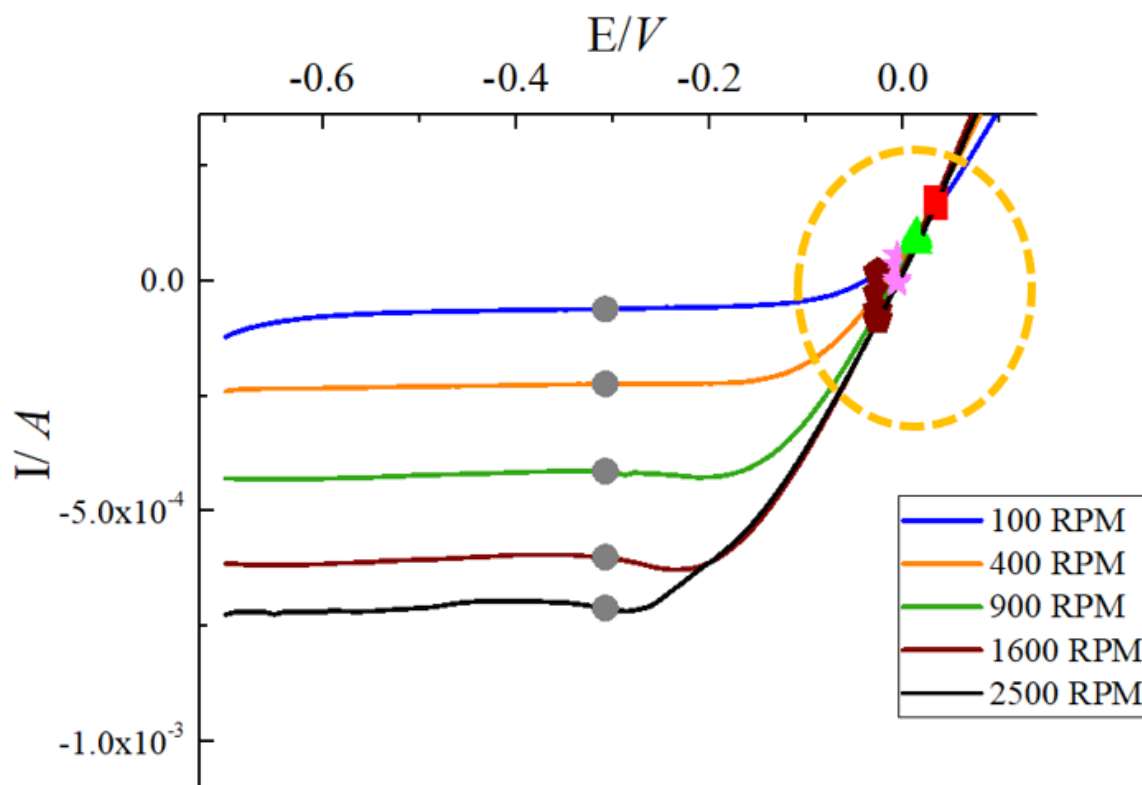
Fig. 6.1 (a) Linear sweep voltammogram for different rotation rates for reduction of Ag(I) to Ag(0) in 0.01 moldm^{-3} AgCl in Ethaline 200, 10 mVs^{-1} scan rate, at 20 °C with **platinum** RDE working electrode, IrO$_2$ coated titanium mesh counter electrode (CE) and Ag pseudo reference electrode (RE).The area within the circle is expanded in Fig. 6.2
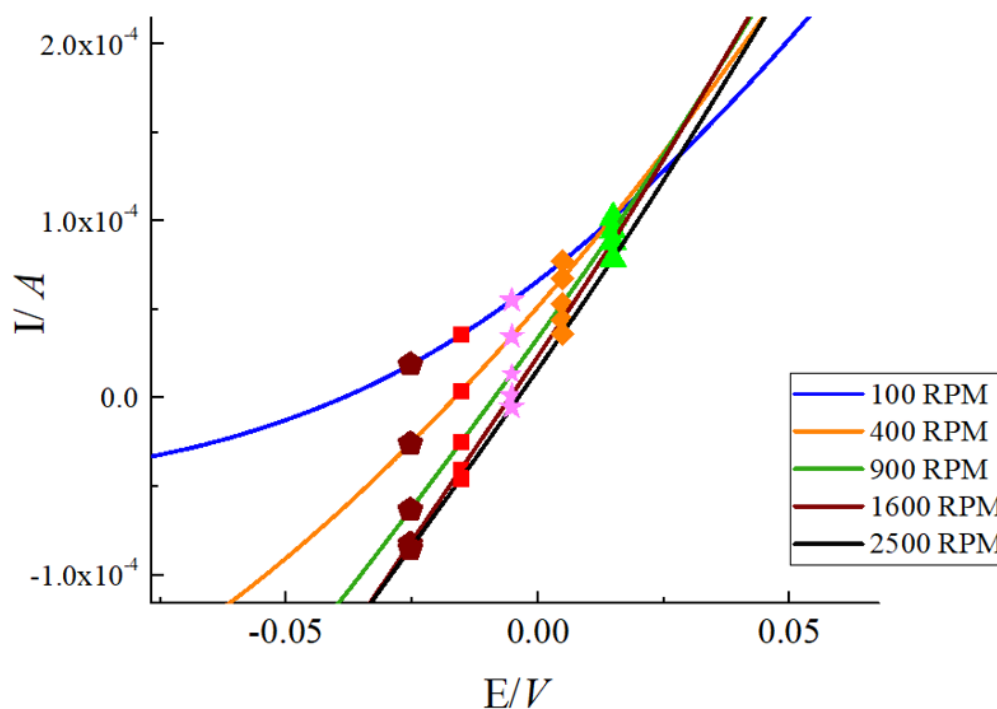

Fig. 6.2 (a) Rising part of the linear sweep voltammogram for different rotation rates for reduction of Ag(I) to Ag(0) in 0.01 moldm^{-3} AgCl in Ethaline 200, 10 mVs^{-1} scan rate, at 20 °C with **platinum** RDE working electrode, IrO$_2$ coated titanium mesh counter electrode (CE) and Ag pseudo reference electrode (RE)
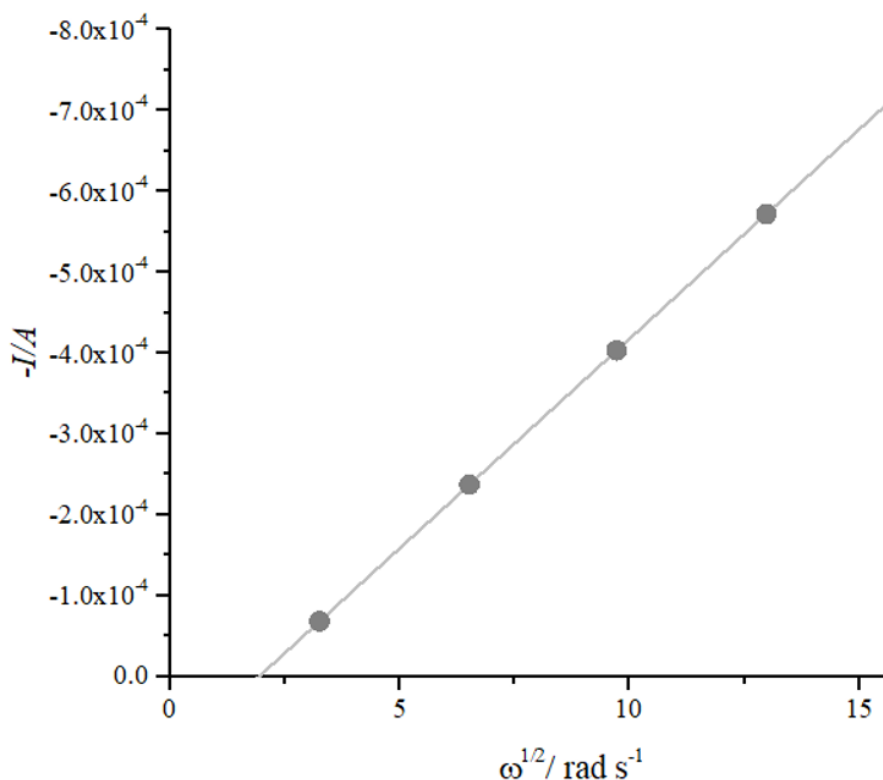
Fig. 6.3 Levich plot of limiting current versus rotation rate ($\omega^{1/2}$) from data in Fig. 6.1 for reduction of Ag(I) to Ag(0) in 0.01 moldm^{-3} AgCl in Ethaline 200, -10 mVs^{-1} scan rate, at 20 °C with **platinum** RDE working electrode, IrO$_2$ coated titanium mesh counter electrode (CE) and Ag pseudo reference electrode (RE)
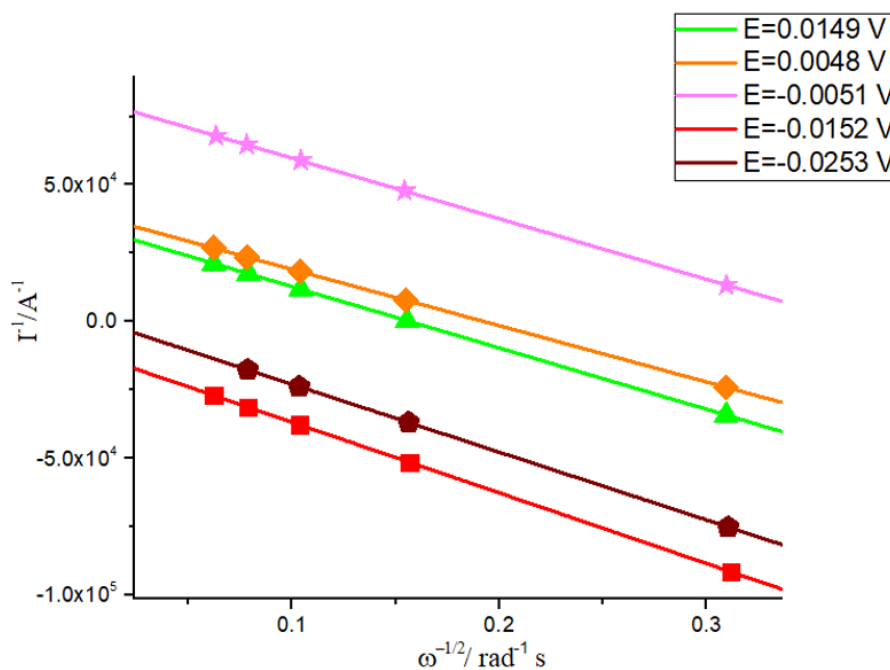

Fig. 6.4 Koutecky-Levich plot of inverse of limiting current versus rotation rate ($\omega^{-1/2}$) from data in Fig. 6.1 for reduction of Ag(I) to Ag(0) in 0.01 moldm^{-3} AgCl in Ethaline 200, 10 mVs^{-1} scan rate, at 20 °C with **platinum** RDE working electrode, IrO$_2$ coated titanium mesh counter electrode (CE) and Ag pseudo reference electrode (RE)

Fig. 6.5   Plot of overpotential (η) vs ln k_h from data shown in Fig. 6.6 that was used to calculate k_0 and α.

Fig. 6.6   Linear sweep voltammogram for different rotation rates for reduction of Ag(I) to Ag(0) in 0.01 moldm^{-3} AgCl in Ethaline 200, 10 mVs^{-1} scan rate, at 20 °C with **gold** RDE working electrode, IrO$_2$ coated titanium mesh counter electrode (CE) and Ag pseudo reference electrode (RE).The area within the circle is expanded in Fig. 6.7
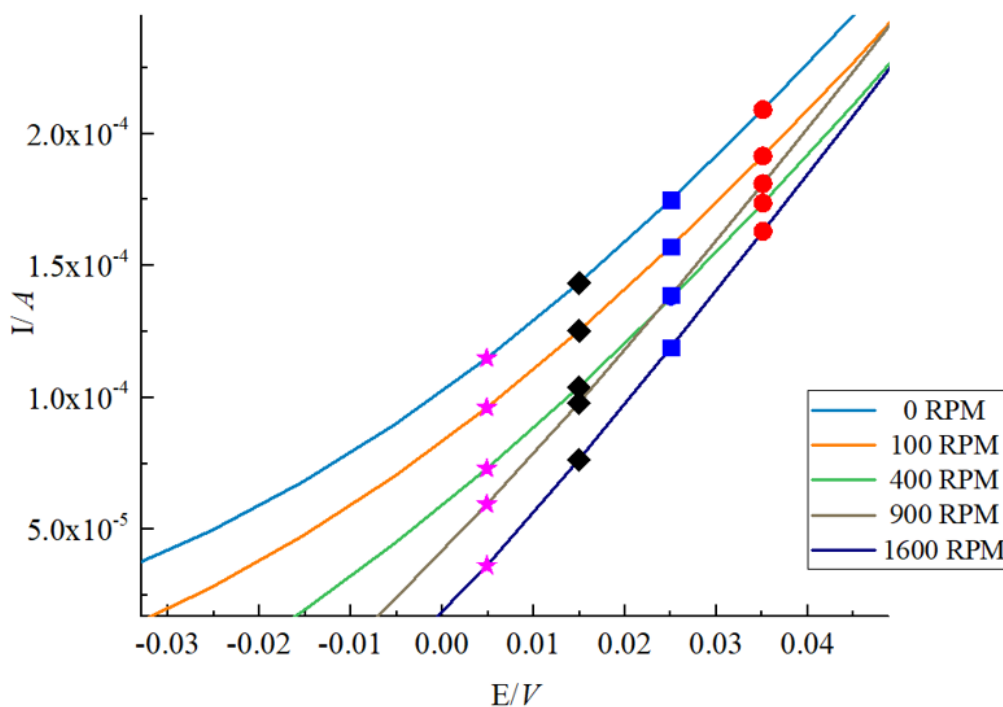
Fig. 6.7 Rising part of the linear sweep voltammogram for different rotation rates for reduction of Ag(I) to Ag(0) in 0.01 moldm^{-3} AgCl in Ethaline 200, 10 mVs^{-1} scan rate, at 20 °C with **gold** RDE working electrode, IrO$_2$ coated titanium mesh counter electrode (CE) and Ag pseudo reference electrode (RE)
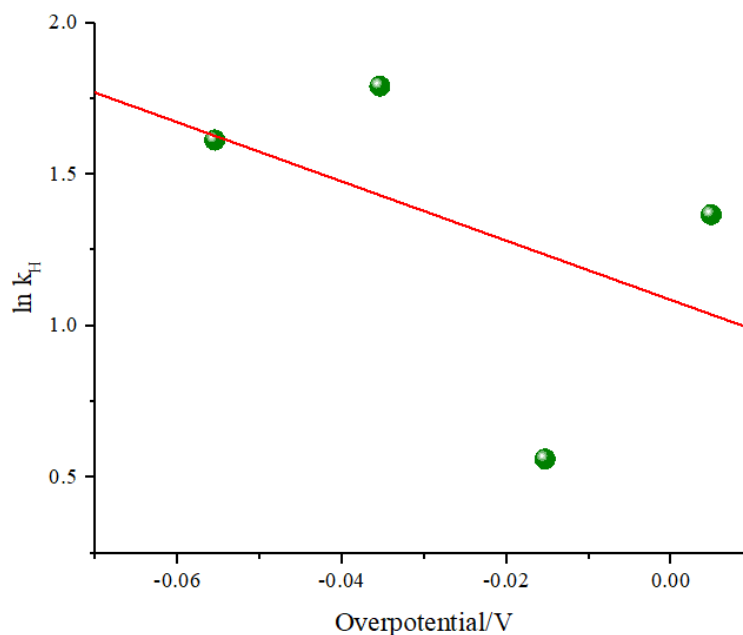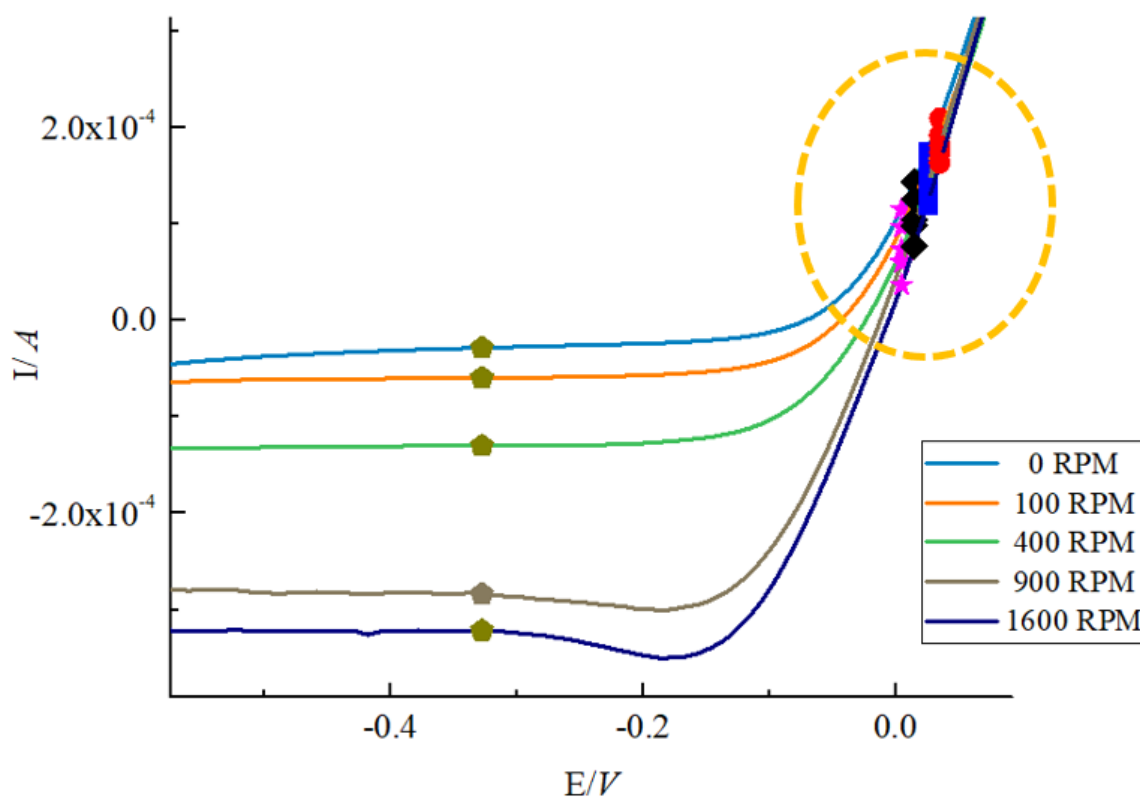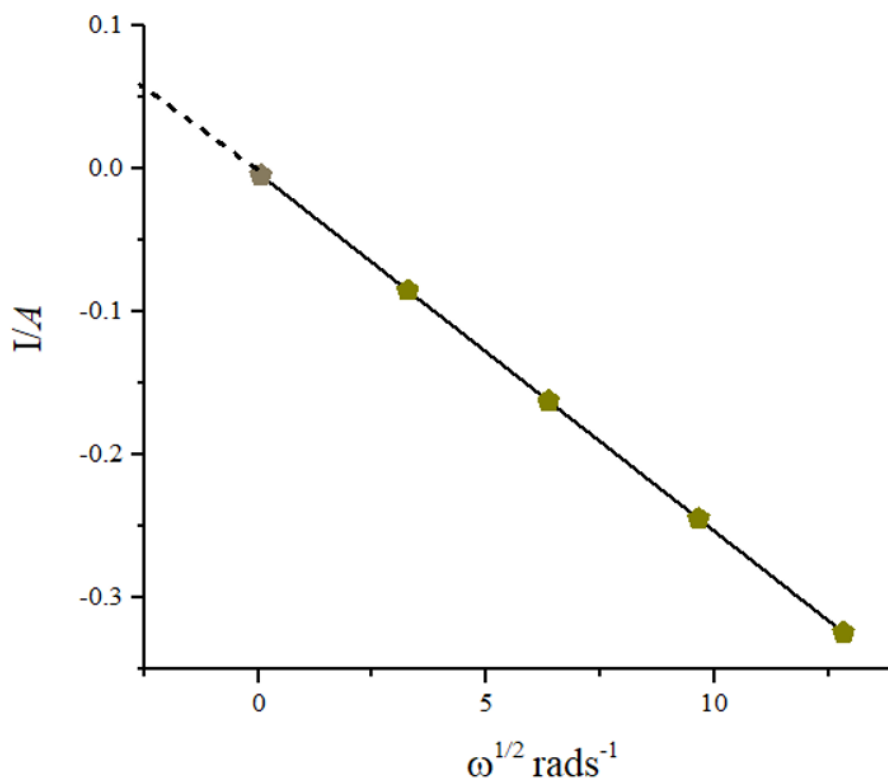

Fig. 6.8 Levich plot of limiting current versus rotation rate ($\omega^{1/2}$) from data in Fig. 6.6 for reduction of Ag(I) to Ag(0) in 0.01 moldm^{-3} AgCl in Ethaline 200, 10 mVs^{-1} scan rate, at 20 °C with **gold** RDE working electrode, IrO$_2$ coated titanium mesh counter electrode (CE) and Ag pseudo reference electrode (RE)

Fig. 6.9 Koutecky-Levich plot of inverse of limiting current versus rotation rate ($\omega^{-1/2}$) from data in Fig. 6.6 for reduction of Ag(I) to Ag(0) in 0.01 moldm^{-3} AgCl in Ethaline 200, 10 mVs^{-1} scan rate, at 20 °C with **gold** RDE working electrode, IrO$_2$ coated titanium mesh counter electrode (CE) and Ag pseudo reference electrode (RE).
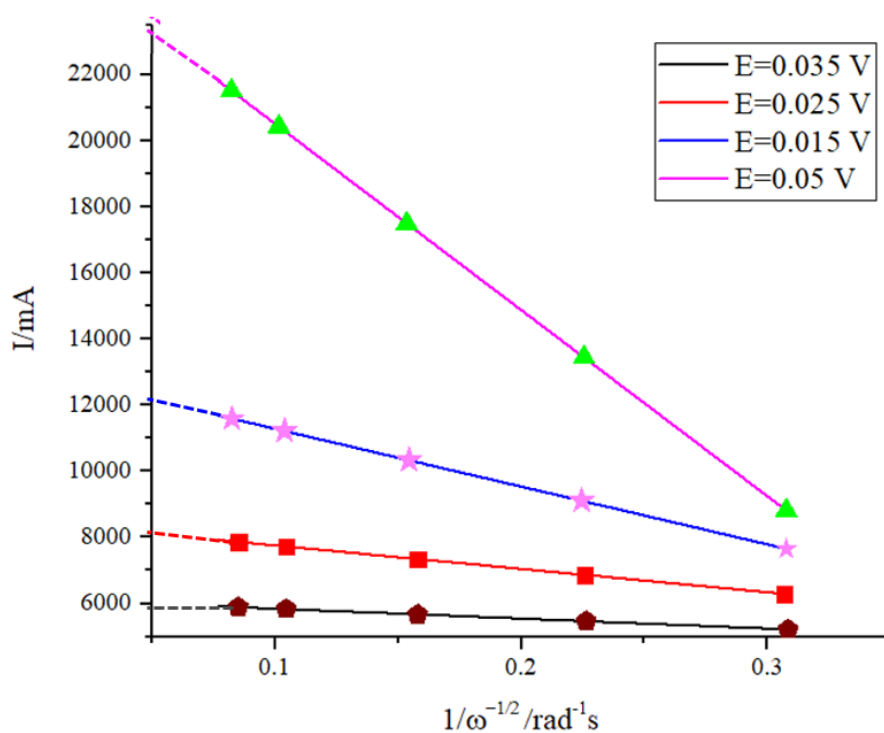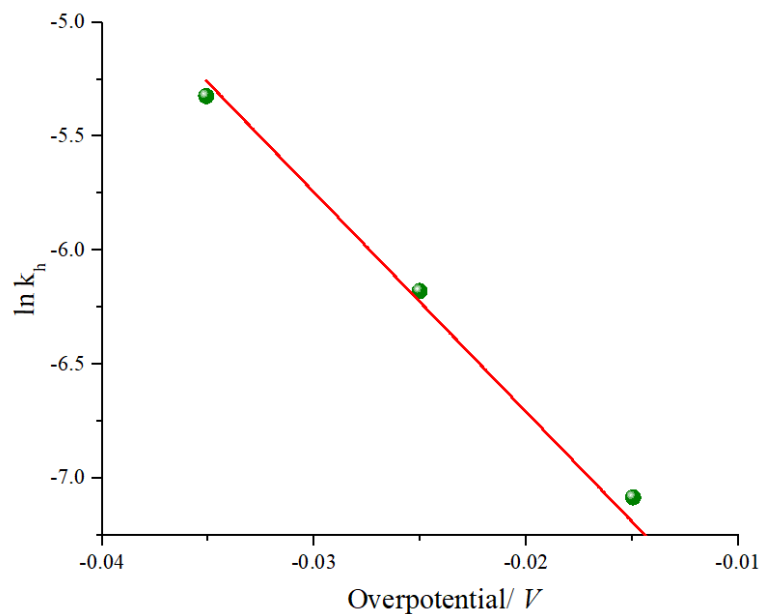

Fig. 6.10 Plot of overpotential (η) vs ln k$_H$ from data shown in Fig. 6.6 that was used to calculate k$_0$ and α.

By −0.3 V all rotation speeds have reached the current maximum for both gold and platinum disc electrodes. At large cathodic overpotentials the characteristics of the electrode reaction were dominated by the rate of forward reaction (reduction). At large overpotentials, the kinetics are rapid, so the response is dominated by mass transport. At a certain high negative overpotential for gold and platinum RDE electrodes (ca. -0.3 V) the kinetics cease to depend on overpotential (see Fig. 6.1 and Fig. 6.6). The surface concentration of the metal ions species may reach zero and hence increasing the overpotential can no longer result in an increase in current. At this point the system becomes completely mass transport controlled. This explains the plateau in current observed in Fig. 6.1 and Fig. 6.6 can be defined as the limited current.

The limiting currents for all three electrode systems were analysed by applying Levich model which can be used to derive diffusion coefficients for the mobile species (plot (b) of Fig. 6.3 and Fig. 6.3). The values derived are discussed in Table 6.3.

At overpotentials which are lower than those observed for limiting current, the rate constants show a dependency on overpotential. The hypothetical case where the rate of rotation reaches infinity while avoiding the transition from laminar to turbulent flow can be considered here. In this scenario the Nernst layer thickness would become zero and the mass transport control would cease to exist. As a result, the surface and bulk concentration would be equal. The current observed would be purely kinetically controlled. This aspect has been analysed by Koutecky-Levich analysis in Fig. 6.4 and Fig. 6.9.

Plots of ln k_h vs overpotential were used to calculate k_0 and α for each system (Fig. 6.5 and Fig. 6.10). This distortion of the exponential curve and the high overpotential needed to overcome the kinetic barrier to reach the mass transport controlled limiting current indicate slow kinetics. The substrate has a strong influence on the nucleation and the initial growth stage of thin films but these effects depreciate as the deposit outgrow few monolayers.[1] The study by Badea et al. report that cathodic depositions are catalysed by platinum electrodes and the onset of these reactions are pushed to high negative values with the use of inert electrodes such as glassy carbon.[9]

Although Ethaline is the most conductive and least viscous deep eutectic solvent known to date[10] hence the diffusion coefficients were only ten fold less than these in water. The average diffusion coefficient obtained for silver with platinum system was 3.58E-07$\pm$ 0.05 cm^2 s^{-1} and this value was 3.28E-07$\pm$ 0.05 cm^2 s^{-1} was for the gold electrode system. Transfer co-efficient can be calculated to be ca. 0.20$\pm$ 0.05. Standard rate constant for each substrate, transfer co-efficient etc. are given in the table.

Table 6.3 The calculated values for the Diffusion coefficient (D), Transfer coefficient (α) and standard rate constant (k_0) are tabulated below.

	Potential/V	Diffusion Coefficient D / cm^2 s^{-1}	Transfer coefficient (α)	k_0/cm s^{-1}
	-0.05	1.83E-06		
	-0.15	9.55E-07		
Ag-Pt	-0.25	1.09E-07	1.45E-01	1.57E-05
	-0.35	1.20E-07		
	-0.45	**1.30E-07**		
	0.035	9.64E-06		
Ag-Au	0.025	2.68E-07	2.43E-01	1.78E-05
	0.015	6.88E-07		
	0.005	**1.19E-07**		

6.2.3   Analysis of bismuth deposition

Fig. 6.11 to Fig. 6.15 gives results obtained from linear sweep voltammogram for different rotation rates for reduction of Bi(III) to Bi(0) in 0.01 moldm^{-3} BiCl$_3$ in Ethaline 200, at 10 mVs^{-1} scan rate, at 20 °C with platinum RDE. The analysis using Levich plot of limiting current versus rotation rate ($\omega^{1/2}$) is given in Fig. 6.13. The Koutecký-Levich plot is given in Fig. 6.14 whereas the plot of overpotential (η) vs ln k$_H$ that was used to calculate k$_0$ and α is given in Fig. 6.15.

Fig. 6.16 to Fig. 6.20 gives results obtained from linear sweep voltammogram for different rotation rates for reduction of Bi(III) to Bi(0) in 0.01 moldm^{-3} BiCl$_3$ in Ethaline 200, at 10 mVs^{-1} scan rate, at 20 °C with platinum RDE. The analysis using Levich plot of limiting current versus rotation rate ($\omega^{1/2}$) is given in Fig. 6.13. The Koutecký-Levich plot is given inFig. 6.14 whereas the plot of overpotential (η) vs ln k$_H$ that was used to calculate k$_0$ and α is given in Fig. 6.20.

By −0.2 V all current responses measured for every rotation speed have reached the current maximum for platinum. (see Fig. 6.11). This value for gold was -0.3 V. The calculated values for the diffusion coefficient(D) for bismuth mobile species transfer coefficient (α) and standard rate constant (k$_0$) were calculated and tabulated in the Table 6.4. Average diffusion coefficient for bismuth mobile species calculated for platinum electrode system was 7.37E-07 cm^{-2}s^{-1} whereas the value for gold substrate was 2.56E-07 cm^{-2}s^{-1}. The standard rate constant was found to be 2.89E-05 cms^{-1}. Transfer coefficient alpha showed a significant difference in value for the two substrates. Standard rate constant for bismuth deposition on platinum substrate was 4 times larger that for gold substrate.
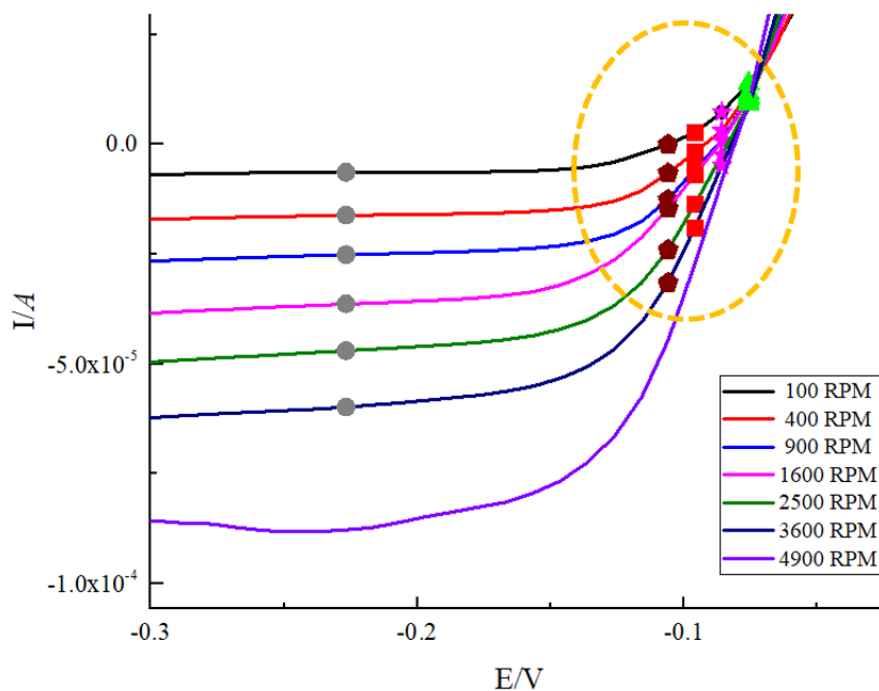
Fig. 6.11 (a) Linear sweep voltammogram for different rotation rates for reduction of Bi(III) to Bi(0) in 0.01 moldm-3 BiCl$_3$ in Ethaline 200, 10 mVs^{-1} scan rate, at 20 °C with **platinum** RDE working electrode, IrO$_2$ coated titanium mesh counter electrode (CE) and Ag pseudo reference electrode (RE).The area within the circle is expanded in Fig. 6.2
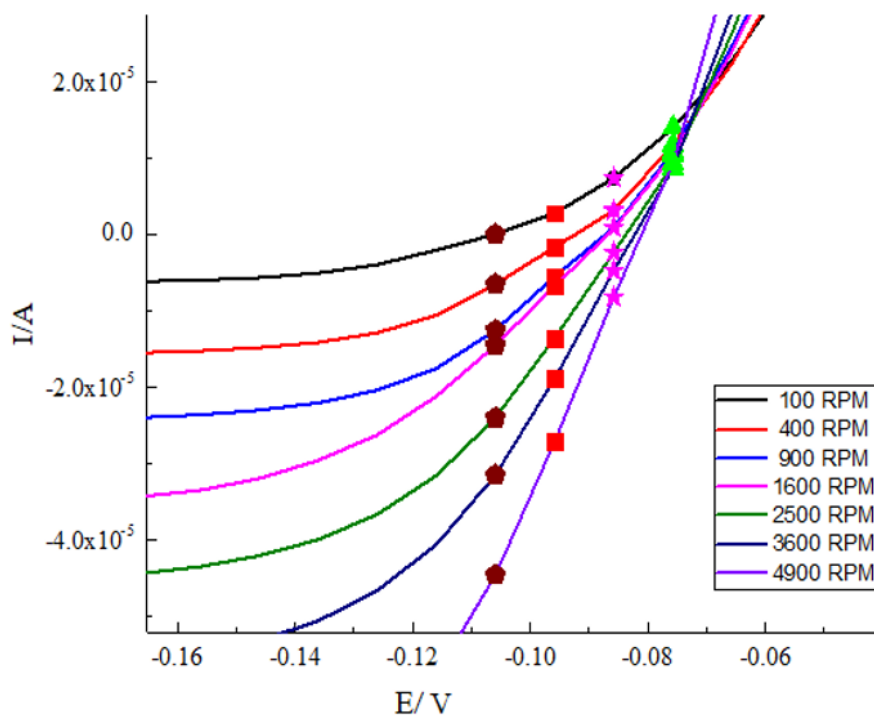

Fig. 6.12 (a) Rising part of the linear sweep voltammogram for different rotation rates for reduction of Bi(III) to Bi(0) in 0.01 moldm-3 BiCl$_3$ in Ethaline 200, 10 mVs^{-1} scan rate, at 20 °C with **platinum** RDE working electrode, IrO$_2$ coated titanium mesh counter electrode (CE) and Ag pseudo reference electrode (RE)

Fig. 6.13 Levich plot of limiting current versus rotation rate ($\omega^{1/2}$) from data in Fig. 6.1 for reduction of reduction of Bi(III) to Bi(0) in 0.01 moldm-3 BiCl$_3$ in Ethaline 200, 10 mVs^{-1} scan rate, at 20 °C with **platinum** RDE working electrode, IrO$_2$ coated titanium mesh counter electrode (CE) and Ag pseudo reference electrode (RE).

Fig. 6.14 Koutecky-Levich plot of inverse of limiting current versus rotation rate ($\omega^{-1/2}$) from data in Fig. 6.1 for r reduction of Bi(III) to Bi(0) in 0.01 moldm-3 BiCl$_3$ in Ethaline 200, 10 mVs^{-1} scan rate, at 20 °C with **platinum** RDE working electrode, IrO$_2$ coated titanium mesh counter electrode (CE) and Ag pseudo reference electrode (RE).
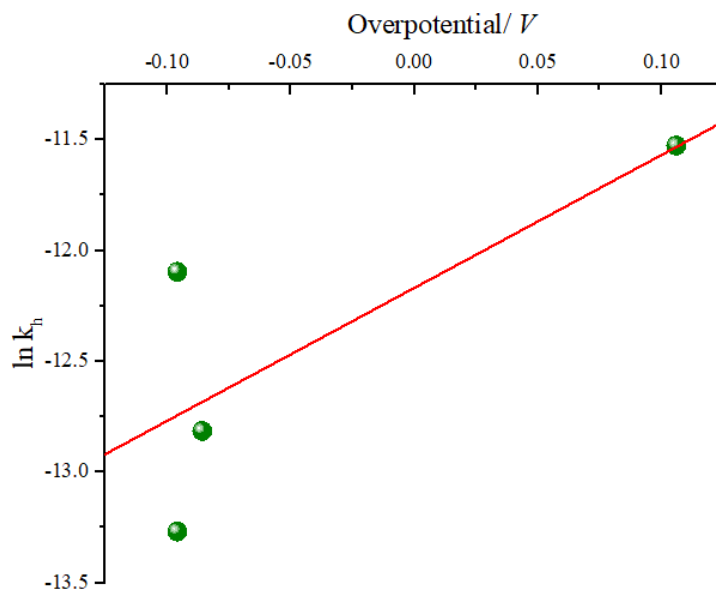
Fig. 6.15 Plot of overpotential (η) vs ln k_H from data shown in Fig. 6.6 that was used to calculate k_0 and α.
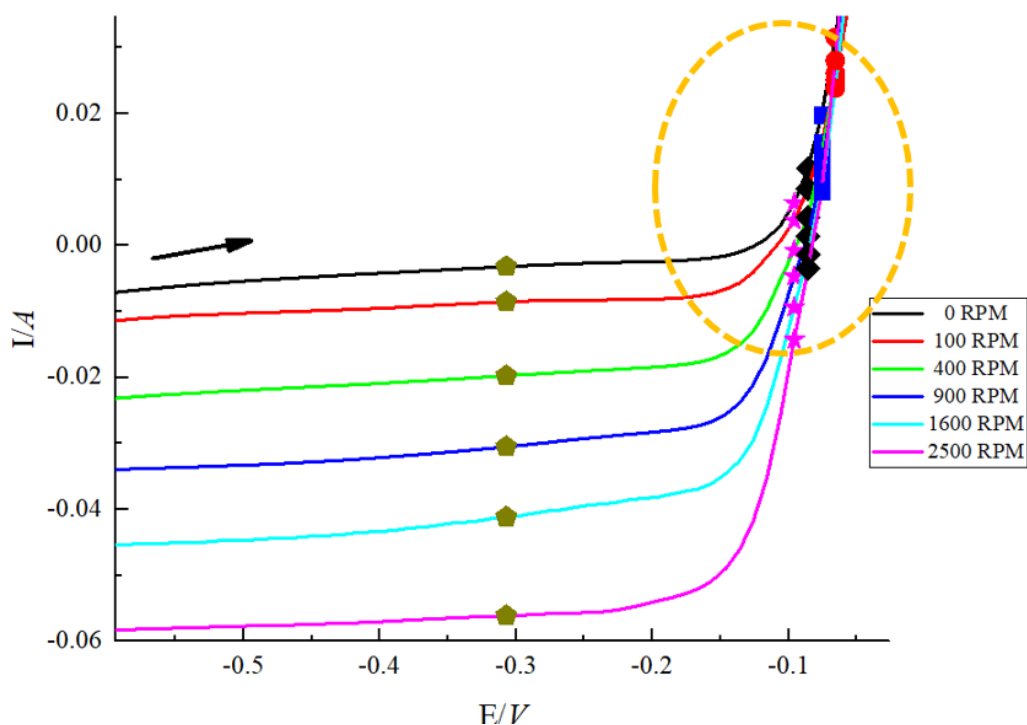
Fig. 6.16 (a) Linear sweep voltammogram for different rotation rates for reduction of Bi(III) to Bi(0) in 0.01 moldm-3 $BiCl_3$ in Ethaline 200, 10 mVs^{-1} scan rate, at 20 °C with **gold** RDE working electrode, IrO_2 coated titanium mesh counter electrode (CE) and Ag pseudo reference electrode (RE).The area within the circle is expanded in Fig. 6.7
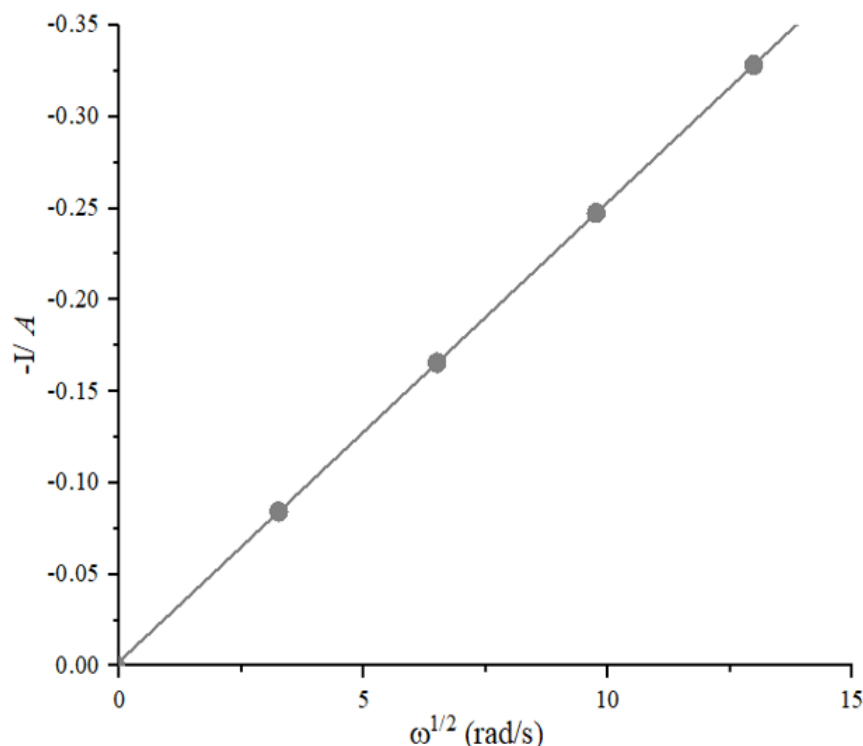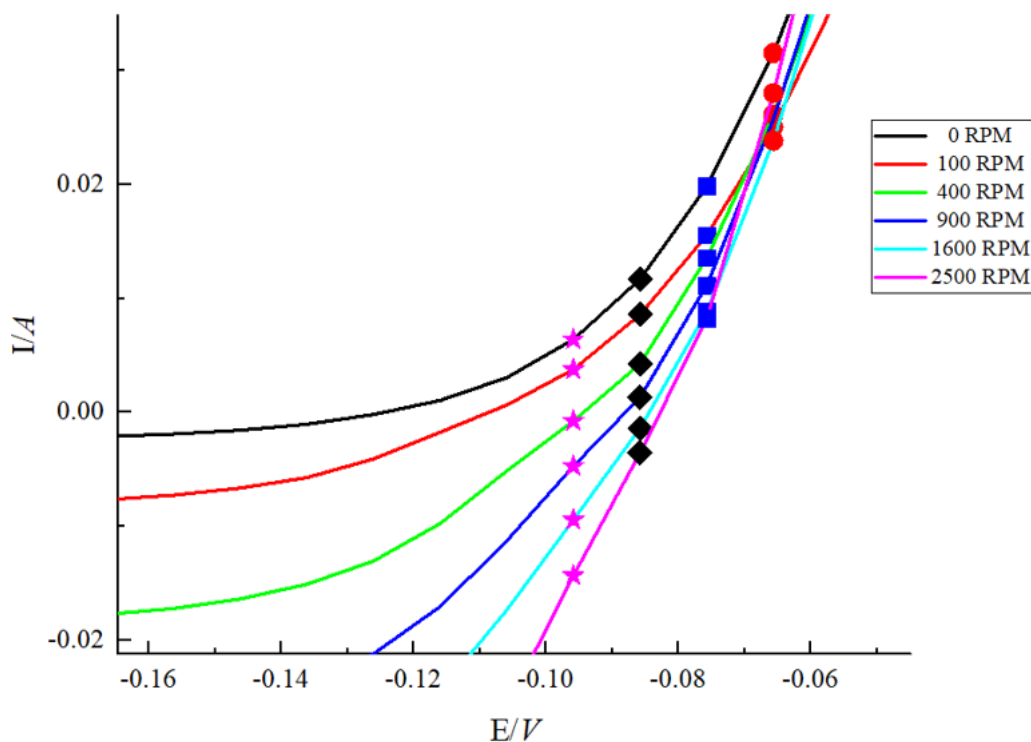
Fig. 6.17 (a) Rising part of the linear sweep voltammogram for different rotation rates for reduction of Bi(III) to Bi(0) in 0.01 moldm-3 BiCl$_3$ in Ethaline 200, 10 mVs^{-1} scan rate, at 20 °C with **gold** RDE working electrode, IrO$_2$ coated titanium mesh counter electrode (CE) and Ag pseudo reference electrode (RE)
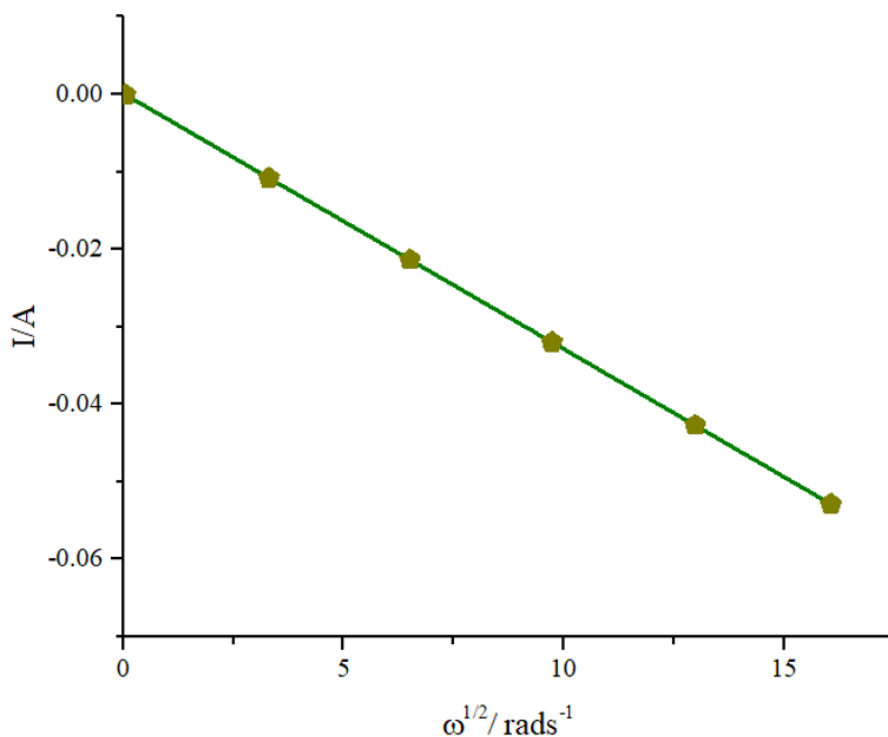
Fig. 6.18 Levich plot of limiting current versus rotation rate ($\omega^{1/2}$) from data in Fig. 6.6 for reduction of reduction of Bi(III) to Bi(0) in 0.01 moldm-3 BiCl$_3$ in Ethaline 200, 10 mVs^{-1} scan rate, at 20 °C with **gold** RDE working electrode, IrO$_2$ coated titanium mesh counter electrode (CE) and Ag pseudo reference electrode (RE)
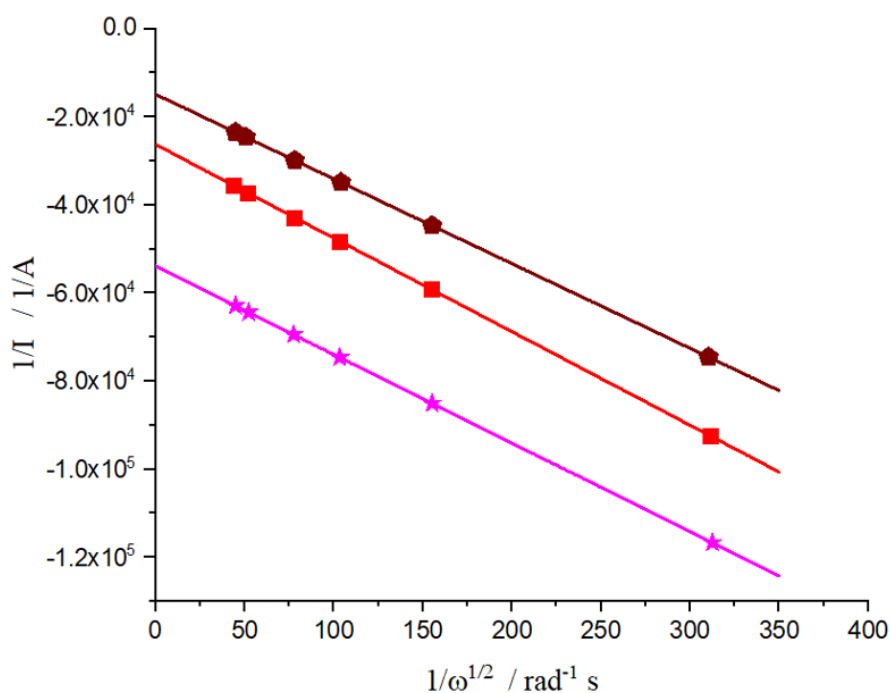
Fig. 6.19 Koutecky-Levich plot of inverse of limiting current versus rotation rate $(\omega^{-1/2})$ from data in Fig. 6.16 for r reduction of Bi(III) to Bi(0) in 0.01 moldm-3 BiCl$_3$ in Ethaline 200, 10 mVs^{-1} scan rate, at 20 °C with **gold** RDE working electrode, IrO$_2$ coated titanium mesh counter electrode (CE) and Ag pseudo reference electrode (RE).

Fig. 6.20 Plot of overpotential (η) vs ln k$_h$ from data shown in Fig. 6.6 that was used to calculate k$_0$ and α.
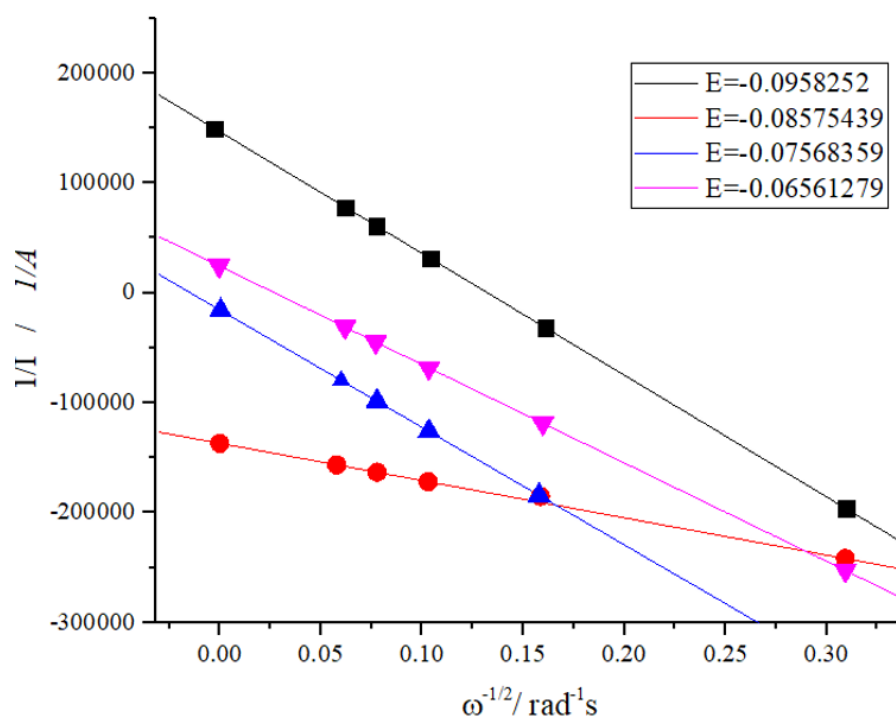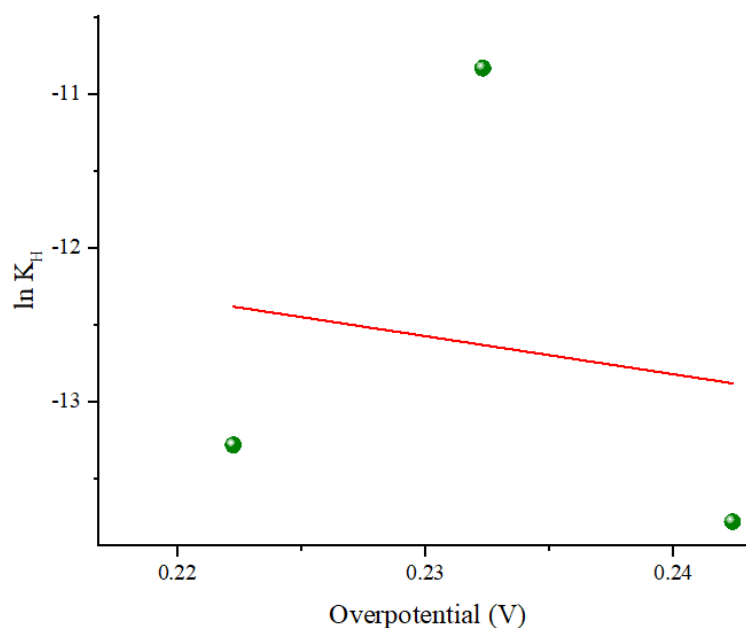
Table 6.4 The calculated values for the diffusion coefficient (D), Transfer coefficient (α) and standard rate constant (k_0) are tabulated below.

	Potential/V	Diffusion Coefficient D / cm^2 s^{-1}	Transfer coefficient (α)	k_0/cms^{-1}
Bi-Pt	-0.15	6.25E-08		
	-0.20	7.36E-07	0.39	4.76E-05
	-0.25	**7.38E-07**		
Bi-Au	-0.095	2.63E-07		
	-0.085	1.55E-08		
	-0.075	2.77E-07	0.63	1.03E-05
	-0.065	3.61E-07		
	-0.30	**1.21E-07**		

6.2.4 Analysis of silver-bismuth co-deposition

Fig. 6.21 to Fig. 6.29 gives results obtained from linear sweep voltammogram for different rotation rates for reduction of Bi(III) to Bi(0) and Ag(I) to Ag(0) in 0.05 moldm^{-3} BiCl$_3$:0.05 moldm^{-3} AgCl in Ethaline 200, at 10 mVs^{-1} scan rate, at 20 °C with platinum RDE. The analysis using Levich plot of limiting current versus rotation rate (ω) is given in Fig. 6.23and and Fig. 6.27 for limiting current 1 and 2 respectively. The Koutecký-Levich plot for limiting current 1 and 2 are given in Fig. 6.24 and Fig. 6.28 respectively. The plots for overpotential (η) vs ln k_H that were used to calculate k_0 and α (d) are given in Fig. 6.25 and Fig. 6.29.

Fig. 6.31 to Fig. 6.37 gives results obtained from linear sweep voltammogram for different rotation rates for reduction of Bi(III) to Bi(0) and Ag(I) to Ag(0) in 0.05 moldm^{-3} BiCl$_3$:0.05 moldm^{-3} AgCl in Ethaline 200, at 10 mVs^{-1} scan rate, at 20 °C with gold RDE. The analysis using Levich plot of limiting current versus rotation rate ($\omega^{1/2}$) is given in Fig. 6.33 and Fig. 6.37 for limiting current 1 and 2 respectively. The Koutecký-Levich plot for limiting current1 is given in Fig. 6.34. The plot for overpotential (η) vs ln k_H that were used to calculate k_0 and α (d) for limiting is given in Fig. 6.25.

All the diffusion coefficients calculated using Levich plots showed a significant difference (10 times lower or higher) from the values calculated from Koutecky-Levich plots. The average values calculated by diffusion coefficients were compared with diffusion coefficient values calculated by Randle-Sevcik and Cottrell study (see Fig 7.1). The values were in an acceptable range.
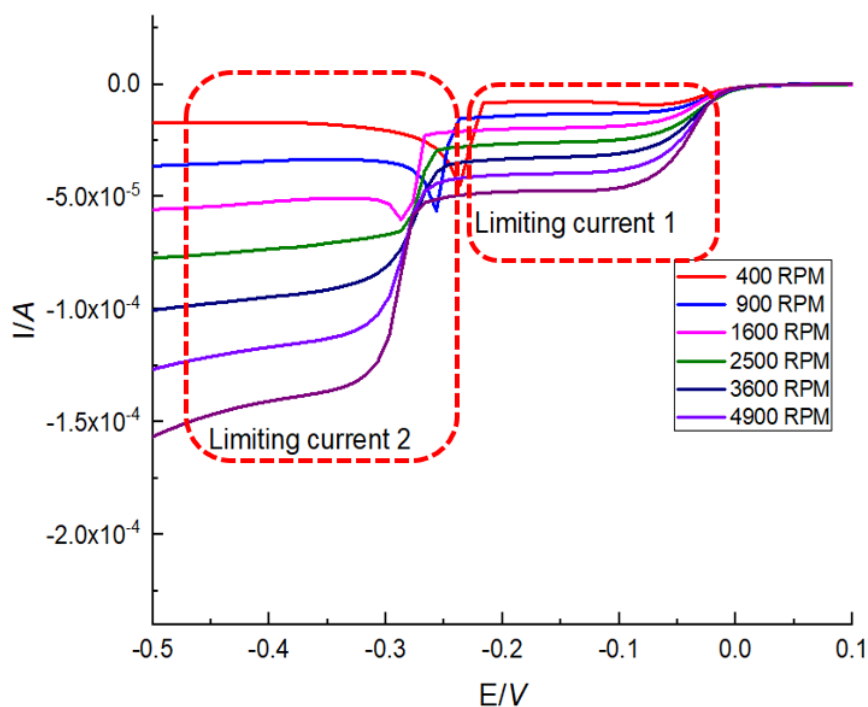
Fig. 6.21   Linear sweep voltammogram for different rotation rates for reduction of Bi(III) to Bi(0) and Ag(I) to Ag(0) in 0.05 moldm^{-3} BiCl$_3$:0.05 moldm^{-3} AgCl in Ethaline 200, 10 mVs^{-1} scan rate, at 20 °C with **platinum** RDE working electrode, IrO$_2$ coated titanium mesh counter electrode (CE) and Ag pseudo reference electrode (RE). For ease of analysis the graph has been divided in to 2 regions based on the two limiting current observed (see Fig. 6.22 and Fig. 6.26).

Fig. 6.22   Linear sweep voltammogram for different rotation rates for reduction of Ag(I) to Ag(0) in 0.05 moldm^{-3} BiCl$_3$:0.05 moldm^{-3} AgCl in Ethaline 200, 10 mVs^{-1} scan rate, at 20 °C with **platinum** RDE working electrode, IrO$_2$ coated titanium mesh counter electrode (CE) and Ag pseudo reference electrode (RE).
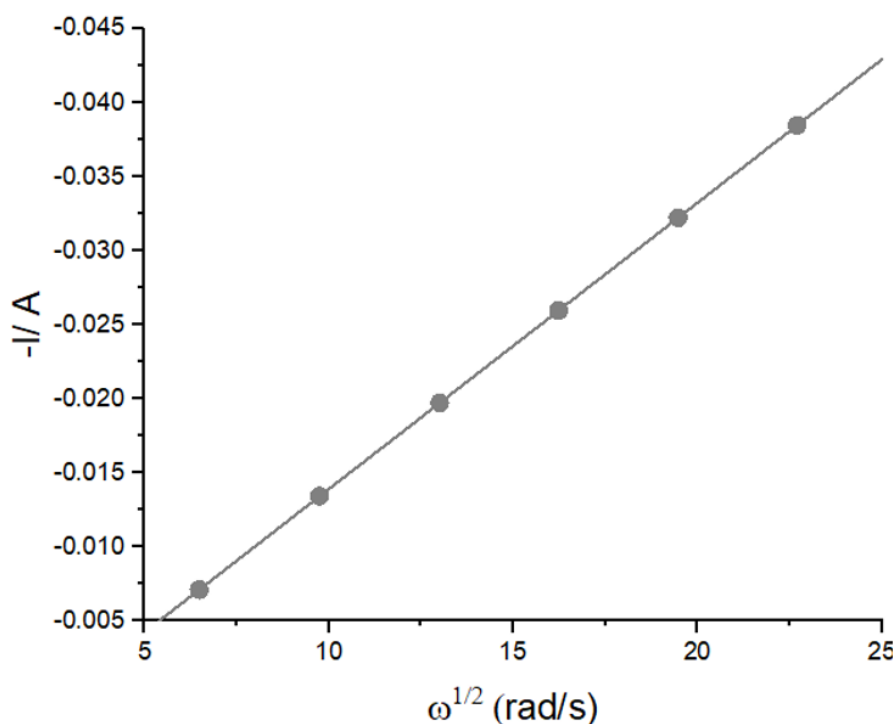
Fig. 6.23 Levich plot of limiting current 1 versus rotation rate ($\omega^{1/2}$) from data in **??** for reduction of Ag(I) to Ag(0) 0.05 moldm^{-3} BiCl$_3$:0.05 moldm^{-3} AgCl in Ethaline 200, 10 mVs^{-1} scan rate, at 20 °C with **platinum** RDE working electrode, IrO$_2$ coated titanium mesh counter electrode (CE) and Ag pseudo reference electrode (RE).
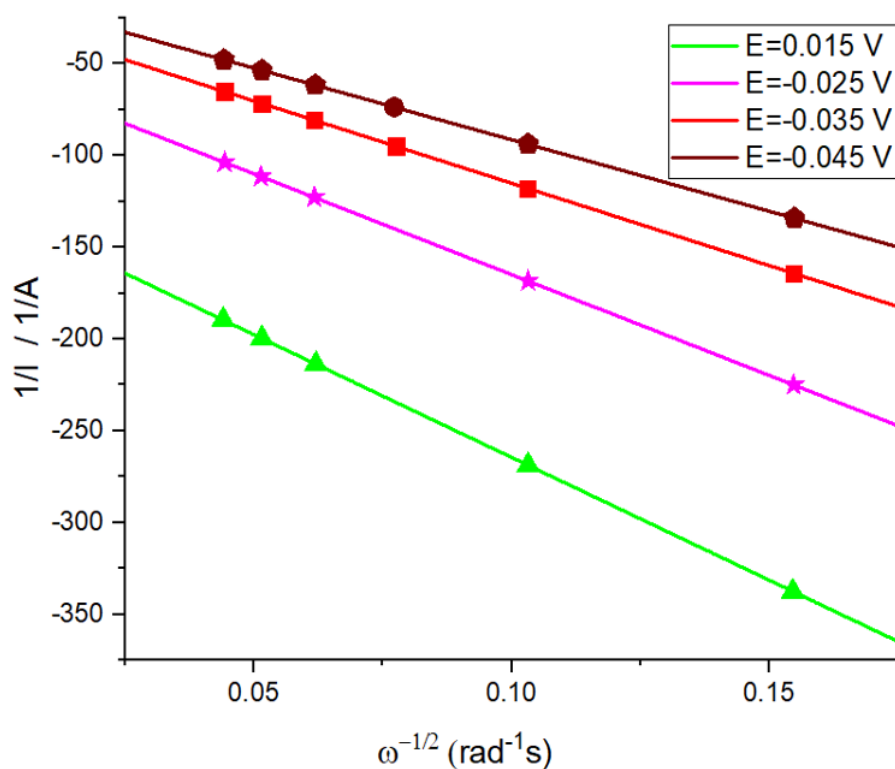
Fig. 6.24 Koutecky-Levich plot of inverse of limiting current 2 versus rotation rate ($\omega^{-1/2}$) for reduction of Ag(I) to Ag(0) 0.05 moldm^{-3} BiCl$_3$:0.05 moldm^{-3} AgCl in Ethaline 200, 10 mVs^{-1} scan rate, at 20 °C with **platinum** RDE working electrode, IrO$_2$ coated titanium mesh counter electrode (CE) and Ag pseudo reference electrode (RE).

**Fig. 6.25** Plot of overpotential (η) vs ln k_H from data shown in Fig. 6.6 that was used to calculate k_0 and α.

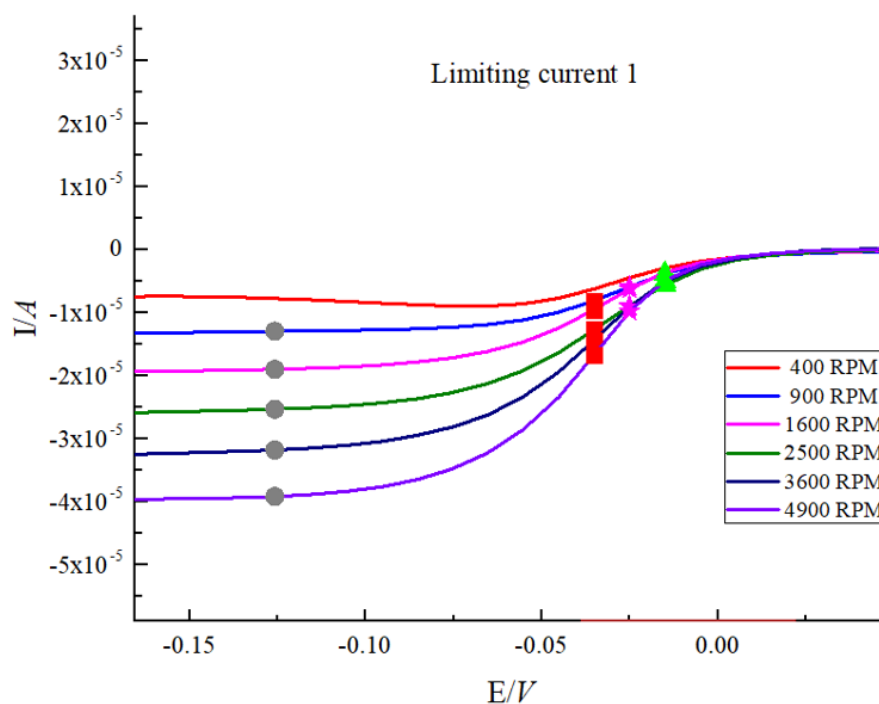**Fig. 6.26** Linear sweep voltammogram for different rotation rates for reduction of Ag(I) to Ag(0) in 0.05 moldm^{-3} BiCl$_3$:0.05 moldm^{-3} AgCl in Ethaline 200, 10 mVs^{-1} scan rate, at 20 °C with **platinum** RDE working electrode, IrO$_2$ coated titanium mesh counter electrode (CE) and Ag pseudo reference electrode (RE).

Fig. 6.27 Levich plot of limiting current 2 versus rotation rate ($\omega^{1/2}$) from data in Fig. 6.26 for reduction of Ag(I) to Ag(0) 0.05 moldm^{-3} BiCl$_3$:0.05 moldm^{-3} AgCl in Ethaline 200, 10 mVs^{-1} scan rate, at 20 °C with **platinum** RDE working electrode, IrO$_2$ coated titanium mesh counter electrode (CE) and Ag pseudo reference electrode (RE).

Fig. 6.28 Koutecky-Levich plot of inverse of limiting current 2 versus rotation rate ($\omega^{-1/2}$) from data in Fig. 6.26 for reduction of Ag(I) to Ag(0) 0.05 moldm^{-3} BiCl$_3$:0.05 moldm^{-3} AgCl in Ethaline 200, 10 mVs^{-1} scan rate, at 20 °C with **platinum** RDE working electrode, IrO$_2$ coated titanium mesh counter electrode (CE) and Ag pseudo reference electrode (RE).
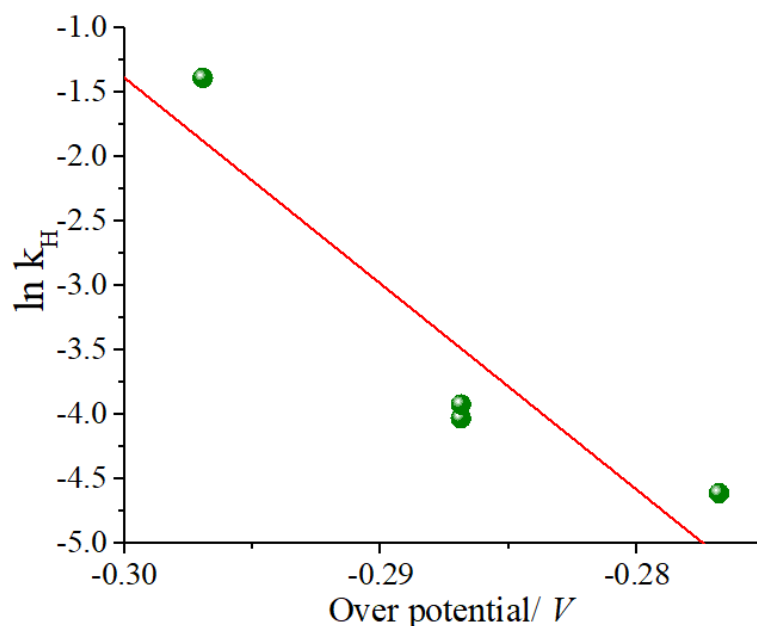
Fig. 6.29 Plot of overpotential (η) vs ln k_h from data shown in Fig. 6.6 that was used to calculate k_0 and α.
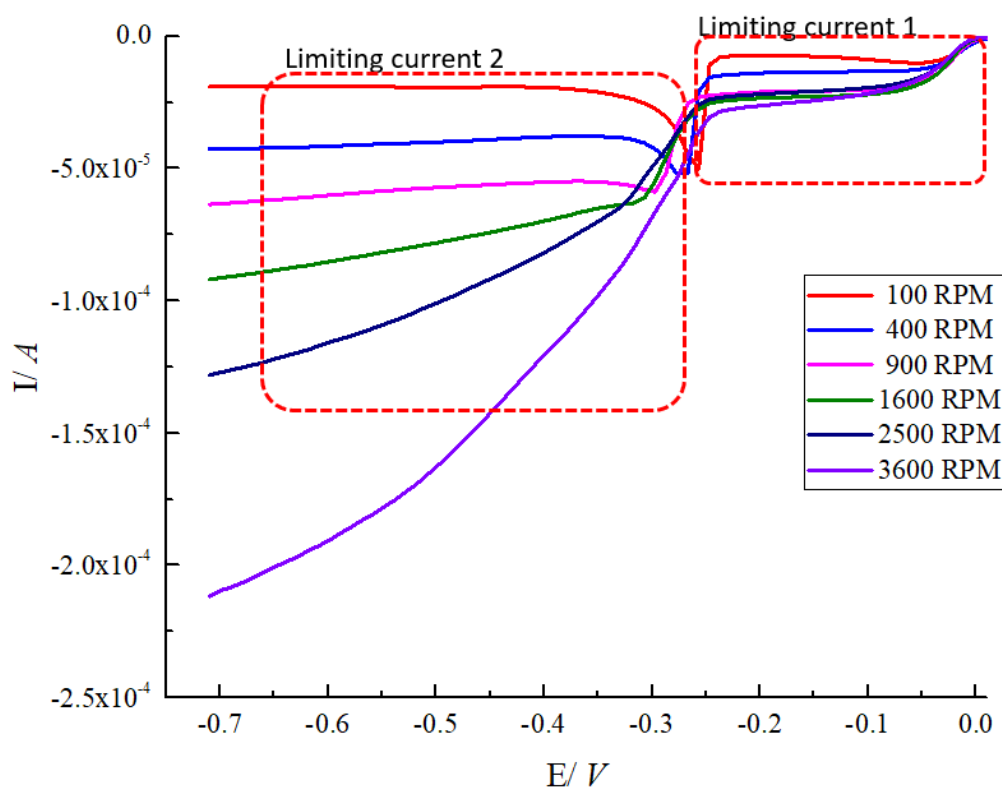
Fig. 6.30 Linear sweep voltammogram for different rotation rates for reduction of Bi(III) to Bi(0) and Ag(I) to Ag(0) in 0.05 moldm^{-3} BiCl$_3$:0.05 moldm^{-3} AgCl in Ethaline 200, 10 mVs^{-1} scan rate, at 20 °C with **gold** RDE working electrode, IrO$_2$ coated titanium mesh counter electrode (CE) and Ag pseudo reference electrode (RE). For ease of analysis the graph has been divided in to 2 regions based on the two limiting current observed (see Fig. 6.31 and Fig. 6.36).
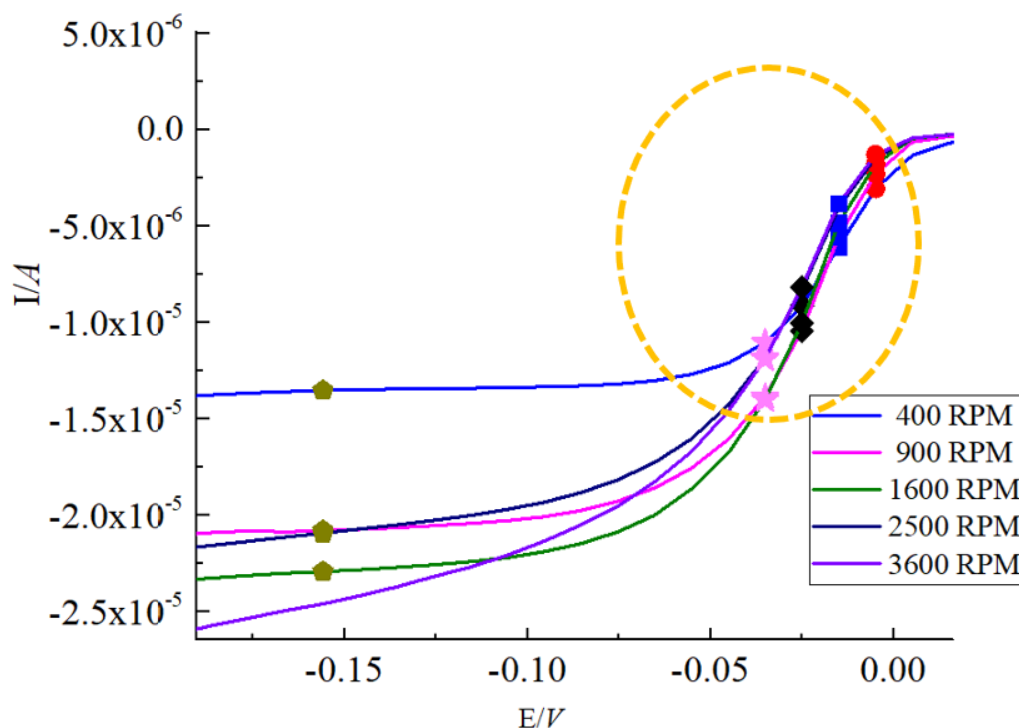
Fig. 6.31 Linear sweep voltammogram for different rotation rates for reduction of Ag(I) to Ag(0) in 0.05 moldm^{-3} BiCl$_3$:0.05 moldm^{-3} AgCl in Ethaline 200, 10 mVs^{-1} scan rate, at 20 °C with **platinum** RDE working electrode, IrO$_2$ coated titanium mesh counter electrode (CE) and Ag pseudo reference electrode (RE).
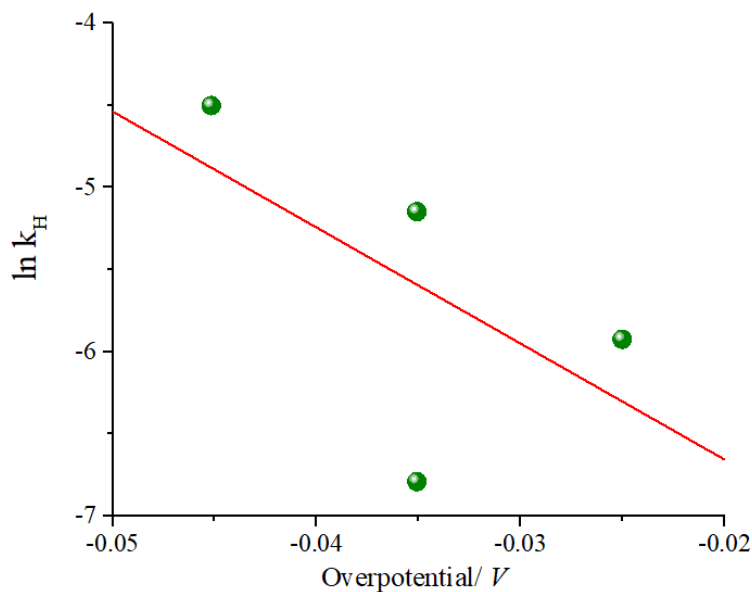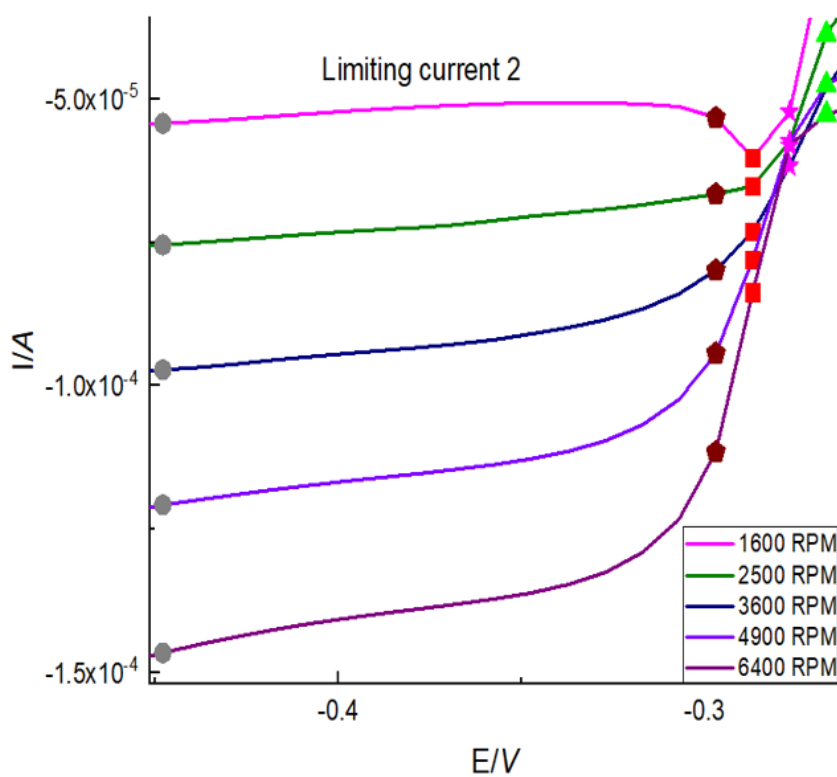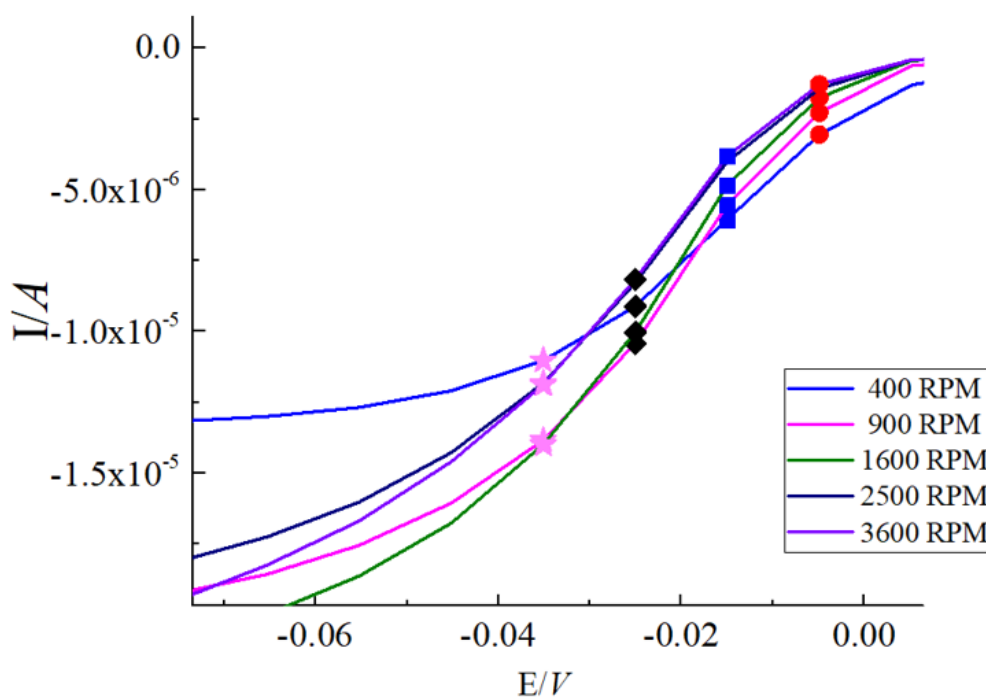

Fig. 6.32 Rising part of linear sweep voltammogram for different rotation rates for reduction of Ag(I) to Ag(0) in 0.05 moldm^{-3} BiCl$_3$:0.05 moldm^{-3} AgCl in Ethaline 200, 10 mVs^{-1} scan rate, at 20 °C with **gold** RDE working electrode, IrO$_2$ coated titanium mesh counter electrode (CE) and Ag pseudo reference electrode (RE).
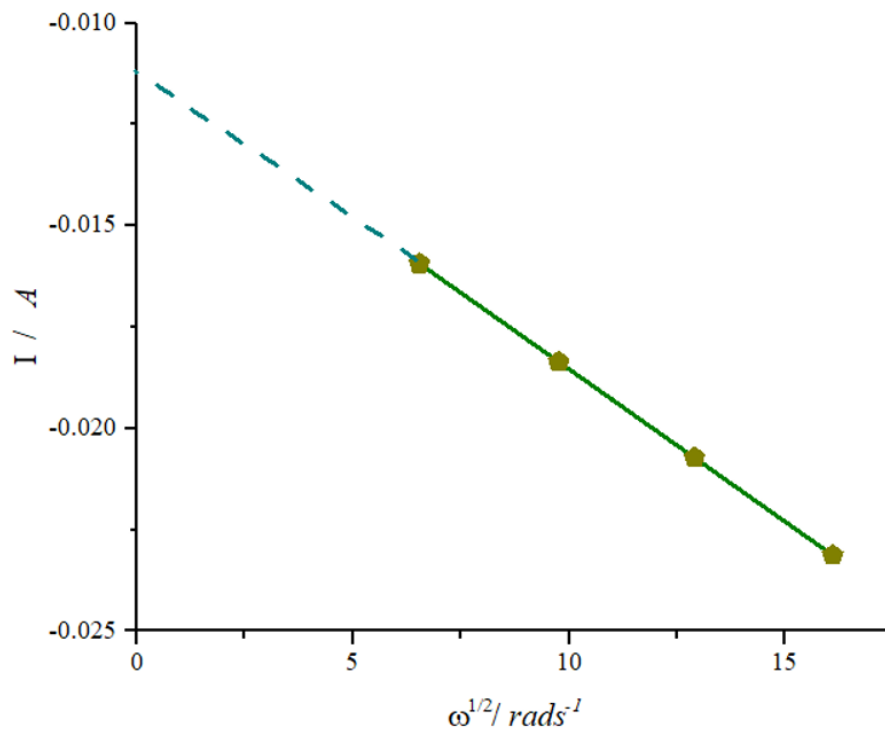
Fig. 6.33   Levich plot of limiting current 1 versus rotation rate ($\omega^{1/2}$) from data in Fig. 6.31 for reduction of Ag(I) to Ag(0) 0.05 moldm^{-3} BiCl$_3$:0.05 moldm^{-3} AgCl in Ethaline 200, 10 mVs^{-1} scan rate, at 20 °C with **gold** RDE working electrode, IrO$_2$ coated titanium mesh counter electrode (CE) and Ag pseudo reference electrode (RE).
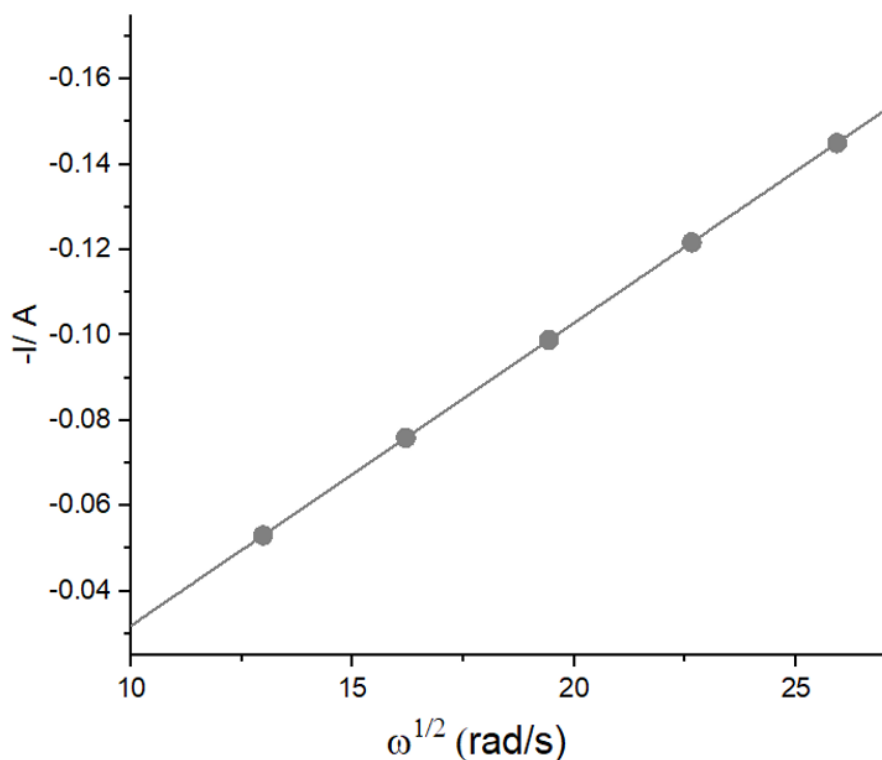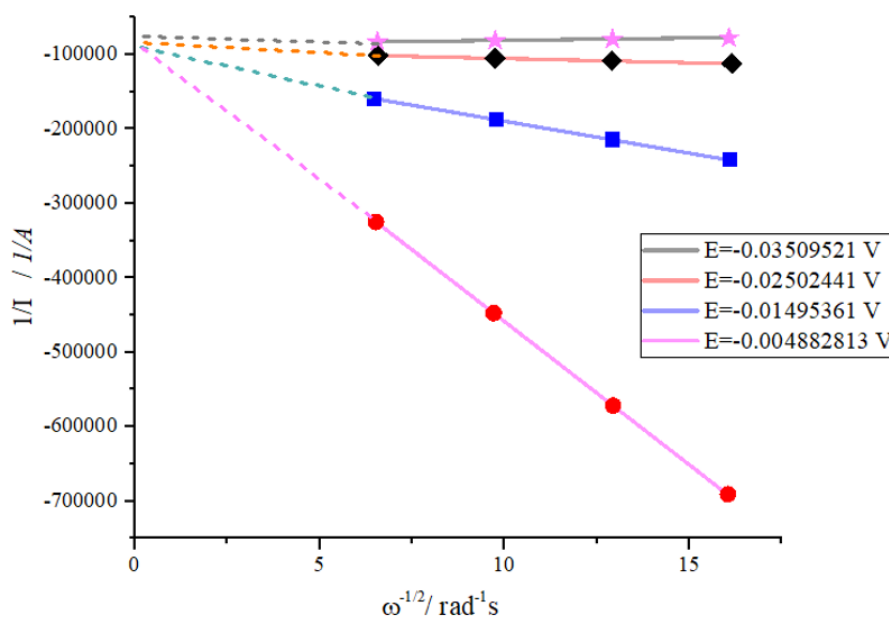

Fig. 6.34   Koutecky-Levich plot of inverse of limiting current 1 versus rotation rate ($\omega^{-1/2}$) from data in Fig. 6.31 for reduction of Ag(I) to Ag(0) 0.05 moldm^{-3} BiCl$_3$:0.05 moldm^{-3} AgCl in Ethaline 200, 10 mVs^{-1} scan rate, at 20 °C with **platinum** RDE working electrode, IrO$_2$ coated titanium mesh counter electrode (CE) and Ag pseudo reference electrode (RE).
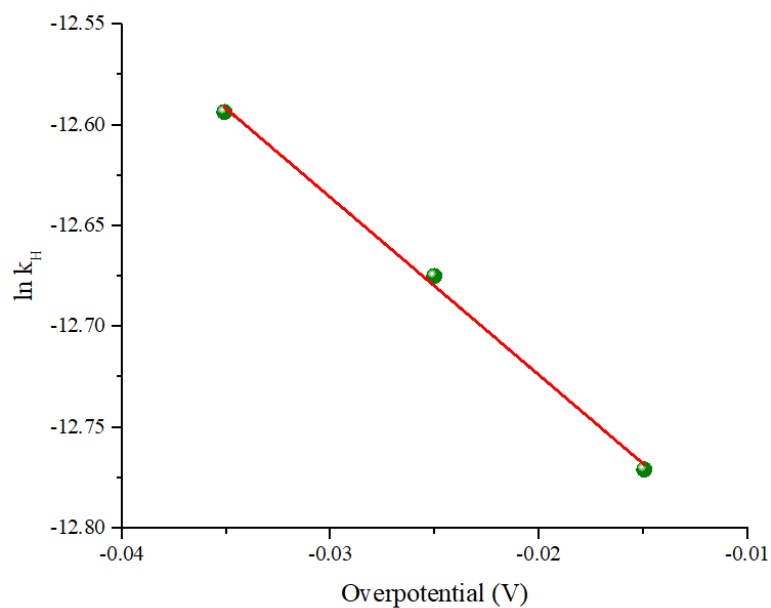
Fig. 6.35 Plot of overpotential (η) vs ln k_h from data shown in Fig. 6.6 that was used to calculate k_0 and α.
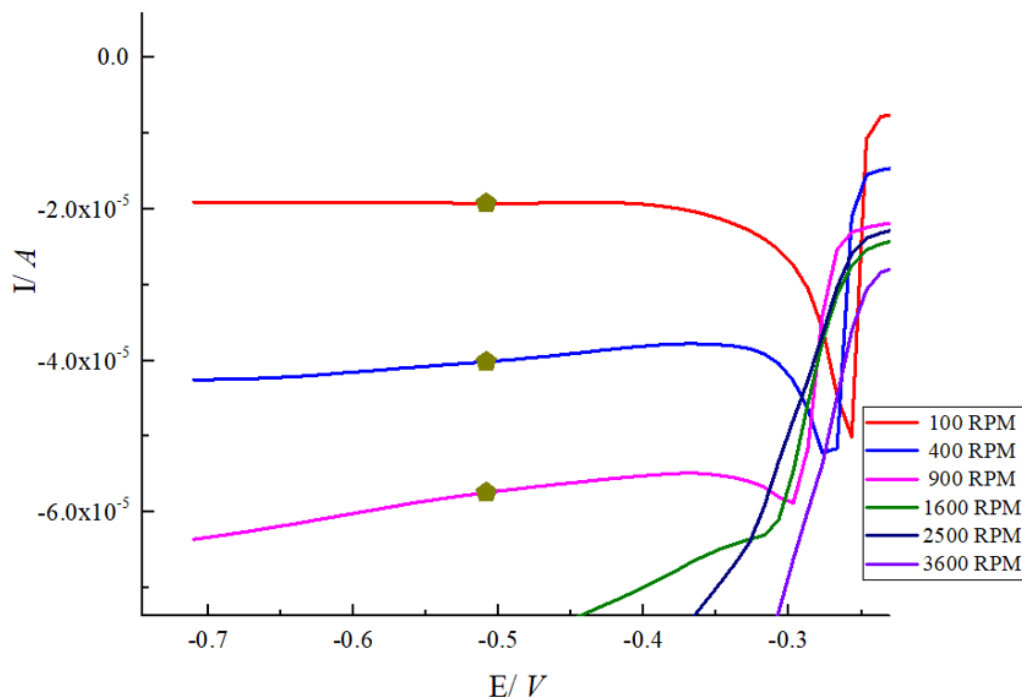
Fig. 6.36 Linear sweep voltammogram for different rotation rates for reduction of Ag(I) to Ag(0) in 0.05 moldm^{-3} BiCl$_3$:0.05 moldm^{-3} AgCl in Ethaline 200, 10 mVs^{-1} scan rate, at 20 °C with **gold** RDE working electrode, IrO$_2$ coated titanium mesh counter electrode (CE) and Ag pseudo reference electrode (RE).
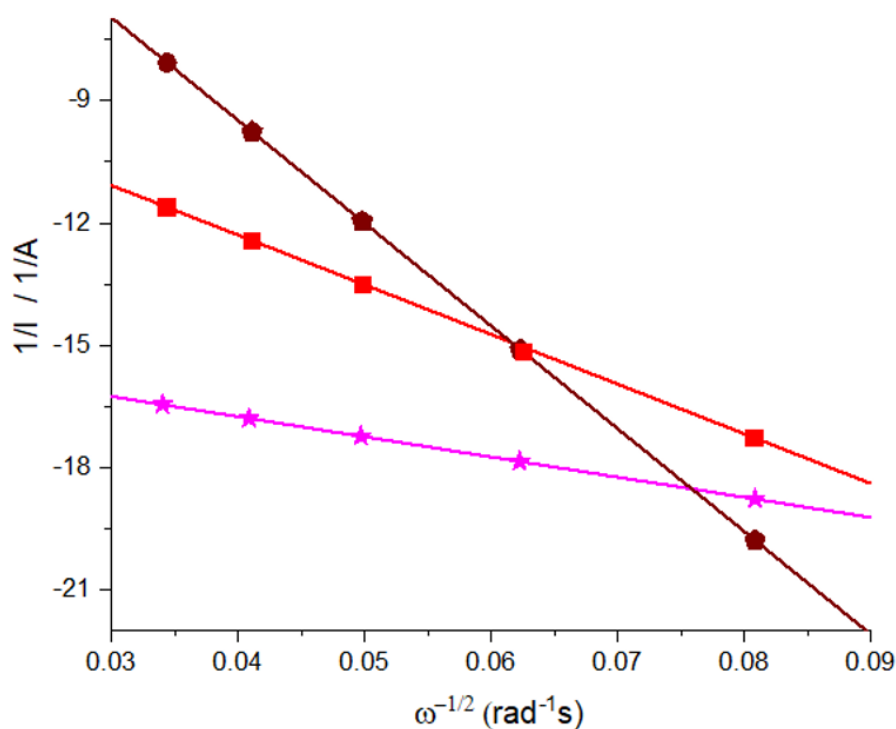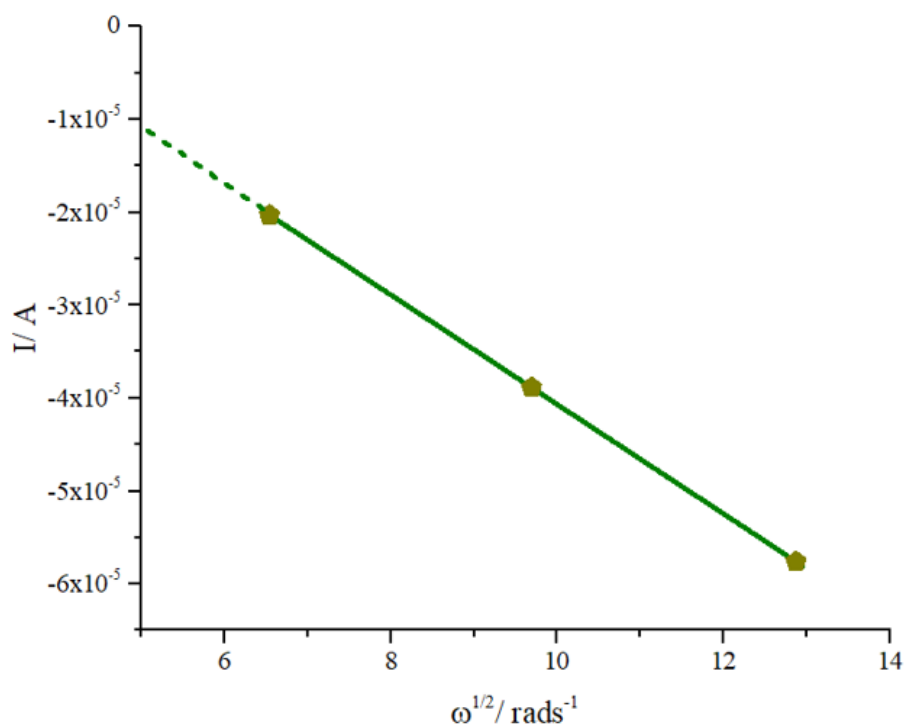
Fig. 6.37 Levich plot of limiting current 2 versus rotation rate ($\omega^{1/2}$) from data in Fig. 6.36 for reduction of Ag(I) to Ag(0) 0.05 moldm^{-3} BiCl$_3$:0.05 moldm^{-3} AgCl in Ethaline 200, 10 mVs^{-1} scan rate, at 20 °C with **gold** RDE working electrode, IrO$_2$ coated titanium mesh counter electrode (CE) and Ag pseudo reference electrode (RE).

Table 6.5 The calculated values for the diffusion coefficient (D), Transfer coefficient (α) and standard rate constant (k$_0$) are tabulated below.

	Potential/V	Diffusion Coefficient D / cm^2 s^{-1}	Transfer coefficient (α)	k_0/cms^{-1}
AgBi-Pt (Ag)	-0.015	1.03E-07	0.56	4.58E-06
	-0.045	1.63E-07		
	-0.085	1.93E-07		
	-0.125	5.69E-08		
	-0.286	7.21E-08	0.33	1.08E-06
	-0.307	5.77E-08		
	-0.357	4.40E-08		
	-0.407	2.95E-07		
AgBi-Au (Ag)	-0.035	3.02E-07	0.22	2.50E-06
	-0.025	1.18E-07		
	-0.015	5.64E-07		
	-0.005	5.96E-07		
	-0.2	1.57E-08		
AgBi-Au (Bi)	K-L not calculated	-	N/A	
	-0.6	2.94E-07		

To analyse the codeposition of silver-bismuth, it is necessary to assume that Bi(III) is reduced to Bi(0) and Ag(I) is reduced to Ag(0) and no new complexes are formed. There are two reduction peaks observed in the current transients and it is also necessary to assume that the two depositions are independent of each other and silver is deposited at a lower negative potential compared to Bi. The average diffusion coefficient for silver was calculated to be 2.74E-07 cm^2s^{-1} is in the same order of magnitude as the value obtained when silver is deposited alone. However, for bismuth, average diffusional forces were calculated to be 5.77E-08 cm^2s^{-1} which is lower than the value obtained for bismuth deposition (as a single metal). This indicates that there is an unexpected factor that comes into play. Furthermore, when analysing the linear sweep voltagrammes for codeposition (for gold and platinum substrates) a current spike is observed when the electrodeposition switches from silver to bismuth. This unexpected increase in current maybe due to the changing substrate for deposition of bismuth on silver (initially) to bismuth on bismuth.

The comparison of diffusion coefficients derived from Levich and Koutecky Levich analysis have been compared to the values obtained by Cottrell and Randles-Sevcik methods in chapter 7 (table 1).

For silver-bismuth codeposition using gold rotation disc electrode, the Koutecky Levich analysis could not be conducted due to the current increase and the shift observed the rising part (see Fig. 6.30).

6.3 Simultaneous thickness and electrochemical potential (STEP) measurements for multilayer metals

Simultaneous thickness and electrochemical potential (STEP) method can be applied as a fast technique for determination of potential differences and thicknesses of separate metal deposits in multilayer metal plates.[11] This method was first used by E.P. Herbulak in 1980 for the study of sulphur-free semi-bright nickel, sulphur-containing bright nickel and micro-discontinuous chromium multilayer system for corrosion protection of exterior automotive hardware.[12,13]

6.3.1 Application of STEP for metal systems

In the current study, this method was improved by using atomic force microscopy (AFM) for thickness calculations. For each system (silver, bismuth, co-deposition of silver and bismuth) first, metals were deposited potentiostatically (chronoamperometry) and stripped galvanostatically (chronopotentiometry). A set of experiments were conducted to determine optimum current density to be used for anodic stripping and optimum potential range for cathodic deposition.

Gold coated glass slides were used as the substrate for preparation of deposition samples. The preparation of these glass slides were discussed in Chapter 3. 10 mmol dm^{-3} silver chloride, 20

mmol dm^{-3} silver chloride, 10 mmol dm^{-3} bismuth chloride and 20 mmol dm^{-3} bismuth chloride solutions in Ethaline 200 were used as electrolytes. The procedures for preparing solutions were given in chapter 3.

The glass slides (each measuring ca. 35 mm by 25 mm) were used as working electrodes (WE). These glass slides had a deposited MPTS layer and a gold layer. Iridium oxide coated titanium mesh counter electrode (CE) and silver pseudo reference electrode (RE) were used as the other two electrodes in the three electrodes setup for all the experiments.

All the experiments were carried out in room temperature (20 °C). Chronoamperometry was conducted at predetermined potential values, for the deposition of metal layers on the glass slides. The layers of metals were then stripped using positive currents (chronopotentiometry) until all the metal layers were stripped off the glass slide. The experiments were repeated for two other slides to assess reproducibility.

6.3.2 Analysis of current transients

The schematic diagram below explains the process of consecutive deposition of metal layers on gold coated slides and the order of dissolution (Fig. 6.38).
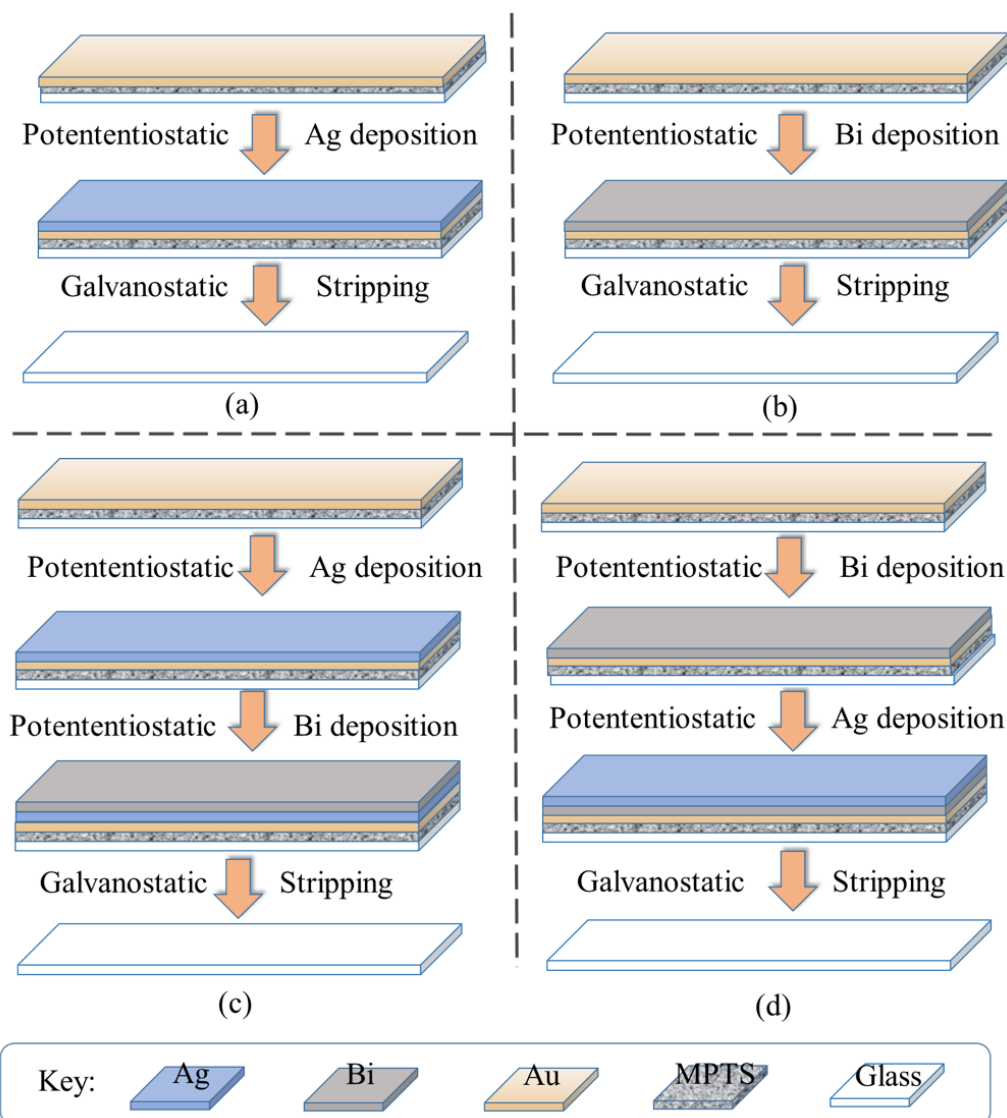
Fig. 6.38 Schematic diagram of the STEP process analysed in this section is given above. (a) the deposition of silver (b) the deposition of bismuth (c) the deposition of silver followed by deposition of bismuth (d) the deposition of bismuth followed by deposition of silver and stripping of metal layers were conducted. 10 mmol dm^{-3} silver chloride, 20 mmol dm^{-3} silver chloride, 10 mmol dm^{-3} bismuth chloride and 20 mmol dm^{-3} bismuth chloride solutions in Ethaline 200 were used for deposition and Stripping was conducted in Ethaline 200 at room temperature (20 °C)

The stripping potential regions for pure silver, bismuth and gold metal layers that were observed are as follows.

Gold → 0.68 V
Bismuth → -0.103 V and 0.036 V (due to formation of different chloride complexes/ UPD dissolution)
Silver → 0.14 V

For each experiment potential changes observed were plotted and the following analysis were carried out. Results and deductions of each representative experiment were grouped and discussed separately.

For the potentiostatic deposition process

$$Q = \int I dt \tag{6.2}$$

However although deposition was done potentionstaticaly, for the overwhelming majority of the experiment, the current was observed to be approximately constant. Therefore, $Q = \int I dt$ simplifies to $I * t$.

Charge involved in deposition $(Q_{dep}) = I_{dep} \times t_{dep}$

where I_{dep} - applied current (A)
t_{dep} - time taken for the deposition (s)

Mass of the deposited metal (m) (in grams) $= \dfrac{M \times I \times t}{n \times F}$

where M - molar mass of the metal (g mol^{-1})
M_{silver} - 107.86 g mol^{-1}
$M_{bismuth}$ - 208.98 g mol^{-1}
n - number of electrons transferred
F - Faraday constant (96490 C mol^{-1})

Height of the deposit $= \dfrac{m}{\rho \times A}$

where ρ - density of the metal (g cm^{-3})
A - area of the working electrode (8.75 cm^2)

For the galvanostatic stripping process

Charge involved in stripping $(Q_{strip}) = I_{strip} \times t_{strip}$

where I_{strip} - applied current (A)
t_{strip} - time taken for stripping of each layer (s)

For the gold coated layer

Average height of the layer measured by the AFM $= h$ (nm)

Volume of the gold layer $= A \times h \times 10^{-7}$ (cm^3)

Mass of the gold layer $= (A \times h \times 10^{-7}) \times \rho$ (g)

where A - area of the working electrode (8.75 cm^2)
ρ - density of gold (19.32 g cm^{-3})

Moles of gold deposited $= \dfrac{A \times h \times 10^{-7} \times \rho}{M_{gold}}$

Charged needed to strip the gold $= \dfrac{A \times h \times 10^{-7} \times \rho}{M_{gold} \times n \times F}$

where $M_{gold} = 196.96$ g mol^{-1}

A set of experiments were conducted to determine the anodic potential range (stripping) for single metal systems and to determine the optimum current density (for stripping).[11] The use of high anodic current densities caused loss of metal layers with poor adhesion (i.e. small amounts of metal can be pulled off the surface) without the charge involved being accounted for. Slow stripping was used to overcome this issue although very low current densities could make the stripping non-uniform and prevent complete dissolution of layers.

A representative set of results are given below to illustrate the findings of these experiments (Fig. 6.39, Fig. 6.40, Fig. 6.41 and Fig. 6.42). The calculations involved in the analysis of each experiment are given in Table 6.6.

Part (a) in Fig. 6.39, represent potentiostatic bismuth deposition from 20 mmol dm^{-3} BiCl$_3$ on Au coated glass slide (WE) for 7200 s at −0.4 V followed by potentiostatic silver deposition from 20 mmol dm^{-3} AgCl on the same glass slide for 7200 s at −0.4 V (part b). The sample was immediately galvanostatically stripped at 3 μA in Ethaline 200, using the same 3 electrode cell set-up with an interval of 0.5 s (part c). According to Fig. 6.39, bismuth stripped at 0.07 V for ca. 1250 s. Calculation of the charge percentage indicate that this represent only 27% of the expected charge of stripping for bismuth compared to the initial deposition charge of bismuth.

From 0.07 V to 0.16 V, silver stripping takes place . However, pure silver stripping is usually seen at 0.14 V. This indicate that silver is mixed with another element which lowers the stripping potential of silver. This indicates that it may be bismuth incorporated silver. From t = 6474 s to ca. 8000 s there is a clear intermetallic region representing bismuth-gold intermetallic region which may or may not include silver. This conclusion was made due to the following reason: the AFM step height measurements for pure gold indicate height of 14 nm for the gold layer. When the theoretical stripping charge of gold (derived from AFM data applying Faraday's law) is compared to the experimental stripping charge for pure gold (from 8000 s to 16798 s at 0.74 V stripping voltage), a significant difference of charge was noted (Table 6.6).

The difference in charge calculated indicated that the gold deposited is stripped in other regions as well as the pure gold stripping region. The pure gold stripping region exhibit a sharp step.

Fig. 6.39   (a) Potentiostatic Bi deposition from 20 mmol dm^{-3} BiCl$_3$ on Au coated glass slide (WE) for 7200 s at -0.4 V (b) potentiostatic Ag deposition from 10 mmol dm^{-3} AgCl on the same glass slide for 7200 s at -0.4 V (c) Galvanostatic stripping using 3 μA in Ethaline 200. All systems used the 3 electrode system (WE, IrO$_2$ coated titanium mesh counter electrode (CE) and Ag pseudo reference electrode (RE)). T = 20 °C.

The experiment shown in Fig. 6.41 follows the same order of deposition of metals as Fig. 6.39 (i.e. deposition of bismuth followed by silver) but with a lower deposition potential. This indicates several anomalies in silver stripping and two intermetallic regions. The amount of bismuth involved in intermetallic formation (Table 6.6) is high (86%) similar to that seen in Fig. 6.14 (73%).

Fig. 6.40 represents a data set that was derived by applying similar potentials but depositing silver followed by bismuth and stripping of layers galvanostatically at 50 μA. This experiment showed clear steps for stripping of pure bismuth, pure silver and pure gold with intermetallic regions in between them. As explained previously, similar calculations were carried out for deposition and stripping charges for gold, silver and bismuth. This indicated that the amount of bismuth involved in intermettalic formation is less (58%) than for the previous case where bismuth was deposited first. This was again observed (i.e. 58% of bismuth being involved in intermetallic formation) for the experiment shown in Fig. 6.42 where silver was deposited first but stripped at a very low current (3 μA) in Ethaline 200 (Table 6.6). From the Fig. 6.42: part (c) it is clear that intermetallic formation is more prevalent with bismuth than with silver since the silver and gold stripping is clearly defined into steps.

When considering the overall charge for the systems, it can be concluded that the charge for stripping is considerably less compared to that of deposition. This could be caused by low current efficiency during deposition or mechanical removal of poorly adhered metallic components during stripping. STEP method indicates the formation of intermetallic layers during the deposition of silver and bismuth layers. However, this does not give the composition of intermetallic alloy formed.
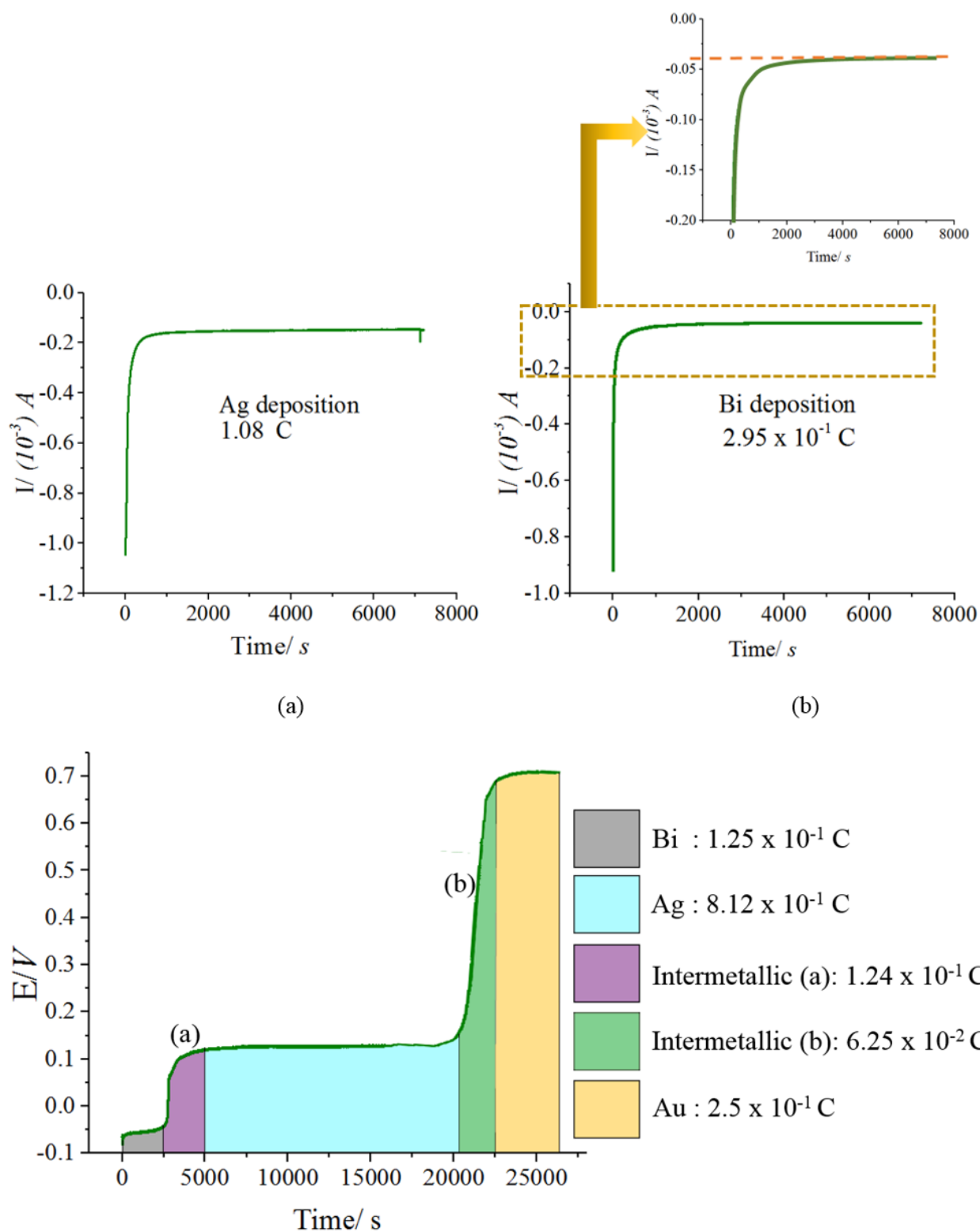
Fig. 6.40 (a) Potentiostatic Ag deposition from 10 mmol dm^{-3} AgCl on Au coated glass slide (WE) for 7200 s at -0.4 V (b) potentiostatic Ag deposition from 20 mmol dm^{-3} BiCl$_3$ on the same glass slide for 7200 s at -0.4 V (c) Galvanostatic stripping using 50 μA in Ethaline 200. All systems used the 3 electrode system (WE, IrO$_2$ coated titanium mesh counter electrode (CE) and Ag pseudo reference electrode (RE)). T = 20 °C.
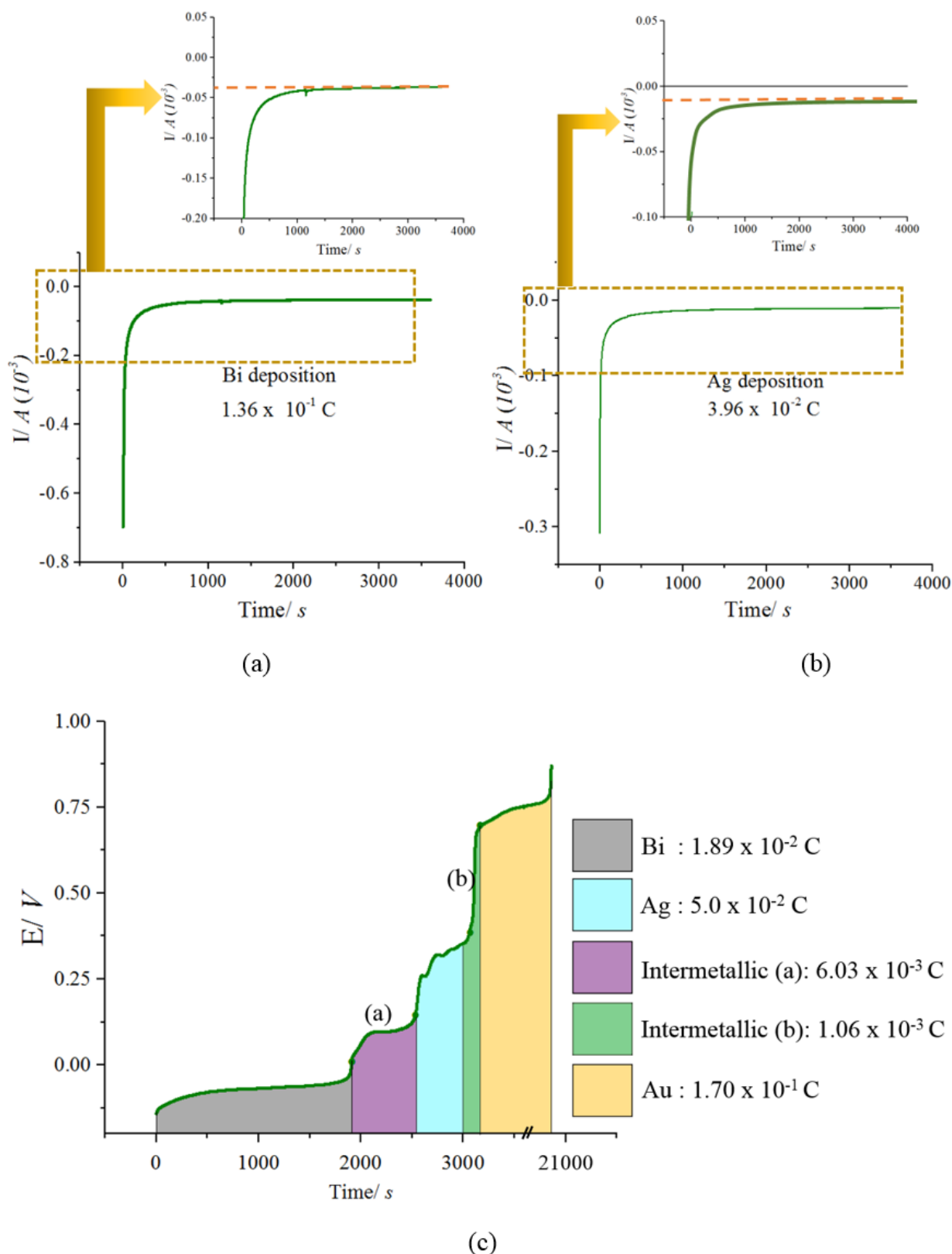
Fig. 6.41 (a) Potentiostatic Bi deposition from 20 mmol dm^{-3} BiCl$_3$ on Au coated glass slide (WE) for 7200 s at -0.25 V (b) potentiostatic Ag deposition from 10 mmol dm^{-3} AgCl on the same glass slide for 7200 s at -0.25 V (c) Galvanostatic stripping using 10 μA in Ethaline 200. All systems used the 3 electrode system (WE, IrO$_2$ coated titanium mesh counter electrode (CE) and Ag pseudo reference electrode (RE)). T = 20 °C.

(a)

(b)

(c)

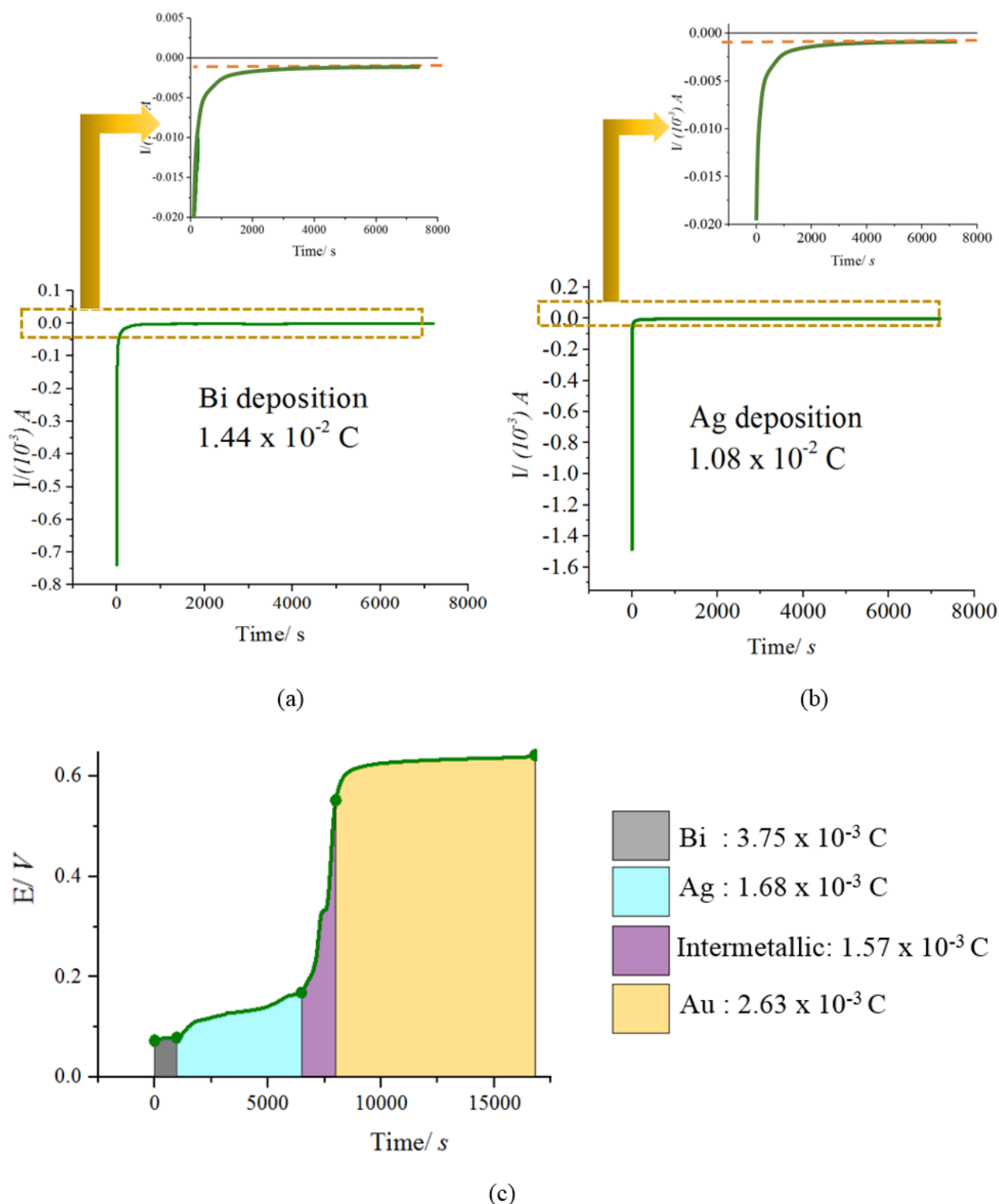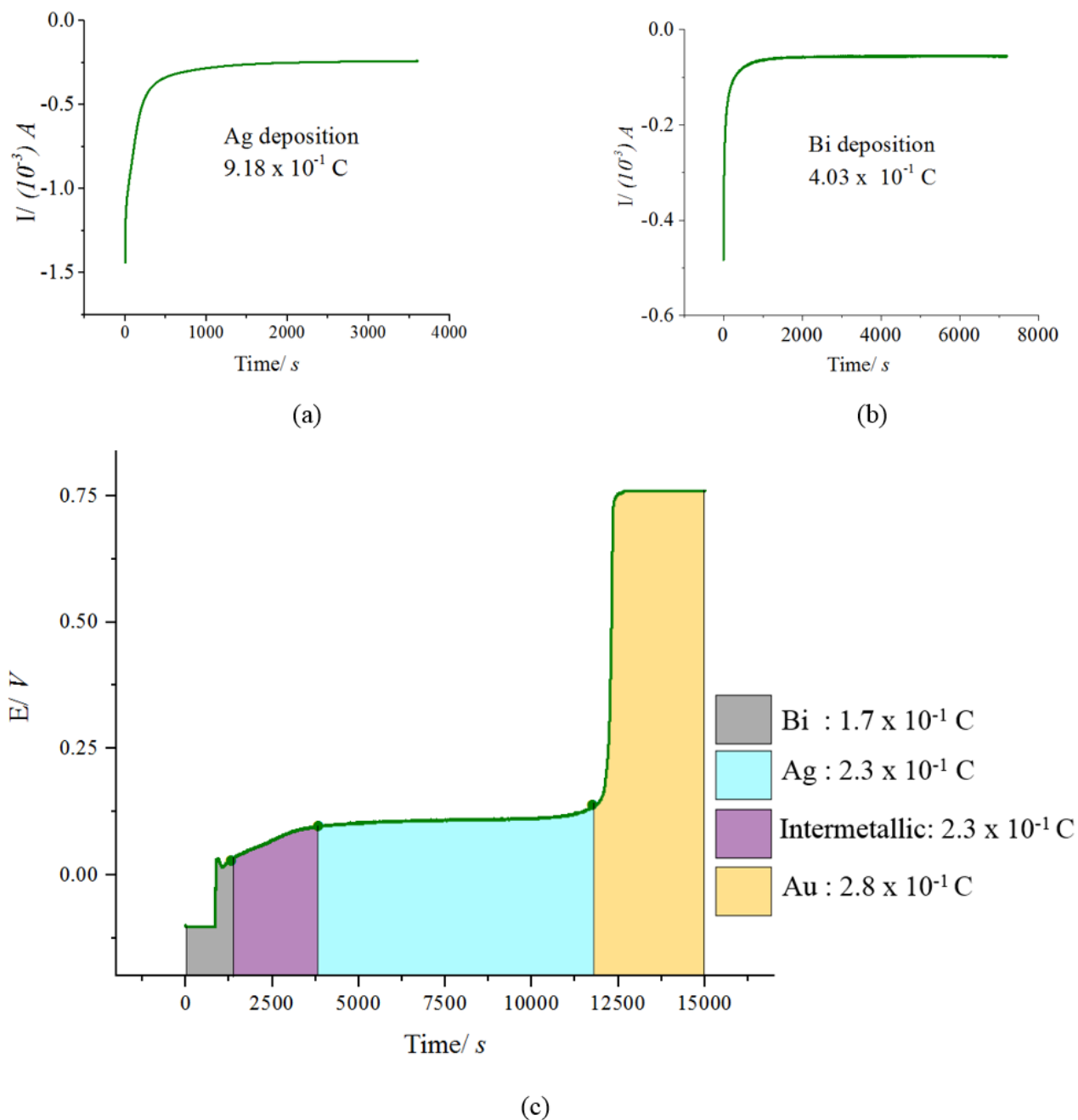**Fig. 6.42** (a) Potentiostatic Ag deposition from 10 mmol dm^{-3} AgCl on Au coated glass slide (WE) for 7200 s at -0.4 V (b) potentiostatic Ag deposition from 20 mmol dm^{-3} BiCl$_3$ on the same glass slide for 7200 s at -0.4 V (c) Galvanostatic stripping using 3 μA in Ethaline 200. All systems used the 3 electrode system (WE, IrO$_2$ coated titanium mesh counter electrode (CE) and Ag pseudo reference electrode (RE)). T = 20 °C.

Table 6.6 Analysis of step experiments

Step experiment (Figure and order of deposition)	Fig. 6.39 $Bi \rightarrow Ag$	Fig. 6.40 $Ag \rightarrow Bi$	Fig. 6.41 $Bi \rightarrow Ag$	Fig. 6.42 $Ag \rightarrow Bi$
Average height calculated by AFM readings (h)	14 nm	52 nm	45 nm	66 nm
Theoretical: Au stripping charge (C)	1.50×10^{-1}	4.30×10^{-1}	3.70×10^{-1}	4.97×10^{-1}
Experimental: pure Au stripping charge (C)	2.63×10^{-3}	2.50×10^{-1}	1.70×10^{-1}	2.80×10^{-1}
Difference in charge (C)	1.13×10^{-1}	1.80×10^{-1}	2.02×10^{-1}	2.17×10^{-1}
Number of moles of Au stripping with other metals (mol)*	1.70×10^{-6}	1.86×10^{-6}	2.09×10^{-6}	2.24×10^{-6}
Deposition charge of Bi metal (C)*	1.44×10^{-2}	2.95×10^{-1}	1.36×10^{-1}	4.03×10^{-1}
Stripping charge for pure Bi metal (C)	3.75×10^{-3}	1.25×10^{-1}	1.89×10^{-2}	1.70×10^{-1}
Difference in charge (C)	1.06×10^{-2}	1.7×10^{-1}	1.17×10^{-1}	2.33×10^{-1}
Number of moles of Bi stripping with other metals (mol)	3.67×10^{-8}	5.80×10^{-7}	6.01×10^{-6}	8.05×10^{-7}
Charge percentage with other metals	73%	58%	86%	58%
Deposition charge of Ag metal (C)	1.08×10^{-2}	1.08×10^{0}	3.60×10^{-2}	9.18×10^{-1}
Stripping charge for pure Ag metal (C)	1.68×10^{-3}	8.12×10^{-1}	5.0×10^{-2}	2.3×10^{-1}
Difference in charge (C)	9.12×10^{-3}	2.68×10^{-1}	†	6.88×10^{-1}
Number of moles of Ag stripping with other metals (mol)	9.45×10^{-8}	2.77×10^{-7}	†	7.13×10^{-6}
Charge percentage with other metals	83%	24%	†	74%

†Remaining values not calculated due to multiple processes being involved.

6.4 X-ray diffraction for electrodeposition of metals

The morphology of thin films can be analysed by X-ray diffraction (XRD).[14] This is commonly used to characterise alloys/ intermetallics.[15–19] Frequently, when thin films are prepared on glass substrates, they are polycrystalline and may contain different crystalline phases.[20] The experimental results take the form of a diffractogram: intensity versus diffraction angle 2θ. The position, intensity and half width of the peak carries physically relevant information. Each peak position is characteristic for a particular crystalline structure. Small shifts from ideal position may indicate a mechanical strain caused by lattice defects created at the deposition stage. Combination of X-ray diffractograms and energy dispersed analysis of X-rays (EDAX) were used to analyse crystalline phases and the composition of films. Atomic Force Microscopy (AFM) was used to study surface morphology and film thickness. In this investigation, gold coated glass slides were used to study deposition of silver, deposition of bismuth and co-deposition of silver/bismuth.For comparison purposes the silver/bismuth deposition on copper, which is a more commercially applicable surface, was also used. To prepare thin films of copper, the metal was sputter coated on to the MPTS layer instead of gold when preparing the working electrodes (see Chapter 3).

6.4.1 Application of XRD for metal systems

Gold/ copper coated glass slides were used as the substrate for preparation of deposition samples. The preparation of these glass slides was discussed in Chapter 3. 10 mmol dm^{-3} silver chloride, 20 mmol dm^{-3} silver chloride, 10 mmol dm^{-3} bismuth chloride and 20 mmol dm^{-3} bismuth chloride solutions in Ethaline 200 were used as electrolytes. The procedures for preparing solutions were given in Chapter 3. The glass slides (each measuring ca. 35 mm by 25 mm) were used as working electrodes (WE). Iridium oxide coated titanium mesh counter electrode and silver pseudo reference electrode were used as the other two electrodes in the three electrode setup for all the experiments. All experiments were carried out at room temperature (20 °C). Chronoamperometry was conducted at predetermined potential value for the deposition of metal layers on the glass slides. Concentration of the electrolyte, deposition potential and time duration for deposition were varied to derive smoother, more adherent coatings with full coverage. The experimental conditions deemed successful (and hence used) are given in the Table 6.7. These prepared plates were used to get the diffraction patterns given in Figs. 6.18 to 6.21. Atomic force microscopy was carried out for silver, bismuth and silver/ bismuth thin

layer deposits to analyse the surface morphology, thickness of the layers and surface roughness. Energy dispersive X-ray analysis (EDAX) was carried out for these slides to assess elemental composition. The analysis of XRD, AFM, EDAX data is also shown in Table 6.7.

6.4.2 Analysis of XRD patterns

The diffraction patterns were obtained using a Rigaku Smartlab diffractometer at a scan range from 22 to 86 degrees with scan rate of 0.01 s/step. The material was characterised in continuous scanning mode using K-Alpha1 (radiation wavelengths 1.54059 Å and 1.54441 Å). The raw data was processed and compared against the STFC Crystallography Open Database (updated 31-08-2018).

XRD pattern of deposited metals (silver, bismuth) are shown from Fig. 6.18 to Fig.6.21. Match! software (version 3.6) from Crystal Impact GbR was used to compare peak positions and peak intensity and ascertain the crystalline phases in the thin film. Further information of phases identified below are given in Table 6.8.

Fig. 6.18 shows multiple peaks for gold and silver which were matched to gold [96-901-2954] and silver [96-901-3048] in the database. No other peaks that correspond to any alloy or intermetallics of these elements were observed. The EDAX showed 30% weight percentage of silver. The average height of the silver layer was 134 nm (Table 6.7) . The surface morphology (Fig. 6.22 b) indicated a nano porous coating of silver with average surface roughness of $R_a =$ 6.2 nm.
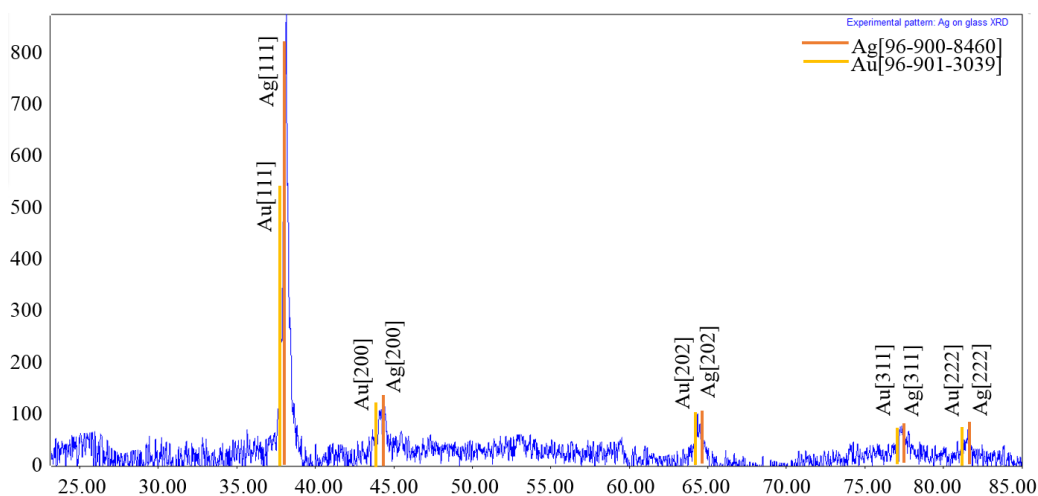
Fig. 6.43 XRD pattern of silver on Au coated glass deposited using -0.4 V for 900 s potentiostatically. Background data has been substracted but not smoothed: since the primary features are clear without applying smoothing functions

The Fig. 6.19 shows the diffraction pattern for bismuth on gold. No diffraction peak corre-

Table 6.7 AFM/EDAX analysis with corresponding experimental details

Figure no	Sample	Sample preparation	Observed color of the sample	Thickness of the layer (b)/ nm	Surface roughness (Ra/nm)	Composition of the layer (by EDAX)
Fig 6.18	Glass / Au / Ag	Au sputter coated on MPTS (a) Ag coated potentiostatically (-0.4 V) for 900 s	White coating	134	6.2	Ag ca. 30%
Fig 6.19	Glass / Au / Bi	Au sputter coated on MPTS (a) Bi coated potentiostatically (-0.5 V) for 900 s	Black coating	273	37	Bi ca. 7%
Fig 6.20	Glass / Au / Ag-Bi	Au sputter coated on MPTS (a) Ag coated potentiostatically (-1.0 V) for 400 s	Coating with grey and black regions	95	15.3	Ag:Bi ca. 30% (w/w%) Ag:Bi ratio ca. 1:1
Fig 6.21	Glass / Cu / Ag-Bi	Au sputter coated on MPTS (a) Ag-Bi coated potentiostatically (-1.0 V) for 300 s	Grey coating	74	42	Ag:Bi ca. 50% (w/w%) Ag:Bi ratio ca. 2:1

Preparation method is given in Chapter 3. (b) Thickness of the sample was found by deducting the initial height of the gold from the final height obtained by AFM. (c) The surface roughness (R_a) was found by AFM measurements taken for separate areas of the sample and calculating the average.
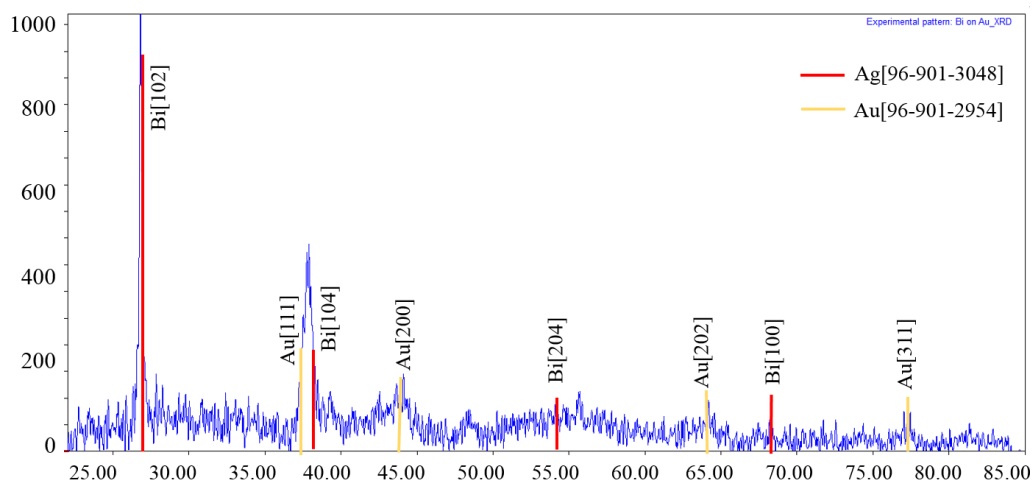
Fig. 6.44 XRD pattern of bismuth on gold coated glass deposited using -0.5 V for 900 s potentiostatically.
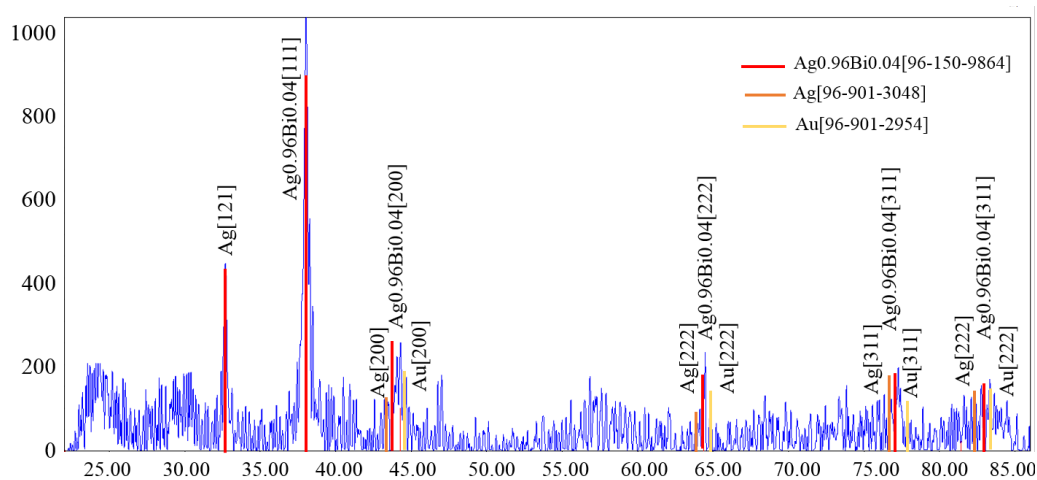
Fig. 6.45 XRD pattern of silver-bismuth on gold coated glass deposited using -1.0 V for 400 s potentionstatically.
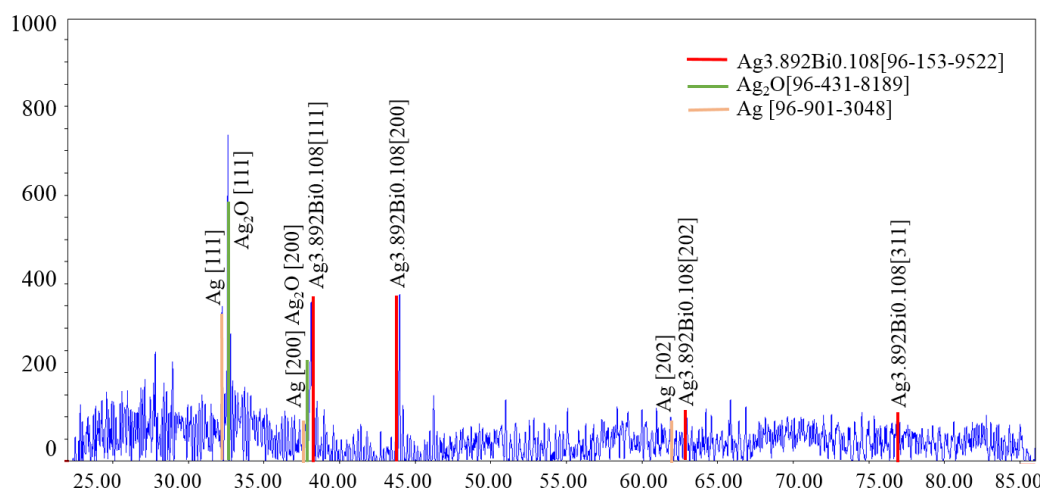
Fig. 6.46 XRD pattern of silver-bismuth on copper coated glass deposited using -1.0 V for 300 s potentiostatically.

sponding to other alloy phases were found in the sample. The AFM gives a surface roughness of R_a = 37 nm (see Fig. 6.22 (a)) and 273 nm layer thickness. EDAX showed 7% weight percentage of bismuth.

The possibility of depositing coatings with high bismuth content can be analysed by evaluating the phases produced in a silver-bismuth coating.[21] Krastev et al showed that 3% bismuth could be incorporated in to the silver lattice to form a solid solution.[21] Work done by Raub et al. concluded that the maximum bismuth solubility in silver is 25%.[22] The Fig. 6.20 shows the diffraction pattern for silver-bismuth deposited on gold coated glass. The solid solution of silver and silver-bismuth intermetallic phases were found as Ag[121], Ag[200], Ag[222], Ag[311] and $Ag_{0.96}Bi_{0.04}$ alloy. Pure gold phases were also found.

To investigate the applicability of silver/ bismuth on other substrates, silver-bismuth was deposited on copper coated glass and the X-ray resultant diffraction pattern obtained is shown in Fig. 6.21. The diffraction of silver/ bismuth pattern matches with $Ag_{3.892}Bi_{0.108}$ [96-153-9522] phase and $Ag_{3.96}Bi_{0.04}$ [96-150-9863] according to the database. Pure phase of silver is also seen with Ag_2O phase. The EDAX of the sample indicates oxygen as an incorporated element. However, oxygen incorporated alloy phases were not detected in the XRD.

The step height of silver-bismuth (Fig. 6.23 a,b) on gold indicated the layer thickness to be 95 nm and Fig. 22 c indicated surface roughness of 15.3 nm (R_a). The EDAX (Fig. 6.25) shows the weight percentage ratio between silver and bismuth to be 54.5:45.4 (Fig. 6.25 - right panel). The SEM of the silver-bismuth surface (Fig. 6.24) shows a smooth surface deposit.

Table 6.8 XRD entries matched to Crystallographic Open Database (COD)[a].

Database entry	COD ID	Formula	Cell parameters		Cell volume /Å^3
			a:b:c /Å	$\alpha : \beta : \gamma$	
96-901-3048	9013047	Ag	4.117; 4.117; 4.117	90; 90; 90	69.782
96-901-2954	9012953	Au	4.0699; 4.0699; 4.0699	90; 90; 90	67.414
96-200-2478	1509863	Ag$_{3.96}$Bi$_{0.04}$	4.0832; 4.0832; 4.0832	90; 90; 90	68.077
96-900-8460	9008459	Ag	4.0862; 4.0862; 4.0862	90; 90; 90	68.227
96-901-3039	9013038	Au	4.103; 4.103; 4.103	90; 90; 90	69.072
96-153-9522	1539521	Ag$_{3.892}$Bi$_{0.108}$	4.09; 4.09; 4.09	90; 90; 90	68.418
96-431-8189	4318188	Ag$_2$O	4.73061; 4.73061; 4.73061	90; 90; 90	105.865

[a] Further details for each entry can be obtained by searching the COD ID on http://www.crystallography.net/cod/search.html
[b] Phase entry (9 digit) in the analysis software is used during the peak matching.
[c] The analysis software also provides a Crystallographic Open Database ID (COD ID) which allows searching online

(a)

(b)

(c)
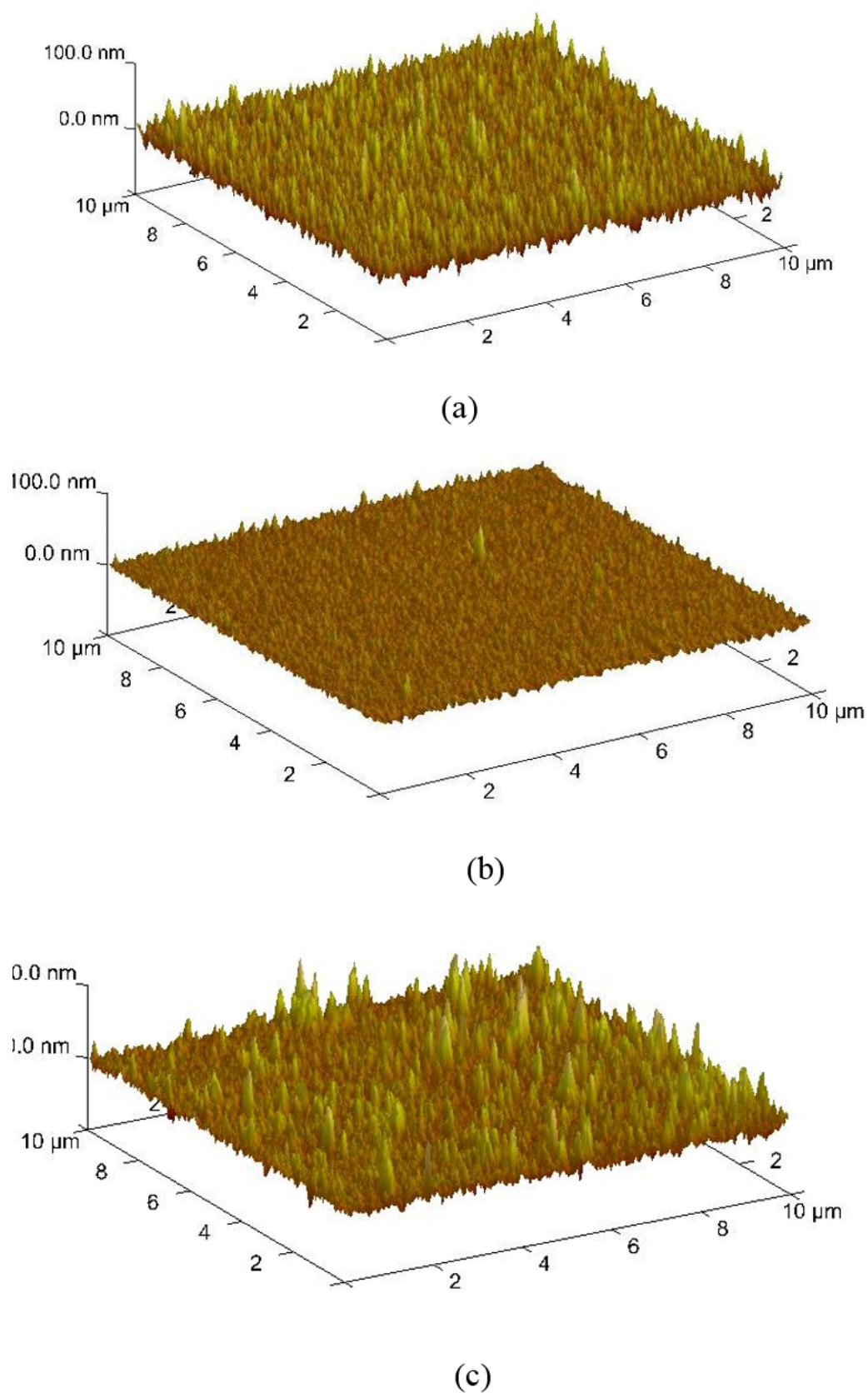
Fig. 6.47 AFM imaging (a) bismuth (R_a= 37 nm)[23] (b) silver (R_a= 6.2 nm)[23] (c) silver/ bismuth (R_a= 15.3 nm)

(a)

(b)
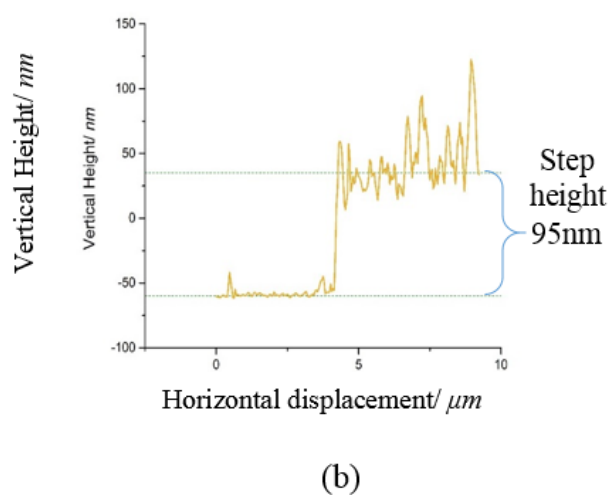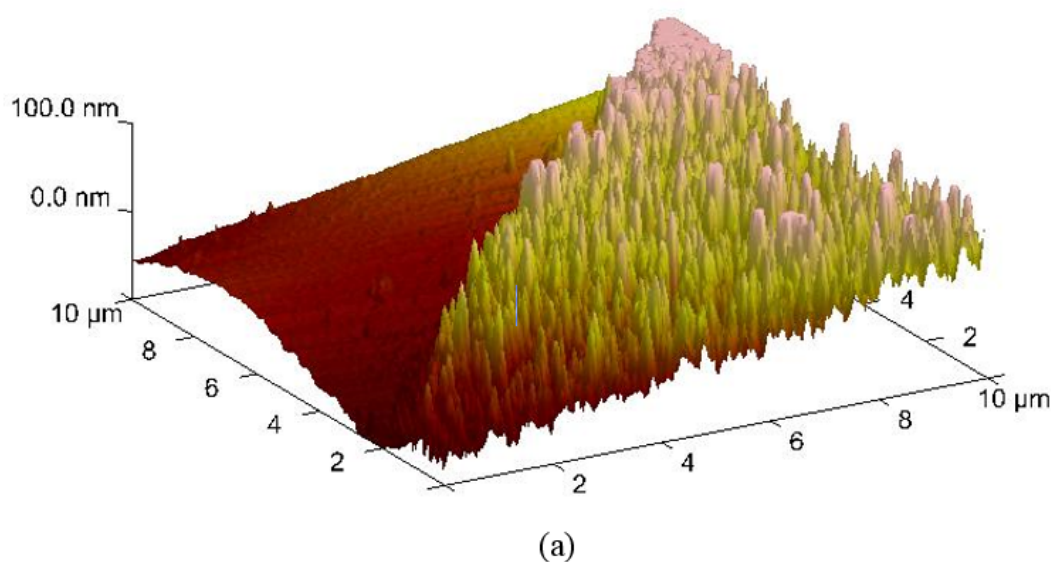
Fig. 6.48 AFM imaging (a) silver/ bismuth border to measure height (b) silver/ bismuth height graph corresponding to (a) .
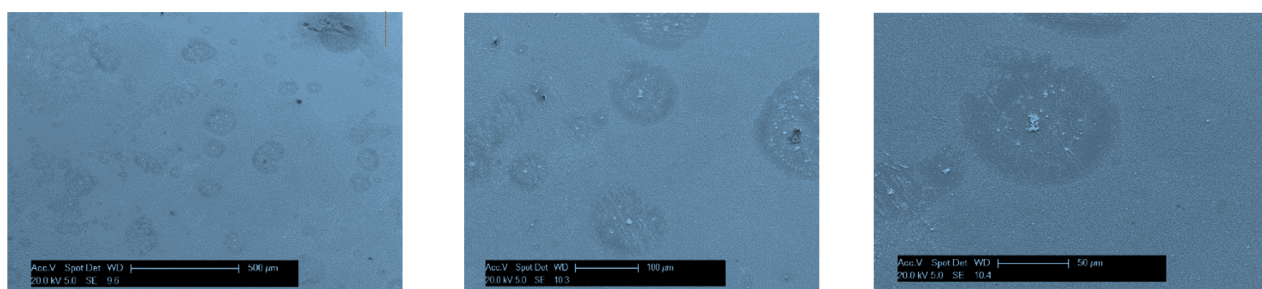
Fig. 6.49 SEM images for silver/ bismuth deposited on gold captured at magnifications (a) X 150 (b) X 500 (c) X 1000 shows smooth coatings of silver/ bismuth with occasional blisters
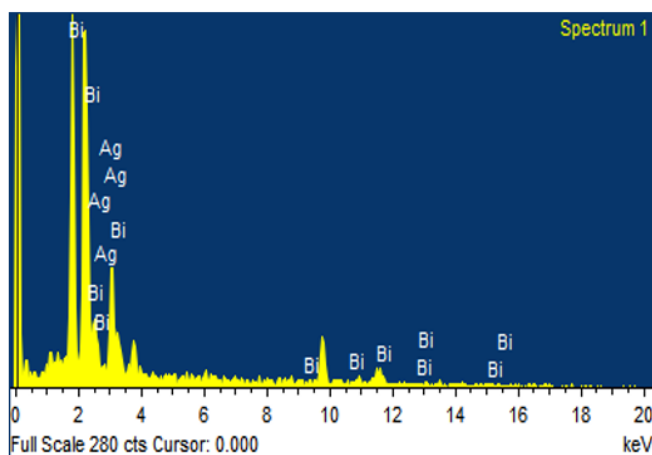
Fig. 6.50 Left panel: EDAX of silver/ bismuth on gold deposited for sample featured in Fig 6.20, Right panel: weight percentage and atomic percentage of EDAX sample (a)

6.5 Summary

The rotating disk electrode method was applied to individual and combined silver, bismuth metal systems. Diffusion coefficient (D), heterogeneous rate constant (k'$_H$), transfer coefficient (α) and standard rate constant (k'$_0$) were found for silver, bismuth and silver/bismuth deposition reactions and the average D values and transfer coefficients found are given below. The silver/ bismuth co-deposition was studied as two separate regions assuming that the deposition limiting currents for the two metals are independent of each other.

Table 6.9 Average diffusion/ transfer coefficient obtained for metal deposition reactions in Ethaline 200 at 20 °C

Metal system	Diffusion coefficient/ $(\times 10^{-7})$ cm^2 s^{-1}	Transfer coefficient/ α
Ag	1.04	0.14
Bi	1.62	0.35
AgBi	9.48 (Ag)[a] 5.13 (Bi)[b]	0.70

[a]Value of silver calculated from limiting current 1
[b]Value of bismuth calculated from limiting current 2

α is a measure of the symmetry of the energy barrier. It provides insight into how the applied voltage would affect the transition state and therefore affects the rate constant (k) of the electron transfer reaction. For silver deposition reactions, α is very low indicating that change in electrode potential will have less of an effect on rate constant compared to that of Bi deposition ($\alpha = 0.35$). For Ag/Bi deposition $\alpha = 0.70$. Diffusion coefficient calculated by the co-deposition reaction gave higher values for individual metal ions compared to values calculated by single deposition. The diffusion coefficient values for the co-deposition may be different

compared to the values calculated for single metal deposition due to variation in speciation of metal ions in Ethaline.

The deposition behaviour on glassy carbon electrode was different to gold and platinum disk electrodes and hence were not used for finding the above averages.

Application of STEP method indicated intermetallics being formed when bismuth is deposited on silver and gold. Considering the metallic radii of the metals involved, we can assume that bismuth forms a substitutional solid solution with gold and silver (metallic radii for bismuth, silver and gold are respectively 230 pm, 172 pm and 166 pm). More studies are needed to confirm this assumption.

XRD experiments that were carried out to check the validity of these observations, were used to analyse the phases present in these silver, bismuth and silver/ bismuth deposits. Silver deposition on gold indicated pure silver phase formation on gold coatings. Bismuth deposition on gold coated glass slides exhibited similar results. However, co-deposition of silver and bismuth on gold surfaces indicated the formation of pure silver phase (Ag[121], Ag[200], Ag[222], Ag(311) and $Ag_{0.96}Bi_{0.04}$ alloy phase.

Silver and bismuth co-deposition as thin films carried out on copper coatings generated films that contained pure silver phase (Ag[111], Ag [200], Ag[202] corresponding to [96-901-3048], silver rich bismuth alloy ($Ag_{3.892}Bi_{0.108}$) and silver oxide (Ag_2O[111], Ag_2O[200])

EDAX results confirmed the percentage ratio between Ag:Bi of Ag/Bi films to be 50%: 50%.

The AFM imaging showed a decrease in surface roughness in silver/ bismuth films (R_a= 15.3 nm) compared to that of bismuth thin films (R_a= 37 nm). The height analysis on silver/ bismuth thin films (electrodeposited by using -1.0 V for 400 s potentiostatically had a thickness of 95 nm. SEM imaging however did not give significant information as the films were too thin for SEM analysis. Surface roughness, thickness are sample parameters can be tuned according to the application.

References

[1] W. D. Sides and Q. Huang, Electrochimica Acta, 2018, **266**, 185–192.

[2] M. Steichen, M. Thomassey, S. Siebentritt and P. J. Dale, Physical Chemistry Chemical Physics, 2011, **13**, 4292–4302.

[3] L. Vieira, A. Whitehead and B. Gollas, Journal of The Electrochemical Society, 2014, **161**, D7–D13.

[4] D. Lloyd, T. Vainikka, S. Schmachtel, L. Murtomäki and K. Kontturi, Electrochimica Acta, 2012, **69**, 139–145.

[5] D. Lloyd, T. Vainikka, L. Murtomäki, K. Kontturi and E. Ahlberg, Electrochimica Acta, 2011, **56**, 4942–4948.

[6] L. Vieira, R. Schennach and B. Gollas, Electrochimica Acta, 2016, **197**, 344–352.

[7] J. C. Malaquias, M. Steichen, M. Thomassey and P. J. Dale, Electrochimica Acta, 2013, **103**, 15–22.

[8] L. Vieira, J. Burt, P. W. Richardson, D. Schloffer, D. Fuchs, A. Moser, P. N. Bartlett, G. Reid and B. Gollas, ChemistryOpen, 2017, **6**, 393–401.

[9] M. M. Badea, A. Cojocaru and L. Anicai, UPB Sci. Bull. Series B, 2014, **76**, 21–32.

[10] A. P. Abbott, R. C. Harris and K. S. Ryder, The Journal of Physical Chemistry B, 2007, **111**, 4910–4913.

[11] T. Dobrev, M. Monev, S. Nikolova et al., Surface and Coatings Technology, 1986, **29**, 27–39.

[12] E. P. Harbulak, Method for simultaneous determination of thickness and electrochemical potential in multilayer plated deposits, 1982, US Patent 4,310,389.

[13] E. P. Harbulak, SAE Transactions, 1980, 1760–1768.

14 P. L. Davies, U. Gather, M. Meise, D. Mergel, T. Mildenberger et al., The Annals of Applied Statistics, 2008, **2**, 861–886.

15 V. B. Kumar, G. Kimmel, Z. Porat and A. Gedanken, New Journal of Chemistry, 2015, **39**, 5374–5381.

16 T. Dobrovolska, I. Krastev, B. Jović, V. Jović, G. Beck, U. Lačnjevac and A. Zielonka, Electrochimica Acta, 2011, **56**, 4344–4350.

17 S. P. Singh and B. Karmakar, Plasmonics, 2011, **6**, 457–467.

18 V.-F. Ruiz-Ruiz, I. Zumeta-Dube, D. Díaz, M. J. Arellano-Jimenez and M. Jose-Yacaman, The Journal of Physical Chemistry C, 2016, **121**, 940–949.

19 P. Kumar, J. Singh and A. C. Pandey, RSC Advances, 2013, **3**, 2313–2317.

20 M. Birkholz, P. Fewster and C. Genzel, Wiley VCH, ISBN, 2006, **3**, 31o25.

21 I. Krastev, T. Valkova and A. Zielonka, Journal of Applied Electrochemistry, 2004, **34**, 79–85.

22 E. Raub and A. Engel, Z. Metallkunde, 1950, **41**, 485.

23 C. J. Zaleski, Ph.D. thesis, University of Leicester, 2015.

Chapter 7

Conclusions and future work

Contents

7.1 Conclusions

The overarching aim of this thesis was to investigate electrodeposition of bismuth and silver/bismuth metal coatings using environmentally friendly deep eutectic solvents (Fig. 7.1). Investigation of redox chemistry at the electrode/ electrolyte interface, interfacial mass transport is important in developing electroplating and electropolishing techniques. Optical methods are not commonly used for this purpose despite their many advantages. In the current study, applications of the novel technique of using Probe Beam Deflection with Electrochemical Quartz Crystal Microbalance (PBD/ EQCM) for studying metal deposition/ dissolution processes was investigated. The high viscosity of deep eutectic solvents causes a temporal delay of species, travelling between electrode surface and the focal point of the beam. This challenge was successfully overcome through the application of very low scan rate (ca. 0.0625 mV s^{-1}) and by reduction of beam/ electrode distance. The experimental setup was calibrated and the method was validated by following the experimental approach by Henderson et al.[1] The PBD/ EQCM method was then successfully applied to the metal systems: silver and bismuth. The method was used to determine the following,

1. Speciation of metal ions present at the near electrode area: $[AgCl_2^-]$ and $[AgCl_3]^{2-}$ for silver in Ethaline

2. Changes in redox oxidation states [Bi(I) or Bi(III)] involved in bismuth deposition at various stages using dm vs Q graphs

3. Underpotential deposition occurring in bismuth deposition and the localised effects of dissolution of this UPD layer

4. Possible species and their ratios in silver/ bismuth co-deposition

Understanding fundamentals of electrodeposition of metal systems of interest in DES is important for potential applications. For this purpose a systematic study of bismuth deposition, silver deposition and bismuth-silver co-deposition in 1:2 ChCl:EG was conducted. The electrochemical behaviour of these metals in 1:2 ChCl:EG were studied using potentiodynamic, potentiostatic and electrogravimetric methods. These studies were used to find diffusion coefficients and kinetic parameters for each metal system (see Table 7.1).

Application of theoretical models for nucleation and initial growth proposed by Hills et al.[2,3] and Sharifker and Monstany,[4] graphical and non-dimensional comparison of the early part of current transients indicated the following
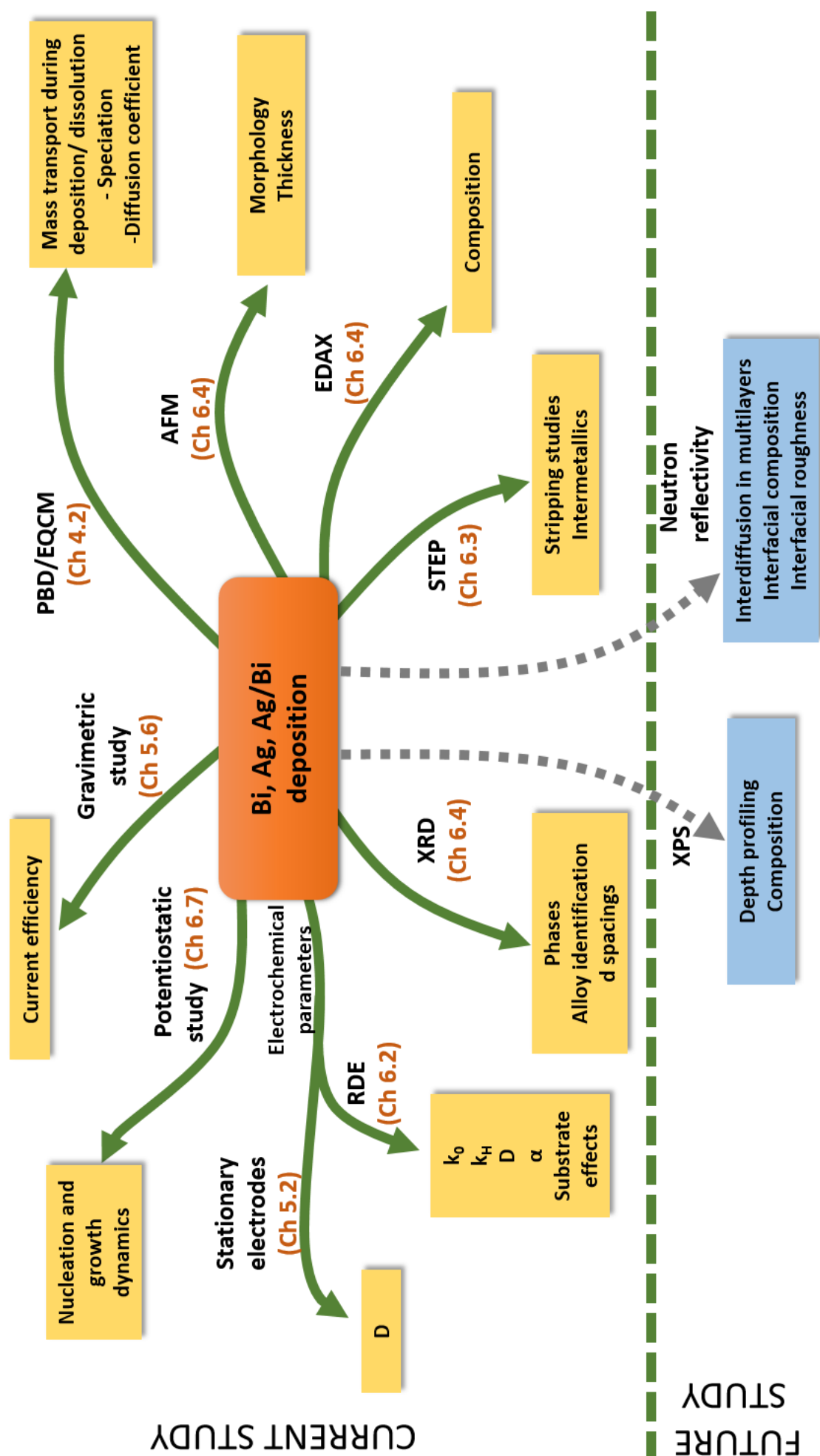
Fig. 7.1 Methodology and derived outcomes (including planned future work)

1. At low applied potentials silver deposition and bismuth deposition followed progressive nucleation and diffusion control 3D growth

2. At high applied potentials silver followed instantaneous nucleation and diffusional controlled 3D growth

3. For bismuth for intermediate applied potentials, current density plots indicated that the nucleation happens through instantaneous and progressive mechanisms.

4. For silver deposition for intermediate applied potentials current transient were more closer to the instantaneous theoretical curve indicating that instantaneous mechanism is favoured.

5. When the same models were applied to the co-deposition the variable plots fell between theoretical instantaneous and progressive lines only in the $t/t_{max} < 1$ region indicating that these models cannot be applied to study the $t/t_{max} > 1$ region for co-deposition.

Applications of hydrodynamic electrode (mainly RDE) method was used for metals systems in DES. Gold, platinum and glassy carbon rotating disk electrodes were used for this purpose. The behaviour of deposition current transients under non-diffusion control conditions were used to calculate fundamental parameters involved in electrodeposition. These values were then compared to values derived from potentiodynamic studies using stationary electrodes and values derived from the probe beam method (see Table 7.1).

The fundamentals of nucleation, growth, interfacial kinetics, redox chemistry and mass transport at electrode-electrolyte interface for bismuth deposition and silver-bismuth deposition was investigated successfully. To complete the investigation of behaviour of these metals in DES it is crucial to study the products of these electrochemical depositions. To achieve this, thin films of bismuth, silver and silver-bismuth were deposited on gold coated glass slides and STEP experiments were conducted. From STEP experiments, by analysing the stripping potentials for silver and bismuth layers it was evident that silver and bismuth deposition formed intermetallic compounds. In order to analyse this aspect further, X-ray diffraction, EDAX and AFM studies were used. Using XRD it was possible to identify the composition of silver-bismuth intermetallics that were formed. AFM studies were used to analyse the thickness and surface morphology of deposited films (thickness of silver bismuth film was ca. 95 nm for selected experimental conditions). The EDAX showed the percentages of bismuth and silver for silver/ bismuth intermetallic was in 1:1 ratio. To check the applicability of these methods to substrates such as copper, same experiments were repeated by replacing gold slides with copper coated slides. Successful deposition of silver/ bismuth coatings were achieved on the surfaces.

Table 7.1 Diffusion coefficients and kinetic parameters for each metal system at T= 20 °C

	AgCl/ Ethaline	BiCl3/ Ethaline	AgCl/ BiCl3/ Ethaline 200
D calculated for each system from PBD/EQCM (Chronoamperometry) /cm^{2}s^{-1}	4.30 E-07	2.20 E -07	1.65 E-07 (Ag) 1.65 E -07 (Bi)
Average D calculated from Randles Sevcik equation (Cyclic voltammetry) /cm^{2}s^{-1}	2.01 E-07	1.77 E-07	3.09 E-07 (Ag) 2.10 E-07 (Bi)
Average D calculated from Cottral equation (Chronoamperometry) /cm^{2}s^{-1}	2.16 E-07	2.4 E-07	N/A
Diffusion coefficient from Koutecky Levich equation (Linear sweep voltammetry) /cm^{2}s^{-1}	3.43 E-07	4.96 E-07	2.77 E-07 (Bi) 1.35 E-06 (Ag)
Transfer coefficient (α) from Koutecky Levich equation (Linear sweep voltammetry) /cm^{2}s^{-1}	Pt - 0.14 Au- 0.24	Pt - 0.39 Au- 0.63	Pt (Ag)-0.22 Au (Ag)-0.56
Standard rate constant (k_0) from Koutecky Levich equation (Linear sweep voltammetry) /cm s-1	Pt - 1.57 E-05 Au - 1.78 E-07	Pt - 4.76 E-05 Au - 1.03 E-05	Pt (Ag) - 4.56 E-06 Au (Ag) - 1.08 E-06

These results were verified by XRD to be $Ag_{3.892}Bi_{0.108}$ [96-153-9522] phase and $Ag_{3.96}Bi_{0.04}$ [96-150-9863] on copper.

Overall silver-bismuth codeposition and bismuth electrodeposition have been achieved using deep eutectic solvents at room temperature. The fundamental electrochemical parameters for the electrodeposition of these metals in DES were calculated using various methods. The novel technique of PBD/ EQCM method was applied successfully to study mass transport and redox chemistry of metal and codeposition in DES.

7.2 Future work

Time resolved neutron reflectivity (NR) methods can be used to measure the interfacial composition of bilayers and alloys of silver and bismuth deposited under potentiodynamic conditions in DES media. Deposit morphology, composition, surface interfacial roughness and interfacial mixing of metals have an essential role in the function of the coating. This can be explored using time resolved NR. Scattering length densities (SLD) of gold, silver and bismuth have been shown to be suitably different to be studied by neutron scattering (Fig. 7.2).
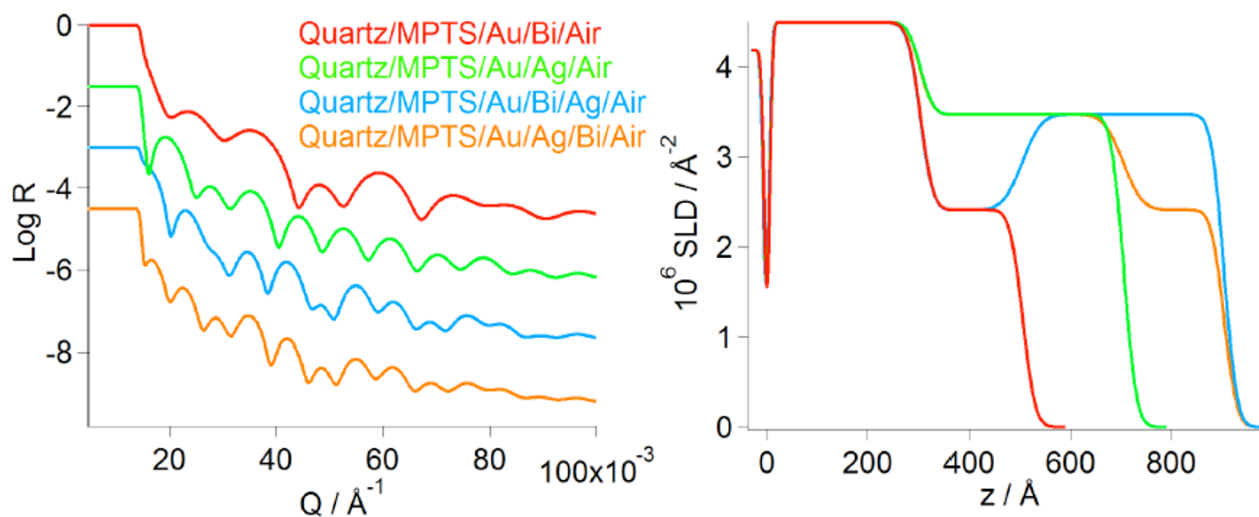
Fig. 7.2 Simulated NR and SLD profiles for bismuth and silver deposited on gold coated quartz.

The simulated model for deposition of these metals (silver followed by bismuth and vice versa) on gold coated quartz blocks using MPTS as an adhesion layer is shown in Fig. 7.2. The model proves that profiles are easily identifiable even with an interfacial roughness set at 10% (of layer thickness).

The preliminary measurements conducted have indicated that NR studies are feasible and viable and could be used to investigate: time scale of interdiffusion of electrodeposited (silver,

bismuth) bilayers, interdiffusion of first layer (gold) with substrate layer, interfacial roughness during growth phase of metal layers and mechanism of penetration down the grain boundaries during alloy deposition.

EDAX, with penetration depth in μm range, effectively gives the bulk concentration of elements present in a sample. X-ray photoelectron spectroscopy (XPS) on the other hand gives the composition of the near surface region of a sample (i.e. the elements present in the top few nanometers in the sample). Therefore, using XPS, the composition of thin films (few atomic layers at the surface) can be studied.

References

[1] M. J. Henderson, A. R. Hillman, E. Vieil and C. Lopez, Journal of Electroanalytical Chemistry, 1998, **458**, 241–248.

[2] B. Scharifker and G. Hills, Electrochimica Acta, 1983, **28**, 879–889.

[3] G. Gunawardena, G. Hills, I. Montenegro and B. Scharifker, Journal of Electroanalytical Chemistry and Interfacial Electrochemistry, 1982, **138**, 225–239.

[4] B. Scharifker and J. Mostany, Journal of Electroanalytical Chemistry and Interfacial Electrochemistry, 1984, **177**, 13–23.

Bibliography

[1] J.-P. Celis, M. De Bonte and J. Roos, Transactions of the IMF, 1994, **72**, 89–93.

[2] C. Raub, in Metal Plating and Patination, Elsevier, 1993, pp. 284–290.

[3] A. Volta et al., Philosophical Transactions of the Royal Society of London, 1800, **90**, 403–431.

[4] P. D. Buchanan, Platinum Metals Review, 1981, **25**, 32–41.

[5] G. Di Bari, Modern Electroplating, Edited by Mordechay Schlesinger and Milan Paunovic, 2000.

[6] J. Dini, Electrodeposition: the materials of coating and substrates (chapter 9), 1993.

[7] K. Robbie, L. Friedrich, S. Dew, T. Smy and M. Brett, Journal of Vacuum Science & Technology A: Vacuum, Surfaces, and Films, 1995, **13**, 1032–1035.

[8] I. Gurrappa and L. Binder, Science and Technology of Advanced Materials, 2008, **9**, 043001.

[9] J. D. Madden and I. W. Hunter, Journal of Microelectromechanical Systems, 1996, **5**, 24–32.

[10] J. Whitaker, J. Nelson and D. Schwartz, Journal of Micromechanics and Microengineering, 2005, **15**, 1498.

[11] A. M. van der Putten and J. W. G. de Bakker, Journal of The Electrochemical Society, 1993, **140**, 2221–2228.

[12] J. Hu and M.-F. Yu, Science, 2010, **329**, 313–316.

[13] H. Sato, T. Homma, K. Mori, T. Osaka and S. Shoji, Electrochemistry, 2005, **73**, 275–278.

[14] H. Sato, T. Homma, H. Kudo, T. Izumi, T. Osaka and S. Shoji, Journal of Electroanalytical Chemistry, 2005, **584**, 28–33.

15 I. S. F. Policy, <u>Policy, ICSU Scientific Freedom</u>, 2013, 1.

16 L. J. Durney, <u>Graham's Electroplating Engineering Handbook</u>, Springer Science & Business Media, 1984.

17 G. Gottstein and L. S. Shvindlerman, <u>Grain boundary migration in metals: thermodynamics, kinetics, applications</u>, CRC press, 2009.

18 S. Tjong and H. Chen, <u>Materials Science and Engineering: R: Reports</u>, 2004, **45**, 1–88.

19 L. P. Bicelli, B. Bozzini, C. Mele and L. D'Urzo, <u>Int. J. Electrochem. Sci</u>, 2008, **3**, 356–408.

20 M. Datta and D. Landolt, <u>Electrochimica Acta</u>, 2000, **45**, 2535–2558.

21 E. Koukharenko, X. Li, I. Nandhakumar, N. Fréty, S. Beeby, D. Cox, M. Tudor, B. Schiedt, C. Trautmann, A. Bertsch <u>et al.</u>, <u>Journal of Micromechanics and Microengineering</u>, 2008, **18**, 104015.

22 F. Xiao, C. Hangarter, B. Yoo, Y. Rheem, K.-H. Lee and N. V. Myung, <u>Electrochimica Acta</u>, 2008, **53**, 8103–8117.

23 P. Allongue, F. Maroun, H. F. Jurca, N. Tournerie, G. Savidand and R. Cortès, <u>Surface Science</u>, 2009, **603**, 1831–1840.

24 K. Rajeshwar, N. De Tacconi and C. Chenthamarakshan, <u>Current Opinion in Solid State and Materials Science</u>, 2004, **8**, 173–182.

25 I. Dharmadasa and J. Haigh, <u>Journal of the Electrochemical Society</u>, 2006, **153**, G47–G52.

26 C. Koch, Journal of Physics: Conference Series, 2009, p. 012081.

27 Q. Huang, A. Kellock and S. Raoux, <u>Journal of The Electrochemical Society</u>, 2008, **155**, D104–D109.

28 N. Kanani, <u>Electroplating: basic principles, processes and practice</u>, Elsevier, 2004, p. 14.

29 M. Miranda-Hernández, M. Palomar-Pardavé, N. Batina and I. González, <u>Journal of Electroanalytical Chemistry</u>, 1998, **443**, 81–93.

30 D. Hernández-Santos, M. B. González-García and A. Costa-García, <u>Electrochimica Acta</u>, 2005, **50**, 1895–1902.

31 M. Antler, <u>Wear</u>, 1985, **106**, 5–33.

32 F. Findik and H. Uzun, Materials & design, 2003, **24**, 489–492.

33 I. Krastev, T. Valkova and A. Zielonka, Journal of Applied Electrochemistry, 2004, **34**, 79–85.

34 F. Mao, M. Taher, O. Kryshtal, A. Kruk, A. Czyrska-Filemonowicz, M. Ottosson, A. M. Andersson, U. Wiklund and U. Jansson, ACS Applied Materials & Interfaces, 2016, **8**, 30635–30643.

35 S. L. Tay, Ph.D. thesis, University of Auckland, 2016.

36 M. Kumar and S. Deka, ACS applied materials & interfaces, 2014, **6**, 16071–16081.

37 M. Adamik, P. Barna and I. Tomov, Thin Solid Films, 2000, **359**, 33–38.

38 S. Zhong, T. Koch, M. Wang, T. Scherer, S. Walheim, H. Hahn and T. Schimmel, Small, 2009, **5**, 2265–2270.

39 K. Kumar, S. Suresh, M. Chisholm, J. Horton and P. Wang, Acta Materialia, 2003, **51**, 387–405.

40 B. Yu, K. M. Leung, Q. Guo, W. M. Lau and J. Yang, Nanotechnology, 2011, **22**, 115603.

41 P.-A. Gay, P. Bercot and J. Pagetti, Surface and Coatings Technology, 2001, **140**, 147–154.

42 R. Pasricha, S. Gupta and A. K. Srivastava, Small, 2009, **5**, 2253–2259.

43 I. Krastev, T. Valkova and A. Zielonka, Journal of Applied Electrochemistry, 2003, **33**, 1199–1204.

44 W. Butler and G. Stocks, Physical Review B, 1984, **29**, 4217.

45 S. Chithra, S. Lele and K. Chattopadhyay, Acta Materialia, 2011, **59**, 2009–2019.

46 T. Alford, D. Adams, T. Laursen and B. Manfred Ullrich, Applied Physics Letters, 1996, **68**, 3251–3253.

47 R. Crisp and J. Rungis, Philosophical Magazine, 1970, **22**, 217–236.

48 B. Navinšek, P. Panjan and I. Milošev, Surface and Coatings Technology, 1999, **116**, 476–487.

49 Y. Wang, Y. Ju, S. Wei, W. Lu, B. Yan and W. Gao, Materials Characterization, 2015, **102**, 189–194.

[50] A. Blair, Metal Finishing, 2002, **100**, 284–290.

[51] M. A. Berding, A. Sher, A.-B. Chen and W. Miller, Journal of Applied Physics, 1988, **63**, 107–115.

[52] J. Weeks, Lead, Bismuth, Tin and Their Alloys as Nuclear Coolants, Brookhaven national lab., upton, ny technical report, 1971.

[53] G. G. Briand and N. Burford, Chemical reviews, 1999, **99**, 2601–2658.

[54] J. Amneklev, A. Augustsson, L. Sörme and B. Bergbäck, Journal of Industrial Ecology, 2016, **20**, 99–106.

[55] C. H. Chen and A. A. Gewirth, Journal of the American Chemical Society, 1992, **114**, 5439–5440.

[56] C. A. Jeffrey, D. A. Harrington and S. Morin, Surface Science, 2002, **512**, L367–L372.

[57] C. A. Jeffrey, S. H. Zheng, E. Bohannan, D. A. Harrington and S. Morin, Surface science, 2006, **600**, 95–105.

[58] S. Jiang, Y.-H. Huang, F. Luo, N. Du and C.-H. Yan, Inorganic Chemistry Communications, 2003, **6**, 781–785.

[59] F. Yang, K. Liu, K. Hong, D. Reich, P. Searson and C. Chien, Science, 1999, **284**, 1335–1337.

[60] S. Cho, Y. Kim, A. Freeman, G. Wong, J. Ketterson, L. Olafsen, I. Vurgaftman, J. Meyer and C. Hoffman, Applied Physics Letters, 2001, **79**, 3651–3653.

[61] P. Kapitza, Proc. R. Soc. Lond. A, 1928, **119**, 358–443.

[62] Y.-M. Lin, S. B. Cronin, J. Y. Ying, M. Dresselhaus and J. P. Heremans, Applied Physics Letters, 2000, **76**, 3944–3946.

[63] L. Hicks and M. Dresselhaus, MRS Online Proceedings Library Archive, 1993, **326**, year.

[64] L. L. Y. J. X. Yongqi, Journal of Beijing University of Aeronautics and Astronautics, 2003, **3**, 014.

[65] D. DeLongchamp and P. T. Hammond, Advanced Materials, 2001, **13**, 1455–1459.

[66] G. A. Snook, P. Kao and A. S. Best, Journal of Power Sources, 2011, **196**, 1–12.

67 R. Bhattacharya, M. M. de KOK and J. Zhou, Applied Physics Letters, 2009, **95**, 314.

68 Y. Xu, Y. Wang, J. Liang, Y. Huang, Y. Ma, X. Wan and Y. Chen, Nano Research, 2009, **2**, 343–348.

69 M. A. Namboothiry, T. Zimmerman, F. M. Coldren, J. Liu, K. Kim and D. L. Carroll, Synthetic Metals, 2007, **157**, 580–584.

70 T. Christen and M. W. Carlen, Journal of Power Sources, 2000, **91**, 210–216.

71 E. Frackowiak, V. Khomenko, K. Jurewicz, K. Lota and F. Béguin, Journal of Power Sources, 2006, **153**, 413–418.

72 E. W. Paul, A. J. Ricco and M. S. Wrighton, The Journal of Physical Chemistry, 1985, **89**, 1441–1447.

73 A. Jean-Louis and C. Hamon, Physica Status Solidi (b), 1969, **34**, 329–340.

74 B. Joukoff and A. Jean-Louis, Journal of Crystal Growth, 1972, **12**, 169–172.

75 K. Oe, S. Ando and K. Sugiyama, Japanese Journal of Applied Physics, 1981, **20**, L303.

76 A. Noreika, W. Takei, M. Francombe and C. Wood, Journal of Applied Physics, 1982, **53**, 4932–4937.

77 A. Noreika, J. Greggi Jr, W. Takei and M. Francombe, Journal of Vacuum Science & Technology A: Vacuum, Surfaces, and Films, 1983, **1**, 558–561.

78 J. Zilko and J. Greene, Applied Physics Letters, 1978, **33**, 254–256.

79 J. Zilko and J. Greene, Journal of Applied Physics, 1980, **51**, 1560–1564.

80 GB Patent 590 412 (1947).

81 V. Povetkin and T. Shibleva, Protection of metals, 2006, **42**, 516–519.

82 B. Powell and D. Woodruff, Philosophical magazine, 1976, **34**, 169–176.

83 B. Powell and H. Mykura, Acta metallurgica, 1973, **21**, 1151–1156.

84 M. Yan, M. Šob, D. E. Luzzi, V. Vitek, G. J. Ackland, M. Methfessel and C. Rodriguez, Physical Review B, 1993, **47**, 5571.

85 G. Duscher, M. F. Chisholm, U. Alber and M. Rühle, Nature materials, 2004, **3**, 621.

[86] I. Karakaya and W. Thompson, Journal of Phase Equilibria, 1993, **14**, 525–530.

[87] D. F. B.M. Luce, in Modern Electroplating, ed. F. Lowenheim, J. Wiley and Sons, New York, 1974, ch. 14, p. 358.

[88] P. Vjacheslavov, Lenizdat, Leningrad, 1974, 213.

[89] P. Vjacheslavov, S. J. Grilihes, G. Burkat and E. Kruglova, Mashinostroenie, Leningrad, 1970, **1**, year.

[90] I. Krastev, Journal of Engineering & Processing Management, 2009, **1**, 104–112.

[91] E. Raub and A. Engel, Z. Metallkunde, 1950, **41**, 485.

[92] G. Li, L. Kay, G. Liu, P. Liu and Y. Tong, Electrochemical and solid-state letters, 2006, **9**, C32–C35.

[93] Y. Wang, G. Cheng, S. L. Tay, Y. Guo, X. Sun and W. Gao, Materials, 2017, **10**, 932.

[94] R. M. Shalaby, M. Allzeleh and M. Kamal, Journal of Advances in Physics, 2018, **14**, 5504–5519.

[95] V. M. Donnelly, I. P. Herman and M. Hirose, 1987.

[96] A. Sherman, Chemical vapor deposition for microelectronics: principles, technology, and applications, 1987.

[97] R. F. Bunshah and C. Weissmantel, Handbook of hard coatings, Noyes publications Park Ridge, NJ, 2001.

[98] K. Choy, Progress in Materials Science, 2003, **48**, 57–170.

[99] C. Ryu, K. Kwon, A. Loke, H. Lee and T. Nogami, IEEE Trans. Electron Devices, 1999, **46**, 1113.

[100] B. Chin, P. Ding, B. Sun, T. Chiang, D. Angelo, I. Hashim, Z. Xu, S. Edelstein and F. Chen, Solid State Technology, 1998, **41**, 141–145.

[101] J. Reid, S. Mayer, E. Broadhent, E. Klawuhn and K. Ashtiani, Solid State Technology, 2000, **43**, 86–86.

[102] C. G. Fink, Science, 1950, **112**, 12.

103 A. P. Abbott, I. Dalrymple, F. Endres and D. R. MacFarlane, Electrodeposition from Ionic Liquids, 2008, 1.

104 K. Izutsu, Electrochemistry in nonaqueous solutions, John Wiley & Sons, 2009.

105 M. Galiński, A. Lewandowski and I. Stępniak, Electrochimica Acta, 2006, **51**, 5567–5580.

106 V. Kumar and S. V. Malhotra, Ionic liquid applications: Pharmaceuticals, therapeutics, and biotechnology, 2010, 1–12.

107 P. D. de María, Ionic liquids in biotransformations and organocatalysis: solvents and beyond, John Wiley & Sons, 2012.

108 Z. Fang, R. L. Smith and X. Qi, Production of biofuels and chemicals with ionic liquids, Springer, 2014.

109 J. Dupont, T. Itoh, P. Lozano and S. Malhotra, Environmentally friendly syntheses using ionic liquids, CRC Press, 2014.

110 A. Kokorin, InTech, New York, NY.

111 R. Rogers, N. Plechkova and K. Seddon, ACS Symposium Series, 2009.

112 K. R. Seddon, Nature materials, 2003, **2**, 363.

113 T. Welton, Chemical Reviews, 1999, **99**, 2071–2084.

114 H. L. Chum, V. Koch, L. Miller and R. Osteryoung, Journal of the American Chemical Society, 1975, **97**, 3264–3265.

115 J. S. Wilkes, J. A. Levisky, R. A. Wilson and C. L. Hussey, Inorganic Chemistry, 1982, **21**, 1263–1264.

116 A. P. Abbott, G. Capper, D. L. Davies, R. K. Rasheed and V. Tambyrajah, Chemical Communications, 2003, 70–71.

117 R. A. Sheldon, Green Chemistry, 2007, **9**, 1273–1283.

118 I. J. Lin and C. S. Vasam, Journal of Organometallic Chemistry, 2005, **690**, 3498–3512.

119 F. Endres, ChemPhysChem, 2002, **3**, 144–154.

120 Q. Zhang, K. D. O. Vigier, S. Royer and F. Jérôme, Chemical Society Reviews, 2012, **41**, 7108–7146.

121 G.-B. Pan and W. Freyland, <u>Electrochimica Acta</u>, 2007, **52**, 7254–7261.

122 Y.-C. Fu, Y.-Z. Su, H.-M. Zhang, J.-W. Yan, Z.-X. Xie and B.-W. Mao, <u>Electrochimica Acta</u>, 2010, **55**, 8105–8110.

123 C. Agapescu, A. Cojocaru, A. Cotarta and T. Visan, <u>Journal of Applied Electrochemistry</u>, 2013, **43**, 309–321.

124 C. Agapescu, A. Cojocaru, F. Golgovici, A. Cristian Manea and A. Cotarta, <u>Rev. Chim.(Bucharest)</u>, 2012, **63**, 911.

125 A. Abbott, J. Barron and K. Ryder, <u>Transactions of the IMF</u>, 2009, **87**, 201–207.

126 A. P. Abbott, J. C. Barron, G. Frisch, K. S. Ryder and A. F. Silva, <u>Electrochimica Acta</u>, 2011, **56**, 5272–5279.

127 F. Endres, A. P. Abbott and D. R. MacFarlane, <u>Phys. Chem. Chem. Phys</u>, 2006, **8**, 4265–4279.

128 A. P. Abbott, K. El Ttaib, G. Frisch, K. J. McKenzie and K. S. Ryder, <u>Physical Chemistry Chemical Physics</u>, 2009, **11**, 4269–4277.

129 A.-M. Popescu, A. Cojocaru, C. Donath and V. Constantin, <u>Chemical Research in Chinese Universities</u>, 2013, **29**, 991–997.

130 A. Abbott, K. El Ttaib, K. Ryder and E. Smith, <u>Transactions of the IMF</u>, 2008, **86**, 234–240.

131 A. P. Abbott, K. El Ttaib, G. Frisch, K. S. Ryder and D. Weston, <u>Physical Chemistry Chemical Physics</u>, 2012, **14**, 2443–2449.

132 H. M. Abood, A. P. Abbott, A. D. Ballantyne and K. S. Ryder, <u>Chemical Communications</u>, 2011, **47**, 3523–3525.

133 E. Gómez, P. Cojocaru, L. Magagnin and E. Valles, <u>Journal of Electroanalytical Chemistry</u>, 2011, **658**, 18–24.

134 E. L. Smith, A. P. Abbott and K. S. Ryder, <u>Chemical Reviews</u>, 2014, **114**, 11060–11082.

135 A. P. Abbott, G. Capper, D. L. Davies and R. K. Rasheed, <u>Chemistry–A European Journal</u>, 2004, **10**, 3769–3774.

[136] E. S. Ferreira, C. Pereira and A. Silva, Journal of Electroanalytical Chemistry, 2013, **707**, 52–58.

[137] J. Vijayakumar, S. Mohan, S. A. Kumar, S. Suseendiran and S. Pavithra, International journal of hydrogen energy, 2013, **38**, 10208–10214.

[138] J. C. Malaquias, M. Steichen, M. Thomassey and P. J. Dale, Electrochimica Acta, 2013, **103**, 15–22.

[139] P. De Vreese, A. Skoczylas, E. Matthijs, J. Fransaer and K. Binnemans, Electrochimica Acta, 2013, **108**, 788–794.

[140] P. Chung, P. Cantwell, G. Wilcox and G. W. Critchlow, Transactions of the IMF, 2008, **86**, 211–219.

[141] H. Yang, X. Guo, X. Chen, S. Wang, G. Wu, W. Ding and N. Birbilis, Electrochimica Acta, 2012, **63**, 131–138.

[142] S. M. Gengan Saravanan, Int. J. Electrochem. Sci, 2011, **6**, 1468–1478.

[143] M. Steichen, M. Thomassey, S. Siebentritt and P. J. Dale, Physical Chemistry Chemical Physics, 2011, **13**, 4292–4302.

[144] E. Budevski, G. Staikov and W. Lorenz, Electrochimica Acta, 2000, **45**, 2559–2574.

[145] H. Fischer, Elektrolytische Abscheidung und Elektrokristallisation von Metallen, Springer, 1954.

[146] G. Hills, D. Schiffrin and J. Thompson, Electrochimica Acta, 1974, **19**, 657–670.

[147] M. Avrami, The Journal of Chemical Physics, 1941, **9**, 177–184.

[148] B. Scharifker and G. Hills, Electrochimica Acta, 1983, **28**, 879–889.

[149] B. Scharifker and J. Mostany, Journal of Electroanalytical Chemistry and Interfacial Electrochemistry, 1984, **177**, 13–23.

[150] L. Heerman and A. Tarallo, Journal of Electroanalytical Chemistry, 1999, **470**, 70–76.

[151] M. Azam, Ph.D. thesis, University of Leicester, 2012.

[152] T. Erdey-Grúz and M. Volmer, Zeitschrift für physikalische Chemie, 1930, **150**, 203–213.

[153] M. E. Hyde and R. G. Compton, Journal of Electroanalytical Chemistry, 2003, **549**, 1–12.

154 N. Kaiser, Applied optics, 2002, **41**, 3053–3060.

155 J. Venables, G. Spiller and M. Hanbucken, Reports on Progress in Physics, 1984, **47**, 399.

156 M. J. Henderson, A. R. Hillman and E. Vieil, Journal of Electroanalytical Chemistry, 1998, **454**, 1–8.

157 M. J. Henderson, A. R. Hillman, E. Vieil and C. Lopez, Journal of Electroanalytical Chemistry, 1998, **458**, 241–248.

158 R. Taylor and R. Krishna, Multicomponent Mass Transfer, John Wiley & Sons, 1993, vol. 2.

159 S. J. Kline, W. C. Reynolds, F. Schraub and P. Runstadler, Journal of Fluid Mechanics, 1967, **30**, 741–773.

160 What is Reynolds Number - Definition of Reynolds Number, `https://www.nuclear-power.net/nuclear-engineering/fluid-dynamics/reynolds-number/`.

161 Reynolds Number, 2014, `https://www.grc.nasa.gov/WWW/BGH/reynolds.html`.

162 O. Fischer and E. Fischerová, in Experimental Techniques in Bioelectrochemistry, Springer, 1995, vol. 91, pp. 41–157.

163 S. P. Kounaves, Voltammetric Techniques, 1997.

164 A. J. Bard and J. Ketelaar, Journal of The Electrochemical Society, 1974, **121**, 212C–212C.

165 L.-H. L. Miaw and S. Perone, Analytical Chemistry, 1979, **51**, 1645–1650.

166 T. M. Nahir, R. A. Clark and E. F. Bowden, Analytical Chemistry, 1994, **66**, 2595–2598.

167 J. Heinze, Angewandte Chemie International Edition in English, 1984, **23**, 831–847.

168 N. Elgrishi, K. J. Rountree, B. D. McCarthy, E. S. Rountree, T. T. Eisenhart and J. L. Dempsey, Journal of Chemical Education, 2017, **95**, 197–206.

169 R. S. Nicholson, Analytical Chemistry, 1965, **37**, 1351–1355.

170 P. T. Kissinger and W. R. Heineman, Journal of Chemical Education, 1983, **60**, 702.

171 G. A. Mabbott, Journal of Chemical Education, 1983, **60**, 697.

172 F. Cottrell, Z Physik Chem, 1902, **42**, 385.

173 R. G. Compton and C. E. Banks, Understanding voltammetry, World Scientific, 2011.

174 H. Matsuda and Y. Ayabe, <u>Bulletin of the Chemical Society of Japan</u>, 1955, **28**, 422–428.

175 C. Du, Q. Tan, G. Yin and J. Zhang, in <u>Rotating Electrode Methods and Oxygen Reduction Electrocatalysts</u>, Elsevier, 2014, pp. 171–198.

176 W. D. Sides and Q. Huang, <u>Electrochimica Acta</u>, 2018, **266**, 185–192.

177 A. J. Bard, L. R. Faulkner <u>et al.</u>, <u>Electrochemical Methods</u>, 2001, **2**, 482.

178 Q.-X. Zha, <u>Science Press, Beijing</u>, 2002, 182.

179 M. Lovrić and J. Osteryoung, <u>Journal of Electroanalytical Chemistry and Interfacial Electrochemistry</u>, 1986, **197**, 63–75.

180 S. Treimer, A. Tang and D. C. Johnson, <u>Electroanalysis</u>, 2002, **14**, 165.

181 J. Curie, <u>Bull. Soc. Fr. Mineral.</u>, 1880, **3**, 90.

182 O. Kurtz, J. Barthelmes, R. Rüther, M. Wünsche and C. Donner, <u>Electrochemistry a. Plating Technology</u>, 2010, **5**, year.

183 A. R. Hillman, <u>Journal of Solid State Electrochemistry</u>, 2011, **15**, 1647–1660.

184 G. Sauerbrey, <u>Zeitschrift für physik</u>, 1959, **155**, 206–222.

185 T. Nomura and M. Iijima, <u>Analytica Chimica Acta</u>, 1981, **131**, 97–102.

186 S. Bruckenstein and M. Shay, <u>Electrochimica Acta</u>, 1985, **30**, 1295–1300.

187 K. K. Kanazawa and J. G. Gordon, <u>Analytical Chemistry</u>, 1985, **57**, 1770–1771.

188 K. K. Kanazawa and J. G. Gordon II, <u>Analytica Chimica Acta</u>, 1985, **175**, 99–105.

189 M. Françon, in <u>Neutron Interferometry</u>, 1979.

190 P. Hariharan, <u>Optical Interferometry, 2e</u>, Elsevier, 2003.

191 A. Baumann, A. Faust, M. P. Law, M. T. Kuhlmann, K. Kopka, M. Schafers and U. Karst, <u>Analytical Chemistry</u>, 2011, **83**, 5415–5421.

192 P. Y. Apel, Y. E. Korchev, Z. Siwy, R. Spohr and M. Yoshida, <u>Nuclear Instruments and Methods in Physics Research Section B: Beam Interactions with Materials and Atoms</u>, 2001, **184**, 337–346.

193 Y.-K. Sun, D.-H. Kim, C. S. Yoon, S.-T. Myung, J. Prakash and K. Amine, Advanced Functional Materials, 2010, **20**, 485–491.

194 I. H. Omar, H. Pauling and K. Jüttner, Journal of The Electrochemical Society, 1993, **140**, 2187–2192.

195 P. Andricacos, J. Tabib and L. Romankiw, Journal of the Electrochemical Society, 1988, **135**, 1172–1174.

196 C. Barbero, M. Miras, R. Kötz and O. Haas, Solid State Ionics, 1993, **60**, 167–172.

197 C. A. Barbero, Physical Chemistry Chemical Physics, 2005, **7**, 1885–1899.

198 C. Barbero, M. Miras and R. Kötz, Electrochimica Acta, 1992, **37**, 429–437.

199 L. Abrantes, M. Oliveira and E. Vieil, Electrochimica Acta, 1996, **41**, 1515–1524.

200 A. R. Hillman, K. S. Ryder, C. J. Zaleski, V. Ferreira, C. A. Beasley and E. Vieil, Electrochimica Acta, 2014, **135**, 42–51.

201 E. Vieil, Journal of Electroanalytical Chemistry, 1994, **364**, 9–15.

202 P. L. Davies, U. Gather, M. Meise, D. Mergel, T. Mildenberger et al., The Annals of Applied Statistics, 2008, **2**, 861–886.

203 V. B. Kumar, G. Kimmel, Z. Porat and A. Gedanken, New Journal of Chemistry, 2015, **39**, 5374–5381.

204 T. Dobrovolska, I. Krastev, B. Jović, V. Jović, G. Beck, U. Lačnjevac and A. Zielonka, Electrochimica Acta, 2011, **56**, 4344–4350.

205 S. P. Singh and B. Karmakar, Plasmonics, 2011, **6**, 457–467.

206 V.-F. Ruiz-Ruiz, I. Zumeta-Dube, D. Díaz, M. J. Arellano-Jimenez and M. Jose-Yacaman, The Journal of Physical Chemistry C, 2016, **121**, 940–949.

207 P. Kumar, J. Singh and A. C. Pandey, RSC Advances, 2013, **3**, 2313–2317.

208 D. M. Moore and R. C. Reynolds, X-ray Diffraction and the Identification and Analysis of Clay Minerals, Oxford university press Oxford, 1989, vol. 322.

209 M. A. Skopek, M. A. Mohamoud, K. S. Ryder and A. R. Hillman, Chemical Communications, 2009, 935–937.

210 C. J. Zaleski, <u>Ph.D. thesis</u>, University of Leicester, 2015.

211 U. Schröder, J. D. Wadhawan, R. G. Compton, F. Marken, P. A. Suarez, C. S. Consorti, R. F. de Souza and J. Dupont, <u>New Journal of Chemistry</u>, 2000, **24**, 1009–1015.

212 D. MacFarlane, S. Forsyth, J. Golding and G. Deacon, <u>Green Chemistry</u>, 2002, **4**, 444–448.

213 B. Huber and B. Roling, <u>Electrochimica Acta</u>, 2011, **56**, 6569–6572.

214 A. Yavuz, <u>Ph.D. thesis</u>, University of Leicester, 2015.

215 V. Colvin, A. Goldstein and A. Alivisatos, <u>Journal of the American Chemical Society</u>, 1992, **114**, 5221–5230.

216 I. U. Vakarelski, C. E. McNamee and K. Higashitani, <u>Colloids and Surfaces A: Physicochemical and Engineering Aspects</u>, 2007, **295**, 16–20.

217 M. B. Ali, F. Bessueille, J.-M. Chovelon, A. Abdelghani, N. Jaffrezic-Renault, M. Maaref and C. Martelet, <u>Materials Science and Engineering: C</u>, 2008, **28**, 628–632.

218 A. Kaminska, O. Inya-Agha, R. J. Forster and T. E. Keyes, <u>Physical Chemistry Chemical Physics</u>, 2008, **10**, 4172–4180.

219 K. C. Grabar, K. J. Allison, B. E. Baker, R. M. Bright, K. R. Brown, R. G. Freeman, A. P. Fox, C. D. Keating, M. D. Musick and M. J. Natan, <u>Langmuir</u>, 1996, **12**, 2353–2361.

220 K. C. Grabar, P. C. Smith, M. D. Musick, J. A. Davis, D. G. Walter, M. A. Jackson, A. P. Guthrie and M. J. Natan, <u>Journal of the American Chemical Society</u>, 1996, **118**, 1148–1153.

221 J. A. Harnisch, A. D. Pris and M. D. Porter, <u>Journal of the American Chemical Society</u>, 2001, **123**, 5829–5830.

222 O. Seitz, M. M. Chehimi, E. Cabet-Deliry, S. Truong, N. Felidj, C. Perruchot, S. J. Greaves and J. F. Watts, <u>Colloids and Surfaces A: Physicochemical and Engineering Aspects</u>, 2003, **218**, 225–239.

223 J. Coenen, <u>RDE2 User Manual</u>, Metrohm Autolab B.V., Utrecht, The Netherlands, 2nd edn., 2007.

224 C. Barbero and M. Miras, Journal of the Argentine Chemical Society, 2003, pp. 1–40.

225 G. G. Láng and C. A. Barbero, <u>Laser techniques for the study of electrode processes</u>, Springer Science & Business Media, 2012.

226 S. Gražulis, A. Daškevič, A. Merkys, D. Chateigner, L. Lutterotti, M. Quiros, N. R. Serebryanaya, P. Moeck, R. T. Downs and A. Le Bail, Nucleic acids research, 2011, **40**, D420–D427.

227 M. J. Henderson, E. Bitziou, A. R. Hillman and E. Vieil, Journal of the Electrochemical Society, 2001, **148**, E105–E111.

228 H. M. French, M. J. Henderson, A. R. Hillman and E. Vieil, Solid State Ionics, 2002, **150**, 27–37.

229 R. Eriksson, Electrochimica Acta, 1996, **41**, 871–878.

230 A. R. Hillman, K. S. Ryder, C. J. Zaleski, C. Fullarton and E. L. Smith, Zeitschrift für Physikalische Chemie, 2012, **226**, 1049–1068.

231 A. R. Hillman, K. S. Ryder, V. C. Ferreira, C. J. Zaleski and E. Vieil, Electrochimica Acta, 2013, **110**, 418–427.

232 D. Johannsmann, Physical Chemistry Chemical Physics, 2008, **10**, 4516–4534.

233 S. Servagent and E. Vieil, Journal of Electroanalytical Chemistry and Interfacial Electrochemistry, 1990, **280**, 227–232.

234 N. Lassalle, A. Roget, T. Livache, P. Mailley and E. Vieil, Talanta, 2001, **55**, 993–1004.

235 O. Schneider, A. Bund, A. Ispas, N. Borissenko, S. Zein El Abedin and F. Endres, The Journal of Physical Chemistry B, 2005, **109**, 7159–7168.

236 M. A. Mohamoud and A. R. Hillman, Journal of Solid State Electrochemistry, 2007, **11**, 1043–1050.

237 M. Skompska and A. Tarajko-Wazny, Electrochimica Acta, 2011, **56**, 3494–3499.

238 H. Gomez, R. Henrıquez, R. Schrebler, G. Riveros and R. Cordova, Electrochimica Acta, 2001, **46**, 821–827.

239 Z. Jusys, H. Massong and H. Baltruschat, Journal of the Electrochemical Society, 1999, **146**, 1093–1098.

240 P. Kern and D. Landolt, Electrochimica Acta, 2001, **47**, 589–598.

241 A. Glidle, A. R. Hillman, K. S. Ryder, E. L. Smith, J. M. Cooper, R. Dalgliesh, R. Cubitt and T. Geue, Electrochimica Acta, 2009, **55**, 439–450.

242 M. Hepel, S. Bruckenstein and K. Kanige, Journal of the Chemical Society, Faraday Transactions, 1993, **89**, 251–254.

243 M. Santos, M. Cabral and S. Machado, Electrochimica Acta, 2011, **58**, 1–5.

244 A. R. Hillman, D. C. Loveday and S. Bruckenstein, Journal of Electroanalytical Chemistry and Interfacial Electrochemistry, 1989, **274**, 157–166.

245 A. R. Hillman, M. J. Swann and S. Bruckenstein, Journal of Electroanalytical Chemistry and Interfacial Electrochemistry, 1990, **291**, 147–162.

246 J. Bacskai, K. Martinusz, E. Czirok, G. Inzelt, P. Kulesza and M. Malik, Journal of Electroanalytical chemistry, 1995, **385**, 241–248.

247 A. Bund and S. Neudeck, The Journal of Physical Chemistry B, 2004, **108**, 17845–17850.

248 A. R. Hillman, S. J. Daisley and S. Bruckenstein, Electrochemistry Communications, 2007, **9**, 1316–1322.

249 L. T. T. Kim, C. Gabrielli, H. Perrot, J. Garcia-Jareno and F. Vicente, Electrochimica Acta, 2012, **84**, 35–48.

250 H. J. Salavagione, J. Arias-Pardilla, J. Pérez, J. Vázquez, E. Morallon, M. C. Miras and C. Barbero, Journal of Electroanalytical Chemistry, 2005, **576**, 139–145.

251 L. Abrantes and J. Correia, Electrochimica Acta, 1999, **44**, 1901–1910.

252 J. P. Correia, E. Vieil and L. M. Abrantes, Journal of Electroanalytical Chemistry, 2004, **573**, 299–306.

253 J. Hartley, Ph.D. thesis, University of Leicester, 2013.

254 T. Kekesi and M. Isshiki, Journal of Applied Electrochemistry, 1997, **27**, 982–990.

255 S. Bruckenstein, A. Fensore, Z. Li and A. R. Hillman, Journal of Electroanalytical Chemistry, 1994, **370**, 189–195.

256 A. R. Hillman, S. J. Daisley and S. Bruckenstein, Electrochimica Acta, 2008, **53**, 3763–3771.

257 A. P. Abbott, G. Frisch, J. Hartley, W. O. Karim and K. S. Ryder, Progress in Natural Science: Materials International, 2015, **25**, 595–602.

258 J. M. Hartley, C.-M. Ip, G. C. Forrest, K. Singh, S. J. Gurman, K. S. Ryder, A. P. Abbott and G. Frisch, Inorganic chemistry, 2014, **53**, 6280–6288.

259 A. P. Abbott, G. Capper, K. J. McKenzie and K. S. Ryder, Journal of Electroanalytical Chemistry, 2007, **599**, 288–294.

260 B. K. Niece and A. A. Gewirth, Langmuir, 1996, **12**, 4909–4913.

261 C. H. Chen, K. D. Kepler, A. A. Gewirth, B. Ocko and J. Wang, The Journal of Physical Chemistry, 1993, **97**, 7290–7294.

262 K. Tamura, J. Wang, R. Adžic and B. Ocko, The Journal of Physical Chemistry B, 2004, **108**, 1992–1998.

263 L. Heerman and W. D'Olieslager, Journal of The Electrochemical Society, 1991, **138**, 1372–1376.

264 G. R. Stafford and U. Bertocci, The Journal of Physical Chemistry B, 2006, **110**, 15493–15498.

265 M. Hepel, K. Kanige and S. Bruckenstein, Journal of electroanalytical chemistry and interfacial electrochemistry, 1989, **266**, 409–421.

266 S. M. Skogvold, Ø. Mikkelsen and K. H. Schrøder, Electroanalysis: An International Journal Devoted to Fundamental and Practical Aspects of Electroanalysis, 2005, **17**, 1938–1944.

267 Ø. Mikkelsen and K. H. Schrøder, Analyst, 2000, **125**, 2163–2165.

268 T. Valkova and I. Krastev, Transactions of the IMF, 2002, **80**, 13–15.

269 S. Fletcher, C. Halliday, D. Gates, M. Westcott, T. Lwin and G. Nelson, Journal of Electroanalytical Chemistry and Interfacial Electrochemistry, 1983, **159**, 267–285.

270 D. Buttry, In Electroanalytical Chemistry; Bard, AJ, Ed, 1991.

271 M. R. Deakin and D. A. Buttry, Analytical Chemistry, 1989, **61**, 1147–1154.

272 A. Bund, Journal of Solid State Electrochemistry, 2004, **8**, 182–186.

273 A. P. Abbott, S. Nandhra, S. Postlethwaite, E. L. Smith and K. S. Ryder, Physical Chemistry Chemical Physics, 2007, **9**, 3735–3743.

274 A. R. Hillman, I. Efimov and M. Skompska, Journal of the American Chemical Society, 2005, **127**, 3817–3824.

275 A. J. Bard, L. R. Faulkner, J. Leddy and C. G. Zoski, Electrochemical methods: fundamentals and applications, wiley New York, 1980, vol. 2.

[276] A. Mashreghi and H. Zare, Current Applied Physics, 2016, **16**, 599–604.

[277] G. Gunawardena, G. Hills, I. Montenegro and B. Scharifker, Journal of Electroanalytical Chemistry and Interfacial Electrochemistry, 1982, **138**, 225–239.

[278] M. Abyaneh and M. Fleischmann, Journal of Electroanalytical Chemistry and Interfacial Electrochemistry, 1981, **119**, 187–195.

[279] A. Abbott, M. Azam, K. Ryder and S. Saleem, Transactions of the IMF, 2018, **96**, 297–303.

[280] G. Oskam, J. Long, A. Natarajan and P. Searson, Journal of Physics D: Applied Physics, 1998, **31**, 1927.

[281] M. Palomar-Pardavé, B. Scharifker, E. Arce and M. Romero-Romo, Electrochimica Acta, 2005, **50**, 4736–4745.

[282] L. Vieira, A. Whitehead and B. Gollas, Journal of The Electrochemical Society, 2014, **161**, D7–D13.

[283] D. Lloyd, T. Vainikka, S. Schmachtel, L. Murtomäki and K. Kontturi, Electrochimica Acta, 2012, **69**, 139–145.

[284] D. Lloyd, T. Vainikka, L. Murtomäki, K. Kontturi and E. Ahlberg, Electrochimica Acta, 2011, **56**, 4942–4948.

[285] L. Vieira, R. Schennach and B. Gollas, Electrochimica Acta, 2016, **197**, 344–352.

[286] L. Vieira, J. Burt, P. W. Richardson, D. Schloffer, D. Fuchs, A. Moser, P. N. Bartlett, G. Reid and B. Gollas, ChemistryOpen, 2017, **6**, 393–401.

[287] M. M. Badea, A. Cojocaru and L. Anicai, UPB Sci. Bull. Series B, 2014, **76**, 21–32.

[288] A. P. Abbott, R. C. Harris and K. S. Ryder, The Journal of Physical Chemistry B, 2007, **111**, 4910–4913.

[289] T. Dobrev, M. Monev, S. Nikolova et al., Surface and Coatings Technology, 1986, **29**, 27–39.

[290] E. P. Harbulak, Method for simultaneous determination of thickness and electrochemical potential in multilayer plated deposits, 1982, US Patent 4,310,389.

[291] E. P. Harbulak, SAE Transactions, 1980, 1760–1768.

[292] M. Birkholz, P. Fewster and C. Genzel, Wiley VCH, ISBN, 2006, **3**, 31o25.